Doctoral Dissertation
Doctoral Program in Sustainable Materials, Processes and Systems for Energy Transition (38th Cycle)

# Development of novel catalysts for e-fuel production

**Stefano Scognamiglio**
* * * * * *

**Supervisors**
Dr. Gianluca Landi
Dr. Giovanna Ruoppolo
Dr. Valentina Gargiulo

Politecnico di Torino
January 30, 2026

I hereby declare that, the contents and organisation of this dissertation constitute my own original work and does not compromise in any way the rights of third parties, including those relating to the security of personal data.

…….....

Stefano Scognamiglio

Turin, January 30, 2026

# Summary

The urgent need to mitigate anthropogenic $CO_2$ emissions while ensuring energy security has positioned Carbon Capture Utilisation and Storage (CCUS) technologies as a benchmark for the global energy transition.

In the framework of CCU, this thesis investigated the catalytic hydrogenation of $CO_2$ into high-value energy carriers through two primary pathways: Power-to-Methane (PtM) and Power-to-Liquid (PtL). By integrating advanced catalyst synthesis, multi-scale characterisation and process simulation, this work addresses the fundamental challenge of coupling catalyst architecture and process design to overcome kinetic and thermodynamic barriers in circular carbon systems.

The work combines experimental catalysis with process-level thermodynamic and kinetic analysis. In the PtM pathway, $CO_2$ methanation was studied using both conventional steady-state operation and integrated carbon capture and utilisation (ICCU) strategies. Ni-supported on ultra-stable Y (USY) zeolites demonstrated optimal performance, in particular with an exceptional resistance to coke formation. The study also revealed that the hierarchical porosity of the zeolite framework and the size of metal particles are critical aspects governing catalytic behaviour of catalysts, with performance driven by particle size and dispersion rather than by thermodynamic constraints. Furthermore, rhenium-based dual-functional materials enabled temporally decoupled $CO_2$ capture and conversion steps, achieving 100% methane selectivity and demonstrating that the synergy between catalytic sites and adsorbent functions can effectively bypass the selectivity limitations of conventional continuous processes.

In contrast, $CO_2$ hydrogenation to methanol revealed different constraints related to thermodynamics. Cu-based catalysts showed methanol selectivity only within a tight temperature range (150 – 200°C), beyond which the reverse water-gas shift (RWGS) and methanation reactions became dominant, proving that process optimisation relies on catalysts characteristics, such as a precise control of

the metal-support interface, which can be effectively tuned by the choice of metal precursor. This behaviour reflects the intrinsic thermodynamic limitation of methanol synthesis, where higher temperatures improve kinetics but disfavour equilibrium conversion. Process simulations were performed with Aspen Plus® and demonstrated that single-pass adiabatic reactors are inherently limited, achieving low $CO_2$ conversion and methanol yield, whereas syngas recycle significantly enhanced overall performance, increasing $CO_2$ conversion to ~75% and methanol yield to ~65% without altering catalyst formulation.

Exploratory screening of Cu-Fe-Ce and Cu-Fe catalysts at elevated pressure showed predominant selectivity toward CO and $CH_4$ rather than methanol, but they are interesting for further and deeper investigations. These findings confirm that catalyst selectivity is controlled by the combined effects of metal composition, redox behaviour, and operating regime, and that methanol synthesis requires catalyst architectures specifically tailored to its requirements.

Overall, the thesis demonstrates that effective $CO_2$ utilisation cannot rely on catalyst development alone. For PtM, flexibility in catalyst-process coupling enables operation under diverse regime, including dynamic conditions. For PtL, stringent thermodynamic constraints necessitate precise catalyst design supported by advanced reactor configurations. This work contributes to the progress in CO2-based e-fuel technologies providing novel insights in the integrated approach including catalysts development and process engineering, providing a framework for rational design of future circular carbon systems.

# Acknowledgment

This doctoral research was financially supported by the *iENTRANCE* project. The author gratefully acknowledges the funding provided within this framework, which enabled the research activities presented in this thesis.

The author would like to thank his supervisors, Giovanna Ruoppolo and Valentina Gargiulo, for their guidance, support, and constructive scientific discussions throughout the PhD programme.

He also gratefully acknowledges Laurent Piccolo and Franck Morfin at IRCELYON for their supervision during the research stay, as well as for the stimulating scientific environment and valuable exchanges.

Last but not least, the author expresses his deepest gratitude to Gianluca Landi, whose guidance, mentorship, and constant support were fundamental throughout this PhD journey. His influence has been decisive not only for the development of this work, but also for the author's scientific and professional growth.

Finally, the author acknowledges the support of his family throughout this journey.

*To Gaia and my loving parents.*

# 1. Contents

# List of Tables

# List of Figure

# List of Abbreviations

| *Abbreviation* | *Meaning* |
|---|---|
| ***BET*** | Brunauer – Emmett – Teller method |
| ***CCS*** | Carbon Capture and Storage |
| ***CCU*** | Carbon Capture and Utilisation |
| ***CCUS*** | Carbon Capture, Utilisation and Storage |
| ***CLC*** | Chemical Looping Combustion |
| ***CZA*** | $Cu/ZnO/Al_2O_3$ catalyst |
| ***DAC*** | Direct Air Capture |
| ***DFM*** | Dual-Functional Material |
| ***DME*** | Dimethyl Ether |
| ***DRIFTS*** | Diffuse Reflectance Infrared Fourier Transform Spectroscopy |
| ***EEA*** | European Environment Agency |
| ***EOR*** | Enhanced Oil Recovery |
| ***GHG*** | Greenhouse Gas |
| ***HAADF-STEM*** | High-Angle Annular Dark-Field Scanning Transmission Electron Microscopy |
| ***HZSM-5*** | Protonic form of Zeolite Socony Mobil – 5 |
| ***ICCU*** | Integrated Carbon Capture and Utilisation |
| ***IEA*** | International Energy Agency |
| ***IGCC*** | Integrated Gasification Combined Cycle |
| ***IPCC*** | Intergovernmental Panel on Climate Change |
| ***LCA*** | Life Cycle Assessment |
| ***LDH*** | Layered Double Hydroxide |
| ***NOAA*** | National Oceanic and Atmospheric Administration |
| ***PtF*** | Power-to-Fuel |
| ***PtG*** | Power-to-Gas |
| ***PtL*** | Power-to-Liquid |
| ***PtM*** | Power-to-Methane |
| ***RWGS*** | Reverse Water-Gas Shift |
| ***SEM*** | Scanning Electron Microscopy |
| ***STEM*** | Scanning Transmission Electron Microscopy |
| ***TEM*** | Transmission Electron Microscopy |
| ***TOF*** | Turnover Frequency |
| ***TPD*** | Temperature-Programmed Desorption |
| ***TPO*** | Temperature-Programmed Oxidation |
| ***TPR*** | Temperature-Programmed Reduction |
| ***TPSR*** | Temperature-Programmed Surface Reaction |
| ***TRL*** | Technology Readiness Level |
| ***USY*** | Ultra-Stable Y-type zeolite |
| ***WHSV*** | Weight Hourly Space Velocity |
| ***XRD*** | X-ray Diffraction |

# Chapter 1

# 1. Climate Change, Carbon Management and $CO_2$ Conversion Pathways

## 1.1 Global Climate Context and Emission Trends

Climate change and global warming represent some of the most urgent and multifaceted environmental challenges of our time, primarily driven by the continuous rise in greenhouse gas (GHG) emissions. Carbon dioxide ($CO_2$) is the most abundant of these, accounting for about 80% of total GHG emissions, followed by methane ($CH_4$) and nitrous oxide ($N_2O$), with respective shares of 11% and 6%; the remaining few percent consists mainly of fluorinated gases such as HFCs, PFCs, $SF_6$, and $NF_3$[1]. The predominance of $CO_2$ in the global GHG balance explains why its atmospheric accumulation plays a central role in climate change[2,3]. Notably, $CO_2$ concentrations reached 431 ppm in May 2025 according to the U.S. National Oceanic and Atmospheric Administration (NOAA)[4] – the highest level in human history.

The increasing atmospheric $CO_2$ burden is mirrored by a persistent rise in global temperatures. Figure 1.1 displays the annual global surface temperature anomaly from 1880 to 2024 relative to the 20$^{th}$-century mean. According to the NOAA and the Intergovernmental Panel on Climate Change (IPCC), global temperatures have increased by approximately 0.06°C per decade since 1850[5,6]. However, the warming rate has accelerated markedly over the past three decades, reaching nearly 0.2°C per decade, reflecting an alarming intensification of climate change[7].

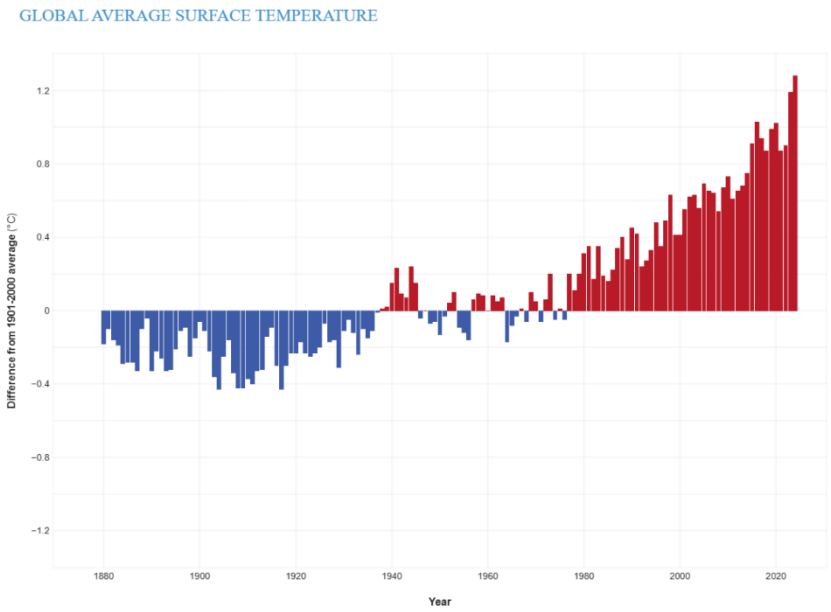


**Figure 1.1. Yearly surface temperature from 1880-2024 compared to the 20th-century average (1901-2000). Blue bars indicate cooler-than-average years; red bars show warmer-than-average years. NOAA Climate.gov graph, based on data from the National Centers for Environmental Information [5].**

The consequences of rising global temperatures extend far beyond atmospheric warming and are increasingly reflected in the degradation of natural ecosystems, including the intensification of extreme weather events such as hurricanes, heatwaves and severe storms[8] – in 2018 there were 315 cases of natural disaster mainly climate-related according to the Centre for Research on the Epidemiology of Disaster (CRED)[9]. Marine environments, in particular, are experiencing severe impacts such as ocean acidification, accelerated glacier retreat, sea-level rise and significant shifts in specie distributions, as documented by the IPCC and the European Environment Agency (EEA)[10,11]. These effects underscore the urgency of reducing $CO_2$ emissions and stabilising the global carbon cycle, including through technologies that actively manage and reuse carbon.

The continuous rise in global average temperatures, estimated to increase by approximately 0.27°C to 0.63°C for every 1000 Gt $CO_2$ emitted by human activity[12], has placed $CO_2$ at the centre of scientific, political, and industrial attention. In this framework, $CO_2$ is not only recognised as the principal driver of anthropogenic climate change, but it is also increasingly being considered as a potential carbon feedstock for sustainable chemical and energy systems, provided that low-carbon energy carriers are available to enable its conversion.

Global energy-related $CO_2$ emissions continue to rise despite the increasing deployment of renewable energy technologies. According to recent analysis of the International Energy Agency (IEA), the total energy-related $CO_2$ emissions increased by around 0.8% in 2024, reaching a new all-time high of about 37.4 Gt $CO_2$, even though the growth rate was lower than in 2023 thanks to the expansion of clean energy sources[13]. Global energy demand grew faster than its recent average in 2024, driven primarily by rising electricity consumption, and the

additional demand was covered not only by solar and wind but also by natural gas, coal, and nuclear power. In the power sector, the renewable share is projected to increase from approximately 30% in 2023 to 46% by 2030, with solar PV and wind accounting for almost all this growth. This trend confirms that, at the global scale, the energy system remains strongly dependent on fossil fuels. Nevertheless, the IEA also highlights a slowdown in emissions growth within advanced economies, largely driven by the rapid expansion of solar PV and wind power.

Beyond global aggregates, the regional distribution of emissions and mitigation efforts is highly uneven. Advanced economies have started to decouple economic growth from $CO_2$ emissions: in 2024, their energy-related emissions decreased by about 1.1%, mainly due to a 5.7% reduction in coal use and the increasing contribution of renewables and nuclear, which together now provide more than half of electricity generation. Within the European Union, quarterly greenhouse gas emissions fell by 4.0% in the first quarter of 2024 compared with the same period in 2023[14], while GDP remained almost unchanged, indicating a partial decoupling between economic activity and emissions. In contrast, emerging and developing economies – particularly in Asia – now account for roughly half of global $CO_2$ emissions, with China alone responsible for around 35% of global $CO_2$ emissions and India having recently overtaken the European Union as the third-largest emitter[15].

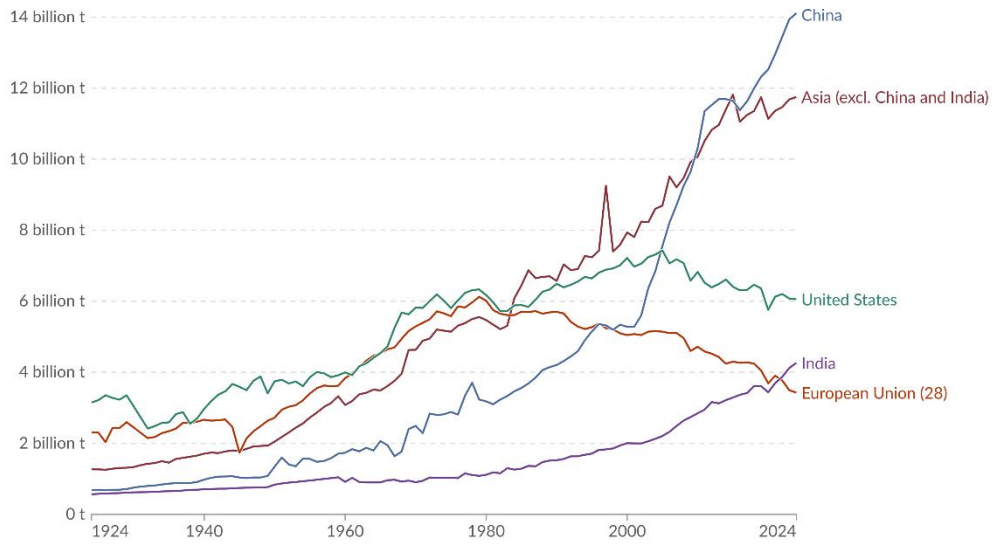


**Figure 1.2. Total greenhouse gas emissions ($CO_2$, $CH_4$ and $N_2O$, including emissions from land-use change), expressed as tonnes of $CO_2$-equivalent over a 100-year time horizon for China, India, Asia (excluding China and India), the United States and the European Union (28). Data adapted from Our World in Data (Jones et al., 2025)[16].**

Figure 1.2 illustrates these trends, highlighting the rapid rise of China's emissions since the early 2000s, the sustained growth of India and the rest of Asia (excluding China and India), and the contrasting decline observed in the United States and the European Union[16]. Together, these regional asymmetries underscore the increasingly central role of emerging Asian economies and show

that progress in advanced economies is outweighed by rising energy demand and continued reliance on fossil fuels in fast-growing regions.

In recent decades, the correlation between fossil fuel combustion and GHG emissions has become evident. Recent IEA estimates indicate that approximately 54% of the global energy mix still relies on fossil-based sources, while renewable and nuclear sources together account for the remaining 46% (Figure 1.3)[13]. Despite the rapid expansion of renewable technologies such as solar PV and wind, their large-scale deployment remains constrained by infrastructural, geographical, and intermittency-related limitations.

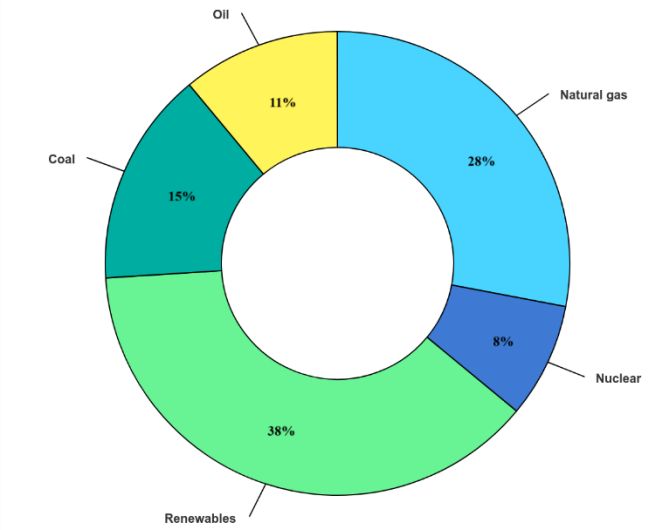


**Figure 1.3. Global breakdown of primary energy source in 2024 (IEA – *Global Energy Review 2025*)[13].**

To devise effective mitigation strategies, it is essential to identify the sectors responsible for the majority of global emissions. As illustrated in Figure 1.4, based on the latest EDGAR dataset[15], global greenhouse gas emissions have more than doubled since 1970, increasing of above 40% in the period 2000-2023, reaching approximately 53 Gt $CO_2$ in 2023. The figure highlights not only the rapid growth in total emissions but also the remarkable stability of their sectoral distribution over the past five decades. Power generation remains the dominant source, followed by industry, transport, buildings, agriculture, fossil fuel extraction and waste management. This persistent sectoral pattern reflects the structural nature of global emissions: most originate from activities that either rely heavily on fossil fuels (power, transport, buildings) or generate process-related emissions that are intrinsically difficult to eliminate (cement, steel, chemicals).
The per-capita emissions curve shown in Figure 1.4 further underscores this rigidity. Despite improvements in energy efficiency and substantial progress in renewable energy deployment, per-capita emissions have remained relatively constant since the 1980s. This indicates that the rise in global emissions cannot be attributed solely to population growth but rather to the continued reliance on carbon-intensive energy and industrial systems.

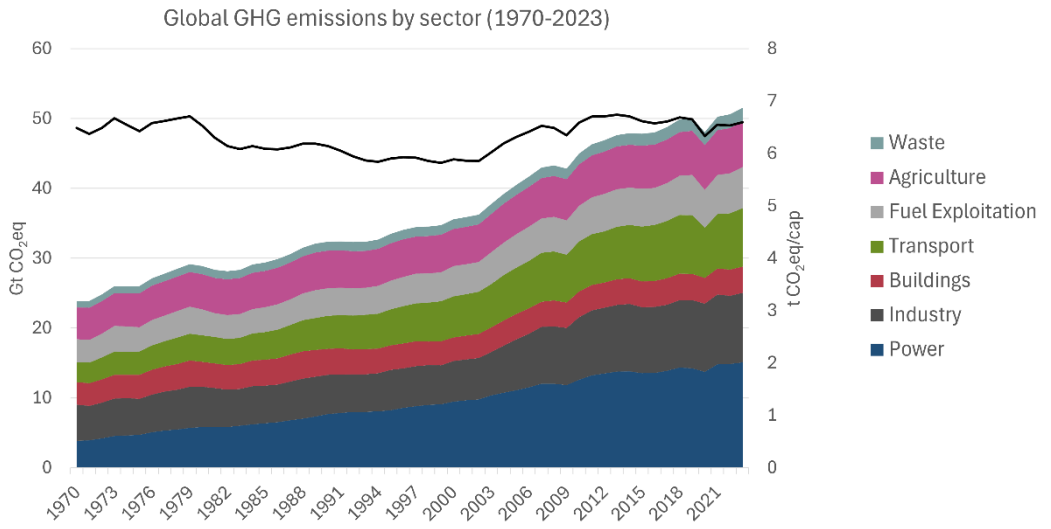


**Figure 1.4. Global GHG emissions by sector (left axis, bars) and per capita (right axis, black line), 1970-2023. Data from EDGAR dataset[15].**

These observations have important implications for climate mitigation. They highlight that deep decarbonisation/defossilization requires not only expanding renewable energy but also addressing hard-to-abate sectors where electrification or fuel switching alone is insufficient. This structural challenge explains why the energy sector, industry, transport and agriculture together persist as the main contributors to global GHG emissions.

Notably, data from the EEA indicate that carbon intensity of the EU energy system declined by more than 20% in 2023 compared to the previous year[17], reflecting ongoing shifts towards renewables and improved energy efficiency. However, this progress remains insufficient to meet short- and medium-term climate targets: as highlighted by the lates IPCC assessments, even a full-scale deployment of renewables alone is unlikely to achieve the necessary reduction in atmospheric $CO_2$ levels within the limited time frame available to avoid the worst consequences of climate change[12].

In this context, the urgency of rapid and deep emission reductions becomes even clearer when viewed against the targets established under the 2015 Paris Agreement, where 196 Parties committed to limiting global warming to 1.5 °C and pursuing efforts to remain well below 2 °C above pre-industrial levels[18,19]. To restrict the warming below these values, GHGs emissions need to be reduced to 45% by 2030, reaching the carbon neutrality by 2050[20,21]. However, recent assessments indicate that current emission trajectories are incompatible with these goals. According to the 2024 update of key climate indicators by Forster et al.[22], the remaining carbon budget compatible with a 50% probability of staying below 1.5 °C is expected to be exhausted within less than three years if emissions continue at present rates. Even the carbon budget associated with the 2 °C target offers only limited temporal flexibility, highlighting the increasing narrowness of feasible mitigation pathways[23].

These findings reinforce the conclusion that accelerating renewable energy deployment – while essential – will not on its own deliver the magnitude and speed of emissions reductions required to stabilise the climate system. The gap between current trajectories and the Paris temperature goals underscores the need for comprehensive mitigation strategies capable of addressing both energy-related and process-related emissions across all sectors.

## 1.2 Carbon Capture, Utilisation and Storage (CCUS)

Carbon Capture, Utilisation and Storage (CCUS) has gained increasing prominence as a critical component of contemporary climate mitigation strategies[24]. CCUS encompasses a suite of technologies designed to capture $CO_2$ from large point sources – such as power plants, refineries, and energy-intensive industrial facilities – and to either permanently store it in geological formations (Carbon Capture and Storage, CCS) or convert it into valuable products (Carbon Capture and Utilisation, CCU). By targeting emissions that cannot be fully eliminated through renewable energy deployment and electrification alone, CCUS provides a complementary pathway for the decarbonisation of hard-to-abate sectors such as cement, steel and chemicals[25].

Within this portfolio, CCS is currently the most discussed and widely implemented option. Large-scale demonstrations across multiple regions have shown that millions of tonnes of $CO_2$ per year can be captured, transported and injected into deep saline aquifers or depleted hydrocarbon reservoirs, where they can be retained over decadal to centennial timescales under appropriate geological and regulatory conditions[26]. When applied to power generation or energy-intensive industries, CCS can reduce the global warming potential (GWP) of the associated process by roughly 63-82%[27,28].

Despite these advantages, CCS also presents several structural limitations. Life-cycle assessment (LCA) studies, including those by Lenzen, Radaal and Modahl[29,30], reveal that CCS may increase other environmental impacts – such as acidification, eutrophication, human toxicity and resource depletion – due to the significant energy required for capture, compression, transport and injection, as well as potential long-term storage risks[29,31].

Carbon Capture and Utilisation (CCU) offers a complementary approach in which $CO_2$ is converted into marketable chemicals or fuels, thereby reducing dependence on fossil-derived carbon. Key utilisation pathways include methanation, methanol synthesis and dimethyl ether (DME) production, which can contribute to emission mitigation while simultaneously creating economically valuable products. However, the environmental performance of CCU is highly dependent on the selected conversion pathway and, critically, on the carbon intensity of the energy used for hydrogen production[32]. When hydrogen is produced via water electrolysis powered by renewable electricity, CCU processes can approach carbon neutrality and, in certain cases, achieve net reductions relative to conventional fossil-based production routes[33]. In addition to environmental benefits, CCU can deliver economic value by transforming $CO_2$

from a waste stream into an industrial feedstock, fostering the development of low-carbon markets and enhancing industrial competitiveness[27,34–38].

Taken together, CCS and CCU constitute the core components of CCUS systems, which are recognised as key mitigation tools for achieving net-zero emission pathways[39]. While CCS primarily ensures permanent removal of $CO_2$ from the atmosphere through geological storage, CCU offers a circular-carbon perspective by reintegrating $CO_2$ into chemical and energy value chains. Their combined deployment allows CCUS to address both unavoidable process emissions and the need for sustainable carbon feedstocks in a decarbonised/defossilized economy.

### 1.2.1 $CO_2$ Capture Technologies

Having outlined the role of CCS and CCU within mitigation strategies, attention must now shift to the technological stages that underpin all CCUS pathways. Among these, $CO_2$ capture is the most energy-intensive and cost-determining step (about 70-80% of total cost)[40,41], and its characteristics strongly influence both storage performance and the suitability of $CO_2$ streams for downstream utilisation processes.

A variety of technologies have been developed to separate $CO_2$ from flue gases, syngas, or ambient air, each characterised by distinct principles of operation, levels of technological maturity, and integration requirements. These methods can be broadly classified into post-combustion, pre-combustion, oxy-fuel processes, and a range of emerging alternatives including adsorption-based systems, membrane separation, cryogenic purification and direct air capture (DAC) as showed in Figure 1.5.

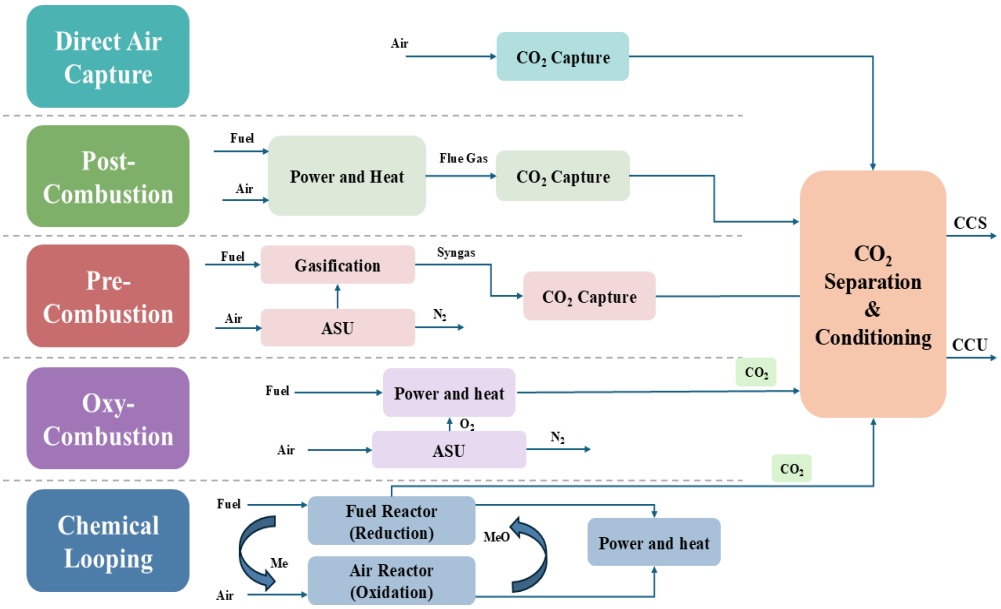


**Figure 1.5. Schematic overview of the main $CO_2$ capture technologies. All routes converge toward $CO_2$ separation and conditioning, enabling both CCS and CCU pathways. Adapted from Dubey & Arora (2022)[40].**

### *Pre-combustion Capture*

Pre-combustion capture is based on the decarbonization of the primary fuel (such as coal, natural gas or biomass) prior to its combustion. The process begins with gasification or reforming to convert the feedstock into a synthesis gas (syngas) composed primarily of hydrogen ($H_2$) and carbon monoxide (CO). This is followed by a catalytic Water-Gas Shift (WGS) reaction ($CO + H_2O \rightarrow CO_2 + H_2$), which converts the CO into $CO_2$, resulting in a gas stream with a high concentration of $CO_2$ (typically 15-60%, dry basis[42]) and $H_2$. The carbon dioxide is then separated using physical or chemical absorption, adsorption, or membrane technologies, leaving a $H_2$-rich fuel gas for clean combustion.

A distinct advantage of this pathway is the high partial pressure of the gas stream, typically ranging between 2 and 7 MPa. This significantly facilitates $CO_2$ removal compared to post-combustion systems, allowing for the use of physical solvents (e.g. Selexol, Rectisol, or Purisol) that are less energy-intensive for regeneration. Consequently, the $CO_2$ outlet stream is at an elevated pressure, reducing the downstream energy penalty and equipment size required for compression and transport[43].

However, this separation efficiency is counterbalanced by the high energy and costs requirements of the upstream processes, including air separation, reforming/gasification, and the loss of energy recovery during syngas cooling[44]. Furthermore, widespread deployment in the power sector is constrained by the need for Integrated Gasification Combined Cycle (IGCC) infrastructure, characterized by high capital investment costs, technological complexity, and historically lower reliability compared to conventional combined-cycle plants[45–47]. These economic and operational barriers currently restrict the applicability of pre-combustion capture primarily to industrial settings where syngas generation is

already an intrinsic part of the process. Overall, a decrease in power plant efficiency of 6-11% has been reported for the pre-combustion route[40].

### *Post-combustion*

Post-combustion capture is the most mature and widely deployed $CO_2$ capture technology, with an easy possibility of integration in existing power plants without major modifications, designed to separate $CO_2$ from flue gas streams generated by the combustion of fossil fuels or biomass in air. These streams are characterised by relatively low $CO_2$ concentrations – typically below 20% - and near-atmospheric pressure, conditions that make $CO_2$ separation intrinsically energy-intensive and unsuitable for purely physical separation processes.

The dominant post-combustion route relies on chemical absorption using aqueous amine-based solvents. In this process, the flue gas is brought into contact with the solvent in an absorber column, where $CO_2$ reacts chemically with the amine species. The $CO_2$-rich solvent is subsequently transferred to a stripper column, where thermal regeneration releases a concentrated $CO_2$ stream while restoring the solvent for reuse. Despite its technological maturity, amine-based capture suffers from several well-known limitations, including high regeneration energy demand, solvent degradation, corrosion of process equipment, and operational complexity. These challenges have been reported in large-scale demonstration plants such as Boundary Dam (Canada) and Petra Nova (USA)[48], where solvent management and steam availability significantly affected capture performance and plant availability. These issues cause an efficiency losses for post-combustion capture range from approximately 9 to 14%, generally higher than those observed for pre-combustion route[40].

Prior to $CO_2$ separation, flue gases must undergo extensive conditioning, including denitrification, desulphurisation and particulate removal, in order to prevent solvent degradation and equipment fouling[49,50]. Following this pretreatment, the choice of the separation technology depends on several physicochemical parameters of the exhaust stream, such as temperature, pressure, $CO_2$ concentration, and gas flow rate[47]. While amine absorption remains the only fully commercialised post-combustion option, alternative approaches such as membrane-based separation are under active development. Membrane systems offer potential advantages in terms of modularity, lower capital costs and ease of integration, although multi-stage configurations and gas compression are often required to achieve competitive performance[46].

A fundamental limitation common to all post-combustion capture technologies is that they operate downstream of fuel combustion and therefore treat very large volumes of dilute flue gas[47]. As a result, capture units are inherently large, contributing to high capital expenditure and reinforcing the central role of the capture step as the main economic and energetic bottleneck of CCUS systems.

### *Oxy-fuel combustion*

Oxy-fuel combustion is a capture-ready approach in which the fuel is burned in a mixture of nearly pure oxygen and recycled flue gas instead of air. By eliminating nitrogen from the oxidant, the resulting exhaust gas consists primarily of $CO_2$ and water vapour. After stream condensation, a highly concentrated $CO_2$ stream is obtained, substantially simplifying the downstream separation stage compared with conventional post-combustion systems.

The high $CO_2$ concentration achieved in oxy-fuel combustion represents a major advantage from the capture perspective, as it reduces the need for complex separation units and enables more compact capture equipment. In addition, the process allows operation at lower solvent-to-gas ratios when chemical absorption is used, further decreasing absorber size and solvent circulation requirements. As a result, oxy-fuel systems are often regarded as one of the most energy-efficient capture routes among the conventional CCUS technologies[51], with reported efficiency penalties of approximately 4%, compared with 8-12% typically associated with post-combustion capture[49].

Despite these advantages, the main limitation of oxy-fuel combustion lies in the high energy demand associated with the air separation unit (ASU), whose electricity consumption leads to a significant reduction in net plant efficiency. Recent techno-economic assessments report efficiency penalties in the range of approximately 9-15%, primarily attributable to oxygen production[52,53], which currently represent one of the main barriers to large-scale commercial deployment of oxy-fuel combustion systems, restricting its deployment mainly to pilot- and demonstration-scale facilities[46,54].

### *Emerging capture technologies*

In addition to the established capture routes, several emerging technologies have been proposed to overcome some of the intrinsic limitations of conventional CCUS systems, particularly those related to energy penalties and process integration. Among these, chemical looping combustion (CLC) and direct air capture (DAC) have attracted growing attention in recent years, although both remain at relatively early stages of technological maturity compared to post-combustion, pre-combustion and oxy-fuel combustion.

Chemical looping combustion is based on the indirect oxidation of the fuel using a solid oxygen carrier, typically a low-cost metal oxide, which transports oxygen from an air reactor to a fuel reactor[55,56]. In this configuration, direct contact between fuel and air is avoided, and nitrogen dilution of the exhaust gas is eliminated. As a consequence, the flue gas exiting the fuel reactor consists mainly of $CO_2$ and $H_2O$, allowing straightforward separation through steam condensation. From a conceptual standpoint, CLC can be regarded as an intrinsically capture-ready combustion process, as $CO_2$ separation is achieved without the need for additional downstream capture units. However, despite its clear thermodynamic appeal, large-scale deployment of CLC is hindered by several unresolved challenges, including the long-term stability and attrition resistance of oxygen

carriers, solids circulation control, reactor design complexity, and scale-up of interconnected fluidized-bed systems[57]. To date, CLC remains largely confined to pilot-scale demonstration and laboratory studies, and no full commercial power plants based on this concept are in operation[58,59].

Direct air capture is emerging as one of the most promising carbon dioxide removal technologies, particularly because it is independent of emission source and can therefore address dispersed or hard-to-mitigate sectors. Unlike point-source capture, DAC removes $CO_2$ directly from ambient air, where its concentration is extremely low (~430 ppm). This intrinsic dilution constitutes the primary bottleneck of the technology, as highlighted by the reviews by Sodiq et al.[60] and by Jiang et al.[61], where the low driving force for mass transfer results in high sorbent requirements, elevated regeneration energy, and substantial operational expenditures.

Current research and development efforts focus on two main technological pathways: High-Temperature (HT) liquid-bases systems and Low-Temperature (LT) solid sorbents (e.g., amine-functionalised materials)[61,62]. The LT route is viewed favourably for its potential to integrate with readily available low-grade waste heat (70°C – 100°C), which can substantially reduce operating costs.

Techno-economic assessments indicate that while current capture costs are high (ranging from hundreds of dollars per tonne), sustained investment and technological learning could drive costs to approximately 50$/t$CO_2$ by 2025[62]. In the report "Direct Air Capture 2022", the IEA emphasizes that achieving the required gigatonne-per-year scale of deployment is highly dependent on ambitious policy support and, critically the secure supply of affordable, low-carbon energy (solar, wind, geothermal) to maintain a negative life-cycle carbon footprint[63].

Overall, emerging capture technologies such as CLC and DAC provide valuable long-term perspectives for $CO_2$ mitigation and removal, but their current technical complexity, energy demand and limited level of industrial maturity restrict their near-term contribution to CCUS deployment. Nevertheless, they play an important role in expanding the technological portfolio of carbon management options and in informing future systems-level integration strategies.

### 1.2.2 $CO_2$ separation technologies

The separation of $CO_2$ from gas mixtures is a central step in all CCUS systems and is required regardless of the specific capture route employed, but it depends on process conditions – such as $CO_2$ concentration, temperature, pressure and gas composition[46]. Broadly, $CO_2$ separation technologies can be classified into five main categories, as showed in Figure 1.6: absorption, adsorption, membrane separation, biological separation, cryogenic separation. Each of these technologies operates according to distinct principles, exhibits different energy requirements, and is associated with specific advantages and limitations, ultimately determining its suitability for industrial implementation.

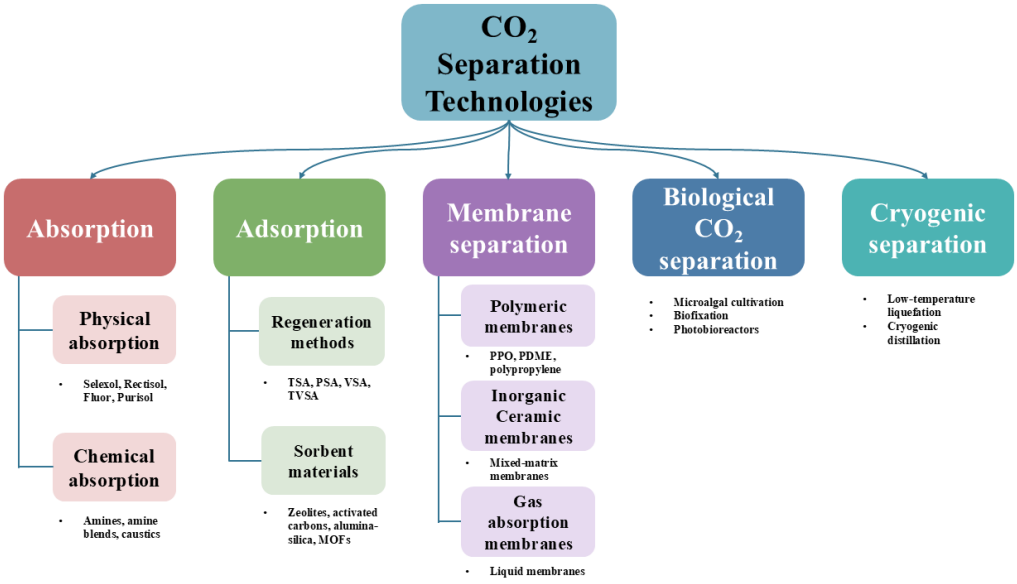


**Figure 1.6. Main $CO_2$ separation technologies and their principal sub-categories: absorption, adsorption, membrane-based, biological $CO_2$ removal, and cryogenic separation.**

### *Absorption*

Absorption is one of the most established technologies for $CO_2$ separation, having been extensively applied for decades in synthetic gas processing, natural gas upgrading, and petroleum refining. Fundamentally, absorption processes are categorised into two distinct classes based on the interaction mechanism between the solute and the solvent: chemical absorption, where $CO_2$ reacts with the solvent via acid-base interactions, and physical absorption, where $CO_2$ dissolution is governed by Henry's Law and depends primarily on temperature and partial pressure[40,46].

Chemical absorption represents the most mature $CO_2$ separation technique, widely recognized as the dominant technology for post-combustion capture. In these systems, $CO_2$ reacts reversibly with a chemical solvent – typically an aqueous alkanolamine solution – to form intermediate ionic species (carbamates or bicarbonates)[49]. This reaction is reversed in a regenerator column through the application of heat, releasing a high-purity $CO_2$ stream and regenerating the solvent for reuse. Chemical absorption is particularly effective for gas streams with low $CO_2$ partial pressure, such as flue gases from coal- or gas-fired power plants[46]. However, efficient operation requires the prior removal of impurities such as $SO_x$, $NO_x$, and particulate matter to prevent solvent degradation and equipment corrosion.

Chemical absorption based on traditional amine solvents is considered to have a Technology Readiness Level (TRL) of 9, with successful deployment in large-scale commercial facilities like the Sleipner and Snøhvit projects. To address the high energy consumption, advanced solvent formulations are being developed, including sterically hindered amines (TRL 6-9), chilled ammonia processes (TRL 6-7), and amino-acid salts, which aim to enhance capture efficiency while reducing degradation rates and regeneration energy requirements[64–66].

In physical absorption, $CO_2$ is absorbed into a non-reactive solvent solely through physical solubility, which increases linearly with $CO_2$ partial pressure according to Henry's Law. Common physical solvents include Rectisol (chilled methanol) and Selexol (dimethyl ethers of polyethylene glycol), both of which are fully commercial technologies (TRL 9). These processes are extensively utilized in high-pressure applications such as coal gasification (IGCC), hydrogen production, and ammonia synthesis. Due to the pressure-dependent nature of the absorption, physical solvents become economically viable primarily when the feed gas has a high $CO_2$ concentration (typically exceeding 15 vol%) and high total pressure, reaching a better efficiency than chemical absorption[46].

A key advantage of physical absorption is that solvent regeneration is achieved mainly through pressure reduction, requiring significantly lower thermal energy input compared to chemical systems. Additionally, physical solvents exhibit minimal corrosivity and do not suffer from the chemical degradation issues common to amines[40]. However, their capture efficiency decreases sharply at low $CO_2$ partial pressures, thereby limiting their applicability for standard post-combustion flue gas treatment.

### *Adsorption*

Adsorption is an established separation method in which specific components of a gas mixture – such as $CO_2$ – are selectively retained on the surface of a porous solid material. The separation process is driven by intermolecular interactions between the adsorbate and the active sites of the adsorbent, which can occur via physisorption, governed by weak Van der Waals forces, or chemisorption involving stronger covalent bonding with surface functional groups[67]. Physisorption is typically characterized by rapid kinetics and lower regeneration energy but may suffer from lower selectivity compared to chemisorption, which offers higher capacity and selectivity at the cost of more energy-intensive regeneration.

The adsorption process is cyclical and consists of two separate steps: first, the flue-gas stream is directed through a packed bed containing spherical or pelletised adsorbent particles, $CO_2$ molecules diffuse into the pore network and bind to the adsorbent surface until equilibrium is reached; once the bed becomes saturated, regeneration is performed to release a concentrated $CO_2$ stream and restore the sorbent for the next cycle.

Nowadays, the most significant challenges of adsorption deployment on industrial scale are four fundamental aspects: cost-effective production on a large scale of adsorbents, reduction of $CO_2$ uptake due to the negative impact of impurities in flue gas mixture, controlling and regulating temperature of flue gas to a proper level, and costs associated with frequent adsorbent replacement.

Current research focuses on a broad spectrum of adsorbent materials, including traditional zeolites and activated carbons, as well as advanced materials like Metal-Organic Frameworks (MOFs) and amine-functionalised solids[68–70]. Zeolites and activated carbons are well-established for their high surface area and

stability but are often limited by their sensitivity to humidity and low selectivity at low $CO_2$ partial pressure. Conversely, MOFs and amine-grafted silicates are gaining attention for their tunable pore structures and enhanced chemical affinity for $CO_2$, although issues regarding long-term stability and synthesis costs remain barriers to large-scale deployment[71,72].

Industrial implementation relies on cyclic processes where the adsorbent is regenerated by manipulating thermodynamic conditions. The most established strategy is Pressure Swing Adsorption (PSA), which operates at TRL 9 for hydrogen purification and natural gas upgrading. Alternative regeneration cycles include Vacuum Swing Adsorption (VSA), Temperature Swing Adsorption (TSA), and hybrid configurations like Vacuum Pressure Swing Adsorption (VPSA). Emerging concepts such as Electric Swing Adsorption (ESA), which utilizes resistive heating for rapid and direct energy transfer to the sorbent, are currently being explored to reduce thermal inefficiencies, though they are still at lower TRLs compared to pressure-driven cycles[46].

Despite the advantages of adsorbent technique, the widespread application of adsorption for post-combustion capture faces significant challenges like the degradation of adsorbent capacity due to flue gas impurities. Consequently, while adsorption is mature for specific industrial applications (TRL 8-9 for high pressure streams), its deployment for low-pressure flue gas treatment in sectors like cement and power generation typically ranges between TRL 5 and 7, requiring further optimization in material formulation and process cycle design[46].

### *Membrane separation*

Membrane-based $CO_2$ separation has emerged as a promising alternative to absorption and adsorption owing to its modularity, reduced environmental footprint and the absence of solvent regeneration steps that typically penalise thermal efficiency in conventional capture systems[73]. Membrane separation is based on a thin layer of semipermeable barrier material that carries on the separation when a driving force is applied – pressure difference, temperature, or electric potential on both sides of the membrane – which selectively allows $CO_2$ to permeate through the membrane while retaining the remaining flue-gas components.

Membranes are classified on three general criteria: origin, morphology, and structure[74]. Polymeric membranes (e.g. cellulose acetate, polysulfone, polyimides…) dominate commercial and industrial applications due to their low fabrication cost, ease of processing and mechanical robustness[46]. Polymeric membranes have reached TRL 7, but their deployment in post-combustion capture remains limited by plasticisation at high $CO_2$ partial pressures, reduced selectivity at elevated temperatures, and degradation in the presence of impurities[40,75,76]. The inorganic membranes, mainly zeolites, metal, carbon or silica, are costly but capable of operating at high temperatures with high mechanical stability.

Depending on the structure, membranes can be classified as gas separation membrane or gas absorption membrane. Gas separation membranes are designed focusing on selectivity and permeability and they operate with preferential permeation of mixture constituents through the pores of the membrane, with one component diffusing through the membrane faster than the others. Gas absorption membrane, instead, consists of micro porous solid membrane which is used as contacting device between the gas and liquid flow. The $CO_2$ is separated by the flue gas diffusing through membrane and then it is recovered by liquid absorbent by absorption. This process is more efficient than gas separation membrane due to high driving force[73,77].

Overall, membrane separation technologies offer compelling advantages, like compact design, modular installation, absence of energy-intensive solvent regeneration, but still face important practical limitations to be deployed in large-scale applications[78,79].

### *Biological $CO_2$ separation*

Biological $CO_2$ separation represents a distinct class of carbon capture technologies, relying on natural photosynthetic pathways rather than physico-chemical separation mechanisms[80–82]. Among biological routes, microalgae have attracted significant attention due to their high photosynthetic efficiency, rapid growth rates and ability to assimilate $CO_2$ from both atmospheric air and concentrated industrial emissions streams[83,84].

Microalgal $CO_2$ fixation occurs through photosynthesis, in which inorganic carbon is converted into organic biomass via the Calvin-Benson cycle. Several studies report that many microalgal strains can tolerate and efficiently utilise $CO_2$ concentrations in the range of 5-15 vol%, characteristics of flue gases from power plants and industrial facilities, provided that temperature and contaminant levels are properly controlled[85,86].

A key advantage of microalgal $CO_2$ separation lies in its intrinsic link to carbon utilisation. The captured carbon is not stored as a pure $CO_2$ stream, but incorporated into biomass that can be further valorised into a wide range of products, including biofuels (biodiesel, bioethanol, biogas and biohydrogen), animal feed, pigments, and high-value biochemicals. This dual function positions microalgae at the interface between CCS and CCU, offering a circular-carbon pathway in which mitigation is combined with resource recovery rather than permanent geological storage alone[86,87].

Despite these advantages, biological $CO_2$ separation via microalgae remains constrained by substantial technical and economic limitations. Large-scale deployment is hindered by low volumetric $CO_2$ capture rates compared to absorption- or adsorption- based technologies, high land and water requirements, and the sensitivity of algal growth to environmental conditions such as light intensity, temperature and pH. Closed photobioreactor systems offer improved productivity and process control but are associated with high capital and operating

costs, whereas open pond systems suffer from low areal efficiency and contamination risks[84,88].

. In addition to bioenergy applications, microalgae have demonstrated promising performance in environmental remediation and wastewater treatment. Species such as *Chlorella* have been reported to remove high fractions (91%) of dissolved organic carbon (DOC) as well as nutrients such as nitrogen and phosphorus under optimised cultivation conditions, thereby enabling integrated approaches that couple $CO_2$ capture with nutrient recovery and waste treatment[80,83]. Moreover, under specific conditions, microalgal activity can promote the precipitation of calcium carbonate, contributing to temporary or medium-term carbon stabilisation through biomineralization pathways[49,89]. However, the extent to which such mechanisms can provide long-term carbon storage remains highly site- and process- dependent and is generally limited compared with geological sequestration routes.

In summary, biological $CO_2$ separation via microalgal systems should be regarded as a complementary option within the CCUS portfolio rather than a stand-alone solution for large-scale carbon mitigation. Despite their high photosynthetic efficiency and intrinsic link to carbon utilisation, microalgal processes are constrained by biological limitations, low volumetric capture rates and significant land, water and capital requirements. As a result, their applicability is currently restricted to lab-scale or integrated configurations, such as wastewater treatment and bio-refinery concepts, rather than to the mitigation of large, continuous $CO_2$ emission streams[81,87].

### *Cryogenic separation*

Cryogenic separation enables the production of $CO_2$ streams with very high recovery and purity, typically reaching 99.9% at optimized conditions[90], making it particularly suitable for gas mixtures containing elevated $CO_2$ concentrations, generally above 50 vol% depending on process design[40]. Under such conditions, cryogenic processes are technically and economically viable; conversely, at lower $CO_2$ concentrations, the method becomes unattractive due to the substantial energy demand associated with multi-stage compression and deep refrigeration[46].

Cryogenic $CO_2$ separation is a purely physical process that exploits differences in the boiling points and desublimation behaviour of the components present in the gas mixture. The process involves multistage compression and cooling of the gas stream to temperatures typically ranging from -40 to -120 °C, inducing phase changes that lead to the condensation or solidification of $CO_2$, often together with other condensable species. Depending on the operating pressure and temperature, $CO_2$ can be recovered either in liquid or solid form, followed by further purification steps such as cryogenic distillation or high-pressure phase separation to achieve the target purity[46].

A major advantage of cryogenic separation is that it does not require chemical absorbents or sorbents, thereby avoiding issues related to solvent degradation,

corrosion, regeneration energy penalties, and secondary waste generation. In addition, the process directly produces liquid $CO_2$ under elevated pressure, which is advantageous for downstream handling and transport, particularly for pipeline and ship-based transportation, since further pressurization is not necessary. However, cryogenic processes are inherently energy-intensive, requiring significant electrical input for compression and refrigeration.

The main drawback of this process lies in its extreme sensitivity to impurities, particularly water vapour. Even trace amounts of moisture (ppm levels) can lead to ice formation, equipment blockage, and excessive pressure drops in cooling units. Consequently, extensive and energy-intensive upstream gas conditioning is required to remove water and other highly condensable contaminants, often accounting for 15-30% of the total energy penalty and significantly increasing both capital and operating costs. Moreover, the energy consumption for deep refrigeration is substantial (typically 0.4-1.5 GJ/t$CO_2$ depending on feed gas composition and purity requirements) and remains the dominant factor limiting economic competitiveness[40,91].

For these reasons, cryogenic separation is most suitable for applications involving high-pressure, $CO_2$-rich gas streams such as pre-combustion capture in integrated gasification combined-cycle (IGCC) plants, oxy-fuel combustion systems, and high-pressure syngas processing, where the feed gas already contains elevated $CO_2$ concentration (>30%) and refrigeration requirements are substantially reduced[92]. Cryogenic separation is currently at TRL 6-8 for these applications, with operating demonstration projects in oxy-fuel combustion and IGCC settings. In contrast, its role in conventional post-combustion capture remains limited due to the low $CO_2$ partial pressure, the requirements for energy-intensive deep cooling, and the sensitivity to flue-gas impurities, making standalone cryogenic post-combustion capture economically unattractive[46].

### 1.2.3 Transport

The deployment of CCUS technologies at industrial scale requires the development of reliable and efficient $CO_2$ transport infrastructure. In most practical scenarios, major $CO_2$ emission sources are not co-located with suitable storage sites or utilisation hubs, making transport an essential link within the CCUS value chain[46]. Once captured and conditioned, $CO_2$ must therefore be conveyed from point sources to storage reservoirs or conversion facilities in a safe, continuous and economically viable manner.

From a technological perspective, $CO_2$ transport is benefitting from decades of operational experience in the natural gas and enhanced oil recovery (EOR) industries[93]. Current transport systems are designed to handle large and continuous $CO_2$ flow rates, typically operating with $CO_2$ in a dense or liquid phase in order to maximise volumetric efficiency and minimise compression energy requirements[46,93–96]. The selection of the transport mode is primarily dictated

by transport distance, annual $CO_2$ throughput, geographical and regulatory constraints, and the spatial distribution of emission sources and sinks.

At present, two transport options dominate large-scale CCUS applications: pipeline transport and ship-based transport[94,97–101]. Pipelines constitute the most established solution for both onshore and offshore transport of large $CO_2$ volumes along fixed routes, whereas shipping is increasingly regarded as a flexible and competitive alternative, particularly for long transport distances, offshore storage sites, and early-stage CCUS deployment in regions lacking dedicated pipeline infrastructure. Both options impose specific requirements on $CO_2$ purity, pressure and temperature, thereby tightly linking transport considerations to upstream capture processes and downstream storage or utilisation routes.

The cost of $CO_2$ transport strongly depends on the transported volume and distance and is typically estimated to account for on the order of 20-25% of the total cost of a CCUS project[93]. Numerous studies have addressed the technical challenges associated with $CO_2$ transport, including phase behaviour control, techno-economic comparisons between pipeline and ship-based options, and infrastructure design. $CO_2$ transport systems can be broadly classified into onshore and offshore configurations. Onshore transport mainly relies on pipelines, with limited use of road or rail transport for small-scale or demonstration projects, whereas offshore transport typically involves subsea pipelines or ships. The choice between these options is largely governed by transport distance, accessibility of storage sites and required transport capacity.

From an operational standpoint, there is broad consensus that, for bulk transport, $CO_2$ should be transported either in the liquid or, preferably, in the dense supercritical phase[94,102]. Transport in the dense phase offers favourable hydrodynamic properties, combining gas-like viscosity with liquid-like density, thereby reducing pressure losses and improving energy efficiency compared to gaseous or two-phase flow regime.

An additional critical aspect of $CO_2$ transport concerns gas purity[99,103,104]. Depending on the capture technology, the $CO_2$ stream may contain impurities such as $SO_x$, $NO_x$, amines, $NH_3$, CO, $H_2$, $O_2$ and residual moisture[93,95]. These components can significantly affect the physicochemical and hydrodynamic properties of the $CO_2$ stream, as well as induce corrosion and, in some cases, hydrogen embrittlement of pipelines and transport vessels. In particular, the presence of water is highly problematic, as moist $CO_2$ is strongly corrosive even at moderate temperatures[93]. Consequently, dehydration is generally required prior to compression and transport to avoid the use of expensive corrosion-resistant alloys or internal protective coatings, creating a strong coupling between capture system design and transport specifications.

For long transport distances, often cited as of the order of 1000 km or more[95], ship-based transport is frequently economically favourable and is generally preferred, especially when large $CO_2$ volumes are involved or when transport routes cross maritime regions. This flexibility makes shipping an attractive option for connecting multiple emission sources to offshore storage sites

during the early phases of CCUS deployment. Recent techno-economic assessments by the Zero Emissions Platform suggest that combining ship and pipeline transport within offshore $CO_2$ networks can provide a particularly cost-effective and lower-risk solution for early cluster development, by exploiting the low marginal cost of expanding shared pipelines while retaining the operational flexibility of ship-based transport[105].

## 1.3 Carbon Capture and Storage (CCS)

Once carbon dioxide has been captured and transported, CCUS pathways diverge into two fundamentally different end-routes: permanent geological storage and utilisation. Carbon Capture and Storage (CCS) is specifically designed to prevent $CO_2$ from entering the atmosphere by isolating it from the carbon cycle through long-term sequestration in deep geological formations[26,106]. In this framework, CCS represents the most direct mitigation option for addressing large, continuous emissions from hard-to-abate sectors where full decarbonisation remains technically or economically challenging.

The concept of $CO_2$ capture, transport and storage in the modern sense, as a means of reducing anthropogenic $CO_2$ emissions, was first proposed by Marchetti[107], who in 1977 proposed capturing $CO_2$ from large point sources and disposing of it in long-lived sinks such as the deep ocean. Geological storage of carbon dioxide can be implemented in a range of subsurface environments, whose suitability depends on geological, hydrodynamic and geochemical conditions, with saline aquifers and depleted oil and gas reservoirs as the main options[42,108,109].

Deep saline aquifers consist of porous and permeable reservoir rocks whose pore space is saturated with saline formation water. They are widely regarded as one of the most promising options for long-term $CO_2$ storage due to their large theoretical capacity, favourable trapping mechanism and widespread global occurrence[110–112]. Depleted oil and gas reservoir are geological formations from which hydrocarbons have already been produced and represent attractive storage candidates because their geology, petrophysical properties and caprock integrity have been extensively characterised through decades of exploration and production[113,114]. Storage associated with EOR represents a hybrid configuration in which injected $CO_2$ aids hydrocarbon production and, if retained in the subsurface, can contribute to emission reductions relative to venting. However, the overall mitigation benefit of $CO_2$-EOR strongly depends on project design and on the fate of the additional hydrocarbons produced[115].

Other storage concepts, such as injection into unmineable coal seams, reactive basalt formations enabling in situ mineralisation, hydrate-based storage and direct ocean sequestration, have been investigated at laboratory or pilot scale[116]. Nevertheless, these options remain geographically constrained, technologically immature, or subject to significant environmental and regulatory uncertainty. Consequently, current large-scale CCS deployment strategies primarily focus on

deep saline aquifers and depleted hydrocarbon reservoirs as the most technically and regulatorily mature geological storage options.

The Sleipner project in Norway, operational since 1996, is widely recognised as the first commercial-scale CCS operation, consistently injecting around 1 Mt $CO_2$/year into the Utsira saline aquifer under a thick shale caprock, with decades of monitoring confirming secure retention under site-specific geological conditions[106,117,118]. Similar saline-formation storage has been implemented at the nearby Snøhvit project, further highlighting the technical viability of dedicated geological storage[119].

Other large $CO_2$ injection projects include ExxonMobil's Shute Creek facility in the United States and Petrobras' Santos Basin pre-salt operations in Brazil, currently among the largest injection programmes worldwide by annual volume[26,120]. However, unlike Sleipner and Snøhvit, these projects are tightly coupled to enhanced oil recovery (EOR), a feature that raises concerns regarding their net climate benefit[115,121–123]. Both the IPCC and the IEA note that CCS linked to EOR does not automatically deliver net emissions reductions, as the $CO_2$ stored may be offset – partially or fully – by the additional fossil fuels extracted and subsequently combusted[124]. This issue is particularly evident in the case of Shute Creek, where independent assessments report substantial reliance on EOR markets and periods of high uncaptured emissions, reducing the overall mitigation effectiveness[122].

While advanced monitoring programs, such as the 4D seismic analysis used in EOR sites like Bell Creek, have improved geological interpretation and dynamic reservoir models[125], several high-profile capture projects have struggled to achieve their design performance. Facilities such as Petra Nova (Texas) and Boundary Dam Unit 3 (Canada) operated at significantly lower capacity factors than originally projected[122,126], highlighting challenges associated with energy penalties, solvent degradation, and integration with existing power-generation infrastructure.

Furthermore, even successful projects like Sleipner and Snøhvit demonstrate that long-term $CO_2$ storage in deep saline formations is technically viable, it is not without complexity[106,118,119]. Both sites required iterative recalibration of subsurface models due to unexpected plume migration patterns and local pressure behaviour, underscoring the need for robust monitoring and adaptive reservoir management[127].

Overall, recent IPCC and IEA assessments consistently describe CCS as a potentially important mitigation option for hard-to-abate sectors[26,128], but also emphasise that current deployment remains far below the levels envisioned in 1.5-2 °C pathways and is dominated by EOR-based projects rather than dedicated storage[39]. CCS can therefore be considered technologically mature at the scale of individual demonstration projects (Mt $CO_2$/year), but significant challenges remain regarding large-scale deployment, long-term storage verification, and the high capital, operating and monitoring costs required over project lifetimes.

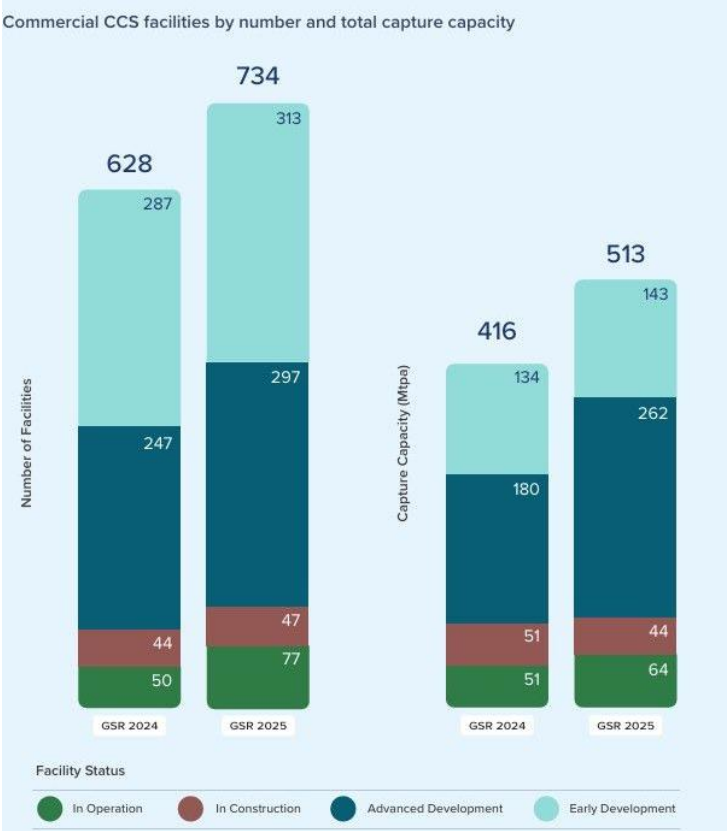


**Figure 1.7. Global CCS project facilities by development stage and associated capture capacity. Data from Global CCS Institute Report 2025[26].**

The trends reported in Figure 1.7 provide a quantitative snapshot of the current momentum of CCS deployment. Between 2024 and 2025, the number of operational CCS facilities increased from 50 to 77, corresponding to a 54% year-on-year growth, while operational capture capacity rose from 51 to 54 $MtCO_2$ $yr^{-1}$. Although projects under construction show only a modest increase in number, a more pronounced expansion is observed at the advanced development stage, where capture capacity increased by approximately 46%, from 180 to 262 $MtCO_2$ $yr^{-1}$. This indicates that a substantial share of future capacity is still concentrated in the project pipeline rather than in fully operational assets. Overall, the data highlight a rapidly expanding CCS portfolio, yet one in which the gap between planned capacity and realised large-scale deployment remains significant, reinforcing the view that CCS growth is accelerating but still falls short of the levels required in near-term climate mitigation pathways[26].

Beyond site-specific demonstrations, the role of CCS must be evaluated at the system level, considering economic constraints and climate policy frameworks. Integrated assessment and techno-economic models consistently indicate that large-scale deployment of CCS is unlikely to occur in the absence of strong carbon-pricing mechanisms. Duan et al.[129] show that carbon taxation is significantly more cost-effective than subsidy-based policies in driving CCS adoption. In these scenarios, CCS contributes a non-negligible but partial share of total $CO_2$ abatement (typically 15-25% by 2100). Importantly, even under

favourable policy conditions, CCS deployment remains hindered by high capital costs and infrastructure constraints.

These findings reinforce the view that CCS should be regarded as a complementary mitigation option for hard-to-abate emissions rather than a stand-alone solution, whose effectiveness is intrinsically linked to broader climate policies and economic instruments. The limitations associated with the high capital costs and long-term liability of CCS have therefore driven significant research into Carbon Capture and Utilisation (CCU), which seeks to transform the $CO_2$ liability into an economic asset.

## 1.4 Carbon Capture and Utilisation (CCU)

Carbon Capture and Utilisation (CCU) shares with CCS the initial step of $CO_2$ capture, yet the two approaches diverge substantially in their objectives and systemic roles. While CCS is primarily conceived as a mitigation strategy based on the permanent isolation of $CO_2$ from the atmosphere, CCU focuses on the integration of captured $CO_2$ into industrial value chains through its conversion into fuels, chemicals or materials[130]. As a consequence, CCU does not achieve permanent sequestration, but rather a carbon management strategy aimed at reducing fossil carbon demand and promoting circular carbon flows.

Utilisation of $CO_2$ finds applications in several sectors, such as chemical, oil and power, food, and pharmaceutical sector, in pulp, paper, and steel industry as well as many others[131].

As briefly introduced in Section 1.2, comparative life-cycle assessments have highlighted a structural trade-off between CCS and CCU strategies, whereby CCS generally exhibits a higher theoretical $CO_2$ mitigation potential, while CCU outcomes are strongly conditioned by energy inputs, system boundaries and product lifetimes, making its contribution to global $CO_2$ mitigation challenge negligible[132]. As Koytsoumpa et al. described in their review, CCU has an estimated potential equal to about 10% of the world's current annual[131]. In this respect, the majority of CCU pathways, particularly those targeting fuels and short-lived chemicals, lead to delayed rather than permanent $CO_2$ release, thereby limiting their contribution to long-term atmospheric carbon removal[30,33]. The climate mitigation potential of CCU critically depends on system boundaries, carbon sources and product lifetimes. $CO_2$ may be utilised as a technological fluid, converted into chemicals and fuels, or permanently stabilised through mineralisation to inorganic carbonates. Only in specific cases – namely when atmospheric $CO_2$ is used and transformed into thermodynamically stable solid carbonates[133] – can CCU achieve net carbon-negative performance over its life cycle. When $CO_2$ originates from fossil point sources, CCU pathways cannot be carbon-negative and, at best, may be carbon-neutral[134,135].

Beyond permanent removal, CCU may contribute to climate mitigation through alternative mechanisms, including the displacement of more GHG-intensive conventional products[136] or the temporary storage of carbon in chemicals and materials. However, for fuels and short-lived products, the end-of-

life release of $CO_2$ is unavoidable and must be explicitly accounted for, implying that such pathways should be regarded as carbon-neutral in the best-case scenario rather than as long-term carbon sinks[135].

Nevertheless, when LCA considerations are coupled with techno-economic analysis, CCU may offer additional advantages under specific boundary conditions. Several LCA-TEA studies have shown that selected CCU routes, especially $CO_2$ conversion to value-added chemicals[137,138] (like the production of ethane carbonate), can achieve favourable economic performance relative to CCS and reduce carbon dioxide emissions, primarily due to the generation of marketable products that partially offset capture and processing costs[27,139]. Such findings, however, remain highly context-dependent and cannot be generalised, as they are sensitive to assumptions regarding energy sources, hydrogen availability, process efficiency and market scale[35]. Accordingly, CCU is best interpreted not as an alternative to CCS, but as a complementary option whose relevance emerges within integrated decarbonisation frameworks.

### 1.4.1 Energy Requirements and Source Impact

The viability of CCU is fundamentally dependent on low-carbon energy sources, particularly renewable electricity for hydrogen production via water electrolysis. This dependency arises from the high thermodynamic stability of the $CO_2$ molecule: unlike CCS, which primarily relies on the energy intensity of $CO_2$ compression and transport, CCU conversion pathways are substantially more energy-intensive, requiring 5-25 MWh per tonne of $CO_2$ converted depending on the specific synthesis route[140,141]. This energy requirement constitutes the primary bottleneck governing the life-cycle performance of CCU systems: when electricity is supplied from fossil-dominated grids, utilisation pathways may lead to higher net atmospheric emissions than the reference fossil process, whereas low-carbon electricity can substantially improve environmental outcomes.

Hydrogen production pathways exemplify this trade-off clearly. Conventional grey hydrogen, produced via steam methane reforming (SMR) without carbon capture, generates ~12-14 kg $CO_2$-eq per kg $H_2$, depending on the natural gas route (pipeline vs. liquefied natural gas, LNG), while blue hydrogen (SMR + CCS with 60-90% capture rates) reduces emissions to approximately 8-9 kg $CO_2$-eq per kg $H_2$, corresponding to a partial mitigation that remains significantly higher than renewable alternatives. By contrast, green hydrogen produced via PEM or alkaline electrolysis powered by wind or solar electricity achieves markedly lower emissions, typically below 1 kg $CO_2$-eq per kg $H_2$ for wind-based systems and around 2-3 kg $CO_2$ per kg $H_2$ for solar-based configurations. These differences underscore a fundamental principle: the climate performance of CCU routes is dominated by upstream energy supply rather than by the utilisation reaction itself[142,143].

The economic implications are equally critical. As of 2024-2025, green hydrogen production costs in Europe remain substantially higher than those of grey hydrogen, driven by elevated electricity prices and electrolyser capital costs (currently exceeding €7.50/kg compared to €3.50-4.50/kg for grey hydrogen)[144,145]. Furthermore, the intermittency of renewable sources poses an operational challenge: relying solely on solar or wind can reduce the electrolyser capacity factor, thereby increasing the levelized cost of hydrogen due to underutilised capital assets[146,147]. Although learning effects, manufacturing scale-up and declining renewable electricity costs are expected to reduce green hydrogen prices over the medium to long term, cost parity with fossil-based hydrogen remains uncertain within the current decade and strongly region-dependent[144,145,148]. Consequently, hydrogen cost and availability represent binding economic constraints for CCU deployment under low-carbon operating conditions.

The influence of energy sourcing becomes particularly evident in hydrogen-intensive CCU routes, such as $CO_2$ hydrogenation to fuels or platform chemicals. In such systems, the emissions associated with hydrogen production may exceed the amount of $CO_2$ converted if fossil-derived hydrogen is employed, resulting in a net climate burden rather than mitigation. Conversely, the use of renewable-sourced hydrogen can enable substantial emission reductions or, in specific cases involving long-lived products, near-neutral or net-negative cradle-to-gate balances[140,149,150]. This strong dependence on low-carbon electricity and hydrogen availability has been highlighted not only in comparative LCA studies, but also in recent system-level renewable by the International Renewable Energy Agency (IRENA), which identify renewable hydrogen supply as a prerequisite for the climate viability of $CO_2$-based fuels and chemicals[151]. This inversion, from climate liability to potential benefit, is therefore driven almost entirely by energy inputs, highlighting the central role of both energy system integration and process efficiency in shaping CCU feasibility.

### 1.4.2 Functional Classification of CCU Routes

Various $CO_2$ utilisation routes were successfully researched in terms of technical and economic feasibility. The wide range of fuels, chemicals and materials from $CO_2$ conversion are already available in today's market and have an application in the current industry including transportation, agriculture, cosmetics, construction and aviation[152]. Applicability of waste $CO_2$ in different fields and set of technologies are currently operated, but to correctly define the boundaries of this analysis, it is necessary to distinguish between physical applications of $CO_2$ and its chemical transformation, as schematically illustrated in Figure 1.8.

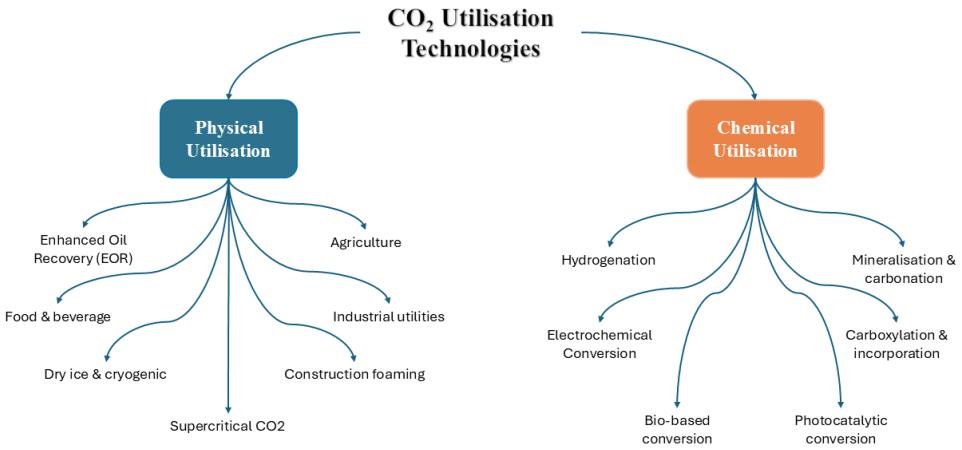


**Figure 1.8. Schematic classification of $CO_2$ utilisation technologies into physical and chemical pathways.**

To complement the functional classification of $CO_2$ utilisation pathways, an additional perspective is provided by considering their relative level of technological maturity. While TRL does not capture environmental performance, scalability or economic viability, it offers a useful framework to contextualise the current deployment landscape of $CO_2$ utilisation technologies and to rationalise differences in their maturity.

Physical utilisation routes are generally characterised by high technological readiness, with several applications operating at commercial scale[153–155]. Enhanced Oil and Gas Recovery (EOR/EGR) represents the most mature and widely adopted pathway and largest-scale deployment, reaching TRL 9 with ~80 $MtCO_2$ injected annually into depleted reservoirs to improve hydrocarbon recovery[33]. Other physical uses, including food and beverage processing (~15-30 $MtCO_2$/year), dry ice and cryogenic applications, supercritical $CO_2$ as a process medium, construction foaming, agricultural enrichment and industrial working fluids, also exhibit high to medium TRL values[124,135,140,156–158]. Despite their maturity, these routes typically involve short carbon retention times and therefore provide limited or no net climate mitigation at the system level, as the utilised $CO_2$ is eventually released back to the atmosphere.

In contrast, chemical utilisation pathways display a much broader distribution of technological readiness (Figure 1.9)[152,159–161] and are associated with a potentially significant long-term $CO_2$ mitigation capacity[160]. Mineralisation and carbonation processes have reached high TRL levels in specific construction and materials applications, reflecting their operational simplicity and long-term carbon stabilisation. Carboxylation and chemical incorporation routes, including the synthesis of urea (~130 $MtCO_2$/year)[33,162], carbonates and polymer precursor, occupy an intermediate/high maturity range, with several industrial implementations. Electrochemical and photochemical conversion routes remain predominantly at low to medium TRL (3-6), reflecting ongoing challenges related to energy efficiency, current density and long-term stability. Bio-based pathways, instead, exhibit greater heterogeneity, with microalgae-based $CO_2$ utilisation

reaching TRL 6-7 in demonstration settings – or higher in limited number of projects targeting bio-methane (e.g., BioCat-3, BioPower2Gas[158]) – whereas enzymatic and microbial conversion routes remain at lower maturity.

Hydrogenation-based $CO_2$ conversion routes also have a medium/higher TRL. While certain processes, such as $CO_2$ methanation and methanol synthesis, have reached pilot or commercial stages, their large-scale deployment remains strongly dependent on the availability of low-carbon hydrogen and renewable energy integration.

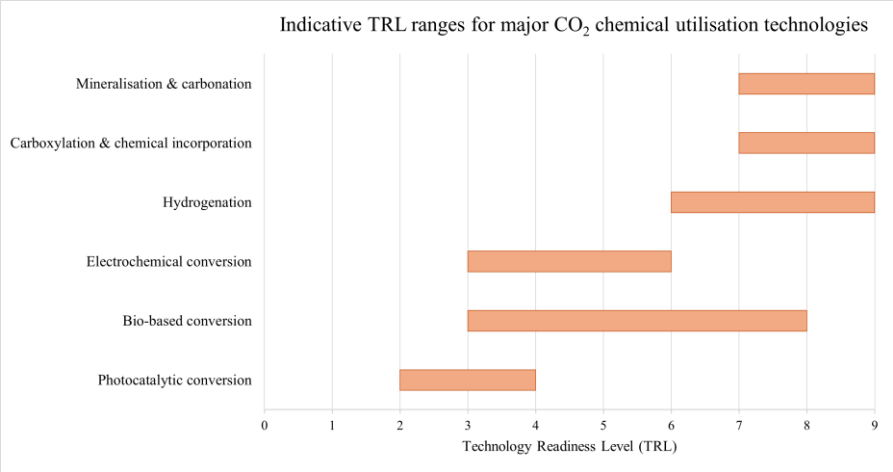


**Figure 1.9. Indicative Technology Readiness Level (TRL) ranges for major $CO_2$ chemical utilisation technologies. The reported ranges reflect the variability in process configurations and product targets within each technology class and do not imply uniform technological maturity or economic viability.**

Within this specific domain, the selection of an appropriate reaction pathway represents a central engineering challenge; Otto et al. systematically evaluated 123 potential routes for converting $CO_2$ into chemicals[163].

Within the broad landscape of $CO_2$ utilisation technologies, this thesis focuses primarily on catalytic $CO_2$ conversion pathways, which enable the transformation of captured $CO_2$ into fuels and chemicals. Accordingly, these routes – particularly hydrogenation-based Power-to-Fuel (PtF) processes – are discussed in greater detail in the following sections, while other utilisation pathways are addressed at a higher level.

### 1.4.3 Power-to-fuel

Power-to-Fuel encompasses Power-to-Gas (PtG) routes – including hydrogen and synthetic natural gas (SNG) – as well as the production of liquid fuels and platform chemicals such as methanol, dimethyl ether (DME), and other oxygenated derivatives. In this framework, synthetic fuels including methanol, DME, methane, and higher hydrocarbons are increasingly promoted as energy vectors capable of storing surplus renewable electricity and partially substituting fossil fuels and fossil-derived products across multiple sectors, most notably transportation and energy-intensive industries.

The conversion of renewable electricity into chemical energy carriers in gaseous or liquid form (Power-to-Gas and Power-to-Liquid) represents one of the

most widely discussed strategies to address the intrinsic intermittency of renewable energy sources (RES). By transforming electricity into storable fuels, these pathways offer a means to buffer temporal mismatches between energy generation and demand, thereby alleviating one of the major constraints limiting large-scale deployment of RES. Moreover, synthetic fuels present a structural advantage in that they can be integrated into existing fuel infrastructures with limited modifications, avoiding excessive capital investments, technical barriers, or radical changes in end-user behaviour.

Although hydrogen is often proposed as the most direct and environmentally attractive energy carrier due to its carbon-free end-use, its large-scale deployment as a final energy vector remains constrained by substantial technological, economic, and safety challenges[164]. The storage, transport, and distribution of hydrogen require dedicated infrastructures that are currently sparse or non-existent in many regions, and the cost of transforming the entire energy system to accommodate hydrogen-based logistics is likely to be economically prohibitive in the short to medium term[165–167]. As discussed in Section 1.4.1, the availability of low-carbon hydrogen remains the central challenge for all Power-to-Fuel technologies, as hydrogen production itself must not lead to indirect $CO_2$ emissions that undermine the intended climate benefits.

Within this context, PtF concepts combine energy storage and $CO_2$ utilisation in a single system level approach. Electrolyser technologies convert electrical power into hydrogen while simultaneously offering grid-balancing services, particularly valuable under conditions of fluctuating renewable electricity supply. Captured $CO_2$ and electrolytic hydrogen can then be combined, compressed, and fed into catalytic reactors, where chemical energy storage is realised through the synthesis of fuels or chemical intermediates[131].

$CO_2$ hydrogenation pathways can be broadly classified into direct and indirect routes[152]. Direct hydrogenation involves a single-step reaction in which captured $CO_2$ reacts with hydrogen to produce $C_1$ compounds such as methane (Eq. 1) or methanol (Eq. 2). Alternatively, indirect routes proceed via intermediate formation of carbon monoxide or synthesis gas. In *modified Fischer-Tropsch synthesis* (FTS)[168–170], $CO_2$ is first reduced to CO through the Reverse Water-Gas Shift (RWGS) reaction (Eq. 3), followed by CO hydrogenation to higher hydrocarbons. Similarly, methanol-mediated routes involve $CO_2$ hydrogenation to methanol, which can subsequently undergo dehydration reactions to yield DME or other derivatives.

$$CO_2 + 4H_2 \leftrightarrow CH_4 + 2H_2O \quad (1)$$
$$CO_2 + 3H_2 \leftrightarrow CH_3OH + H_2O \quad (2)$$
$$CO_2 + H_2 \leftrightarrow CO + H_2O \quad (3)$$

Although indirect routes introduce additional reaction steps and complexity, their strategic advantage lies not in simplicity but in operational flexibility. While direct pathway reactions are constrained by fixed stoichiometry, syngas-based

routes allow the $H_2$/CO ratio to be tuned in situ, enabling adaptation to the kinetic and thermodynamic requirements of downstream processes. In this sense, $CO_2$ hydrogenation via RWGS-based process transforms thermodynamically stable $CO_2$ into more reactive intermediates, facilitating broader product flexibility at the expense of additional energy input.

### *Power-to-Gas*

Among these routes, Power-to-Gas (PtG) has attracted significant attention due to the technological maturity of methane-based infrastructure and its compatibility with existing energy distribution systems. While the thermochemical and catalytic principles of methanation are well-established, large-scale commercial deployment remains limited. As of 2025, only a handful of pilot and demonstration projects are operational globally (maximum TRL 8), with a geographic concentration in Germany and Northen Europe, where abundant renewable electricity and existing natural gas infrastructure provide favourable conditions[156].

To overcome limitations related to hydrogen storage, transport and usage, mentioned in Section 1.4.2, methanation represent the second, optional step in the PtG chain, but with a great potential. In a typical PtM configuration, hydrogen produced via electrolysis reacts with $CO_2$ in a catalytic reactor to form synthetic natural gas (SNG) through the Sabatier reaction (Eq. 1). A PtM plant generally consists of a water electrolyser, a $CO_2$ separation or conditioning unit if $CO_2$ is not available in a suitable form, and a methanation module. The resulting SNG is fully compatible with existing natural gas infrastructures, enabling its transport, storage, and end-use without significant modifications.

Methane as an end-product of the PtG process offers several advantages. It enables the conversion of surplus electricity into a widely traded energy commodity, supports large-scale and long-term energy storage due to its high volumetric energy density, and allows direct utilisation within established gas grids and storage facilities[171]. These features make PtM particularly attractive in regions where natural gas infrastructures are already deeply embedded. Nevertheless, PtM faces significant technical, economic, and environmental challenges. From a technological perspective, further research is required to de-risk the process and support large-scale deployment. Economically, competitiveness with fossil-derived natural gas depends on access to low-cost electricity, low specific capital expenditure, and high operational hours – the catalyst used is also a key factor; only under low-carbon electricity scenarios can synthetic methane offer net $CO_2$ reduction compared to fossil gas[171].

From a purely economic standpoint, methanation may appear questionable, as methane generally has lower market value than hydrogen. However, when $CO_2$ costs, infrastructure constraints, and system integration are taken into account, PtM can become a rational option under well-defined conditions. One particularly relevant application is the methanation of biogas derived from anaerobic digestion of waste or biomass. Since biogas is primarily composed of $CO_2$ and $CH_4$,

methanation can efficiently increase methane yield while leveraging the relatively small and decentralised scale of both biogas plants and renewable hydrogen production units.

While methane has lower volumetric energy density than some alternative carriers, PtM avoids the infrastructure and safety challenges that constrain deployment of alternative pathways, making it a pragmatic option in regions with existing gas networks[172].

### *Integrated Carbon Capture and Utilisation (ICCU)*

Integrated Carbon Capture and Utilisation (ICCU) has emerged as a conceptual evolution of conventional CCU strategies, aiming to reduce the energy and cost penalties associated with the separation between $CO_2$ capture and its subsequent conversion. In contrast to classical CCU configurations, where $CO_2$ is captured, purified, compressed, transported, and finally converted in a dedicated downstream unit, ICCU seeks to integrate capture and utilisation within a single process or a tightly coupled system. The primary motivation behind this approach is the simplification and intensification of existing reaction pathways at the process level[173,174].

In typical ICCU concepts, $CO_2$ is first captured directly from diluted gas streams and subsequently converted after the introduction of hydrogen in a second step[175]. Capture and conversion may occur either within the same reactor or across interconnected reactor units operating in a cyclic or dual-bed configuration. In these systems, the same functional material can act sequentially as $CO_2$ sorbent and as active phase for conversion reactions, thereby avoiding intermediate $CO_2$ purification, compression, and transport steps. This integration has the potential to lower overall energy consumption and reduce capital expenditure compared to conventional CCU layouts[176–179].

In ICCU, methane production is achieved through total hydrogenation of $CO_2$ via the Sabatier reaction – as in classical methanation pathways – while syngas formation can proceed through the RWGS reaction. The novelty of ICCU therefore lies not in reaction mechanism, but in the temporal and spatial coupling of capture and conversion steps, which may enable improved heat management, reduced process complexity, and enhanced system efficiency.

Several techno-economic assessments have suggested that ICCU could lead to lower specific $CO_2$ utilisation costs compared to conventional CCU processes. Reported estimates indicate production costs on the order of \$700 per ton of $CO_2$ converted, compared to values exceeding \$1000 per ton of decoupled CCU configurations, under specific assumptions and process setup[180]. These estimates are, however, highly sensitive to assumptions on electricity price, hydrogen cost and plant scale, such as CCU technologies, and should be interpreted cautiously, as most ICCU concepts remain at low to intermediate TRL, and large-scale validation under realistic operating conditions is still limited.

Despite its conceptual appeal, ICCU also introduces additional constraints. The integration of capture and conversion imposes compromises on operating

conditions, material stability, and process flexibility, as optimal conditions for adsorption and catalytic conversion are not necessarily aligned[181,182]. Furthermore, ICCU does not eliminate the fundamental dependency of CCU pathways on low-carbon hydrogen supply and low-emission electricity. As such, its environmental performance remains strongly system-dependent, and ICCU should be viewed as a process intensification strategy rather than a stand-alone solution to $CO_2$ mitigation.

Overall, ICCU represents a promising but still developing approach within the broader CCU landscape. Its relevance is highest in applications where dilute $CO_2$ streams, limited space, or strong integration with energy storage concepts justify increased process complexity in exchange for reduced separation penalties. Further experimental validation, long-term stability studies, and system-level assessments are required to clarify its realistic role in future $CO_2$ utilisation chains.

### *Power-to-Liquid*

Power-to-Liquid (PtL) pathways enable the conversion of renewable electricity, hydrogen and captured $CO_2$ into liquid fuels and chemical intermediates, offering energy carriers with higher volumetric energy density compared to gaseous alternatives. This feature makes synthetic liquid fuels particularly attractive for hard-to-abate sectors where direct electrification remains technically or economically challenging, such as aviation, maritime transport and heavy-duty mobility. The most prominent PtL products are methanol, dimethyl ether (DME) and Fischer-Tropsch (FT) hydrocarbons, which differ significantly in molecular structure, infrastructure compatibility and system-level complexity.

As for PtG routes, PtL relies on the availability of low-carbon hydrogen produced via water electrolysis and on a suitable source of captured $CO_2$, both of which have been discussed in previous sections[183–185]. The potential advantage of PtL lies not in the intrinsic novelty of the chemistry involved, but in the possibility of synthesising liquid fuels with a substantially reduced carbon footprint when renewable electricity and sustainable $CO_2$ sources are employed. From a thermodynamic perspective, the hydrogenation of CO, $CO_2$, and syngas to liquid products is strongly exothermic. As a result, equilibrium considerations favour low operating temperatures, while reaction kinetics benefit from higher temperatures, imposing stringent requirements on heat management and process integration. In practical implementations, efficient heat removal and recycling of unconverted reactants are therefore essential to improve overall efficiency[186,187].

From a carbon balance perspective, PtL pathways are often describe as carbon-neutral, as the $CO_2$ released during fuel combustion corresponds to the amount previously captured and converted[135,183]. However, this neutrality is conditional and highly dependent on system boundaries, electricity carbon intensity and hydrogen production pathways.

Despite these constraints, PtL fuels offer several advantages over gaseous energy carriers for medium- and long-term energy storage. Liquid products can be stored and transported using existing infrastructure with relatively low energy penalties, whereas gaseous fuels typically require compression or liquefaction[188,189]. In addition, liquid fuels provide higher energy density per unit volume, exhibit negligible mass losses during long-term storage, and can often be separated from reaction systems with comparatively simple downstream processing. These characteristics make PtL particularly suitable for applications where energy density, logistics and compatibility with current fuel systems are critical.

From an economic perspective, the cost of PtL fuels, is dominated by the production of renewable electricity, electrolytic hydrogen and $CO_2$ capture. Techno-economic assessments consistently indicate that electricity price and electrolyser capital expenditure are the primary cost drivers, with hydrogen production accounting for the largest share of the final fuel cost[188,190]. Consequently, the economic viability of PtL pathways is strongly linked to continued reductions in renewable electricity costs and improvements in electrolyser efficiency and scalability.

Within the PtL landscape, methanol- and Fischer-Tropsch-based routes represent two distinct synthesis strategies. In methanol pathways, $CO_2$ is directly hydrogenated to methanol, which can be used as a fuel, a hydrogen carrier or a platform chemical. In contrast, FT-based routes typically involve the intermediate formation of CO-rich syngas, followed by chain growth reactions leading to a distribution of higher hydrocarbons compatible with conventional liquid fuels[183]. While FT fuels offer superior drop-in compatibility, they are generally associated with higher process complexity and more demanding integration requirements. In the present work, detailed discussion of methanol synthesis from $CO_2$ is deferred to Chapter 2, where the underlying chemistry, catalysis and thermodynamic aspects are analysed in depth.

A comparative overview of representative synthetic fuels derived from $CO_2$ hydrogenation and conventional fossil fuels is reported in Table 1.1. The comparison highlights key differences in energy density, storage conditions and infrastructure compatibility among the main PtL options. Fischer-Tropsch fuels exhibit gravimetric heating values comparable to those of conventional diesel, reflecting their hydrocarbon nature and drop-in potential. In contrast, oxygenated fuels, methanol and DME, are characterised by lower heating values, which are partly compensated by favourable liquid-phase storage and distinct end-use characteristics. Differences in fuel properties and infrastructure requirements underline that no single PtL product represent a universal solution, and that the suitability of each option strongly depends on system-level constraints and targeted applications.

Table 1.1. Comparison of selected physical, energetic and fuel-related properties of representative Power-to-Liquid products and conventional fuels.

| *Properties* | *Gasoline* | *Diesel* | *Methanol* | *DME* | *FT-fuels* |
|---|---|---|---|---|---|
| ***Physical state (STP)*** | Liquid | Liquid | Liquid | Gas (liquid under pressure) | Liquid |
| ***Chemical formula*** | $C_5$-$C_{12}$ | $C_{10}$-$C_{22}$ | $CH_3OH$ | $CH_3OCH_3$ | $C_{10}$-$C_{23}$ |
| ***Density (kg/m3)*** | 720-760 | 815-855 | 791 | 668 | 770-860 |
| ***LHV (MJ/kg)*** | ~32 | ~36 | ~15.6 | ~19 | ~34 |
| ***Boiling point at 1 atm (°C)*** | 25-215 | 170-380 | 64.7 | -24.9 | 150-320 |
| ***TRL*** | - | - | 8 | 7 | 8 |
| ***Octane number*** | 90-95 | - | 110-112 | - | - |
| ***Cetane number*** | - | 45-53 | 5 | 55-60 | 70-80 |
| ***Ref.*** | [156,191,192] | [156,191,192] | [156,191,192] | [156,191,192] | [156,191,192] |

## 1.5 Conclusions on the state of the art and scope of the thesis

The analysis developed throughout this chapter demonstrates that carbon capture-based mitigation strategies cannot be evaluated as universally optimal solutions, but rather as context-dependent options whose environmental effectiveness and economic viability are governed by system boundaries, energy supply, technological maturity and integration within existing industrial and energy infrastructures. Comparative life-cycle and techno-economic assessments consistently show that Carbon Capture and Storage represents the most efficient option for permanent $CO_2$ mitigation, particularly in the case of large point-source emissions. By contrast, Carbon Capture and Utilisation does not intrinsically ensure net emission reductions and should therefore be interpreted as a complementary strategy whose relevance depends on specific operating conditions rather than as a direct alternative to CCS. Within this perspective, $CO_2$ utilisation contributes to emission mitigation primarily through the partial displacement of fossil-derived fuels and chemicals within existing value chains, rather than through permanent carbon removal. A key outcome emerging from the present state-of-art analysis is that the environmental performance of CCU technologies is governed less by the intrinsic efficiency of individual conversion reactions and more by the characteristics of the surrounding energy and material systems in which they are implemented.

Across all Power-to-Fuel routes, hydrogen availability emerges as the dominant limiting factor. Both climate performance and economic feasibility are strongly influenced by the carbon intensity of electricity supply, the efficiency and scalability of water electrolysis technologies, and the resulting cost of hydrogen production. In addition, the selected $CO_2$ capture strategy and the degree of integration between capture and conversion units play a decisive role in determining overall system efficiency, capital costs and operational complexity. These considerations emphasise the need to assess CCU technologies as integrated system components rather than as isolated catalytic processes.

Based on these system-level considerations, the scope of the present work is focused on catalytic $CO_2$ conversion pathways that span different levels of process integration, product lifetime and infrastructure compatibility within CCU-oriented frameworks. In particular, the work addresses three complementary research directions: Power-to-Methane, Integrated Carbon Capture and Utilisation, and Power-to-Liquid routes. Taken together, these approaches enable a structured analysis of $CO_2$ utilisation strategies ranging from fully drop-in energy carriers to more complex chemical platforms.

PtM was selected due to its high degree of compatibility with existing natural gas infrastructure, its relevance for large-scale and long-term energy storage, and its role as one of the most technologically mature Power-to-Fuel options. In parallel, ICCU concepts are investigated as system-level solutions in which $CO_2$ separation and catalytic conversion are combined within a single unit, potentially reducing energy penalties and capital costs compared to conventional sequential CCU configurations. Finally, PtL pathways targeting mainly methanol are examined as representative routes to obtain liquid energy carriers and platform chemicals, offering higher volumetric energy density and broader application potential in sectors where direct electrification remains technically or economically challenging.

The selected pathways are not selected as universally optimal solutions, but rather as technologically meaningful case studies that occupy distinct positions along the CCU spectrum in terms of product stability, infrastructure compatibility and degree of system integration. By jointly addressing PtM, ICCU and PtL routes, the present work enables a comparative assessment of catalytic $CO_2$ conversion strategies under different system constraints.

The following chapters therefore focus on the catalysis framework and experimental investigation of $CO_2$ conversion within these selected CCU routes. Rather than aiming to identify a single best-performing technology, this work seeks to elucidate the conditions under which catalytic $CO_2$ hydrogenation processes may contribute meaningfully to carbon utilisation strategies across the Power-to-Methane, Integrated Carbon Capture and Utilisation, and Power-to-Liquid pathways investigated herein.

# Chapter 2

# 2. Catalytic $CO_2$ hydrogenation: Power-to-Methane

## 2.1 Introduction

Within the broader context of $CO_2$ utilisation and Power-to-Fuel strategies outlined in Chapter 1, Power-to-Methane represents one of the most mature and technologically established routes for catalytic $CO_2$ hydrogenation. Owing to its full compatibility with existing natural gas infrastructures and its relevance for large-scale energy storage, methanation has been extensively investigated both from a fundamental and an applied perspective.

This section therefore focuses on the fundamental aspects governing $CO_2$ methanation, with particular emphasis on catalytic materials, reaction pathways and the interplay between thermodynamics and kinetics. Rather than providing a general overview of Power-to-Gas concepts, the discussion is intentionally narrowed to the physicochemical principles that control activity, selectivity and stability under conditions relevant to CCU applications. These aspects form the scientific basis for the experimental investigations presented in the following chapters.

## 2.2 Catalytic materials for power-to-methane

As previously discussed in Chapter 1, $CO_2$ hydrogenation represents a promising strategy for converting carbon dioxide into energy carriers with enhanced volumetric energy density or into value-added chemicals[193–195]. Excluding the reverse water gas shift, all the $CO_2$ hydrogenation processes are inherently exothermic and, thus, thermodynamically limited at high temperatures, where kinetics is generally favourable. Consequently, methanation, which falls within this category, requires relatively low operating temperatures to achieve high $CO_2/H_2$ conversions and optimal methane yields[196].

Within this context, nickel-based catalysts have gained significant attention due to their advantageous combination of low costs, high catalytic activity and stability[197,198]. Various strategies have been explored to further enhance their performance and to improve resistance against deactivation mechanisms such as coking and sintering[199–201]. These approaches include the incorporation of promoters (e.g., MgO, $CeO_2$, etc.) and the formation of alloys[202], which have been shown to beneficially modify the structural and electronic properties of nickel, or the rational selection of support materials, including zeolites (e.g., MCM-41[203]) and mesoporous silicas, which has been widely investigated as an effective strategy to optimise the performance of Ni-based methanation catalysts[204–209].

According to Ronsch et al., although the intrinsic activity trend for $CO_2$ methanation follows the sequence Ru > Fe > Ni > Co > Mo, nickel stands out as the most selective catalyst for methane formation under practical reaction conditions[197]. The support material plays a crucial role not only in facilitating the dispersion of the Ni metallic phase, but also in mitigating carbon deposition and CO poisoning, which represent common deactivation pathways for Ni-supported catalysts. In particular, the presence of surface acid sites can promote the formation of carbonaceous deposits, ultimately leading to catalyst deactivation. Therefore, selecting supports with a balanced acid-base character, or incorporating suitable promoters, represents an effective approach to limiting carbon formation. Additionally, carbon accumulation can be partially counteracted by gasification phenomena in the presence of water. These considerations highlight the importance of support materials exhibiting adequate resistance under the pressure and temperature conditions characteristic of $CO_2$ methanation[197].

Zeolites, characterised by high surface area and well-defined porous networks, are particularly attractive as catalyst supports. Their structural properties facilitate the dispersion of the Ni metallic phase, thereby limiting sintering and enhancing catalyst stability[205,210–213]. The acidic functionality of zeolites also exerts a strong influence on catalytic activity, as supports exhibiting pronounced acidity generally display lower activity compared to those with more basic characteristics[205,210]. The acidity and hydrophobicity of zeolites can be effectively tuned by adjusting the Si/Al ratio. Materials with higher Si/Al ratios exhibit increased hydrophobicity, which promotes more efficient removal of water from active sites and is therefore beneficial for the progression of the methanation reaction. in this context, the present work investigates the use of a commercial ultra-stable Y (USY) zeolite, characterised by a very high Si/Al ratio (>300), as a support for Ni nanoparticles. This strategy aims to simultaneously manage acidity and enhance Ni dispersion and stability, ultimately improving catalytic activity, durability, and resistance to fouling. Relatively low Ni loadings, ranging from 5 to 20%, were employed in order to ensure a high dispersion of the active phase while minimising overall metal content[214].

Beyond conventional Ni-based systems, rhenium (Re) and rhenium-based catalysts have attracted increasing interest for $CO_2$ hydrogenation due to their remarkable thermal stability and resistance to sintering[215–218]. However, despite these favourable properties, the intrinsic activity of rhenium for conventional $CO_2$ methanation is generally lower than that of nickel-based catalysts, limiting its applicability in classic power-to-methane processes. In contrast, the relevance of rhenium becomes more pronounced in the context of Integrated Carbon Capture and Utilisation (ICCU) strategies, where catalyst robustness and multifunctionality are essential.

In this framework, the concept of Dual-Functional Materials (DFMs) has gained increasing attention[219–221]. DFMs are designed to integrate $CO_2$ adsorption and catalytic conversion within a single material, combining an adsorbent phase with a catalytic component, typically based on Ni, Ru, or Rh[175,222–225].

To optimise the adsorption capacity of DFMs, various adsorbent materials have been combined with catalytically active components. Zeolites, activated carbon[226,227], mesoporous silicas, and metal-organic frameworks (MOFs)[228] showed effectiveness at lower temperatures. In contrast, layered double hydroxides (LDHs) and hydrotalcite-like compounds exhibit optimal adsorption performance in the intermediate temperature range of 200-400 °C[229,230]. At temperatures exceeding 400 °C, calcium-based and alkali ceramic materials are generally preferred due to their higher sorption capacity and thermal stability[231]. Calcium oxide (CaO), despite its low cost and high $CO_2$ capture capacity, suffers from sintering-induced deactivation, which leads to surface area loss and reduced adsorption efficiency over time. Dispersing CaO on inert supports, such as $\gamma$-$Al_2O_3$, has been shown to enhance its stability and durability[219,225]. MgO-based $CO_2$ adsorbents, including LDHs and hydrotalcite-like compounds, although characterised by weaker $CO_2$-basic site interactions, exhibit favourable adsorption behaviour in the intermediate temperature range and are particularly well suited for ICCU applications[220,232].

This work specifically investigates the integration of $CO_2$ capture and conversion through DFMs incorporating rhenium as the catalytically active metal, with a nickel-based DFM employed as reference[233]. While DFMs derived from transition metals have been extensively studied, the application of rhenium in ICCU remains largely unexplored. Nevertheless, rhenium is recognised for its exceptional thermal stability and catalytic behaviour in established $CO_2$ hydrogenation processes, making it a promising candidate for ICCU-oriented catalyst design[215]. To further enhance both catalytic activity and $CO_2$ adsorption capacity, highly adsorptive oxide materials, such as $CeO_2$[234,235] and $Al_2O_3$ [225,236], have been employed as supports. $CeO_2$ is well known for its high concentration of oxygen vacancies and redox properties, which promote $CO_2$ adsorption and activation[237]. Conversely, $Al_2O_3$ provides structural stability, high surface area, and porosity, with its simultaneously acid-base properties governing interactions with $CO_2$[238]. The incorporation of LDHs further

enhances adsorption efficiency due to their high density of basic sites and excellent performance at intermediate temperatures[239–241]. The strategic combination of these materials with rhenium and nickel is therefore aimed at optimising both $CO_2$ capture and subsequent hydrogenation, maximising the overall efficiency of ICCU strategies.

The investigation of both Ni-based conventional methanation and Re-based ICCU approaches within a unified experimental campaign allows for a direct comparison of how reaction mode (concurrent vs. sequential), active phase chemistry, and support functionality impact $CO_2$-to-methane conversion efficiency and selectivity.

## 2.3 Materials and Methods

This experimental campaign investigates two complementary approaches to $CO_2$ methanation through a unified exploration of catalytic materials design and synthesis. The first system employs nickel-based catalysts supported on ultrastable Y zeolite (Ni-USY), while the second system employs rhenium- and nickel-based dual-functional materials (DFMs). The samples are labelled in Table 2.1.

### 2.3.1 Materials and Chemicals

Ammonium perrhenate (99.999% Re) from STREM Chemicals and nickel (II) nitrate hexahydrate (99.9985% metals basis) from Alfa Aesar were used as precursors for the preparation of DFMs, while nickel(II) chloride hexahydrate ($NiCl_2{\cdot}6H_2O$, >98 wt%, Aldrich) was used for Ni-based catalysts supported on zeolite. The supports and adsorbent materials for DFMs were: ceria (Solvay ACTALYS HAS 10, cubic), zirconia (Saint-Gobain NorPro SZ 31164, monoclinic), titania (Tronox CristalActiv DT51D, 99.5%, anatase), γ-alumina (Sasol PURALOX SCFa-140 and SCFa-215, 98%, γ phase), and synthetic hydrotalcite ($Mg_6Al_2(CO_3)(OH)_{16}{\cdot}4H_2O$, Sigma-Aldrich, $MgO/Al_2O_3$ = 4.0-5.0).

The zeolite was a commercial ultrastable Y zeolite (Tosoh Corporation HSZ-390HUA, Si/Al molar ratio = 385), hereafter simply named USY. Doubly distilled water (Carlo Erba, reagent grade) served as the impregnation solvent. For catalysts reduction, a controlled $H_2$/Ar mixture (3% by volume, Nippon Gases) was employed. For catalytic testing on Ni catalysts supported on zeolite, ultra-high-purity gases were used ($CH_4$: 99.995 %), $CO_2$: 99.998 %, $N_2$: 99.9990 %) from Air Liquid and Nippon Gases.

### 2.3.2 Materials Preparation

#### *DFMs preparation*

Target rhenium and nickel loadings were set to 5.8 wt% and 5.0 wt%, respectively. For both Ni- and Re-based samples a standard wet impregnation

procedure was applied: 25 mL of distilled water was added to a 100 mL flask containing 2 g of powdered oxide support. To this mixture, 177 mg of $NH_4ReO_4$ or 522 mg of $Ni(NO_3)_2 \cdot 6H_2O$ was added, and the mixture was kept under agitation for 2 hours. Water was removed by rotary evaporation (65 °C, 110 rpm, under vacuum at <200 mbar), and the resulting solid was dried in an oven at 120 °C for a minimum of 2 hours. Ni-based samples were pre-calcined in air (30 mL/min, 5°C/min) at 550 °C for 4 h, and then reduced in an $H_2$ flow (30 mL/min, 2°C/min) at 600 °C for 2 h. The Re-based samples were instead directly reduced in the same $H_2$ flow at 500 °C for 2 h.

Selected Re- and Ni-samples were diluted with synthetic hydrotalcite (LDH) to create DFMs by gentle manual grinding for 2 min. Dilution factors of 2, 4, and 8 (w/w catalyst:LDH) were explored to optimise the balance between catalytic active sites and $CO_2$ adsorption capacity. $Re/Al_2O_3$ was also diluted in $CeO_2$ by a factor of 4.

#### *Ni-USY catalysts preparation*

Ni-USY catalysts were prepared by incipient impregnation procedure under vacuum: 10 mL of double-distilled water was added to 100 mL flask containing 1 g of zeolite USY and agitated for 10 minutes. Subsequently, 15 mL of $NiCl_2 \cdot 6H_2O$ aqueous solution (concentration calculated for final Ni loadings of 5, 10, or 20 wt%) was added, and the mixture was stirred for 24 hours at room temperature. The solvent was removed by oven evaporation at 80 °C for approximately 24 hours.

The dried, Ni-impregnated zeolite was loaded into high-density $Al_2O_3$ vessels and placed in an $Al_2O_3$ tubular furnace. Samples were then heated (10 °C/min) up to 600 °C and reduced for 2h under a reducing $Ar/H_2$ atmosphere ($H_2$ 3% by volume). Finally, the sample cools down at room temperature.

Moreover, a catalyst containing 10 wt% nickel supported on $\gamma$-$Al_2O_3$ was prepared by impregnation and used as reference. Powder $\gamma$-$Al_2O_3$ (Sasol, South Africa) was impregnated with a proper amount of nickel nitrate hexahydrate (Sigma-Aldrich, USA) in a rotary evaporator (55 °C, 200 mbar, 120 rpm), dried overnight at 120 °C, and finally calcined in air at 600 °C for 2 h.

### 2.3.3 Materials Characterisation

The physicochemical properties of the prepared catalysts were investigated using a combination of structural, textural, and surface-sensitive characterisation techniques.

Powder X-ray diffraction (PXRD) was used to verify the crystallographic integrity of the supports and to identify crystalline metal/oxide phases; for Ni-USY series, crystallite sizes were estimated using the Scherrer approach. For the Re-based catalysts and DFMs, PXRD was complemented by in situ XRD under $H_2$ to monitor structural transformations during thermal activation.

Textural properties were determined by $N_2$ physisorption at -196 °C. Prior to analysis, samples were degassed under vacuum to remove physisorbed species.

The specific surface area was calculated using the Brunauer-Emmett-Teller (BET) method. Total pore volume was determined from the amount of $N_2$ desorption at $P/P^0$=0.98 while pore size distributions was obtained by the Tarazona Non-local density functional theory (NL-DFT). These measurements were used to evaluate the impact of metal loading and preparation procedures on the porous structure of the supports.

Catalyst morphology and microstructure were investigated by electron microscopy. Ni-USY samples were characterised by field-emission scanning electron microscopy (FE-SEM) and by bright-field STEM/TEM in order to determine Ni nanoparticles size distributions based on statistically significant particle populations. Re-based catalysts and dual-functional materials were instead analysed by SEM and high-angle annular dark-field STEM (HAADF-STEM) to evaluate overall morphology and to assess the extent of rhenium dispersion or clustering.

Temperature-programmed techniques were employed to investigate both redox behaviour and surface properties. $H_2$ temperature-programmed reduction ($H_2$-TPR) experiments were performed to investigate the reducibility of the metal species and their interaction with the support, while $O_2$-TPO was carried out after catalytic operations to evaluate the reactivity of deposited carbonaceous species (when present) and to support stability and deactivation analysis. The acidity of selected catalysts was characterised by $NH_3$ temperature-programmed desorption ($NH_3$-TPD).

For selected samples, additional temperature-programmed experiments, including $CO_2$-TPD and temperature-programmed surface reaction (TPSR), were performed to evaluate $CO_2$ adsorption capacity and reactivity under conditions relevant to ICCU operation. These experiments provided information on the distribution of adsorption strengths and on the temperature range over which $CO_2$-derived species are released or converted.

Thermogravimetric and differential thermal analyses coupled to mass spectrometry (TGA/DTA-MS) were additionally used to track dehydration/decarbonation and reduction-related events during programmed heating under reducing atmospheres.

Advanced spectroscopy techniques were applied to selected Re-based catalysts to gain molecular-level insight into surface species and oxidation states under reaction-relevant conditions. Operando diffuse reflectance infrared Fourier transform spectroscopy (DRIFTS) was employed to identify adsorbed intermediates formed during both conventional $CO_2$ hydrogenation and ICCU cyclic operation, while in situ Raman spectroscopy was used to monitor changes in the oxidation state and coordination environment of rhenium species. These techniques were specifically used to elucidate mechanistic differences between simultaneous and sequential reaction modes and were not applied as routine characterisation tools across all samples.

Metal loadings in the freshly prepared catalysts were determined by inductively coupled plasma optical emission spectroscopy (ICP-OES) after

dissolution of samples in a mixture of acids at temperatures up to 110 °C. For Ni-USY catalysts, energy dispersive X-ray fluorescence (EDXRF) was employed as an alternative quantification method, confirming nominal and measured Ni weight percentages in Ni5, Ni10, and Ni20 catalysts described in Table 2.1.

**Table 2.1. Characteristics of the prepared samples. (LDH, Layered Double Hydroxide).**

| | *Sample* | *Dilution factor* | *Label* | *Specific surface area ($m^2/g$)* | *Metal loading (wt%)* |
|---|---|---|---|---|---|
| *DFM* | **$Ni/Al_2O_3$** | 0 | NAL_0 | 209 | 2.2 |
| | **$Ni/Al_2O_3$ + LDH** | 4 | NAL_4 | - | - |
| | **$Re/Al_2O_3$** | 0 | RAL_0 | 157 | 5.2 |
| | **$Re/Al_2O_3$ + LDH** | 2 | RAL_2 | - | - |
| | **$Re/Al_2O_3$ + LDH** | 4 | RAL_4 | - | - |
| | **$Re/Al_2O_3$ + LDH** | 8 | RAL_8 | - | - |
| | **$Re/Al_2O_3$ + $CeO_2$** | 4 | RAC_4 | - | - |
| | **$Re/CeO_2$** | 0 | RCL_0 | 123 | 4.4 |
| | **$Re/CeO_2$ + LDH** | 4 | RCL_4 | - | - |
| | **$Re/ZrO_2$** | 0 | RZL_0 | 98 | 4.2 |
| | **$Re/TiO_2$** | 0 | RTL_0 | 85 | 4.8 |
| | **Re/LDH** | 0 | RLL_0 | 214 | 6.3 |
| | | **Theoretical metal loading** | | | |
| *Ni-USY* | **Ni/USY** | 5 | Ni5 | See Section 2.4.1 | 5.9 |
| | **Ni/USY** | 10 | Ni10 | See Section 2.4.1 | 9.4 |
| | **Ni/USY** | 20 | Ni20 | See Section 2.4.1 | 28.3 |
| | **$Ni/Al_2O_3$** | 10 | Ni10-A | - | - |

### 2.3.4 Catalytic Tests

A tubular quartz plug-flow fixed-bed reactor was used for the experimental setup, coupled with an online NDIR gas analyser AK100 from Wi.Tec for the $CO_2$ hydrogenation and ICCU performance of the synthetised Re-based catalysts.

For Ni-USY catalysts tested in conventional gas-phase $CO_2$ hydrogenation, a catalyst weight of 0.5 g was used and a flow rate of 320 mL/min, corresponding to a contact time $\tau$ = 0.09 g s $cm^{-3}$ – evaluated as the ratio of catalyst weight and flow rate. The feed was composed by 3 vol% of $CO_2$ and 12 vol% of $H_2$ in $N_2$.

For Re-based catalysts evaluated in gas-phase mode, 50 mg of material was loaded (bed height ~3 mm), subjected to an in-situ pretreatment performed by heating under $H_2$ flow (40 mL/min) at 5 °C/min up to 400 °C. It is followed by a 1-hour isotherm under $H_2$, then cooling to the reaction temperature while maintaining $H_2$ flow and finally purging with $N_2$ before testing. The samples were tested in a temperature range 180 – 400 °C in 20 °C increments with 30 min isothermal plateaus, with a reaction feed of 50 mL/min – corresponding to a contact time $\tau$ = 0.06 g s $cm^{-3}$ – composed of 10 vol% $CO_2$ and 40 vol% $H_2$ in $N_2$.

Assuming that carbon mass balance is conserved, $CO_2$ conversion is evaluated as

$$X_{CO_2} = \frac{CO_2^{IN} - CO_2^{OUT}}{CO_2^{IN}} \quad (4)$$

The selectivity to $CH_4$ and CO are defined as

$$S_{CH_4} = \frac{CH_4^{OUT}}{CH_4^{OUT} + CO^{OUT}} \quad (5)$$

$$S_{CO} = \frac{CO^{OUT}}{CH_4^{OUT} + CO^{OUT}} \quad (6)$$

Where $X^{in}$ and $X^{OUT}$ represent the inlet and outlet flow rate (mL/min) of the *X* species.

The $CH_4$ yield is defined as

$$Y_{CH_4} = \frac{X_{CO_2} S_{CH_4}}{100} \quad (7)$$

Equilibrium calculations were carried out using Aspen Plus (AspenTech) by considering an isothermal RGIBBS reactor. Once the operating conditions were specified, the results were determined from the minimisation of the Gibbs free energy.

For ICCU cycles, after some optimisation experiments, the oven temperature and step durations were fixed according to the following protocol. The furnace temperature was fixed at 300 °C. A 150 mg charge of DFM was used for testing, with a total gas flow rate of 120 mL/min. The complete ICCU cycle consisted of four sequential steps: $CO_2$ adsorption (7.5% $CO_2$ in $N_2$) for 4 min to accumulate $CO_2$ on active adsorbent sites, followed by $N_2$ purge for 90 s, then hydrogenation (33% $H_2$ in $N_2$) for 4 min to reduce adsorbed $CO_2$ species to methane, and final $N_2$ purge of 60 s to remove unreacted $H_2$ and gaseous products. Typically, 50 consecutive cycles were executed to evaluate deactivation and long-term stability, with analysis based on methane and CO production averaged over the first 10 cycles. Production per cycle was determined by integrating NDIR detector peaks and expressed in three normalised forms: per unit DFM mass, per unit metal mass, and per mole of metal. An additional normalisation with respect to the duration of the hydrogenation step was done to obtain a pseudo reaction rate.

## 2.4 Conventional $CO_2$ methanation over Ni-USY catalysts

This section presents the experimental results obtained for conventional gas-phase $CO_2$ methanation over Nickel catalysts supported on ultra-stable Y zeolite. Structural, textural, and surface characterisation results are first discussed to establish the physicochemical properties of the Ni-USY systems, followed by the analysis of their catalytic performance and stability under methanation conditions. The discussion focuses on identifying structure-performance relationships relevant to Ni dispersion, support acidity, and resistance to deactivation.

### 2.4.1 Structural and physicochemical characterisation of samples

In this work, an ultra-stable Y zeolite (USY-390) has been investigated as nickel metal support. It exhibits a markedly high Si/Al molar ratio of 385, associated with a reduced concentration of Brønsted acid sites. The Brønsted

acidity in dealuminate Y-type zeolites arises from framework aluminium compensated by protons, and the distribution and strength of these acid sites are modified by the degree of dealumination[242–244].

Powder X-ray diffraction (PXRD) was employed to investigate the structural integrity of the USY support after nickel incorporation and to identify crystalline phases formed upon catalyst preparation. Figure 2.1 reports the diffraction patterns of the pure USY zeolite and of the Ni-based catalysts with increasing nickel loading. The diffraction pattern of the USY zeolite is characteristic of a strongly dealuminated Y-type zeolite (JCPDS card no. 81-2467). Importantly, the same set of framework-related reflections is preserved in all Ni-containing samples, indicating that the impregnation and subsequent thermal reduction treatments do not induce detectable structural degradation or collapse in the zeolite framework.

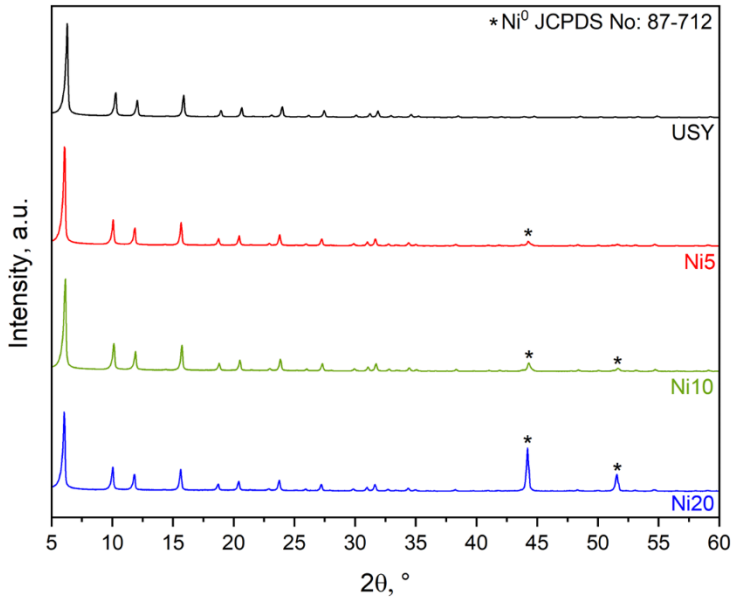


**Figure 2.1. XRD pattern of fresh zeolite (USY) and Ni-impregnated catalysts.**

Upon nickel incorporation, an additional diffraction feature appears at $2\theta \approx 44°$, which can be assigned to the (111) reflection of metallic nickel ($Ni^0$, JCPDS card no. 87-712), confirmed also by a $H_2$-TPR analysis (no hydrogen consumption detected). The relative intensity of this reflection increases systematically with increasing nickel loading, reaching a maximum for the Ni20 sample. This trend indicates a progressive increase in the amount of crystalline metallic nickel formed upon reduction. The average crystallite size of metallic nickel was estimated by applying the Scherrer equation to the most intense $Ni^0$ diffraction peak. Although this approach provides only an approximate estimate and does not account for strain effects or particle shape, it allows for a consistent comparative analysis across samples. The calculated Ni crystallite size increases from approximately 32 nm for the Ni5 catalyst to about 45 nm for Ni20, indicating partial growth and aggregation of nickel particles at higher metal loadings. An XRD pattern collected for the Ni20 catalyst after catalytic testing (Figure 2.2)

shows a further increase in the intensity of the $Ni^0$ reflections, accompanied by a modest increase in the calculated crystallite size to approximately 50 nm.

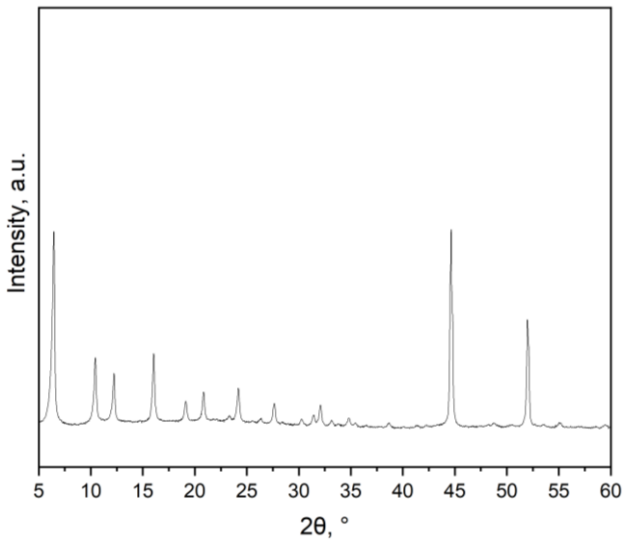


**Figure 2.2. XRD pattern of Ni20_spent catalyst.**

The quantitative phase analysis (QPA) performed on high-resolution diffraction patterns further confirms the progressive increase in the metallic nickel fraction with increasing nominal nickel loading, in agreement with the expected outcome for the impregnation procedure and with elemental analysis data. A corresponding decrease in the relative contribution of the zeolite and amorphous phases is observed at higher nickel contents, which is primarily attributed to the increasing fraction of crystalline metallic nickel rather than to a loss of zeolite crystallinity.

The textural properties of the pristine USY zeolite and Ni-USY catalysts were investigated using $N_2$ physisorption at -196° to evaluate the effect of nickel loading on surface area and pore structure. The adsorption-desorption isotherms (Figure 2.3) and the derived textural parameters (Table 2.2) suggest the presence of large mesopores/macropores likely to be generated by the dealumination treatment of zeolite Y[244]. The pristine USY zeolite exhibits a pronounced uptake at low relative pressure, indicative of microporosity, together with a gradual adsorption increase at higher $p/p_0$ values, consistent with the presence of secondary mesoporosity. Upon increasing nickel loading, the overall adsorption capacity decreases progressively, in agreement with the reduction in BET surface area and pore volumes. The pore size distribution reveals a dominant contribution centred at approximately 8.8 Å, which is distinctive for this specific zeolite. Notably, while the intensity of this contribution decreases with increasing nickel content, no significant shift in pore width is observed.

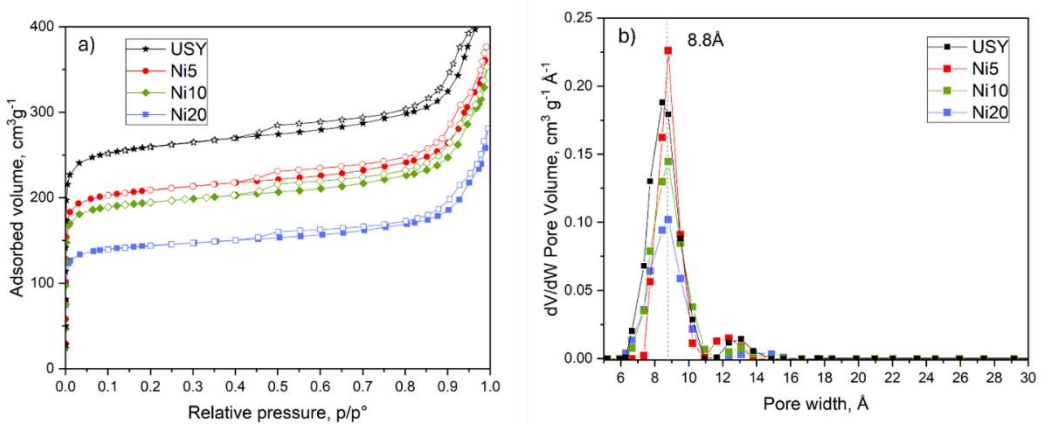


**Figure 2.3. (a) $N_2$ adsorption-desorption isotherms at -196 °C and (b) pore size distribution of pristine USY and Ni-USY catalysts with increasing nickel loading.**

The gradual reduction in surface area from Ni5 to Ni20 suggests an increasing degree of pore coverage and/or partial blockage, rather than a collapse of the zeolite framework[245]. This observation is consistent with the XRD results, which show preservation of the zeolite structure for all samples. Importantly, despite the reduction in surface area, the catalysts retain a substantial fraction of the original porosity, suggesting that the porous network remains accessible to reactant molecules.

Overall, $N_2$ physisorption analysis indicates that nickel incorporation affects the textural properties of the USY support in a loading-dependent manner, primarily through partial pore filling and surface coverage. These modifications to the porous structure are expected to influence metal dispersion and mass transport phenomena[205], and therefore provide an important context for interpreting the catalytic performance discussed in the following sections. Ni20 sample shows a remarkably high surface area compared to Ni-supported zeolite catalysts reported in literature[205,207].

**Table 2.2. Textural properties of USY and Ni-USY catalysts derived from $N_2$ physisorption measurements.**

| *Sample* | *t-plot* | | | | |
|---|---|---|---|---|---|
| | $S_{BET}$ ($m^2\ g^{-1}$) | $S_{ext}$ ($m^2\ g^{-1}$) | $V_{mp}$ ($cm^3\ g^{-1}$) | $V_{meso}$ ($cm^3\ g^{-1}$) | $V_p$ ($cm^3\ g^{-1}$) |
| ***USY*** | 750 | 165 | 0.30 | 0.37 | 0.67 |
| ***Ni5*** | 628 | 136 | 0.26 | 0.29 | 0.55 |
| ***Ni10*** | 584 | 132 | 0.24 | 0.27 | 0.51 |
| ***Ni20*** | 438 | 120 | 0.17 | 0.23 | 0.40 |

In further support of the conclusion that the USY support cannot be regarded as an exclusively microporous material, t-plot analysis reveals the presence of an appreciable external surface area, as showed in Table 2.2. The external surface area estimated by t-plot analysis is highest for the pristine USY and decreases progressively with increasing nickel content, mirroring the trend of the BET surface area. This correlation suggests that the loss of accessible surface upon metal loading affects both microporous and non-microporous domains, consistent

with partial pore filling and surface coverage by nickel species rather than structural degradation of the zeolite framework[210].

Scanning electron microscopy (SEM) was employed to evaluate the morphological integrity of the USY support after nickel incorporation. Representative SEM images of the Ni5, Ni10, and Ni20 catalysts (Figure 2.4) show that the characteristic morphology of ultrastable Y zeolite is preserved across the entire series. The samples consist of irregularly shaped zeolite crystals with dimensions in the 100 – 300 nm range, forming agglomerates. No significant morphological changes or formation of large nickel aggregates are observed upon increasing metal loading, indicating that both the impregnation procedure and the subsequent thermal treatments do not induce structural degradation of the support nor segregation of the active phase.

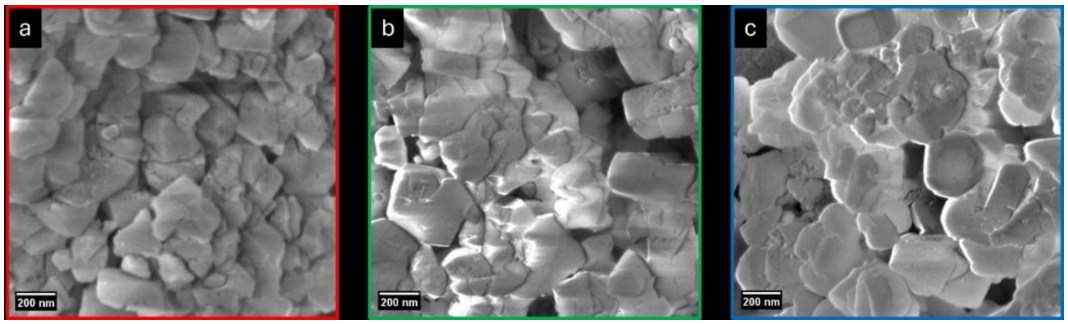


**Figure 2.4. Representative SEM images of Ni-USY catalysts with increasing nickel loading: (a) Ni5, (b) Ni10, and (c) Ni20.**

The dispersion and size distribution of nickel particles were further investigated by TEM and STEM coupled with EDS mapping, showed in Figure 2.5. Dense, globular nanoparticles enriched in nickel are identified and are uniformly distributed over the zeolite crystals. The Ni5 and Ni10 catalysts exhibit similar size distributions of Ni nanoparticles, centered at 15 and 50 nm, respectively (with an average size of approximately 30 nm, as shown in the red and green histograms in Figure 2.5). In the Ni20 sample, the dense material remains uniformly distributed but displays a significantly larger particle size, with the Ni nanoparticle size distribution centered around 180 nm (blue histogram in Figure 2.5).

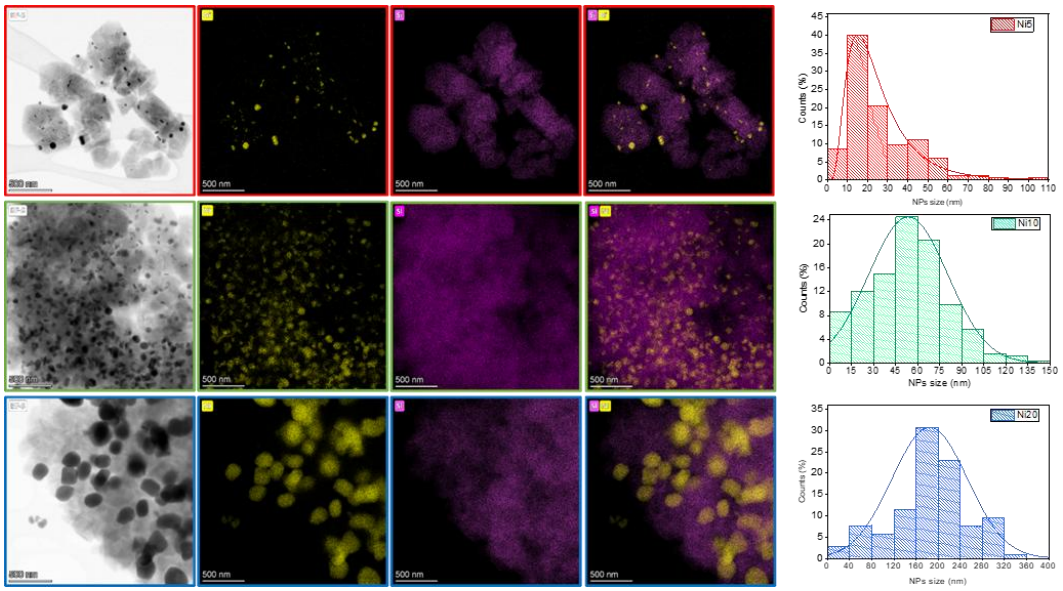


**Figure 2.5. STEM micrographs and corresponding EDS elemental maps of Ni-USY catalysts with increasing nickel loading (from top to bottom: Ni5, Ni10, Ni20). Ni-nanoparticles (identified in yellow) are distributed over the zeolite crystal (Si, purple). The particle size distribution are reported on the right.**

High-angle annular dark-field scanning transmission electron microscopy (HAADF-SEM) was employed to gain direct insight into the internal morphology of the dealuminated USY support at high spatial resolution. As shown in Figure 2.6, the USY crystals exhibit the presence of surface cavities and intra-crystalline mesopores, the coexistence of which allows to define a hierarchical architecture for the prepared catalyst – the two types of pores are interconnected[246,247].

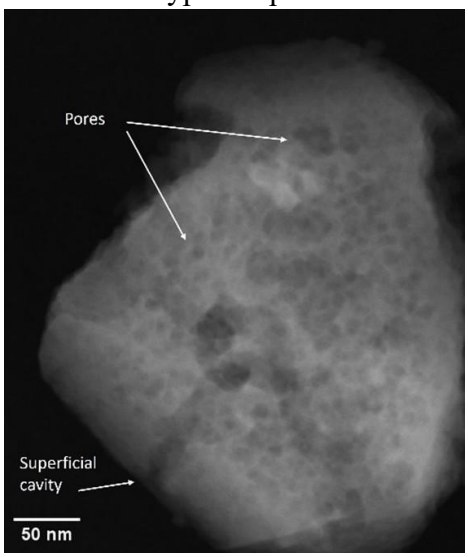


**Figure 2.6. HAADF-STEM micrograph of the dealuminated USY zeolite acquired at high magnification, highlighting the presence of surface cavities and intra-crystalline mesopores.**

The acidity of the Ni-USY catalysts was investigated by $NH_3$ temperature-programmed desorption. The $NH_3$-TPD profiles of fresh and used samples are reported in Figure 2.7. All fresh catalysts exhibit a pronounced low-temperature desorption peak centred at approximately 75 °C, accompanied by a broad

desorption pattern at medium-high temperatures (at 390 °C, 435 °C, and 570 °C). This distribution indicates the presence of acid sites with a wide range of strengths.

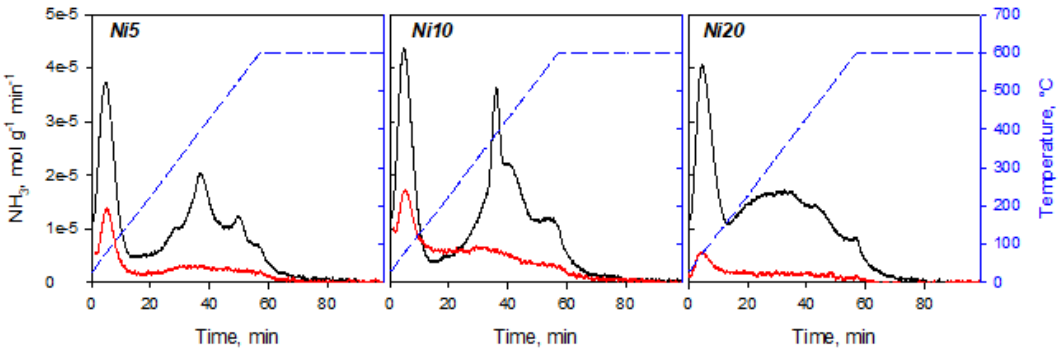


**Figure 2.7. TPD analysis of Ni5, Ni10, and Ni20 samples; dashed lines show temperature profiles.**

Based on comparison with literature data, the low-temperature desorption peak can be attributed to weakly acidic sites associated with Si-OH groups, while the medium- and high-temperature desorption feature are commonly related to Brønsted and Lewis acid sites[244]. Although the Si/Al ratio of the present USY sample is significantly higher than that reported in the reference work, the qualitative similarity of the desorption profiles supports the validity of this peak assignment. Table 2.3 shows the quantitative analysis of $NH_3$-TPD experiments. It suggests that a decreasing in acidity strength, as well as number of acid sites, occurs by increasing the Ni content on fresh samples.

**Table 2.3. $NH_3$ desorption (mmol/g) for Ni-USY samples.**

| | ***Ni5*** | ***Ni10*** | ***Ni20*** |
|---|---|---|---|
| ***Peak 1*** | $1.55 \cdot 10^{-1}$ | $1.86 \cdot 10^{-1}$ | $1.68 \cdot 10^{-1}$ |
| ***Peak 2*** | $1.85 \cdot 10^{-1}$ | $4.04 \cdot 10^{-2}$ | $2.87 \cdot 10^{-1}$ |
| ***Peak 3*** | $5.51 \cdot 10^{-2}$ | $3.40 \cdot 10^{-1}$ | |
| ***Peak 4*** | $1.83 \cdot 10^{-2}$ | $7.26 \cdot 10^{-2}$ | |
| ***Overall*** | $4.13 \cdot 10^{-1}$ | $6.39 \cdot 10^{-1}$ | $4.55 \cdot 10^{-1}$ |

### 2.4.2 $CO_2$ methanation performance

Figure 2.8 reports the $CO_2$ conversion (Figure 2.8a) and $CH_4$ selectivity (Figure 2.8b) as a function of temperature in the range 450 – 600 °C for the Ni5, Ni10, and Ni20 catalysts supported on USY, together with the Ni10-A reference catalyst supported on γ-$Al_2O_3$. Experimental data are compared with two equilibrium envelopes: the complete equilibrium curve accounting for both $CO_2$ methanation and RWGS, and a restricted one to only the Reverse Water-Gas Shift (RWGS) reaction. A clear dependence of catalytic behaviour on nickel loading is observed. The Ni20 catalyst shows an experimental data trend qualitatively following the thermodynamic equilibrium curve that includes the methanation reaction, rather than the equilibrium curve limited solely to the Reverse Water Gas Shift (RWGS) reaction. This behaviour is further confirmed by the

corresponding selectivity trends: the $CH_4$ selectivity of Ni20 is high at low temperature and progressively decreases with increasing temperature, in agreement with the thermodynamic disfavouring of methanation at elevated temperatures.

In contrast, the Ni5 and Ni10 catalysts display substantially different trends. In both cases, the experimental conversion profiles closely resemble the restricted equilibrium curve associated with RWGS. Consistently, the selectivity to methane remains very low across the entire temperature range, not exceeding 15% even at the lowest investigated temperatures, and approaching zero at temperatures above 550 °C. These results demonstrate that, for Ni5 and Ni10, $CO_2$ conversion is almost exclusively governed by the RWGS reaction, with negligible contribution from methanation. The reference sample showed catalytic performance approaching the thermodynamic equilibrium in the whole temperature range.

Overall, the catalytic tests reveal the existence of two distinct catalytic regimes within the investigated catalyst set. Low and intermediate nickel loadings on USY (Ni5 and Ni10) promote a RWGS-dominated behaviour, whereas higher nickel loading (Ni20) enables a transition towards methanation-dominated $CO_2$ hydrogenation, approaching the corresponding thermodynamic equilibrium.

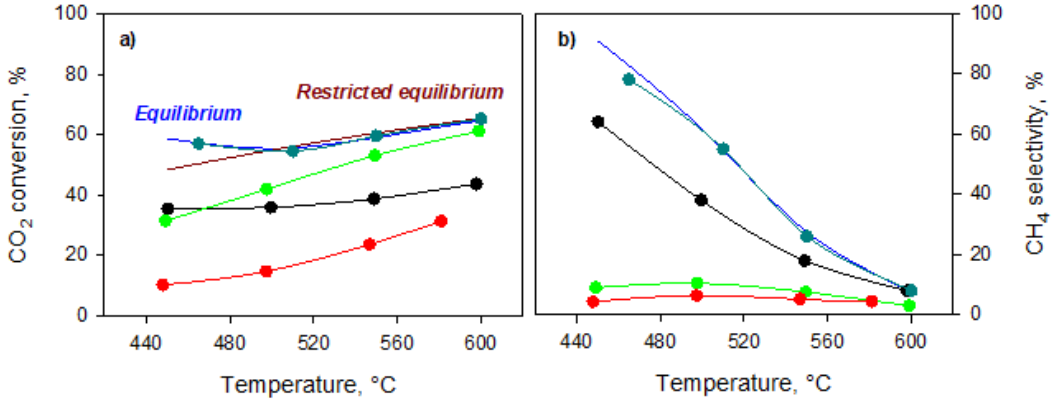


**Figure 2.8. (a) $CO_2$ conversion and (b) $CH_4$ selectivity as a function of reaction temperature (450 – 600 °C) for Ni-USY catalysts with increasing nickel loading (Ni5 red line, Ni10 green line, Ni20 black line) and for the Ni10-A reference catalyst (cyan line). The continuous curves represent the equilibrium, blue line for complete equilibrium, brown line for restricted equilibrium.**

### 2.4.3 Structure-performance relationships and discussion

The combined analysis of structural, textural, and surface characterisation results gave insights into the catalytic behaviour observed for the Ni-USY in $CO_2$ hydrogenation. In particular, the transition from a RWGS-dominated regime (Ni5 and Ni10) to a methanation-dominated (Ni20) can be directly correlated with changes in nickel particle size, support porosity, and surface chemistry.

As showed by electron microscopy analysis, nickel particle size increases with increasing metal loading on the USY support. For the Ni5 and Ni10 catalysts, nickel is present as relatively small nanoparticles with average sizes on the order of tens of nm, whereas the Ni20 catalyst is characterised by a broader

size distribution and the predominance of significantly larger particles. These trends are consistent with the crystallite size evolution derived from XRD analysis using the Scherrer equation.

The catalytic results indicate a strong structure sensitivity of $CO_2$ hydrogenation over Ni-USY catalysts. Small and well-dispersed nickel nanoparticles, as observed for Ni5 and Ni10, promote $CO_2$ conversion predominantly via the RWGS reaction, yielding CO as the main product. In contrast, the larger nickel particles present in the Ni20 catalyst favour the methanation pathway, resulting in high $CH_4$ selectivity and $CO_2$ conversion profiles approaching the complete thermodynamic equilibrium.

Beyond the intrinsic properties of the nickel phase, the porous architecture of the catalyst plays a decisive role in determining catalytic performance[247–249]. As reported in the previous section, with HAADF-STEM analysis, the USY support exhibits a hierarchical architecture, combining intrinsic microporosity (≈8.8 Å) with intra-crystalline mesopores, which combined represent a resistance for mass transfer from the external surface of the catalyst particle to the core[250]. Nickel particles cannot be accommodated within the USY micropores and are instead located within mesoporous regions or on external surfaces (see Table 2.5). As a consequence, reactants and product must diffuse through USY micropores to access or leave active sites of Ni nanoparticle.

The evolution of acidic and surface properties of Ni-USY catalysts under reaction conditions was investigated through post-reaction $NH_3$-TPD analysis. Comparison of the first peak between fresh and spent catalysts reveals a pronounced decrease in total surface acidity following reactions, as showed in Figure 2.7 and summarised in Table 2.4.

**Table 2.4. $NH_3$ desorption comparison of the first peak of fresh and spent Ni-USY catalysts.**

| | ***Ni5*** | | ***Ni10*** | | ***Ni20*** | |
|---|---|---|---|---|---|---|
| | Fresh | Spent | Fresh | Spent | Fresh | Spent |
| ***Peak 1*** | $1.55 \cdot 10^{-1}$ | $4.51 \cdot 10^{-2}$ | $6.39 \cdot 10^{-1}$ | $3.97 \cdot 10^{-2}$ | $4.55 \cdot 10^{-1}$ | $3.07 \cdot 10^{-2}$ |

The stability of the catalyst with respect to carbon deposition has been further evaluated by $O_2$ temperature-programmed oxidation (TPO), as shown in Figure 2.9. Under the investigated reaction conditions, negligible $CO_2$ evolution was detected for the Ni5 and Ni10 samples, indicating minimal coke formation, while the Ni20 catalyst exhibits detectable $CO_2$ release during TPO, with oxidation peaks centred at approximately 450 and 600 °C, attributable to amorphous and filamentous carbon species, respectively[251]. Despite this, the estimated coke selectivity remains extremely low (on the order of $10^{-4}$ mol of coke per mol of reacted carbon in $CO_2$), confirming a high resistance to fouling. In contrast, Ni10-A does not exhibit comparable resistance to coking, displaying a coke selectivity of approximately $9.8 \times 10^{-4}$ (moles of coke formed per mole of reacted carbon from methane and/or $CO_2$) and a coke formation rate of $5.5 \times 10^{-4}$ (moles of coke formed per mole of reacted carbon from methane and/or $CO_2$ per second). The

pronounced oxygen consumption observed in Figure 2.9 can be mainly attributed to the oxidation of Ni.

The limited carbon deposition observed for Ni-USY catalysts can be attributed to the combined effects of low post-reaction surface acidity, controlled nickel particle growth, and the hierarchical pore architecture of the USY support, which restricts carbon nucleation and filament growth[252,253]. These characteristics of Ni-USY samples contribute to preserving catalyst integrity and stable performance over extended operation times.

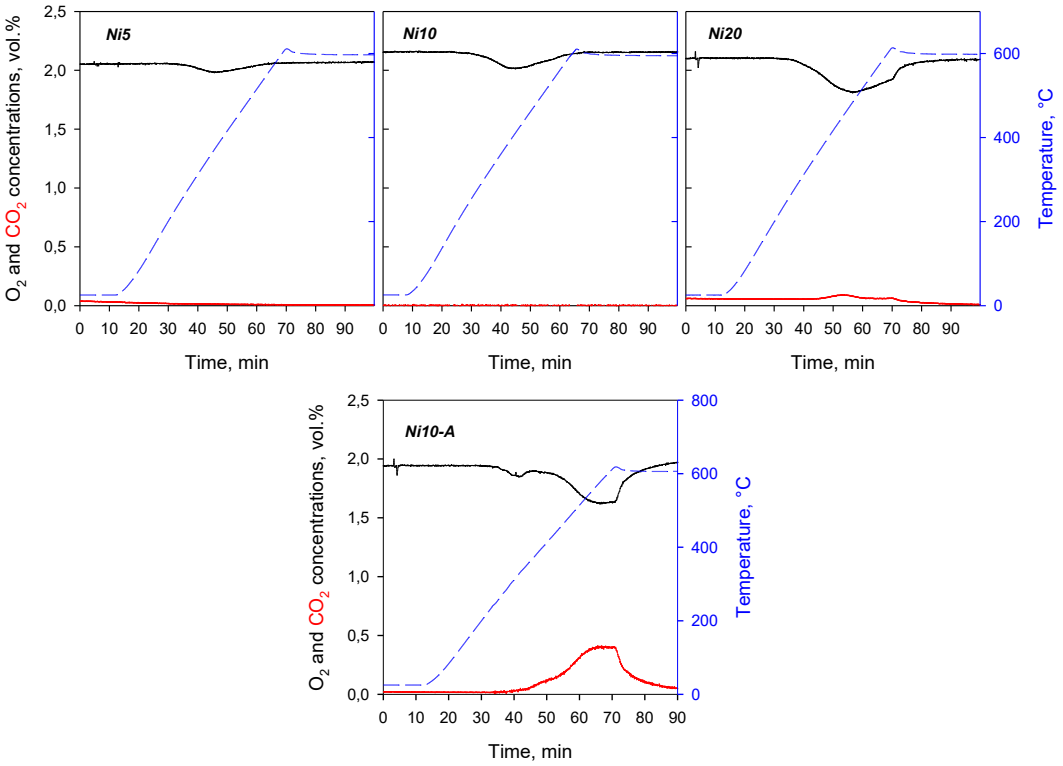


**Figure 2.9. TPO analysis results showing the $CO_2$ production and $O_2$ consumption.**

To conclude, the catalytic performance of the Ni-USY catalysts was compared with representative Ni-based systems reported in the literature. For $CO_2$ methanation, several Ni-supported zeolite catalysts have been reported to achieve conversions close to thermodynamic equilibrium at lower temperatures or under significantly longer contact times than that adopted in this work[205,207,211]. With respect to the RWGS reaction, due to the predominance of small, well-dispersed nickel nanoparticles, Ni5 and Ni10 achieved $CO_2$ conversion levels comparable to or exceeding those reported for Ni supported on nanocrystalline MgO at similar nickel loadings[254], while higher intrinsic RWGS activities have been reported for Ni nanoparticles supported on materials with larger and more open pore structures, such as N-doped silica, where intraparticle mass transport limitations are minimised[255] and bimetallic Cu-Ni systems supported on alumina, whose enhanced activity has been attributed to modified electronic properties of the active phase relative to monometallic nickel[256].

Overall, the comparison with literature data confirms that the catalytic behaviour of Ni-USY catalysts is governed by a complex interplay between nickel particle size, support porosity and acidity, and transport phenomena.

## 2.5 Re-based catalysts for $CO_2$ hydrogenation and ICCU

Rhenium-based catalysts represent an unconventional yet scientifically compelling choice for $CO_2$ hydrogenation and integrated carbon capture and utilisation (ICCU). Unlike traditional methanation catalysts, such as Ni- or Ru-based systems, rhenium does not exhibit outstanding activity or selectivity toward methane under conventional steady-state $CO_2$ hydrogenation conditions, but it displays high thermal stability and the ability to form highly dispersed surface species on oxide supports, which make it particularly suitable for cyclic and non-steady-state operations. These features make rhenium an interesting candidate for ICCU processes, where the decoupling of adsorption and reaction steps can fundamentally alter reaction pathways and product selectivity. In this section, Re-based catalysts supported on various oxides are investigated to elucidate how metal dispersion, support chemistry, and reaction mode govern $CO_2$ conversion and methane selectivity. The catalytic tests were performed at CNRS-IRCELYON (Lyon, France).

### 2.5.1 Structural features of Re-based catalysts

The structural and morphological properties of the Re-based catalysts were investigated by XRD, SEM, and HAADF-STEM to establish a reliable framework for the interpretation of their catalytic activity behaviour under both conventional $CO_2$ hydrogenation and ICCU cycles. The catalysts series includes rhenium supported on $\gamma$-$Al_2O_3$, $CeO_2$, $TiO_2$, $ZrO_2$, and LDH-derived mixed oxides (LDO), as well as selected catalyst-adsorbent mixtures employed during ICCU cycles.

Powder X-ray diffraction (PXRD) patterns of the supported rhenium catalysts, as well as fresh LDH, are reported in Figure 2.10. In all cases, the diffractograms are dominated by reflections associated with the crystalline oxide supports, namely $\gamma$-$Al_2O_3$, cubic $CeO_2$, anatase $TiO_2$, monoclinic $ZrO_2$, and LDO. No diffraction peaks attributable to crystalline rhenium metal or rhenium oxide phases are detected within the sensitivity of the technique, indicating that rhenium is either highly dispersed or present as amorphous species at the investigated loadings. This observation is consistent across all supports and suggests that differences in catalytic behaviour cannot be ascribed to bulk rhenium phases.

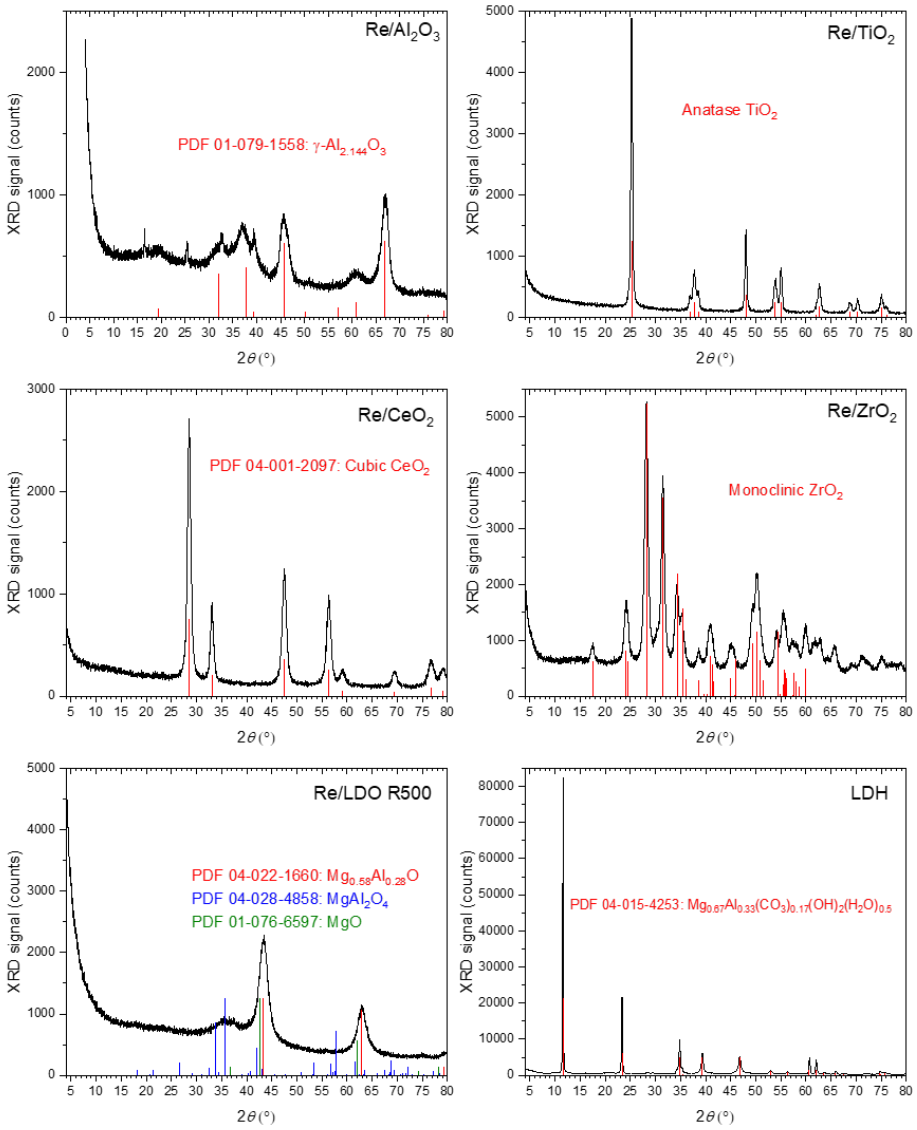


**Figure 2.10. XRD patterns of the main samples.**

The XRD confirms that the commercial hydrotalcite corresponds to a Mg-Al carbonate hydroxide phase, which deviates slightly from the nominal stoichiometry. Upon impregnation with the rhenium precursor and subsequent thermal treatment under reducing conditions, the LDH was converted to a mixed oxide (herein called layered double oxide, LDO) phase with near-$Mg_2AlO_x$ composition. The phase evolution of LDH under reducing atmosphere was further investigated by in situ XRD (Figure 2.11), revealing that the LDO structure becomes stable above approximately 400 °C, which is the temperature of the treatments performed before the ICCU tests.

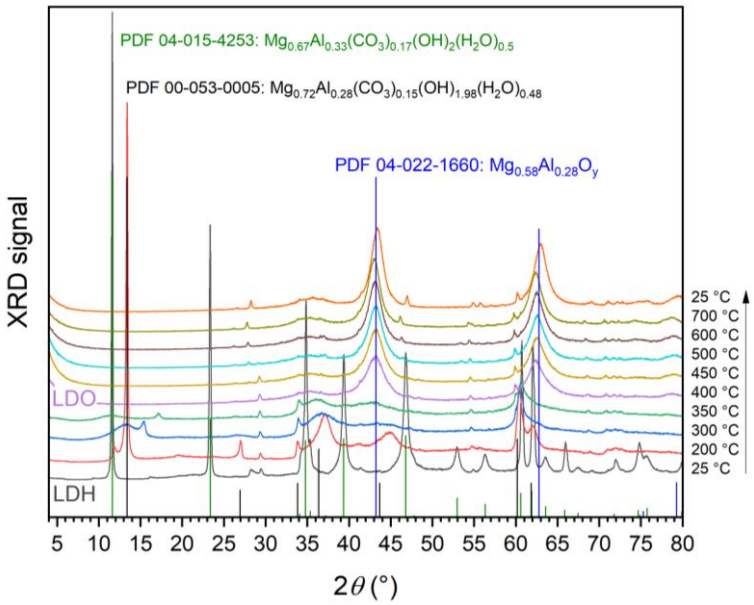


**Figure 2.11. In situ XRD diffractograms of commercial LDH under $H_2$ at various temperatures.**

Electron microscopy analysis provides direct insight into the dispersion and local environment of rhenium species. HAADF-STEM imaging (Figure 2.12a, c, and d) reveals the good dispersion of rhenium at the surface of alumina, LDO, and ceria. On $CeO_2$ and LDO, rhenium is predominantly present as isolated single atoms, homogeneously dispersed at the surface. In contrast, rhenium supported on $\gamma$-$Al_2O_3$ and titania is mainly observed in the form of few-atom clusters, while $Re/ZrO_2$ exhibits a distribution of species, from single atoms to clusters.

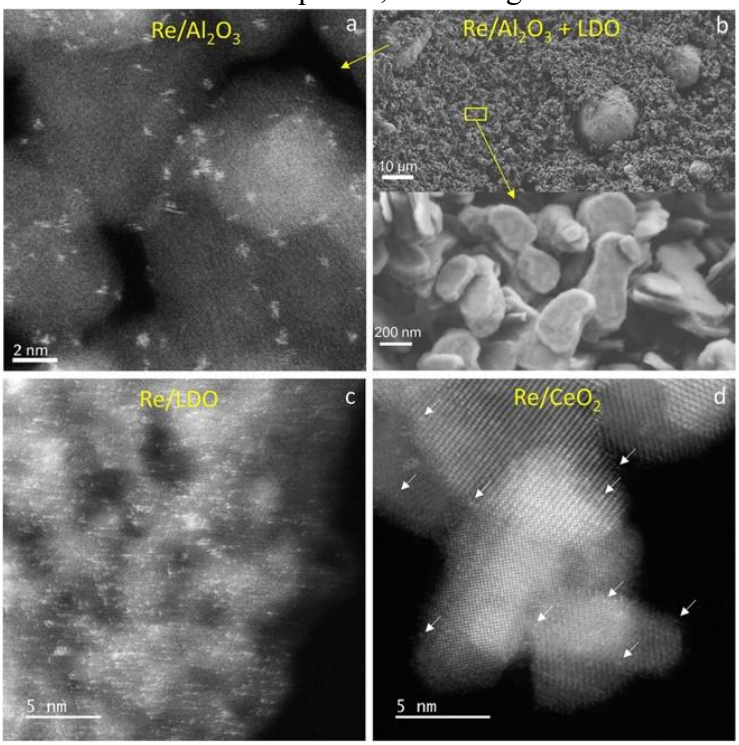


**Figure 2.12. Electron microscopy. HAADF-STEM (a, c, d) and SEM (b) images of supported rhenium samples. In (d) single Re atoms are highlighted by the arrows.**

Scanning electron microscopy (SEM) image in Figure 2.12b and Figure 2.13 further confirm the characteristic platelet-like morphology of LDO and illustrate the intimate physical contact achieved in catalyst-adsorbent mixtures employed for ICCU experiments.

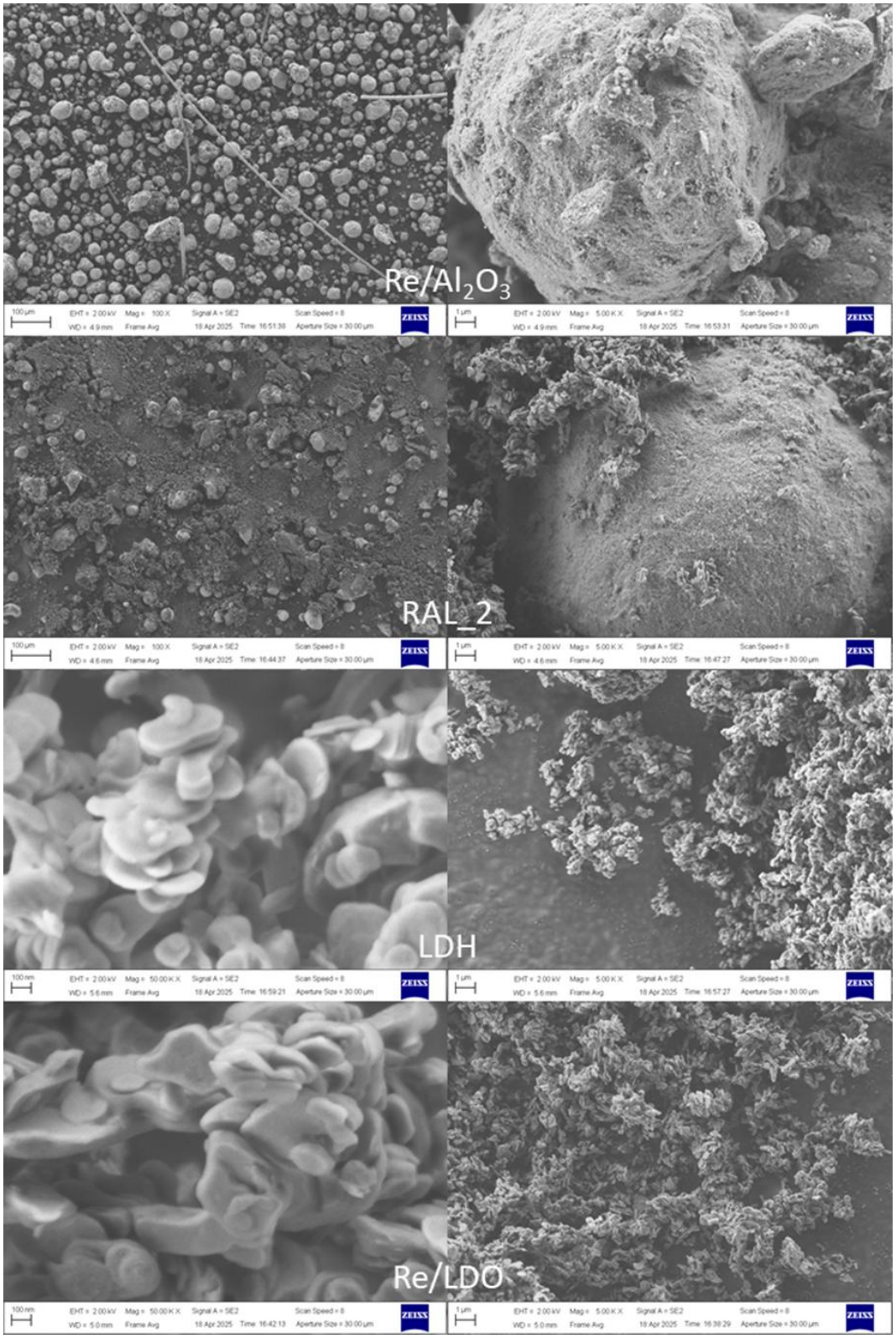


**Figure 2.13. SEM images of Re/γ-$Al_2O_3$, Re/γ-$Al_2O_3$ + LDO (RAL_2), fresh commercial LDH, and Re/LDO.**

### 2.5.2 $CO_2$ hydrogenation

Prior to ICCU operation, all catalysts were evaluated under conventional $CO_2$ hydrogenation in order to assess their intrinsic activity and selectivity independently from cyclic adsorption-reaction effects. Figure 2.14 reports the temperature-dependent $CO_2$ conversion, $CH_4$ selectivity, and $CH_4$ yield for both nickel- and rhenium-based catalysts, together with thermodynamic equilibrium limits for methanation.

As shown in Figure 2.14a, $CO_2$ conversion increases with temperature for all investigated materials in the range 180 – 400 °C. In all cases, the experimental conversions remain sufficiently below the equilibrium curve, indicating that the reverse reaction is negligible under the adopted operating conditions. Among the tested catalysts, $Ni/Al_2O_3$ exhibits the highest overall activity, reaching $CO_2$ conversions close to 50% at 400 °C, combined with a high selectivity towards methane (Figure 2.14b), resulting, clearly, in the highest $CH_4$ yield (Figure 2.14c). this confirms the role of alumina-supported nickel as an effective benchmark for $CO_2$ methanation under steady-state conditions, as underlined in the previous sections.

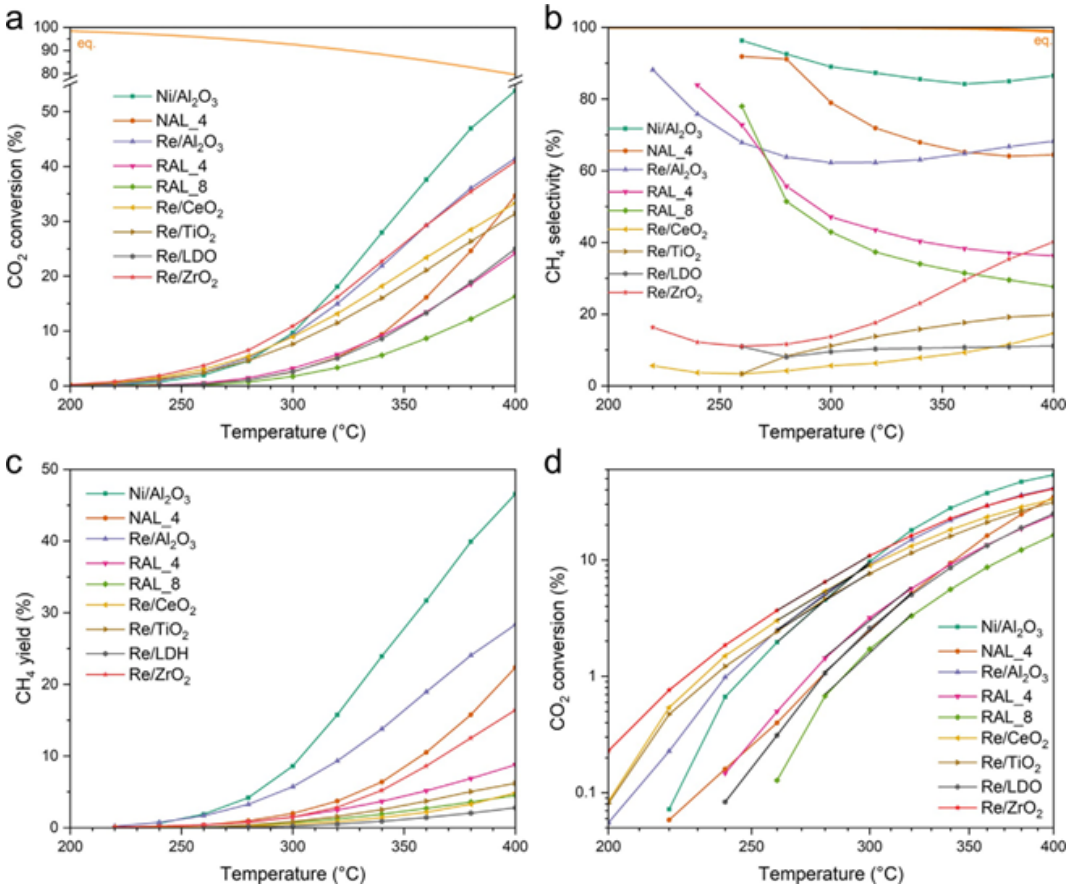


**Figure 2.14. $CO_2$ hydrogenation performance of nickel- and rhenium-based catalysts: (a) $CO_2$ conversion, (b) $CH_4$ selectivity, (c) $CH_4$ yield, and (d) Arrhenius plots of $CO_2$ conversion used to estimate apparent activation energies. Solid orange lines represent thermodynamic equilibrium limits for $CO_2$ conversion and $CH_4$ selectivity.**

Rhenium-based catalysts display a markedly different behaviour depending on the nature of the support. At 300 °C, $Re/Al_2O_3$ displays a $CO_2$ conversion of approximately 9% with a selectivity close to 62%, values comparable to those obtained over $Ni/Al_2O_3$ under the same conditions. By contrast, when rhenium is supported on $CeO_2$, $TiO_2$, $ZrO_2$, and LDO, methane selectivity drops sharply, typically remaining below 15%, despite comparable or even higher overall activity at low temperatures when considering the combined formation of CO and $CH_4$. These results suggest that non-alumina supports strongly promote the RWGS reaction suppressing methanation pathway. A similar trend is observed upon catalyst dilution with LDH-derived oxides. For both nickel- and rhenium-based catalysts, the presence of LDO phase systematically reduces $CO_2$ conversion and $CH_4$ selectivity respect to their undiluted counterparts. This progressive shift toward CO formation can be attributed to the presence of the adsorbent phase, which enhances local $CO_2$ availability while simultaneously limiting hydrogen access to metallic sites, thus kinetically promoting RWGS over methanation.

When the catalytic activity is normalised over the molar amount of metal all alumina-containing catalysts display remarkable similar intrinsic methanation rates at 300 °C (Table 2.5), ranging from 15.0 and 16.5 $mmol_{CH4}/mol_{Me}/s$). This observation indicates that the intrinsic activity of rhenium sites on alumina is largely preserved upon dilution and that the decrease in methane production observed for DFMs primarily originates from the decrease of the amount of the active phase rather than from intrinsic deactivation of the metal phase.

Arrhenius plots of $CO_2$ conversion are showed in Figure 2.14d and were used to estimate apparent activation energies, summarised in Table 2.5. The increase in apparent activation energy upon dilution could be related to the introduction of additional diffusion resistances and with a modified reactant supply to the catalytic sites, effects that become increasingly relevant at lower temperatures.

**Table 2.5. $CO_2$ conversion, $CH_4$ selectivity, intrinsic methanation rate normalised per mole of metal, and apparent activation energy for Ni- and Re-based catalysts under conventional $CO_2$ hydrogenation at 300 °C.**

| *Sample* | *$CO_2$ conv. (%)* | *$CH_4$ selec. (%)* | *Methanation rate ($mmol_{CH4}/mol_{Me}/s$)* | *$Eapp_{CO2}$ (kJ/mol)* |
|---|---|---|---|---|
| ***$Ni/Al_2O_3$*** | 9.7 | 89.0 | 16.5 | 101 ± 1 |
| ***NAL_4*** | 2.5 | 79.0 | 15.3 | 107 ± 3 |
| ***$Re/Al_2O_3$*** | 9.2 | 62.3 | 15.0 | 83 ± 4 |
| ***RAL_4*** | 3.2 | 47.1 | 15.8 | 94 ± 7 |
| ***RAL_8*** | 1.7 | 42.9 | 15.6 | 108 ± 9 |
| ***$Re/CeO_2$*** | 9.0 | 5.6 | 1.6 | 69 ± 1 |
| ***$Re/TiO_2$*** | 7.6 | 11.1 | 2.4 | 73 ± 3 |
| ***Re/LDO*** | 2.6 | 9.5 | 0.5 | 106 ± 7 |
| ***$Re/ZrO_2$*** | 10.9 | 13.7 | 4.8 | 69 ± 1 |

### 2.5.3 Integrated Carbon Capture and Utilisation (ICCU) performance

Following the optimisation of the ICCU operating parameters, the performance of the Re-based dual-functional materials was systematically evaluated under cyclic operations. Based on preliminary tests performed on $Re/Al_2O_3$, a temperature of 300 °C and a phase time of 4 min were selected as a compromise between maximising methane production and avoiding CO formation (Figure A.1 and Figure A.2 in Appendix). At this temperature, CO formation was not detected under steady ICCU conditions, while methane productivity increased slightly with temperature. The durations of the $CO_2$ adsorption and hydrogenation steps were then optimised, leading to the selection of 4/4 min cycles, including intermediate $N_2$ purge steps, as a suitable balance between productivity and process efficiency.

After defining the operating conditions, extended ICCU experiments were carried out over 50 consecutive cycles. Representative concentration profiles for the first ten cycles are reported in Figure 2.15 for non-diluted catalysts, while test on inert material (blank), pure LDH treated in the same conditions as for DFMs, as well as $Re/TiO_2$ (quasi inactive) are shown in Appendix (Figure A.3). Under the selected conditions, no $CO_2$ desorption and no CO formation were detected during the hydrogenation steps for the majority of the investigated materials (the non-zero background signal for CO and $CH_4$ is inherent to the NDIR detector), with a methane produced order as: $Re/CeO_2 > Re/ZrO_2 > Re/Al_2O_3 > Re/TiO_2$. Minor CO evolution was observed only during the early adsorption steps for $Re/ZrO_2$ (the least selective catalyst for methanation), particularly during the first cycle following the $H_2$ pretreatment at 400 °C, suggesting a transient contribution of RWGS involving pre-adsorbed hydrogen. This effect almost vanishes within the first ten cycles and was negligible for the remaining duration of the experiments.

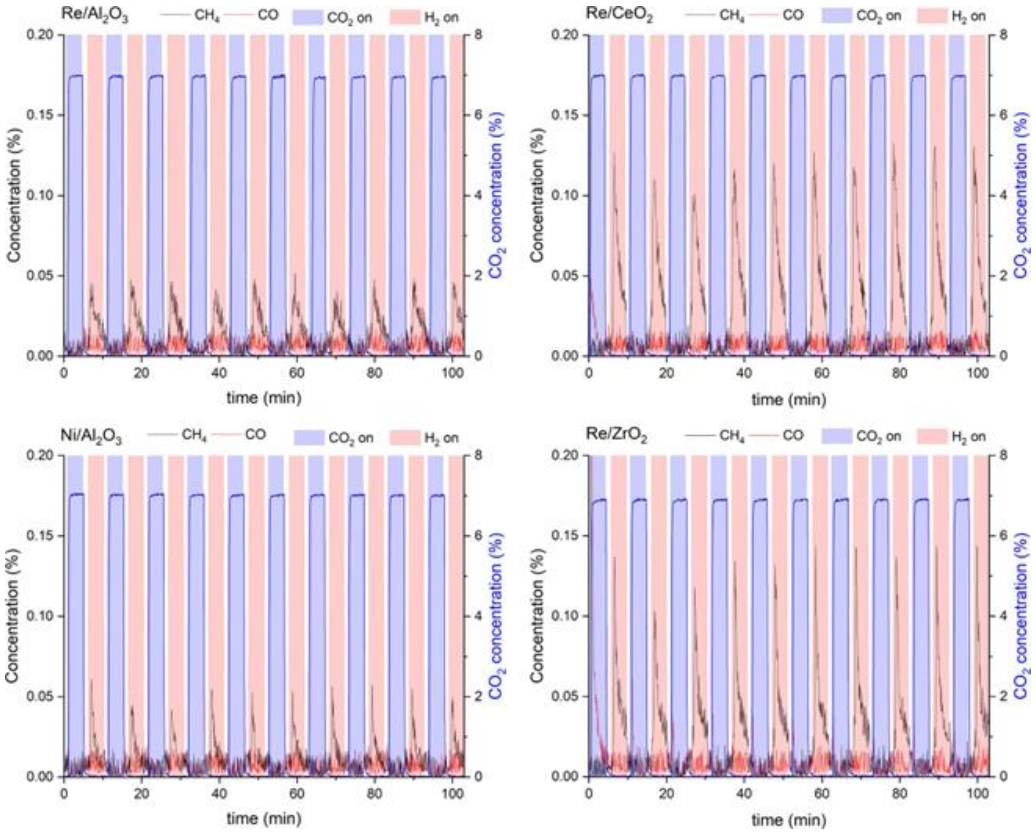


**Figure 2.15. First 10 cycles of ICCU performances of pure catalysts.**

The dilution of Re-based catalysts in LDH was systematically investigated to assess the effect of combining adsorption and catalytic functionalities. As shown in Figure 2.16, dilution of $Re/Al_2O_3$ by factors of 2 and 4 leads to a substantial increase in methane production per cycle, despite the lower amount of catalytic metal. A further increase in dilution (factor 8) results in a decrease in productivity, indicating the existence of an optimal balance between adsorbent and catalytic phases. A Re/LDO material prepared by impregnation exhibits the highest methane production per cycle among all investigated samples, although its intrinsic productivity per mole of rhenium is lower due to the higher metal loading (6.3%, see Table 2.1).

Additional dilution strategies were explored to further elucidate the role of the support. The dilution of $Re/Al_2O_3$ in $CeO_2$ and of $Re/CeO_2$ in LDH both result in a decrease in methane production (Figure A.5 in Appendix), confirming that the intrinsic combination of rhenium with ceria is particularly effective for ICCU operation. Ceria thus emerges not only as a catalytic support but also as an efficient $CO_2$ adsorbent at intermediate temperatures, in agreement with previous reports on ceria-modified systems[257–262].

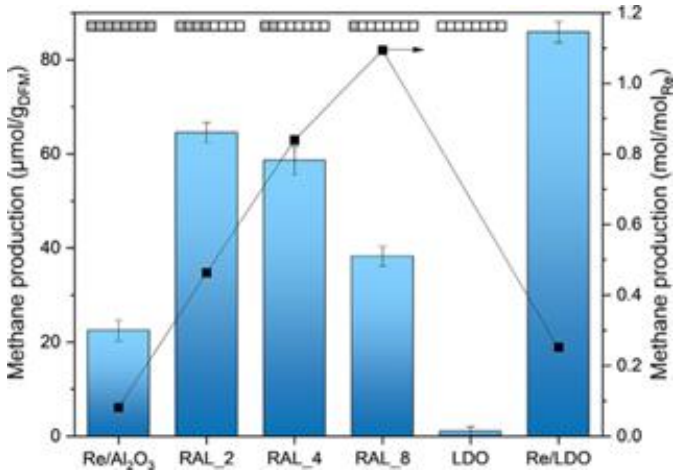


**Figure 2.16. ICCU performance of Re-based DFMs. Methane production per cycle (average on the first 10 cycles).**

A comparison of methane production across the different catalysts reveals a clear hierarchy in ICCU performance. Nickel-based $Ni/Al_2O_3$ also shows measurable ICCU activity, even if lower than that of the most efficient Re-based systems.

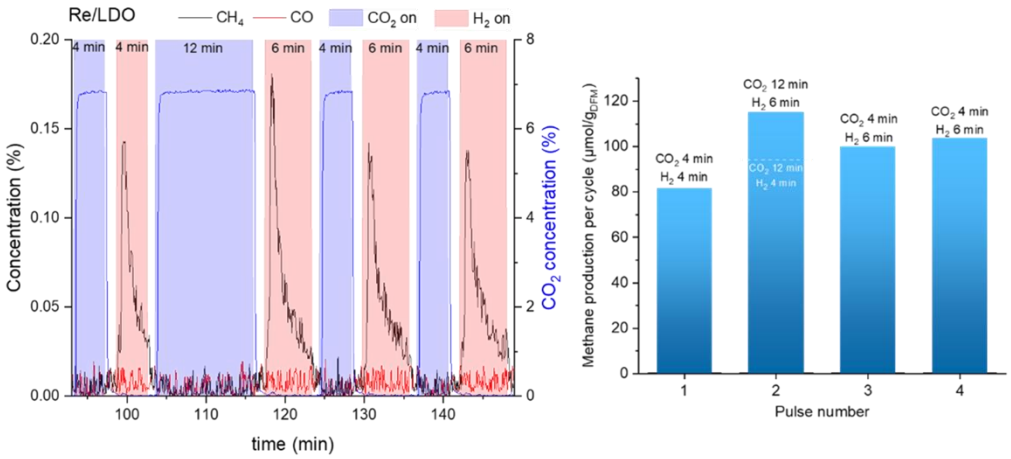


**Figure 2.17. ICCU tests on Re/LDO at variable adsorption and hydrogenation times, and corresponding methane productions.**

Increasing the duration of the adsorption and hydrogenation steps leads to a measurable increase in methane productivity (Figure 2.17). For Re/LDO, extending the $CO_2$ exposure from 4 to 12 min increases methane production by approximately 15%, while prolonging the hydrogenation step from 4 to 6 min provides an additional gain of about 22%. Under extended cycle durations (10/10 min), methane production reaches up to 128 µmol $g^{-1}$ per cycle for both Re/LDO and $Re/CeO_2$. Although these values remain modest in absolute terms, they are consistent with ICCU literature and are achieved with 100% methane selectivity, a condition that is rarely fulfilled in Ni-based DFMs[263,264].

The long-term stability of the catalysts was evaluated over up to 50 ICCU cycles (4/4 min cycle), as shown in Figure 2.18. Among the most efficient materials, $Re/CeO_2$ exhibits the highest stability, with a slight activation observed

during the initial cycles. In contrast, RAL_2 and RAL_4 show a gradual decrease in methane production with cycle number, indicating progressive deactivation or reorganisation under cyclic operation.

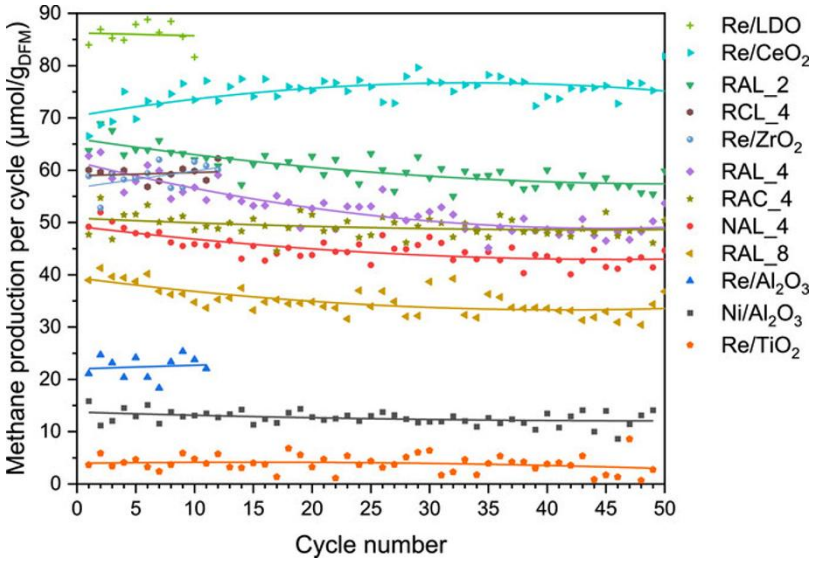


**Figure 2.18. ICCU performance comparison over 50 cycles (4/4 min).**

The ICCU performances were further compared by normalising methane production with respect to the total DFM mass, the mass of metal, and the molar amount of metal (Table 2.6). While Re/LDO, Re/$CeO_2$, and RAL_2 are the most productive materials when considering the total DFM mass, the most diluted catalysts, such as NAL_4 and RAL_8, exhibit the highest productivity per unit mass and per mole of metal, respectively. This result highlights the efficiency of highly dispersed catalytic sites when coupled with an appropriate adsorbent phase.

**Table 2.6. Average $CH_4$ production rate under ICCU conditions at 300 °C, expressed per cycle and normalised per mass of DFM and per molar amount of metal. Averages are calculated over the first ten cycles (4/4 min).**

| *Sample* | *$CH_4$ production ($\mu mol_{CH4}/g_{DFM}$)* | *$CH_4$ production rate ($mmol_{CH4}/mol_{Me}/s$)* |
|---|---|---|
| ***$Ni/Al_2O_3$*** | 13.3 | 0.14 |
| ***NAL_4*** | 48.1 | 2.09 |
| ***$Re/Al_2O_3$*** | 22.5 | 0.34 |
| ***RAL_2*** | 64.5 | 1.93 |
| ***RAL_4*** | 58.6 | 3.50 |
| ***RAL_8*** | 38.2 | 4.56 |
| ***RAC_4*** | 50.6 | 3.58 |
| ***$Re/CeO_2$*** | 72.0 | 1.27 |
| ***RCL_4*** | 59.2 | 4.19 |
| ***Re/LDO*** | 86.0 | 1.05 |
| ***$Re/TiO_2$*** | 4.2 | 0.07 |
| ***$Re/ZrO_2$*** | 58.4 | 0.07 |

In conclusion, Re/LDO and Re/$CeO_2$ emerge as the most efficient DFMs for ICCU operation at intermediate temperature. The enhanced performance of these systems can be attributed to the proximity between $CO_2$ adsorption sites and

catalytically active rhenium species, enabling efficient conversion of adsorbed $CO_2$ during the hydrogenation step. Dilution of $Re/Al_2O_3$ with LDH significantly improves ICCU performance, reaching values comparable to those of $Re/CeO_2$, with an optimal balance achieved at a dilution factor of 2. The diluted Re-based materials are much more active per mol of metal than the best DFMs, implying that similar performances can be achieved with a significantly lower Re content. These results demonstrate that ICCU performance is governed by the interplay between adsorption capacity, catalyst-adsorbent proximity, and intrinsic catalytic activity, rather than by steady-state methanation performance alone.

### *Effect of water on ICCU performance*

The effect of water impurities in the $CO_2$ feed was investigated. The experimental protocol consisted of three consecutive stages: five standard ICCU cycles under dry $CO_2$, followed by five cycles with approximately 5 vol% $H_2O$ introduced in the $CO_2$ stream, and finally five additional cycles under dry conditions to assess performance recovery. As shown in Figure 2.19, the impact of water strongly depends on the nature of the catalyst-adsorbent system. The $Re/Al_2O_3$ catalyst displays an insensitivity to water, maintaining a stable methane production throughout the wet cycles and fully preserving its initial performance. In contrast, Re/LDO undergoes a severe and rapid loss of activity after water introduction, with only partial recovery observed after switching back to dry $CO_2$. The mechanical mixture RAL_4 exhibits an intermediate behaviour, characterised by a modest decrease in methane productivity under wet conditions and an almost complete recovery once water is removed from the feed. The pronounced deactivation observed for Re/LDO can be rationalised by considering the strong interaction between water and the LDH-derived oxide phase. After exposure to steam, partial rehydration of the LDO is likely to occur, leading to lattice expansion and possible coverage or shielding of nearby rhenium sites.

Finally, $Re/CeO_2$ loses approximately one third of its activity, with a full recovery of the initial methane production once dry conditions are restored. No gradual or cumulative deactivation is observed during wet operation, indicating that water-induced inhibition is reversible for this system.

These results highlight that, while the proximity of adsorptive and catalytic functions is detrimental in wet conditions for the Re/LDO system, the mechanical mixture RAL_4 and $Re/CeO_2$ are a good compromises between ICCU activity and water tolerance.

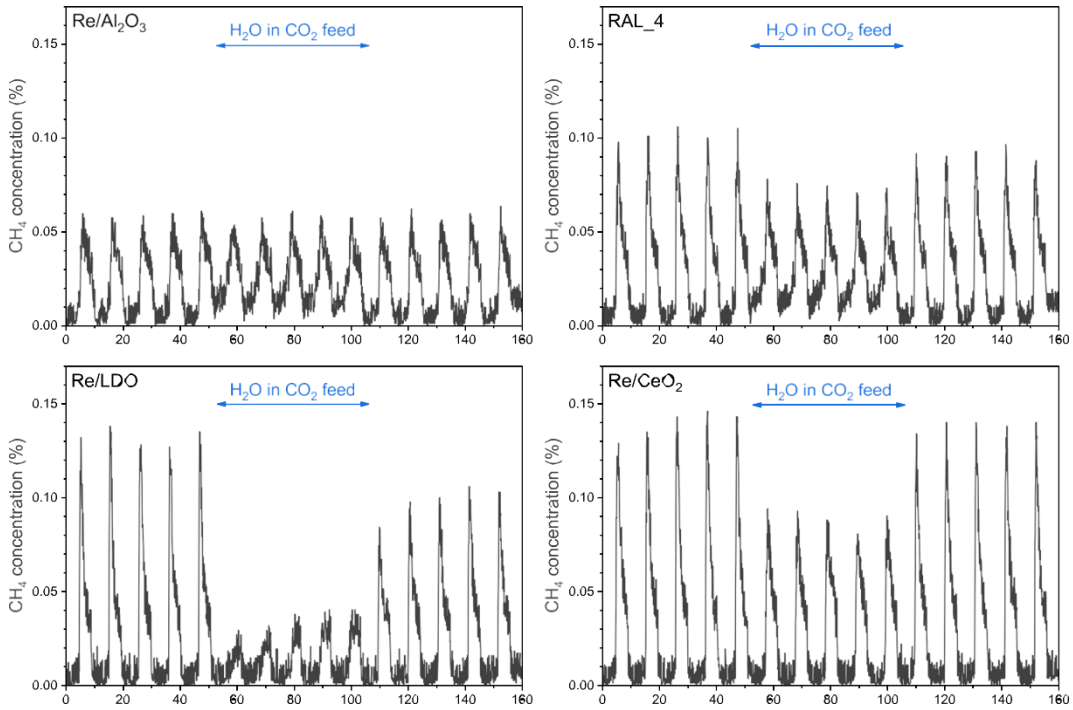


**Figure 2.19. Influence of water introduction in the $CO_2$ feed on methane production during ICCU cycles for $Re/Al_2O_3$, RAL_4, Re/LDO, and $Re/CeO_2$ catalysts.**

### 2.5.4 Temperature-Programmed Measurements

Selected samples were investigated by temperature-programmed desorption ($CO_2$-TPD, Figure 2.20a and Table 2.7) and temperature-programmed surface reaction (TPSR, Figure 2.20b and Table 2.7) to rationalise the different ICCU performances of Re-based catalysts by evaluating the $CO_2$ adsorption capacity, retention at reaction temperature, and reactivity under hydrogen.

$CO_2$-TPD profiles reveal marked differences in both adsorption capacity and thermal stability of adsorbed species depending on the support nature. LDO exhibits the highest $CO_2$ uptake, as showed by the integrated desorption signal, significantly exceeding that of $Re/Al_2O_3$. Accordingly, dilution of $Re/Al_2O_3$ with LDH-derived LDO strongly enhances the overall $CO_2$ adsorption capacity, providing a first explanation for the improved ICCU performance observed for RAL and Re/LDO materials in Section 2.5.3. $Re/CeO_2$ also shows a high initial $CO_2$ adsorption capacity; however, a substantial fraction of adsorbed $CO_2$ is released below 300 °C, indicating weaker binding compared to LDO-based systems.

A key aspect emerging from the TPD experiments is the incomplete $CO_2$ desorption at the ICCU operating temperature (300 °C) for LDO-, ceria-, and LDH-containing materials. While $Re/Al_2O_3$ releases nearly all adsorbed $CO_2$ below this temperature, significant fractions of $CO_2$ remain adsorbed on RAL_4, LDO, Re/LDO, and $Re/CeO_2$. This behaviour points out a stronger adsorption capacity on LDH-based and ceria mixtures samples, which are able to retain $CO_2$ under ICCU conditions and ensure its availability during the subsequent hydrogenation step.

TPSR experiments provide complementary information by directly probing the conversion of pre-adsorbed $CO_2$ under a hydrogen flow. In all investigated materials, a substantial fraction of $CO_2$ is desorbed rather than converted to methane, reflecting the fact that $CH_4$ formation only becomes significant above ~150 °C. Nevertheless, clear differences emerge among the catalysts. Compared to $Re/Al_2O_3$, the RAL_4 sample exhibits both higher $CO_2$ desorption and increased $CH_4$ production, in line with its superior ICCU performance. Re/LDO displays the largest amount of desorbed $CO_2$ while $Re/CeO_2$ the most produced $CH_4$, confirming the strong synergy between high adsorption capacity and catalytic activity.

Overall, the temperature-programmed measurements demonstrate that ICCU performance is not governed solely by the total $CO_2$ adsorption capacity, but rather by the fraction of $CO_2$ retained at the operating temperature and its effective conversion during hydrogenation. Materials such as Re/LDO and $Re/CeO_2$ benefit from a favourable proximity between strong $CO_2$ adsorption sites and highly dispersed Re centres, enabling enhanced methane formation under sequential reaction conditions.

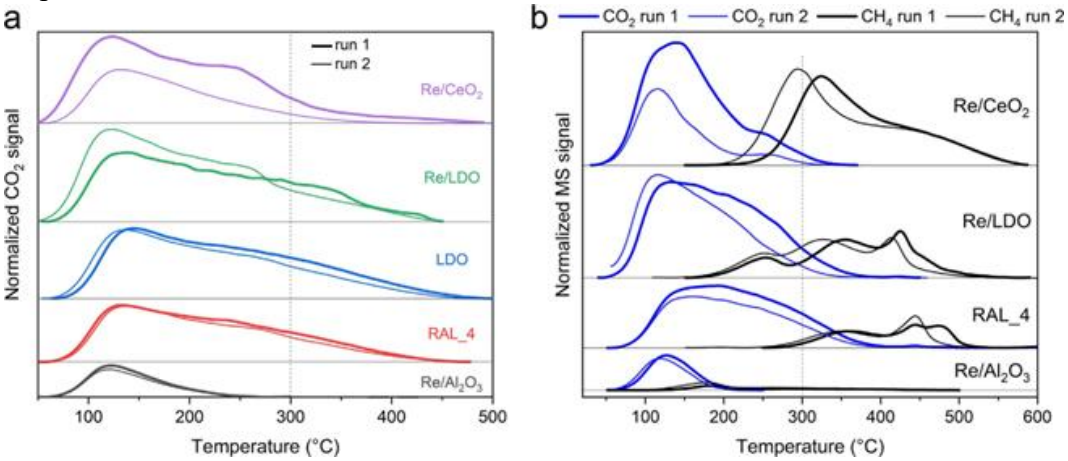


**Figure 2.20. (a) $CO_2$-TPD and (b) TPSR profiles of selected Re-based materials ($Re/Al_2O_3$, RAL_4, Re/LDO, $Re/CeO_2$). Samples were pretreated in $H_2$ flow up to 500 °C (TPD) and 600 °C (TPSR) before each run.**

**Table 2.7. $CO_2$ desorbed during $CO_2$-TPD and TPSR experiments and $CH_4$ produced during TPSR for selected samples. Values refer to two consecutive cycles.**

| *Sample* | *Desorbed $CO_2$ (TPD) (µmol $g^{-1}$)* | *Desorbed $CO_2$ (TPSR) (µmol $g^{-1}$)* | *$CH_4$ produced (TPSR) (µmol $g^{-1}$)* |
|---|---|---|---|
| ***LDO*** | 285/260 | - | - |
| ***$Re/Al_2O_3$*** | 53/46 | 38/35 | 3/7 |
| ***RAL_4*** | 222/200 | 188/146 | 25/25 |
| ***Re/LDO*** | 279/329 | 265/228 | 57/56 |
| ***$Re/CeO_2$*** | 304/141 | 242/111 | 102/112 |

### 2.5.5 Spectroscopic Investigation of $Re/CeO_2$

To rationalise the distinctive ICCU performance of $Re/CeO_2$ in terms of activity, long-term stability and response to water-containing $CO_2$ feeds, this section addresses the nature of surface intermediates formed upon exposure to $CO_2$ and $H_2$ of the rhenium phase under ICCU conditions, using also assessments based on the literature related to CO and $CO_2$ adsorption or hydrogenation on ceria and rhenium-related materials[265–271].

Operando Diffuse Reflectance Infrared Fourier Transform Spectroscopy (DRIFTS), coupled with online mass spectrometry, was employed to investigate the nature and the evolution of surface intermediates formed on $Re/CeO_2$ under ICCU conditions and during conventional $CO_2$ hydrogenation.

Figure 2.21a reports the evolution of the gas-phase composition monitored by mass spectrometry (m/z = 2, 4, 14, and 44 for $H_2$, He, $CH_4$ and $CO_2$, respectively) throughout the entire operando experiment, providing a clear visualisation of the experimental protocol. Two consecutive ICCU were performed at 300 °C, consisting of sequential exposure to He, $CO_2$, $H_2$ and again He, followed by a conventional $CO_2$ + $H_2$ experiment carried out under simultaneous feed conditions.

The DRIFTS spectra recorded during the first ICCU cycle (Figure 2.21a) reveal the progressive formation of different species upon exposure to $CO_2$, characterised by intense absorption bands in the 1000-1700 $cm^{-1}$ region, attributed to surface carbonate-like species ($\nu_{CO3}$), which may include monodentate, bidentate, polydentate, and bridged carbonates, carboxylates, hydrogen carbonates, and formats simultaneously[270]. These species only partially disappeared during the subsequent $H_2$ step, indicating a strong and partially irreversible $CO_2$, consistent with the $CO_2$-TPD results discussed in Section 2.5.4. under hydrogenation conditions, gaseous methane (3016 $cm^{-1}$) evolved, accompanied by the appearance of formate and carbonyl surface species, while no gaseous CO is detected. Formate-related bands gradually banish during the He purge, whereas carbonyl species persist for longer times, suggesting different stabilities and roles of these intermediates on the catalytic surface.

The second ICCU cycle (Figure 2.21c top) exhibits qualitatively similar spectral features, indicating that the surface chemistry rapidly reaches a quasi-steady state under cyclic operation. Notably, a clear correspondence is observed between the temporal evolution of the gaseous methane band at 3016 $cm^{-1}$, and the vibrational bands attributed to formats (2945, 2822, 2710, 1581, 1572, 1367, and 1354 $cm^{-1}$), supporting the involvement of formate species as key intermediates in methane formation during ICCU operation[269].

A direct comparison between ICCU and conventional $CO_2$ hydrogenation conditions is provided by the spectra recorded during the $CO_2$ + $H_2$ experiment in Figure 2.21c (bottom). Although carbonate-, formate-, and carbonyl-related bands are also detected under simultaneous feed conditions, their vibrational frequencies differ from those observed during ICCU. This indicates the formation of chemically distinct surface species, which may arise from different coordination

environments, such as bidentate structures adsorbed on ceria versus species bridged between rhenium atoms and the support[268]. Furthermore, the nature and distribution of these intermediates are strongly influenced by the reduction state of the ceria surface[270], which is itself process-dependent.

A precise assignment of the infrared bands observed under reaction conditions remains inherently challenging, owing to the complexity of $CO_2$-derived surface chemistry on ceria-based materials and to the coexistence of multiple adsorbed species with overlapping vibrational features. According to previous studies, the carbonate-like region at low wavenumber (1000 – 1700 $cm^{-1}$, $\nu_{CO3}$) encompasses a broad family of surface species that may simultaneously coexist on $CeO_2$[270]. Formate species are further know to contribute to the $\nu_{CH}$ stretching region (2700 – 3000 $cm^{-1}$)[265,267]. In particular, adsorbed methoxy species have also been reported on ceria surfaces and may give rise to bands in the same spectral window; accordingly, the features observed at 2822 and 2945 $cm^{-1}$ can be tentatively assigned either to formate $\nu_{CH}$ vibrations or, alternatively, to the symmetric and antisymmetric $\nu_{CH3}$ stretching modes of surface $OCH_3$ species[272,273]. The $\nu_{CO}$ region (1800 – 2100 $cm^{-1}$) exhibits an additional level of complexity, especially under simultaneous $CO_2 + H_2$ conditions. In this range, the bands centred at 2024 – 2032, 1903 – 1910 and around 1870 $cm^{-1}$ may be attributed to $Re(CO)_3$-type tricarbonyl species formed on rhenium sites, as previously proposed for Re-based catalysts[268]. Notably, the relatively weak dependence of the nature and intensity of most adsorbed surface species on temperature under $CO_2 + H_2$ conditions, contrasted with the strong increase in methane production, suggesting that the majority of the detected intermediates behave as spectator species. Only a minor fraction of these surface species is therefore likely to be directly involved in the rate-determining steps of $CO_2$ hydrogenation and ICCU methanation.

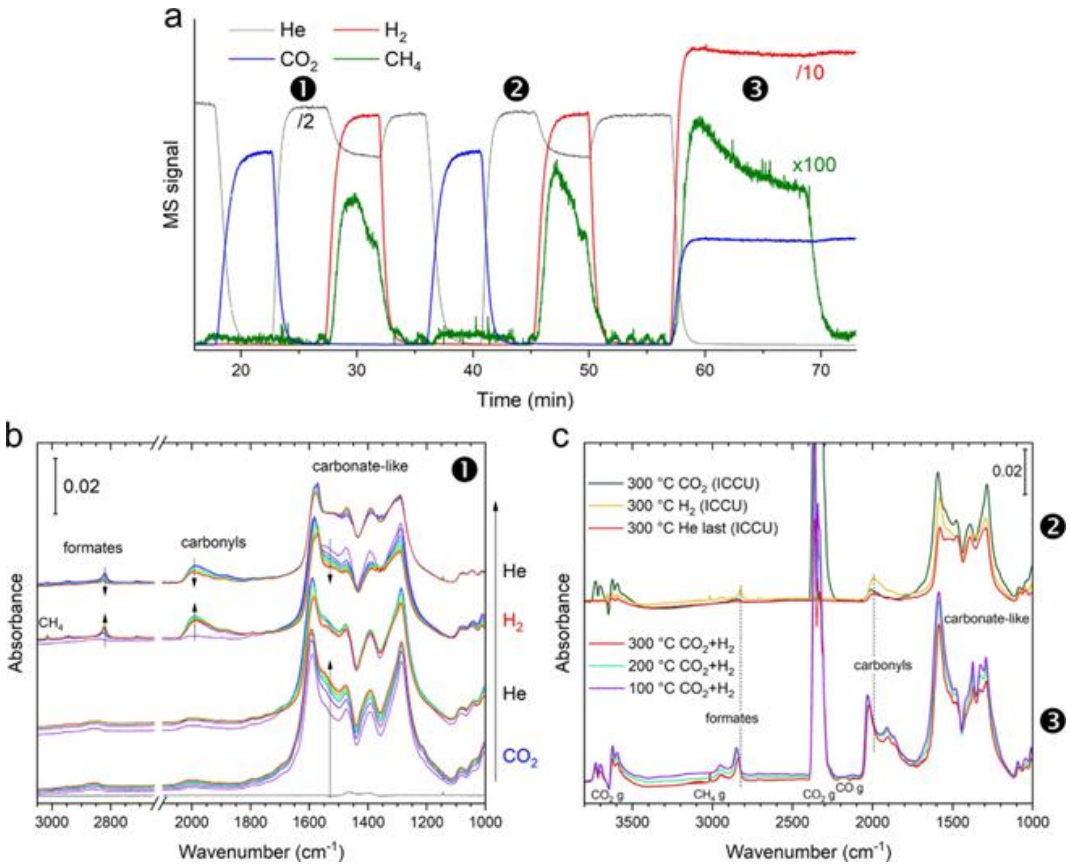


**Figure 2.21. Operando DRIFTS-MS investigation of $Re/CeO_2$ under ICCU and conventional $CO_2$ hydrogenation conditions. (a) Mass spectrometer signal (m/z = 2 for $H_2$, 4 for He, 15 for $CH_4$ and 44 for $CO_2$) recorded during two consecutive ICCU cycles at 300 °C, followed by a classical methanation. (b) Series of DRIFTS spectra collected at each step of the first ICCU cycle. (c) DRIFTS spectra recorded during the second ICCU cycle (top) and during conventional $CO_2$ hydrogenation (bottom).**

### 2.5.6 Structure-function relationships and discussion

The results discussed in the previous sections highlight how the catalytic behaviour of rhenium-based materials strongly depends on the equilibrium between metal dispersion, support chemistry, and reaction mode. In particular, the comparison between conventional $CO_2$ hydrogenation and ICCU operation reveals profound differences in both activity and selectivity, which cannot be inferred from steady-state gas-phase tests alone.

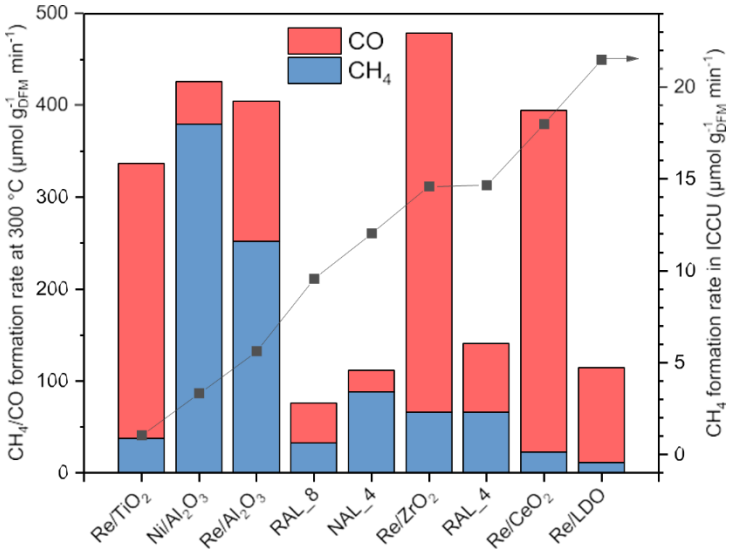


**Figure 2.22. Comparison between conventional $CO_2$ hydrogenation and ICCU operation at 300 °C. The ICCU rate was calculated by dividing the methane production per cycle by the hydrogenation time (4 min).**

A direct comparison between steady-state $CO_2$ hydrogenation and ICCU operation is provided in Figure 2.22, which clearly illustrates the effect of changing the operating mode. Catalysts exhibiting modest methanation rates under conventional $CO_2$ hydrogenation can display among the highest ICCU performances, as observed for $Re/ZrO_2$, Re/LDO and $Re/CeO_2$. This apparent inversion reflects the fundamentally different kinetic and mechanistic constraints imposed by the two reaction modes. Under steady-state conditions, methane formation benefits from the continuous and simultaneous availability of $CO_2$ and $H_2$, which generally leads to higher absolute methanation rates, particularly for Ni-based catalysts. In contrast, ICCU relies on the sequential introduction of reactants, and methane production becomes limited by the amount of $CO_2$ effectively adsorbed and retained during the capture step rather than by intrinsic surface hydrogenation kinetics.

Under conventional $CO_2$ hydrogenation, oxide-supported rhenium catalysts generally exhibit limited methane selectivity when compared to Ni-based references, despite showing appreciable activity at low temperature. This behaviour is largely independent of the oxide support and reflects the intrinsic catalytic properties of rhenium under simultaneous $CO_2$ and $H_2$ feed, being subjected also to competitive RWGS and formation of CO. Under ICCU conditions, a markedly different behaviour is observed. Independently of the oxide support employed ($Al_2O_3$, $CeO_2$, $ZrO_2$, $TiO_2$, or LDH-derived oxides), methane selectivity reaches 100% at 300 °C, with no detectable $CO_2$ release during the hydrogenation step. This pronounced selectivity shift demonstrates that the sequential introduction of $CO_2$ and $H_2$ fundamentally modifies the reaction network, suppressing RWGS pathways and favouring complete hydrogenation of adsorbed carbon species.

The influence of the support becomes particularly evident when comparing diluted and non-diluted systems. While dilution of $Re/Al_2O_3$ or $Ni/Al_2O_3$ with

LDH-derived oxides (LDO) negatively affects conventional methanation performance, due to the reduced availability of metallic active sites under steady-state conditions, the same dilution strategy significantly enhances ICCU performance, up to an optimal dilution factor of four for $Re/Al_2O_3$. Temperature-programmed measurements reveal that LDO increases both the amount of $CO_2$ adsorbed and its thermal stability, extending $CO_2$ retention up to approximately 450 °C instead of ~250 °C for alumina-supported systems. As a consequence, a larger fraction of $CO_2$ remains available for hydrogenation during the ICCU step, leading to significantly enhanced methane production.

Direct interaction between rhenium and LDO, as in Re/LDO materials, further amplifies this effect by lowering the onset temperature for methane formation and maximising the proximity between adsorption and catalytic sites. This configuration leads to the highest ICCU productivity among the investigates systems, while methane yield reaching 128 μmol $g^{-1}$ per 10/10 cycle at 300 °C. These results underline that, in ICCU, catalyst performance is governed less by intrinsic methanation activity and more by the effective coupling between $CO_2$ adsorption and subsequent hydrogenation.

Among the investigated supports, ceria emerges as a particularly effective alternative to LDO. Although $Re/CeO_2$ is unselective in conventional methanation, its high intrinsic $CO_2$ adsorption capacity enables ICCU performances comparable to those of Re/LDO. Moreover, $Re/CeO_2$ exhibits superior stability over repeated cycles and enhanced tolerance to water impurities in the $CO_2$ feed, making it especially relevant for practical ICCU operations.

To place the performance of the Re-based DFMs in the context of the literature, a comparison with selected benchmark systems operating under similar temperature conditions is provided. A direct quantitative comparison between ICCU results reported by different groups remains challenging, however, as methane productivity depends on operating conditions – particularly the $CO_2$ concentration in the capture feed, the duration of adsorption and hydrogenation steps, the total flow rate, and the amount of DFM used – which vary substantially across studies[263]. Sun et al.[274] tested $Ru/CeO_2$-MgO under 35% $CO_2/N_2$ for 60 min followed by 5% $H_2/N_2$ for 30 min, reporting a $CH_4$ yield of 330 μmol/g per cycle. Similarly, Cimino et al.[275] operated 3%Na-1%$Ru/Al_2O_3$ under 5% $CO_2$ for 18 min with a subsequent 14 min hydrogenation step (15% $H_2/N_2$), achieving 183 μmol/g. Arellano-Treviño et al.[225] reported 467 μmol/g for 5%Ru-7%$K_2O/Al_2O_3$ under 20 min of $CO_2$ adsorption and hydrogenation step of 60 min. The present work employs considerably shorter cycles (4+4 min), reaching maximum yields of 86 μmol/g per cycle with 100% $CH_4$ selectivity. When normalised by cycle duration, the pseudo-reaction rates of the best Re-based DFMs are competitive with the literature values, while employing a considerably less expensive and less critical metal than ruthenium.

## 2.6 General implications for Power-to-Methane catalyst design

Building on the process rationale and catalyst requirements outlined in the introductory section of this chapter (Section 2.2), the experimental results discussed herein demonstrate that catalyst design for Power-to-Methane applications cannot be generalised independently of the selected operating concept. Rather, the reaction mode – steady-state versus cyclic, concurrent versus sequential – plays a decisive role in defining the physicochemical properties required to achieve high $CO_2$-to-$CH_4$ conversion efficiency and selectivity.

The investigation of conventional $CO_2$ methanation over Ni-USY catalysts highlights the central importance of intrinsic hydrogenation activity, metal particle size, and support acidity under steady-state conditions. In this framework, nickel-based catalysts benefit from high metal dispersion and controlled surface acidity, which promote methane formation while limiting deactivation phenomena such as coking. The hierarchical porous architecture of the USY support contributes to stablishing Ni nanoparticles and mitigating sintering, but at the same time introduces mass-transfer limitations. These results confirm that, for classical power-to-methane operation, catalyst optimisation is primarily driven by kinetic considerations, where the continuous and simultaneous availability of $CO_2$ and $H_2$ favours materials exhibiting high intrinsic methanation activity.

The study of rhenium-based systems under ICCU conditions reveals a set of design criteria that differ substantially from those governing conventional steady-state methanation. Although oxide-supported rhenium catalysts are generally less selective and less active than nickel under conventional $CO_2$ methanation, their behaviour changes when operated under ICCU conditions. The decoupled introduction of $CO_2$ and $H_2$ suppresses competitive reaction pathways such as RWGS and enables the complete hydrogenation of adsorbed carbon species, resulting in 100% methane selectivity across a wide range of oxide supports.

Under these conditions, catalytic performance is no longer dictated primarily by intrinsic methanation kinetics. Instead, it becomes strongly dependent on the ability of the material to adsorb, stabilise and selectively convert $CO_2$-derived surface species during cyclic operation. This shift is further highlighted by comparing diluted and non-diluted rhenium-based materials. While dilution of $Re/Al_2O_3$ or $Ni/Al_2O_3$ with LDH-derived oxides negatively affects conventional methanation due to the lower density of accessible metal sites, the same approach significantly improves ICCU performance. Temperature-programmed experiments demonstrated that LDH-derived oxides substantially increase both the amount of $CO_2$ adsorbed and its thermal stability, extending $CO_2$ retention to higher temperatures and thereby increasing the fraction of captured $CO_2$ available for hydrogenation. Direct interaction between rhenium and the adsorbing phase, as in Re/LDO materials, further enhances this effect by lowering the onset temperature for methane formation. Among the investigated supports, ceria

emerges as a particularly effective material for ICCU-oriented catalyst design. Despite its limited selectivity in conventional methanation, $Re/CeO_2$ combines a high intrinsic $CO_2$ adsorption capacity with excellent cyclic stability and enhanced tolerance to water impurities in the $CO_2$ feed. These properties make $Re/CeO_2$ especially relevant for practical ICCU applications, where feed impurities and dynamic operating conditions are unavoidable.

In conclusion, the results presented in this chapter demonstrate that catalyst optimisation for power-to-methane processes cannot be considered apart from the operating concept. Materials designed for steady-state $CO_2$ hydrogenation may perform poorly in cyclic or adsorption-limited configurations such as ICCU, and vice versa. From a broader perspective, ICCU shifts the focus of catalyst design from maximising intrinsic hydrogenation kinetics to engineering multifunctional materials capable of stabilising surface carbon species and selectively converting them under decoupled conditions. This distinction has important implications for the rational development of next-generation power-to-methane catalysts and underlined the necessity of integrating process considerations into catalyst design from the earliest stages.

# Chapter 3

# 3. Catalytic $CO_2$ hydrogenation: Power-to-Methanol

## 3.1 Conceptual framework for $CO_2$-to-methanol

While the Power-to-Methane technology discussed in Chapter 2 offers a viable route for injecting renewable energy into the existing natural gas grid, the transition toward a fully decarbonised economy requires addressing sectors where gaseous fuels face intrinsic logistical and infrastructural limitations. High energy-density applications, such as heavy-duty transport, aviation, and large-scale chemical production, continue to rely predominantly on liquid hydrocarbons due to their superior volumetric energy density and ease of storage and transport[276]. In this context, Power-to-Liquid (PtL) technologies, and in particular methanol synthesis, emerge as a complementary and necessary pillar within the CCUS value chain[171,277]. Among the various liquid energy carriers, methanol ($CH_3OH$) stands out as a particularly attractive candidate, as it can act both as an energy vector and as a versatile chemical feedstock[276]. Unlike methane, methanol is a platform molecule: through the Methanol-to-Hydrocarbons (MtH) process, it can be converted into olefins (MtO), propylene (MtP), or gasoline-range hydrocarbons, enabling an indirect replacement of crude oil within the petrochemical supply chain.

From a physico-chemical standpoint, $CO_2$-to-methanol conversion is characterised by an exceptionally narrow operating window. Methanol synthesis is an exothermic, equilibrium-limited reaction, favoured at low temperatures and high pressures[278,279]. While increasing the reaction temperature enhances reaction kinetics and facilitates $CO_2$ activation, it simultaneously shifts the thermodynamic equilibrium towards the undesired RWGS reaction, leading to the formation of CO and $H_2O$ rather than methanol. Moreover, water is an inherent reaction product and strongly influences catalyst structure, surface chemistry, and

long-term stability[280,281]. This fundamental trade-off between kinetic favourability and thermodynamic constraints has traditionally been addressed through process-intensification strategies, such as membrane reactors, catalytic distillation, or sorption-enhanced systems, rather than through purely catalytic innovation[282]. Nevertheless, the development of highly active, selective, and stable catalysts capable of achieving commercially relevant conversion rates at moderate temperatures (ideally below 250 °C) remains a key objective for maximising both the energy efficiency and the economic viability of $CO_2$ utilisation routes.

Heterogeneous catalysts for $CO_2$ hydrogenation to methanol can be broadly classified into three main categories: (i) metallic catalysts based on Cu, Au, Ag, Pd, or Pt; (ii) oxygen-deficient metal oxides characterised by abundant oxygen vacancies and tunable redox properties; and (iii) emerging catalytic architectures based on metal-organic frameworks, nitrogen-doped carbons, or hierarchical porous materials[277,282,283]. Among these approaches, copper-based catalysts have emerged as the dominant class, attracting sustained research interest due to their favourable balance between catalytic activity, cost, and industrial scalability. In particular, the industrial synthesis of methanol has long relied on $Cu/ZnO/Al_2O_3$ (CZA) catalysts[277].

The catalytic performance of CZA systems in methanol synthesis is governed by the complex interplay between the copper phase, which provides sites for $H_2$ dissociation and C-H bond formation, the ZnO promoter, which acts synergistically with copper by facilitating $CO_2$ adsorption, stabilising formate-type intermediates (HCOO*), and preserving copper dispersion, and the $Al_2O_3$ matrix, which ensures structural integrity, high surface area, and suitable textural properties[277,284,285]. The interfacial contact between Cu and ZnO has been widely recognised as a critical descriptor of catalytic activity and methanol selectivity, together with parameters such as copper particles size, $Cu^0$ surface area, and the relative fraction of reduced copper species[286–289].

In recent years, extensive research efforts have focused on improving the performance and stability of CZA catalysts through targeted chemical modification. The incorporation of secondary oxides and promoters has proven particularly effective. Zirconia ($ZrO_2$) addition enhances both $CO_2$ conversion and methanol selectivity by promoting the formation and stabilisation of formate intermediates, while simultaneously improving copper dispersion and introducing oxygen-deficient sites that facilitate $CO_2$ activation[290]. Similarly, silica-modified CZA catalysts have demonstrated remarkable improvements in hydrothermal stability, as the incorporation of silicon into the ZnO lattice inhibits sintering of both copper and zinc oxide phases during prolonged operation[283]. Gallium oxide ($Ga_2O_3$) promotion has also been reported to enhance $CO_2$ adsorption and activation, often leading to improved methanol selectivity under $CO_2$-rich conditions[291]. Additional strategies involving boron-containing modifiers or rare-earth oxides such as $La_2O_3$ have been explored to tune acid-base properties, lower activation barriers, and suppress undesired side reactions[282,292].

Beyond chemical promotion, the nature of the oxide matrix itself plays a decisive role in determining catalytic behaviour. $Al_2O_3$, while often considered an inert support, contributes to surface area, mechanical stability, porosity, and heat dissipation, indirectly influencing water management and catalyst durability[289]. Alternative oxide morphologies, such as one-dimensional $Al_2O_3$ nanorods, have been shown to further enhance $CO_2$ adsorption, promote carbonate and formate formation, and improve methanol space-time yields by mitigating diffusional limitations[293].

In this context, catalyst preparation emerges as a genuine design parameter rather than a secondary experimental detail. The choice of precursors, synthesis route, and activation protocol directly determines copper dispersion, oxide reducibility, and interfacial structure, thereby affecting not only initial activity but also long-term stability and resistance to deactivation.

On this basis, the present chapter focuses on $Cu/ZnO/Al_2O_3$ catalysts as industrially relevant benchmark systems for $CO_2$-to-methanol conversion within PtL schemes. The aim is to rationalise how catalyst preparation and precursor selection influence methanol synthesis performance under conditions relevant to PtL operations.

## 3.2 Materials and Methods

### 3.2.1 Materials and chemicals

Copper (II) nitrate trihydrate (Sigma-Aldrich), zinc nitrate hexahydrate (Sigma-Aldrich), copper (II) chloride dihydrate (Sigma-Aldrich), zinc chloride anhydrous (Sigma-Aldrich), copper (II) acetate anhydrous (Sigma-Aldrich), and zinc acetate dihydrate (Sigma-Aldrich) were used as metal precursors. $Al_2O_3$ (Puralox) was calcined at 600 °C and used as support. Commercial catalyst, supplied by Thermo Fisher Scientific, had a composition of: 63.8 wt% CuO, 24.6 wt% ZnO, 9.9 wt% $Al_2O_3$, and 1.4 wt% MgO.

### 3.2.2 Catalyst preparation

The $Cu/ZnO/Al_2O_3$ catalysts were prepared via a wet co-impregnation route. Three catalysts were synthesized by varying the chemical nature of the copper and zinc precursor (nitrate, acetate, and chloride salts) in order to investigate the influence of precursor chemistry on the resulting Cu-ZnO interface.

In a typical preparation, stoichiometric amounts of the copper and zinc precursor salts were dissolved in distilled water under continuous stirring until complete dissolution was achieved. The alumina support was subsequently introduced into the solution, and the resulting suspension was subjected to ultrasonic treatment to promote homogeneous dispersion of the metal species on the support surface. After sonification, the suspension was continuously stirred

and slowly dried at 80 °C until complete solvent evaporation. The obtained dry solid was then calcined in static at 600 °C for 1 h (with a rate of 5 °C/min).

All catalysts were prepared with a nominal composition of 20 wt% CuO, 55 wt% ZnO, and 15 wt% $Al_2O_3$, with particle size fraction in the range of 180 – 355 µm. The catalysts were denoted as CZA_nitrate, CZA_acetate, and CZA_chloride according to the precursor salts employed during synthesis.

Samples are labelled in Table 3.1.

**Table 3.1. Theoretical and experimental CuO content (wt%) and Specific Surface Area (SSA) from BET analysis for CZA_nitrate, CZA_acetate and CZA_chloride catalysts.**

| *Sample* | *CuO theoretical (wt%)* | *CuO experimental (wt%)* | *Specific Surface Area ($m^2/g$)* |
|---|---|---|---|
| ***CZA_nitrate*** | 30 | 26.5 | 3 |
| ***CZA_acetate*** | 30 | 30.9 | 11 |
| ***CZA_chloride*** | 30 | 32.9 | 9 |

### 3.2.3 Catalyst characterisation

All prepared catalysts were characterised using a combination of textural, structural, spectroscopic, and microscopy techniques in order to comprehensively assess their physicochemical properties.

The specific surface (SSA) was determined by $N_2$ physisorption at -196 °C using the Brunauer-Emmett-Teller (BET) method. Temperature-programmed reduction (TPR) experiments were performed prior to catalytic testing in order to evaluate the reducibility of the oxide phases. Measurements were conducted under a flow of 5 vol% $H_2$ in Ar (500 N $cm^3$ $min^{-1}$), heating the samples up to 600 °C at a rate of 5 °C/min. Temperature-programmed desorption (TPD) analyses were conducted on 0.1 g of catalyst using a Micromeritics AutoChem II instrument equipped with a thermal conductivity detector (TCD). For $NH_3$-TPD measurements, samples were saturated at room temperature under a 2 vol% $NH_3$/He flow (55 $cm^3$ $min^{-1}$) for 30 min, followed by helium purging and temperature ramping up to 550 °C at 10 °C/min. $CO_2$-TPD experiments were performed following an analogous protocol, using a 15 vol% $CO_2/N_2$ mixture (50 $cm^3$ $min^{-1}$) for adsorption prior to helium purging and heating. Desorption profiles were integrated over time, and quantitative calibration enabled conversion of TCD signals into desorbed amounts expressed in mmol. No pretreatment was applied before TPD experiments. A temperature-programmed oxidation (TPO) analysis was performed after the catalytic activity tests to evaluate coke formation during the reaction, at atmospheric pressure using a feed gas mixture of 5 vol% $O_2$/Ar, with a total flow rate of 500 $Ncm^3$ $min^{-1}$ and a heating ramp of 5 °C/min.

Morphological characterisation was performed by field-emission scanning electron microscopy (FESEM). Scanning transmission electron microscopy (STEM) analysis was carried out. Samples were dispersed in ultra-pure ethanol and drop-cast onto Au lacey carbon grids, followed by plasma cleaning under argon atmosphere prior to insertion into the microscope.

### 3.2.4 Catalytic activity tests

Catalytic activity measurements were carried out in a tubular fixed-bed stainless steel reactor (inner diameter 11 mm) placed inside an electrically heated oven. The catalyst, sieved to a particle size fraction of 180 – 355 μm, was physically mixed with inert quartz particles to ensure adequate bed dilution and minimise temperature gradients. The reactant gases were fed to the reactor using mass flow controllers (Bronkhorst), maintaining a $CO_2/H_2$ volumetric ratio of 30/70. The reactor outlet composition was continuously monitored by an online mass spectrometer (Hiden HPR20). The temperature of the catalytic bed was measured by two thermocouples positioned at the inlet and outlet of the reactor, respectively.

Catalyst performance was evaluated in terms of methanol selectivity, turnover frequency (TOF), and stability. Methanol selectivity ($S_{CH3OH}$) and TOF were calculated according to Eqs. (8) and (9), while stability tests were conducted at the optimal operating conditions identified during the screening experiments. Catalytic tests were performed by varying the reaction temperature between 180 and 350 °C and the weight hourly space velocity (WHSV) between 10 and 30 $h^{-1}$ (Eq. (10)). All initial screening experiments were conducted at atmospheric pressure. The catalyst exhibiting the best overall performance was subsequently compared with a commercial reference catalyst (CZA_commercial) and further investigated under elevated pressures in the range 1 – 7 bar.

The expressions used to evaluate methanol selectivity, TOF, and WHSV are reported below:

$$S_{CH_3OH}(\%)=\frac{P_{CH_3OH}}{P_{CH_3OH}+P_{CH_4}+P_{CO}}\,x100 \tag{8}$$

$$TOF\left(h^{-1}\right)=\frac{P_{CH_3OH}\left(mol\,h^{-1}\right)}{n_{Cu}(mol)} \tag{9}$$

$$WHSV\left(h^{-1}\right)=\frac{W_{in}\left(g\,h^{-1}\right)}{W_{catalyst}(g)} \tag{10}$$

Methanol productivity was calculated as:

$$P_{CH_3OH}\left(\mu mol\,min^{-1}\right)=\frac{y_{CH_3OH}\cdot F_{in}}{22.414} \tag{11}$$

Where $P_{CH3OH}$, $P_{CH4}$, and $P_{CO}$ represent the productivities of methanol, methane, and carbon monoxide, respectively; $W_{in}$ is the inlet mass flow rate; $y_{CH3OH}$ is the molar fraction of methanol in the outlet steam; and $F_{in}$ is the inlet volumetric flow rate.

## 3.3 Result and discussion

### 3.3.1 Structural and textural characterisation

The effect of copper and zinc precursor chemistry on the structural properties of the Cu/ZnO/$Al_2O_3$ catalysts was first investigated by X-ray diffraction. The diffraction patterns of the three samples (CZA_nitrate, CZA_acetate, and CZA_chloride) are reported in Figure 3.1a, together with a magnified view of the 30° – 65° 2θ region in Figure 3.1b.

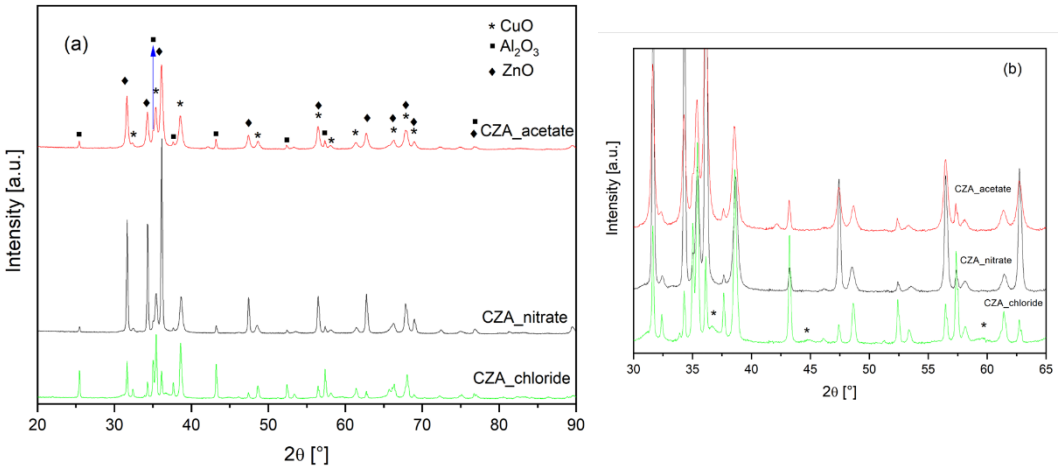


**Figure 3.1. (a) XRD patterns of the catalysts CZA_nitrate, CZA_acetate, and CZA_chloride. (b) magnification of 2θ range 30° – 65°.**

All catalysts display diffraction features associated with α-$Al_2O_3$ (JCPDS card n°10-0173), wurtzite ZnO (JCPDS card n°36-1451), and CuO (JCPDS card n°48-1548), indicating that the overall phase composition is preserved irrespective of the precursor salts employed. However, marked differences in peak intensity and sharpness are observed, pointing to significant precursor-dependent variations in crystallinity and dispersion of the copper oxide phase. In particular, the CZA_chloride sample exhibits significantly sharper and more intense CuO reflections (especially at 2θ ≈ 35.5°, 38.7°, 48.7°, and 53.5°). The increased peak intensity and reduced broadening indicate the formation of larger copper oxide domains, with a diminished dispersion. Consistently, crystallite size estimation using the Scherrer equation yields average CuO crystallite sizes of approximately 35 nm for CZA_chloride, whereas considerably smaller values (around 20 nm) are obtained for both CZA_nitrate and CZA_acetate. This result clearly indicates a poorer dispersion of CuO when chloride precursors are used.

Additional structural differences emerge from the magnified diffraction patterns (Figure 3.1b). In the case of CZA_chloride, weak reflections attributable to the $CuAl_2O_4$ (JCPDS card n°33-0448) spinel phase can be detected, suggesting a strong interaction between copper species and the alumina support. Conversely, such features are absent in the nitrate- and acetate-derived samples, where copper preferentially interacts with ZnO rather than being trapped within the alumina

lattice. This observation anticipates the different reducibility behaviour observed in $H_2$-TPR experiments, discussed in the following sections.

As Lee et al. demonstrated, the specific surface area (SSA) of the catalysts can be significantly influenced by the selection of metal precursor[294]. In this work, the influence of precursor selection on the textural properties of the catalysts was further assessed by $N_2$ physisorption measurements with the specific surface areas (SSA) of the synthetised catalysts reported in Table 3.1. All CZA samples exhibit a pronounced decrease in surface area compared to the parent $Al_2O_3$ (18 $m^2$ $g^{-1}$), which is expected upon catalyst preparation due to partial pore blocking and increased particle agglomeration[294]. Among the three, CZA_nitrate displays the lowest surface area, while higher values are retained for CZA_acetate and CZA_chloride. These differences indicate that precursor chemistry significantly affects the dispersion and deposition of metal oxide phases [294]. In particular, nitrate-derived precursors appear to promote stronger metal-support interactions, leading to a more compact oxide network and a concomitant in accessible surface area. In contrast, acetate precursors favour a more homogeneous distribution of CuO and ZnO, allowing partial preservation of the original support porosity[295]. Despite exhibiting the lowest BET surface area, the CZA_nitrate catalyst is expected to benefit from a higher density of intimate Cu-ZnO interfacial sites, which are widely recognised as the key active centres for $CO_2$ hydrogenation to methanol[296,297].

Field-emission scanning electron microscopy (FESEM) was employed to compare the morphology of the CZA catalysts prepared from different precursor salts (Figure 3.2). At low magnification, all samples appear as agglomerated oxide particles, while higher magnification reveals marked differences in surface texture and aggregation at the sub-micrometric scale. The CZA_acetate catalyst exhibits a more open and finely textured morphology, characterised by smaller and more unfirmly distributed features, whereas CZA_nitrate and CZA_chloride display more compact and irregular aggregates. These qualitative trends are consistent with BET surface area measurements (Table 3.1), where CZA_acetate retains a higher SSA compared to the nitrate- and chloride-derived samples.

While FESEM provides comparative morphological information, high-angle annular dark-field scanning transmission electron microscopy (HAADF-STEM) coupled with EDX mapping was employed to gain insight into the nanoscale distribution of the catalyst components. Figure 3.3 shows a representative HAADF-STEM image of the CZA_nitrate sample, revealing a complex nanostructured morphology in which Cu- and Zn-containing domains are intimately connected and homogeneously distributed at the nanometric scale. EDX elemental maps clearly show regions dominated by the $Al_2O_3$ support, alongside areas where Cu and Zn signals spatially overlap, indicating the absence of segregated bulk CuO or ZnO phases. This nanoscale compositional homogeneity supports the XRD results, which did not reveal the formation of distinct bulk mixed oxide phases, and confirms that copper and zinc are

predominantly present as finely dispersed oxides forming extended interfacial contact.

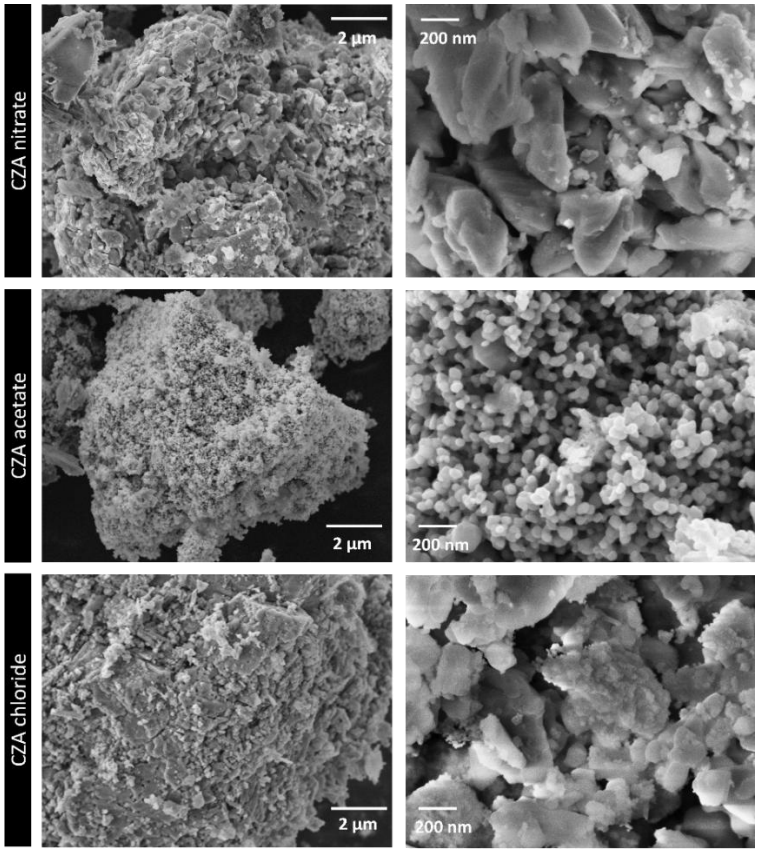


**Figure 3.2. Representative FESEM images of CZA_nitrate, CZA_acetate, and CZA_chloride catalysts at low (left) and high (right) magnification.**

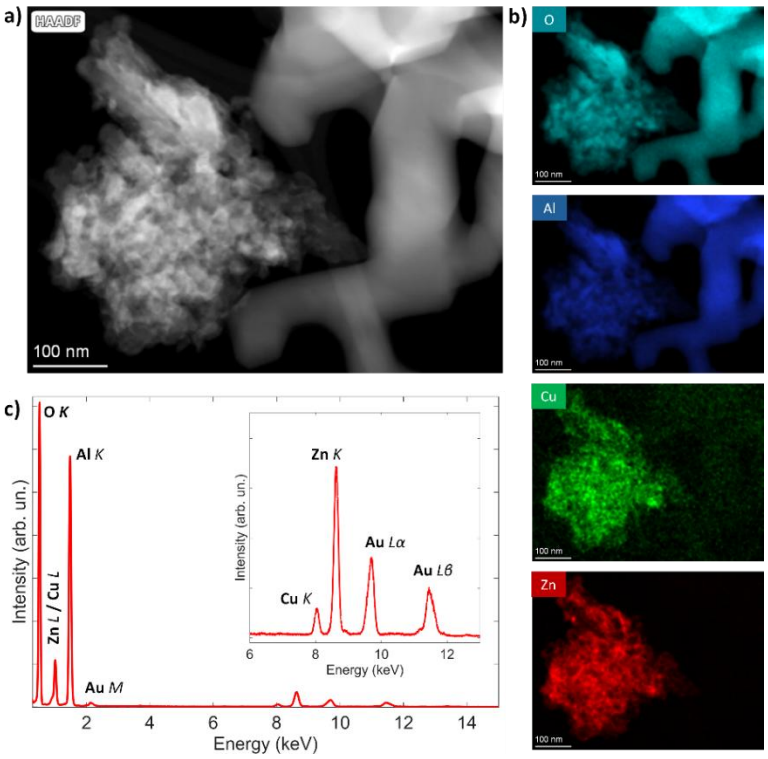


**Figure 3.3. HAADF-STEM image of CZA_nitrate catalyst together with the corresponding EDX elemental maps for O, Al, Cu, and Zn. The Au signal is due to the TEM grid.**

### 3.3.2 Redox and acid-base properties of CZA catalysts

The redox properties and surface acid-base functionality of the CZA catalysts were investigated by combining $H_2$-TPR, $NH_3$-TPD and $CO_2$-TPD analyses, in order to elucidate how precursor selection influences copper reducibility, Cu-ZnO interfacial development and surface chemical properties relevant to $CO_2$ hydrogenation.

$H_2$-TPR profiles (Figure 3.4) reveal marked differences in the reducibility of copper species among the investigated samples, reflecting variations in CuO dispersion, metal-support interaction and phase composition. For CZA_nitrate and CZA_acetate, dominant reduction feature is observed in the 170-250 °C range, typically associated with finely dispersed CuO species and CuO entities interacting with ZnO at the Cu-ZnO interface[298,299]. In contrast, this low-temperature reduction peak is significantly suppressed in CZA_chloride, indicating a reduced fraction of readily reducible copper species. A second reduction event at higher temperature (350-470 °C) is clearly detected for CZA_chloride and is only marginally present in the other samples. This high-temperature feature is attributed to the reduction of $Cu^{2+}$ species strongly bound within a $CuAl_2O_4$ spinel phase[300], in agreement with XRD results showed above. The presence of this stable copper aluminate phase markedly hinders copper reduction and limits the availability of catalytically active Cu sites.

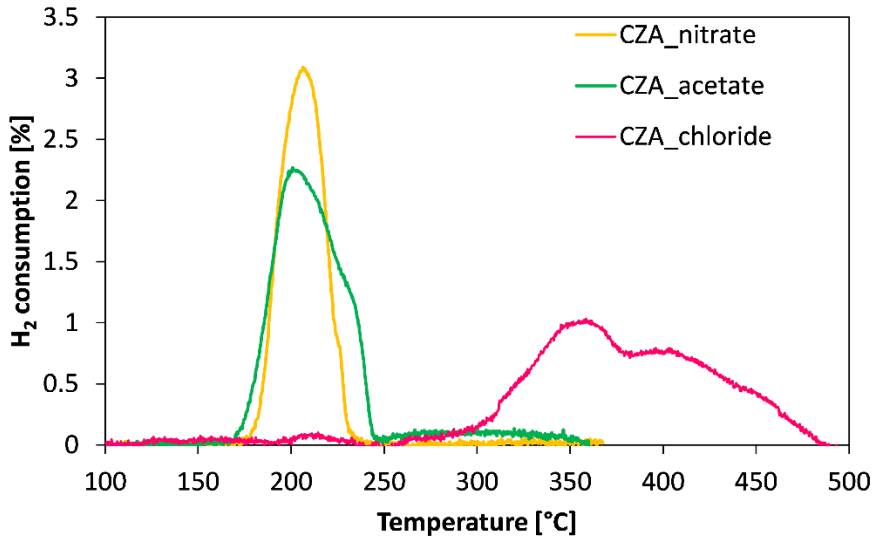


Figure 3.4. $H_2$-TPR profiles of CZA catalysts.

Deconvolution of the low-temperature $H_2$-TPR peak provides further insight into the distribution of copper species (Figure 3.5). The reduction signals can be resolved into contributions associated with highly dispersed CuO (first reduction peak, A)[301], CuO species interacting with ZnO at the interface (second peak, B)[302,303], and large CuO aggregates (third peak, C)[303–305]. Among the investigated samples, CZA_nitrate exhibits the highest relative fraction of Cu species associated with the Cu-ZnO interface, indicating the most effective

development of interfacial sites. In contrast, CZA_acetate shows a larger contribution from isolated CuO species, while CZA_chloride is dominated by poorly reducible CuO aggregates and copper trapped in the aluminate phase. These results demonstrate that precursor chemistry strongly governs the nature of copper species formed during calcination, ultimately controlling the density of reducible and interfacial Cu sites.

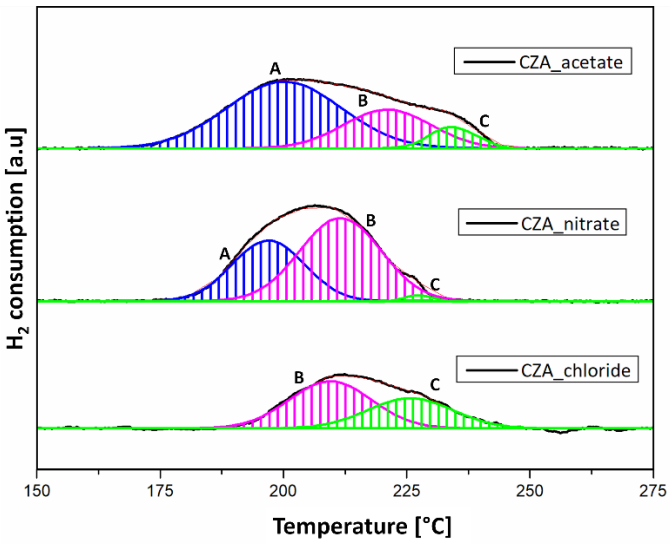


**Figure 3.5. Deconvolution of the firs reduction peak in the $H_2$-TPR profiles of samples. Labelled as A, B, and C, corresponding to different CuO species.**

Surface acidity was evaluated by $NH_3$-TPD (Figure 3.6). Three types of acid sites are generally identified as weak, moderate, and strong[306–308]. The prepared catalysts display distinct acid sites distribution, with CZA_acetate exhibiting the highest total acidity, dominated by moderate-strength acid sites, whereas CZA_nitrate shows the lowest acidity with a broader and weaker desorption profile. The relatively high acidity observed for CZA_acetate is consistent with a more pronounced contribution from the alumina support[309], while the suppressed acidity in CZA_nitrate and CZA_chloride suggests partial masking or modification of alumina acid sites due to stronger interactions with copper and zinc species. These differences indicate that precursor selection affects not only metal dispersion but also the accessibility and strength of surface acid sites.

Complementary information on surface basicity was obtained from $CO_2$-TPD measurements (Figure 3.7); similarly to acid sites, basic sites are often classified as weak, moderate to strong[310,311]. CZA_acetate displays the highest total $CO_2$ uptake, primarily associated with weak basic sites, whereas CZA_nitrate and CZA_chloride exhibit broader desorption profiles extending to higher temperatures, indicative of stronger basic sites. Notably, CZA_nitrate shows enhanced $CO_2$ retention at temperatures above 300 °C, suggesting the presence of stable basic sites capable of interacting with $CO_2$ under reaction-relevant conditions. When combined with $NH_3$-TPD results, this leads to the highest basic-to-acid site ratio for CZA_nitrate, a parameter that has been increasingly

recognised as a more meaningful descriptor of catalytic performance than the absolute concentration of acid or basic sites alone.

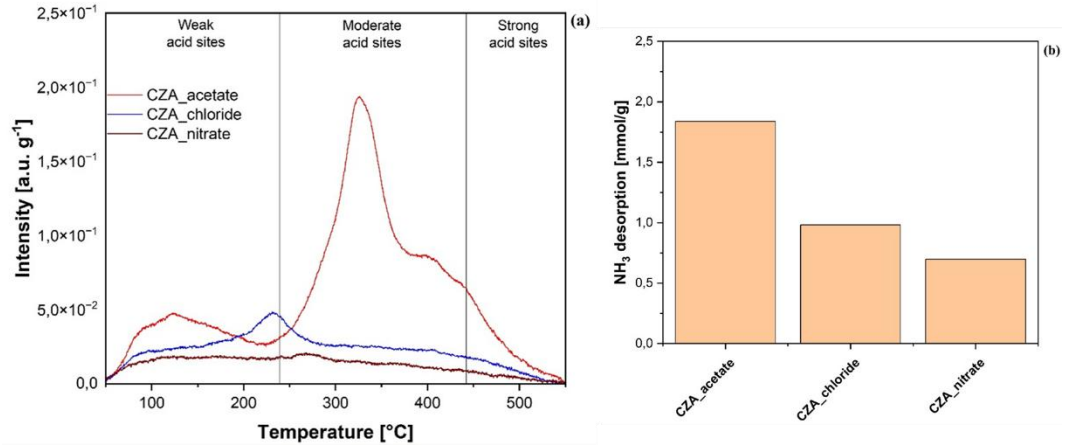


Figure 3.6. (a) $NH_3$-TPD profiles and (b) desorbed amounts of CZA catalysts.

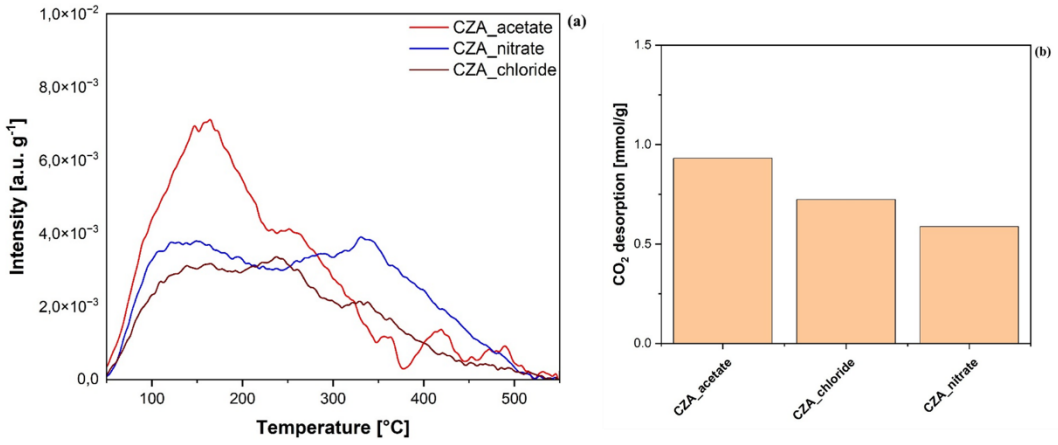


Figure 3.7. (a) $CO_2$-TPD profiles and (b) desorbed amounts for CZA catalysts.

### 3.3.3 Catalytic tests

The catalytic performance of the three CZA catalysts prepared was first evaluated under atmospheric pressure in order to establish a comparative screening of activity, selectivity, and stability. Catalytic tests were carried out by varying both the reaction temperature (180-350 °C) and the weight hourly space velocity (WHSV = 10-30 $h^{-1}$). Methanol selectivity as a function of temperature and WHSV is reported in Figure 3.8. For all three catalysts, methanol selectivity is strongly governed by reaction temperature, while the effect of WHSV remains marginal within the investigated range. At 180 °C and 200 °C, all samples exhibit nearly complete methanol selectivity (≈100%), independently of WHSV. Upon increasing the temperature above 200 °C, a sharp decline in methanol selectivity is observed, with values approaching zero at 300 °C and 350 °C, with a consequently rising of CO production.

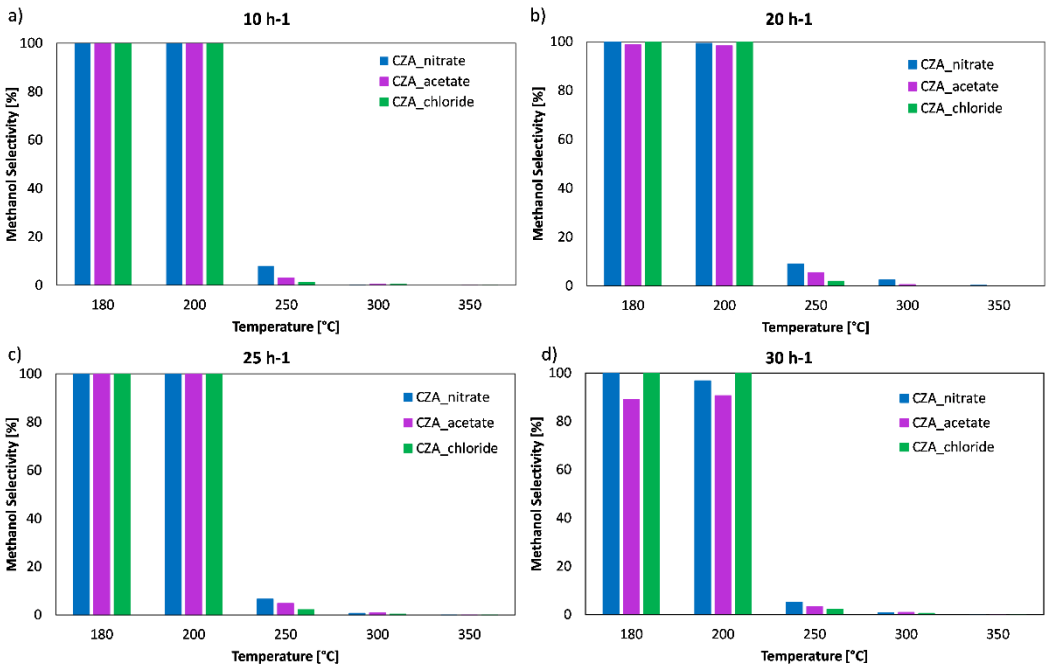


**Figure 3.8. Methanol selectivity as a function of reaction temperature at atmospheric pressure for CZA_nitrate, CZA_acetate, and CZA_chloride, evaluated at different WHSV: (a) 10 $h^{-1}$, (b) 20 $h^{-1}$, (c) 25 $h^{-1}$, (d) 30 $h^{-1}$.**

While methanol selectivity shows similar trends for all formulations, more pronounced differences emerge when methanol turnover frequency (TOF) is considered. Methanol TOF values as a function of temperature and WHSV are reported in Figure 3.9. For all catalysts, TOF increases with temperature and reaches a maximum at approximately 250 °C, before decreasing at higher temperatures.

Despite this common temperature dependence, a clear performance ranking can be identified. CZA_nitrate consistently exhibits the highest TOF across all investigated WHSV values, followed by CZA_acetate, while CZA_chloride shows significantly lower activity, confirming that the presence of $CuAl_2O_4$ limits the availability of active Cu sites. This result highlights that, under atmospheric pressure, catalyst formulation primarily affects intrinsic activity rather than selectivity. The superior performance of CZA_nitrate indicates a higher density of active sites and an enhanced Cu-ZnO interface, as discussed in the characterisation results section.

The sharp decrease in methanol selectivity at temperatures above 200 °C is accompanied by a corresponding increase in CO formation, while methane remains negligible over the entire temperature range. This confirms that the loss of selectivity is primarily driven by the increasing contribution of RWGS reaction, rather than by methanation.

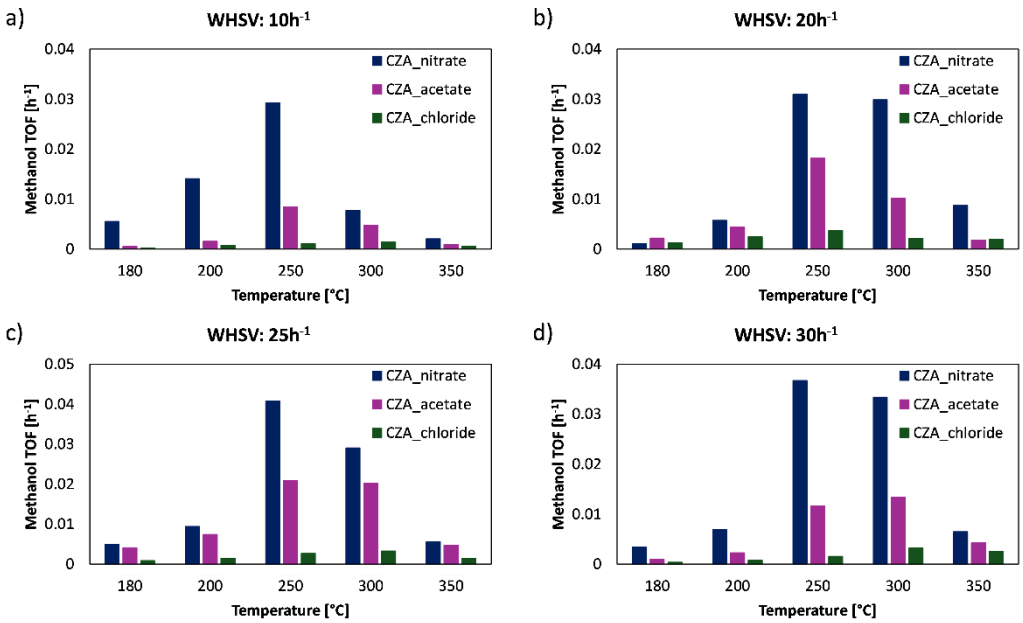


**Figure 3.9. Methanol TOF at atmospheric pressure varying temperatures for CZA_nitrate, CZA_acetate, and CZA_chloride catalysts, evaluated at different WHSV values: (a) 10 $h^{-1}$, (b) 20 $h^{-1}$, (c) 25 $h^{-1}$, (d) 30 $h^{-1}$.**

Based on the combined analysis of selectivity and activity, 200 °C was identified as the most suitable operating temperature for further comparison, as it ensures nearly complete methanol selectivity while maintaining a significantly higher TOF compared to 180 °C. Among the investigated space velocities, WHSV = 10 $h^{-1}$ provides the highest methanol productivity, reflecting the beneficial effect of increased contact time between reactants and active sites. Accordingly, short term stability tests were performed at 200 °C and WHSV = 10 $h^{-1}$ and are shown in Figure 3.10. As illustrated in Figure 3.10a, methanol selectivity remains stable over 10 h of time on stream for both CZA_nitrate and CZA_acetate, while a slight but noticeable decrease is observed for CZA_chloride. Methanol productivity trends, reported in Figure 3.10b, further emphasize the different stability behaviours. CZA_nitrate maintains the highest and most stable productivity throughout the test, whereas CZA_acetate shows lower but steady activity. In contrast, CZA_chloride undergoes a progressive decline in methanol productivity, suggesting the occurrence of deactivation phenomena under reaction conditions.

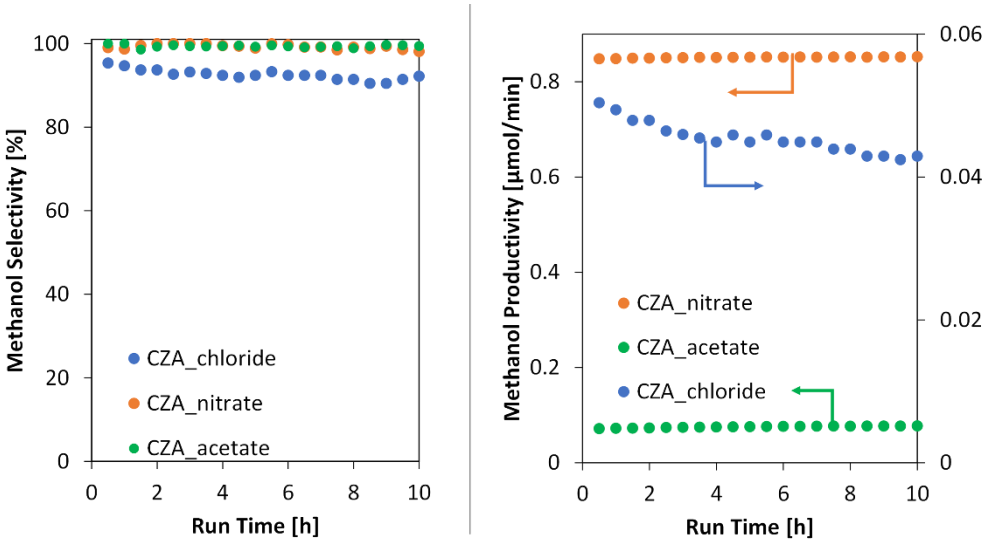


**Figure 3.10. Stability tests performed at atmospheric pressure, 200 °C and WHSV = 10 $h^{-1}$ for CZA_nitrate, CZA_acetate, and CZA_chloride catalysts: (a) methanol selectivity and (b) methanol productivity as a function of time on stream.**

To investigate the origin of the observed deactivation, post-reaction temperature-programmed oxidation (TPO) analysis were performed on both CZA_nitrate and CZA_chloride. The test showed the formation of a $CO_2$ signal in the case of CZA_chloride, indicating the presence of carbonaceous deposits formed during reaction, while no $CO_2$ was detected for CZA_nitrate, confirming its resistance to coke formation. The higher susceptibility of CZA_chloride to carbon deposition can be correlated with its distinct structural features discussed in Section 3.3.1, which favour the formation of less active and more deactivation-prone copper-alumina species[312–314].

On the basis of these results, CZA_nitrate was identified as the most active formulation under atmospheric pressure and was therefore selected for a more detailed analysis.

Methanol synthesis from $CO_2$ and $H_2$ is intrinsically limited by thermodynamic equilibrium, particularly under atmospheric pressure and at increasing reaction temperatures, where the RWGS reaction becomes progressively favoured. As discussed above, under 1 bar the three CZA catalysts exhibit high methanol selectivity at low temperature but with increasing of temperature the equilibrium shifts towards RWGS. To overcome this limitation and to evaluate the process relevance of the most promising formulation, additional catalytic tests were performed on the CZA_nitrate catalyst under elevated pressures, up to 7 bar, while keeping the WHSV constant at 10 $h^{-1}$ and varying the reaction temperature.

The effect of pressure on $CO_2$ conversion, methanol selectivity and methanol TOF is summarised in Figure 3.11. At atmospheric pressure, $CO_2$ conversion remains low across the entire temperature range investigated (Figure 3.11a), reflecting the strong equilibrium constraints of methanol synthesis. Increasing the pressure to 4 bar leads to a measurable enhancement of $CO_2$ conversion, which becomes more pronounced at higher temperatures. A further increase to 7 bar

results in a substantial improvement, with $CO_2$ conversion reaching approximately 23% at 350 °C. This trend is consistent with the thermodynamic favourability of methanol formation at higher pressures, where the reduction in the total number of gas-phase molecules shifts the equilibrium towards the products.

Methanol selectivity as a function of temperature and pressure is reported in Figure 3.11b. At all investigated pressures, a full selectivity to methanol is observed at low temperatures (180-200°C). As temperature increases, selectivity progressively decreases due to the increasing contribution of RWGS reaction, while increasing the pressure mitigates this selectivity loss, extending the temperature window.

The beneficial role of pressure is further evidenced by the methanol TOF trends shown in Figure 3.11c. For all pressures, TOF increases with temperature and reaches a maximum around 250 °C, beyond which the increasing dominance of RWGS limits methanol formation. At elevated pressure, and particularly at 7 bar, the maximum TOF is significantly higher than at atmospheric pressure, demonstrating that increasing pressure not only enhances $CO_2$ conversion, but also effectively translates into higher intrinsic methanol formation rates.

The analysis of product distribution showed in Figure 3.12 confirms that methane formation remains negligible over the entire temperature and pressure range investigated, indicating that RWGS is the only relevant competing reaction under these conditions.

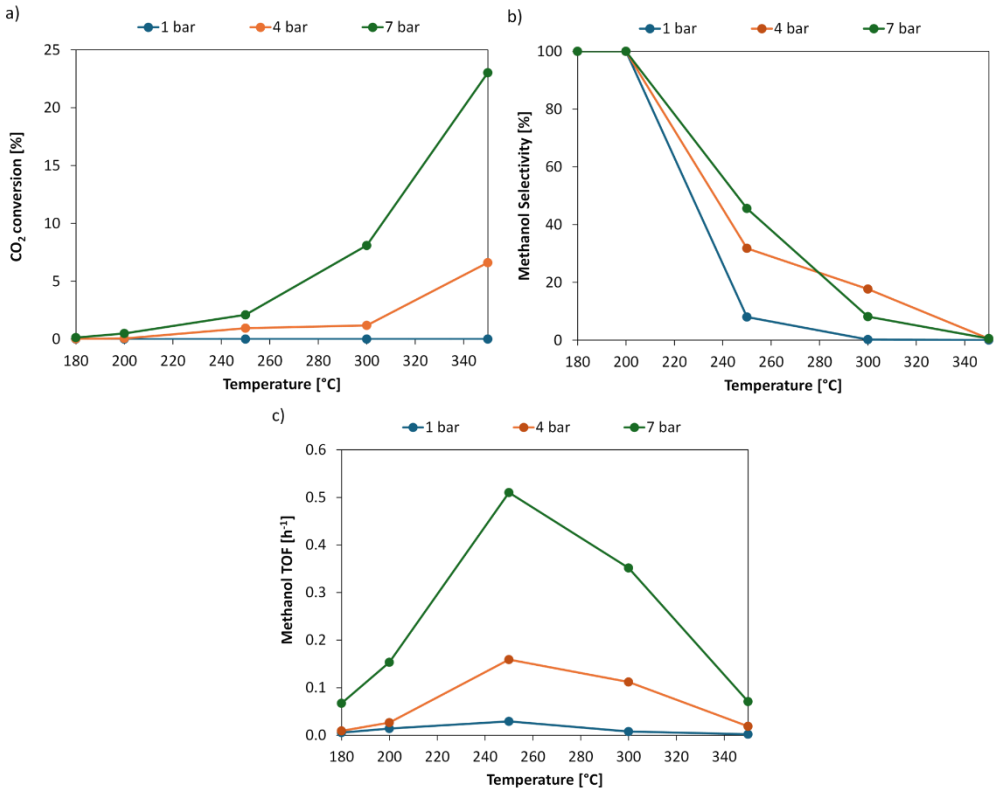


**Figure 3.11. Effect of reaction pressure on the catalytic performance of the CZA_nitrate catalyst during $CO_2$ hydrogenation at WHSV = 10 $h^{-1}$. (a) $CO_2$ conversion, (b) methanol selectivity, and (c) methanol TOF at 1, 4, and 7 bar with varying the temperature.**

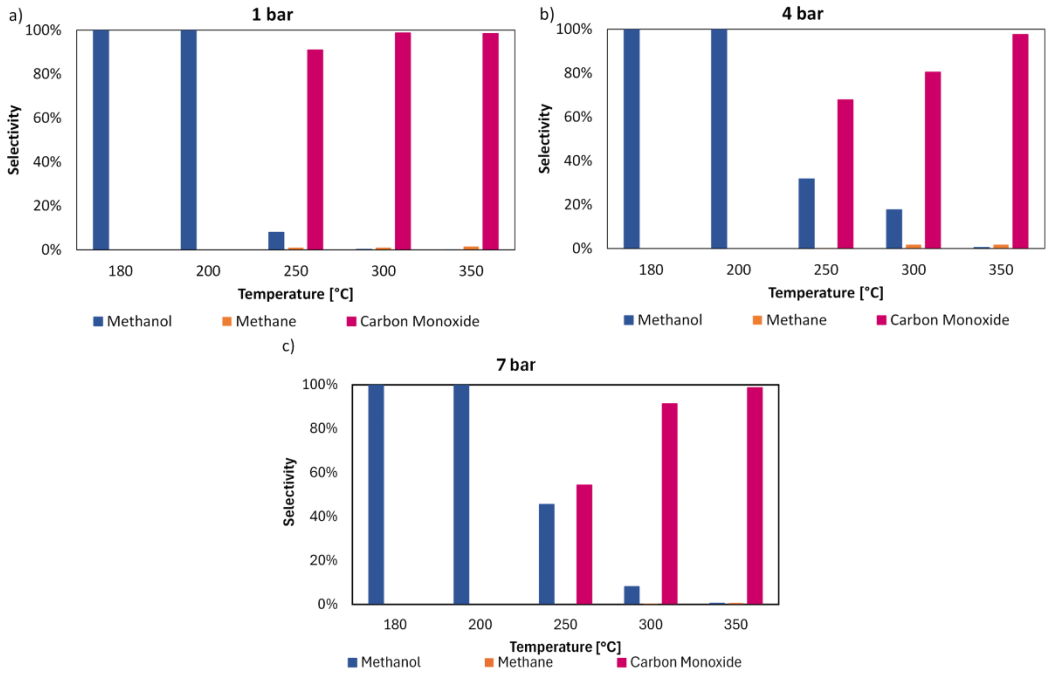


**Figure 3.12. Product selectivity towards methanol, methane, and carbon monoxide during $CO_2$ hydrogenation over the CZA_nitrate catalyst as a function of reaction temperature at (a) 1 bar, (b) 4 bar, and (c) 7 bar, at WHSV = 10 $h^{-1}$.**

In conclusion, these results demonstrate that reaction pressure represents a key factor to overcome thermodynamic limitations in $CO_2$ hydrogenation to methanol. The CZA_nitrate catalyst exhibits a favourable balance between conversion, selectivity, and stability, maintaining high methanol selectivity under mild conditions while achieving significantly enhanced productivity under moderately pressurised conditions. The combined structural and catalytic evidence consistently indicates that this superior performance originates from the formation of a highly reducible and catalytically accessible Cu phase, enabling efficient methanol synthesis across a broad range of conditions.

## 3.4 From catalyst development to process design

Building upon the lab-scale catalytic investigations discussed in the previous section, this section addresses the scale-up of $CO_2$-based fuel synthesis towards an industrially relevant application. In particular, the focus is shifted from catalyst performance under controlled experimental conditions to the process-level assessment of methanol synthesis under realistic operating constraints.

The investigated process is based on the conversion of a synthesis gas derived from biomass gasification, enabling the production of bio-methanol as a renewable liquid energy carrier and chemical feedstock. Compared to conventional methanol synthesis routes based on fossil-derived syngas, biomass gasification typically generates a $CO_2$-rich syngas, characterised by the simultaneous presence of $CO_2$, CO, and $H_2$ in non-stoichiometric proportions. This compositional complexity introduces additional thermodynamic and process

challenges, particularly in terms of equilibrium limitations, heat management and recycle strategy.

In this work, a representative $CO_2$-rich syngas composition was adopted as the design basis for process simulation, reflecting typical ranges reported for biomass gasification streams and industrial specifications provided by technology developers. The feed is characterised by a high hydrogen content, a substantial fraction of CO, and a non-negligible concentration of $CO_2$. The present simulation study was developed in the context of an industrial pilot-scale project, with the objective of evaluating the technical feasibility of bio-methanol production under realistic operating conditions. Aspen Plus® was employed as a process simulation platform to investigate the interplay between reactor configuration, operating pressure, recycle strategy and heat integration, thereby identifying the key trade-offs governing bio-methanol synthesis from $CO_2$-rich syngas.

### 3.4.1 Thermodynamic analysis of methanol synthesis from $CO_2$-rich syngas

To rationalise the operating window selected for the process-scale simulations and to provide a reference framework for the subsequent kinetic modelling, a thermodynamic analysis of methanol synthesis from a $CO_2$-rich syngas was carried out using Aspen Plus®. Equilibrium calculations were performed using a Gibbs reactor, assuming chemical equilibrium at fixed temperature and pressure.

In order to reflect the behaviour of CZA-based catalysts, which are known to exhibit negligible selectivity towards methane under typical methanol synthesis conditions, the equilibrium was intentionally restricted by excluding $CH_4$ from the list of possible products. This approach allows the thermodynamic analysis to better represent the catalytic system of interest, avoiding unrealistic equilibrium states dominated by methanation.

The calculations were performed using the a real syngas composition, characterised by a $CO/CO_2$ molar ratio of approximately 3:1. Temperature and pressure were varied in the ranges 180-380 °C and 20-70 bar, respectively, in order to evaluate their combined effect on methanol yield, reactant conversion and product distribution.

Figure 3.13 reports the contour plot of methanol yield as a function of temperature and pressure. As expected, methanol yield is strongly favoured at low temperature and high pressure, reflecting the exothermic nature of methanol synthesis and the associated decrease in the total number of gas-phase moles. At temperatures below 220-240 °C, increasing pressure leads to a marked enhancement in methanol yield, while at higher temperatures the attainable yield rapidly decreases, even at elevated pressures. This behaviour highlights the intrinsic thermodynamic limitation of methanol synthesis at high temperature, which cannot be fully compensated by pressure alone.

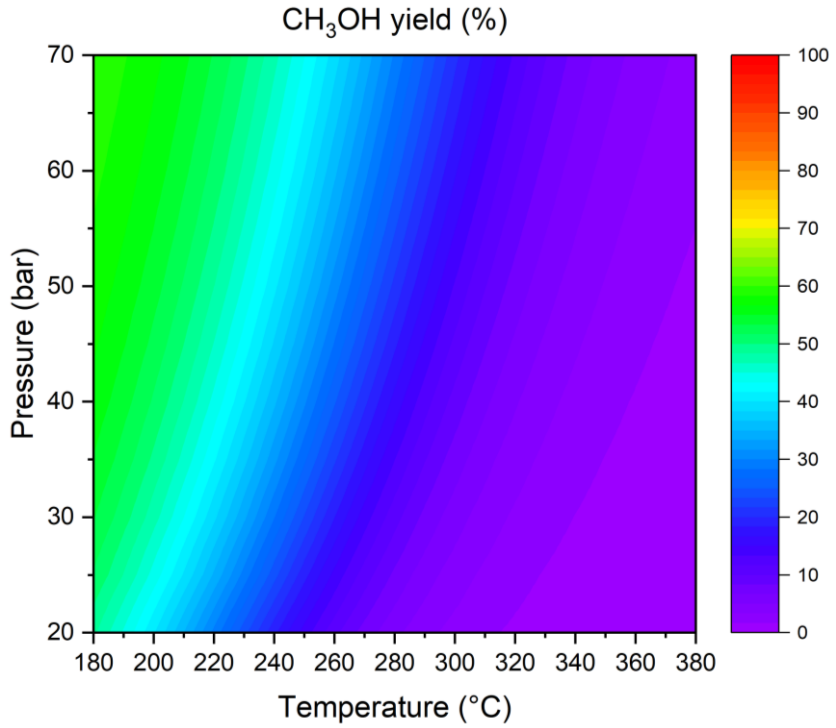


**Figure 3.13. Equilibrium $CH_3OH$ yield as a function of temperature and pressure for the $CO_2$-rich syngas feed, calculated in Aspen Plus® using a Gibbs reactor with restricted equilibrium species ($CO_2$, CO, $H_2$, $H_2O$, and $CH_3OH$).**

Additional insight into the underlying reaction pathways is provided by the contour plots of CO molar fraction and $CO_2$ conversion (Figure 3.14a and Figure 3.14b). The CO molar fraction increases with temperature over the entire pressure range investigated, indicating a progressive shift of the equilibrium towards CO formation at high temperature. This trend is accompanied by an increase in $CO_2$ conversion, which, however, does not translate into higher methanol production. Instead, $CO_2$ conversion at elevated temperature is primarily associated with the activation of the RWGS reaction, leading to net CO formation rather than methanol synthesis.

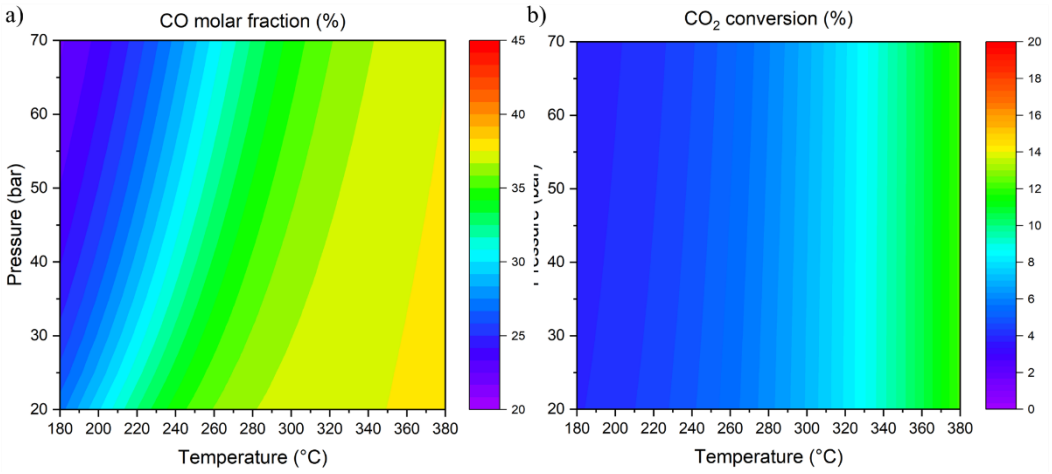


**Figure 3.14. (a) Equilibrium CO molar fraction and (b) equilibrium $CO_2$ conversion as a function of temperature and pressure.**

The observed thermodynamic trends can be rationalised by considering the main reactions governing methanol synthesis from syngas[315,316]:

| | | |
|---|---|---|
| (R-A) $CO+2H_2 \rightarrow CH_3OH$ | $\Delta H_{298K}$ = -90,77 kJ/mol | (12) |
| (R-B) $CO_2+H_2 \rightarrow CO+H_2O$ (RWGS) | $\Delta H_{298K}$= 41,21 kJ/mol | (13) |
| (R-C) $CO_2+3H_2 \rightarrow CH_3OH+H_2O$ | $\Delta H_{298K}$ = -49,16 kJ/mol | (14) |

Given the CO-rich nature of the feed, methanol formation under favourable conditions (low temperature and high pressure) is predominantly governed by the hydrogenation of CO (Eq. 12). Under these conditions, CO is effectively consumed to form methanol, as confirmed by the simultaneous decrease in CO molar fraction and increase in methanol yield. Conversely, as temperature increases, the thermodynamic equilibrium progressively favours the RWGS reaction (Eq. 13), resulting in enhanced CO formation at the expense of methanol. In this regime, $CO_2$ acts primarily as a source of CO rather than as a direct precursor to methanol.

The thermodynamic analysis clearly indicates that methanol synthesis from the investigated $CO_2$-rich syngas is intrinsically constrained by the competition between methanol-forming reactions and the RWGS reaction. Low-to-moderate temperatures combined with elevated pressures are required to maximise methanol yield, while high-temperature operation inevitably shifts the equilibrium towards CO production. These results provide a consistent thermodynamic basis for the selection of operating conditions in the subsequent kinetic simulations and process-scale analysis.

### 3.4.2 Kinetic modelling of methanol synthesis

While thermodynamic equilibrium defines the maximum attainable yield in methanol synthesis, industrial reactors typically operate under kinetic control due to finite residence time, heat release and mass transfer limitations. Therefore, a kinetic description is required to realistically model methanol synthesis under process-relevant conditions and to evaluate the impact of reactor design and operating parameters on conversion, selectivity, and temperature profiles.

In this work, the kinetic model developed by Graaf et al. (1988)[315] was adopted to describe methanol synthesis over CZA catalyst. This model is widely used in the literature for reactor-scale and process-scale simulations, as it provides a consistent description of methanol formation from both CO and $CO_2$, while explicitly accounting for the RWGS reaction.

The kinetic scheme is based on the same set of reaction discussed in the previous thermodynamic analysis (Section 3.4.1), namely (R-A) for the methanol synthesis from CO, (R-B) for the RWGS reaction, (R-C) for the methanol synthesis from $CO_2$. By retaining this reaction set, full consistency between the thermodynamic and kinetic description is ensured.

Reaction rates are expressed as functions of the partial pressures of the reacting species and include equilibrium terms to account for the proximity to thermodynamic equilibrium. In this formulation, methanol formation from CO represents the dominant reaction pathway under CO-rich syngas conditions, while $CO_2$ primarily contributes through the RWGS reaction, particularly at elevated temperatures.

$$r_A = \frac{k_a k_{CO}\left(p_{CO}p_{H_2}^{\frac{3}{2}} - \frac{p_{CH3OH}}{k_{eq,a}p_{H_2}^{\frac{1}{2}}}\right)}{\left(1+k_{CO}p_{CO}+k_{CO_2}p_{CO_2}\right)\left(p_{H_2}^{\frac{1}{2}} + \frac{k_{H_2O}}{k_{H_2}^{\frac{1}{2}}}p_{H_2O}\right)} \quad (15)$$

$$r_B = \frac{k_b k_{CO_2}\left(p_{CO}p_{H_2} - \frac{p_{H_2O}p_{CO}}{k_{eq,b}}\right)}{\left(1+k_{CO}p_{CO}+k_{CO_2}p_{CO_2}\right)\left(p_{H_2}^{\frac{1}{2}} + \frac{k_{H_2O}}{k_{H_2}^{\frac{1}{2}}}p_{H_2O}\right)} \quad (16)$$

$$r_C = \frac{k_c k_{CO_2}\left(p_{CO_2}p_{H_2}^{\frac{3}{2}} - \frac{p_{CH3OH}p_{H_2O}}{k_{eq,c}}\right)}{\left(1+k_{CO}p_{CO}+k_{CO_2}p_{CO_2}\right)\left(p_{H_2}^{\frac{1}{2}} + \frac{k_{H_2O}}{k_{H_2}^{\frac{1}{2}}}p_{H_2O}\right)} \quad (17)$$

With kinetic parameters expressed in Eqs. (18-23) and equilibrium parameters in Eqs. (24-26):

$$k_a = 2{,}69\cdot10^{7}\exp\left(-\frac{109900}{RT}\right) \quad (18)$$

$$k_b = 7{,}31\cdot10^{8}\exp\left(-\frac{123400}{RT}\right) \quad (19)$$

$$k_c = 4{,}36\cdot10^{2}\exp\left(-\frac{65200}{RT}\right) \quad (20)$$

$$K_{CO} = 7{,}99\cdot10^{-7}\exp\left(\frac{58100}{RT}\right) \quad (21)$$

$$K_{CO_2} = 1{,}02\cdot10^{-7}\exp\left(\frac{67400}{RT}\right) \quad (22)$$

$$\frac{K_{H_2O}}{K_{H_2}^{0,5}} = 4{,}13\cdot10^{-11}\exp\left(\frac{104500}{RT}\right) \quad (23)$$

$$K_{eq,a} = 3.04\cdot10^{-13}\exp\left(\frac{98342}{RT}\right) \quad (24)$$

$$K_{eq,b} = 9.28\cdot10^{-1}\exp\left(-\frac{39427}{RT}\right) \quad (25)$$

$$K_{eq,c} = K_{eq,a}\cdot K_{eq,b} = 2{,}82\cdot10^{-11}\exp\left(\frac{58915}{RT}\right) \quad (26)$$

The kinetic expressions and associated parameters reported by Graaf et al. were directly implemented in Aspen Plus® using an adiabatic plug flow reactor

(RPlug). This approach allows the simultaneous evaluation of chemical kinetics, heat release and axial temperature profiles, providing a realistic representation of industrial methanol synthesis reactor. It is worth noting that methane formation is not included in the kinetic model, in agreement with both experimental evidence in CZA catalysts and the restricted thermodynamic analysis presented in the previous section. As a result, the model specifically describes the competition between methanol synthesis and the RWGS reaction, which represents the only relevant side reaction under the investigated conditions.

### 3.4.3 Process definition and base-case assumptions

The starting point of the process analysis is a syngas stream representative of biomass gasification outputs, characterised by a composition fixed according to specification provided by the industrial partner and consisting of CO (0.367), $CO_2$ (0.08), and $H_2$ (0.55). The total syngas flow rate was set to 2 L/min at 10 bar and 25 °C and kept constant throughout the simulation campaign. This inlet flow rate represents a realistic and conservative feed level for a pilot-scale unit, enabling a meaningful evaluation of process performance while avoiding unrealistically high throughputs.

The overall process concept comprises four main sections: syngas conditioning and compression, hydrogen make-up, methanol synthesis, and product separation (the gas-liquid flash separator was set at 60 bar and 30 °C). A simplified block diagram of the process is reported in Figure 3.15, highlighting the logical structure of the system without entering into Aspen-specific details. After feed conditioning, the gas mixture is compressed to the synthesis pressure and heated to the desired reactor inlet temperature. Methanol synthesis is carried out in an adiabatic multi-tubular fixed-bed reactor modelled using an RPlug block, where reaction rates are described by the kinetic model proposed in the Section 3.4.2.

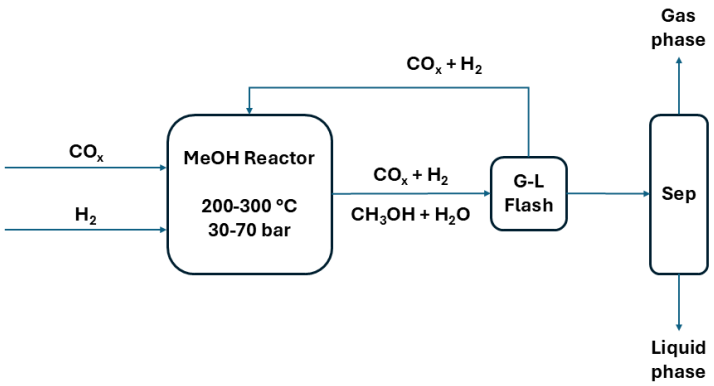


**Figure 3.15. Conceptual process scheme for methanol synthesis from $CO_2$-rich syngas with $H_2$ adjustment, adiabatic reactor section, gas-liquid flash, and downstream separation for methanol/water recovery.**

Downstream of the reactor, a gas-liquid flash separator is employed to separate the condensed methanol-water mixture from the unreacted syngas. The

liquid stream is sent to a simplified separation step aimed at recovering a methanol-rich product, while the gas stream can either be purged or recycled to the reactor inlet, depending on the configuration analysed. No methane formation was allowed in the model, consistently with both experimental observations on CZA catalysts and the restricted-equilibrium thermodynamic analysis previously discussed. An ICI 51-2 CZA catalyst was charged in the reactor, with density and porosity of respectively 1775 kg/m$^3$ and 0.4. The void fraction was set at 0.5.

For the definition of the base-case operating conditions, the reactor pressure was fixed at 60 bar, in line with conventional industrial methanol synthesis and with the constraints imposed by the industrial partner. The reactor inlet temperature was initially set to 200 °C, representing a compromise between thermodynamic favourability for methanol formation and sufficiently high reaction rates.

### 3.4.4 Adjustment of the $H_2$/COx ratio

The raw syngas stream derived from biomass gasification is characterised by a non-stoichiometric hydrogen content for methanol synthesis from CO, which must be $H_2/CO \approx 2$. To overcome this limitation, an external hydrogen source was introduced into the process by integrating a PEM water electrolysis unit upstream of the methanol synthesis section. The electrolyser supplies additional hydrogen that is mixed with the syngas feed prior to compression, allowing controlled adjustment of the overall $H_2$/CO ratio while preserving the original syngas composition.

A sensitivity analysis was performed to evaluate the effect of the additional hydrogen flow rate on process performance. For this preliminary assessment, the simplest process configuration was considered, consisting of a single adiabatic multi-tubular fixed-bed reactor without recycle, operated at 200 °C and 60 bar. The hydrogen flow rate was varied between 0.05 and 0.50 L/min (at 10 bar and 25 °C), while keeping the syngas feed constant.

The results, reported in Figure 3.16, show a monotonic increase in both CO and $CO_2$ conversion with increasing hydrogen addition (Figure 3.16a), accompanied by a corresponding rise in methanol yield (Figure 3.16b). This behaviour reflects the progressive alleviation of hydrogen limitation in the feed and the enhanced driving force for methanol synthesis reactions. However, the observed improvements remain moderate over the investigated range, indicating diminishing returns at higher hydrogen flow rates.

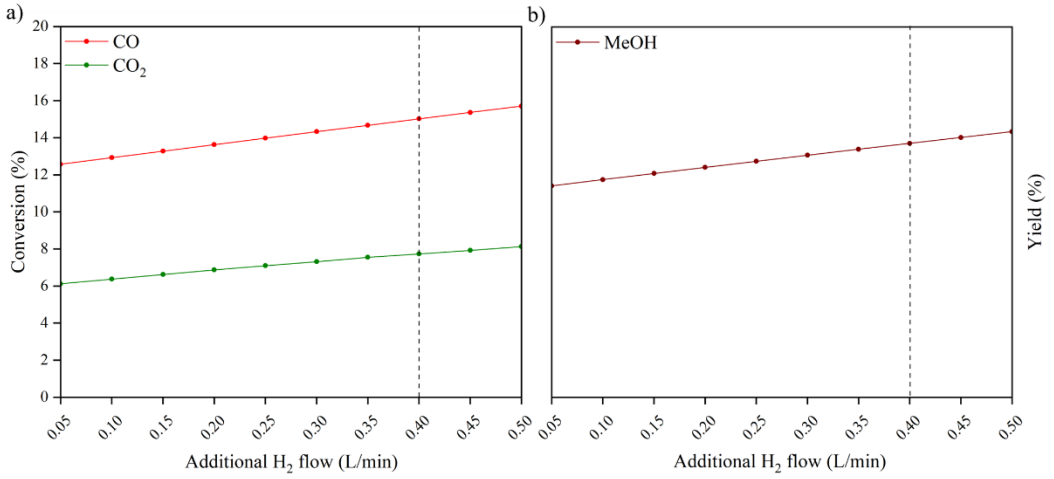


**Figure 3.16. Effect of additional hydrogen flow rate on (a) CO and $CO_2$ conversion and (b) methanol yield in a single-pass methanol synthesis configuration. Simulations were performed at 200 °C and 60 bar. The dashed line indicates the selected operating condition (0.4 L/min), corresponding to an approximately stoichiometric $H_2$/CO ratio of 2.**

Based on these results, an additional hydrogen flow rate of 0.4 L/min was selected as the best additive flow. At this condition, the overall $H_2$/CO ratio approaches the stoichiometric value required for methanol synthesis, ensuring an effective balance between CO conversion, methanol yield, and hydrogen consumption. Importantly, further increases in hydrogen addition would lead to an excess of unreacted $H_2$ in the separated syngas stream downstream of the reactor. Such hydrogen accumulation would complicate process management, increasing the need for additional adjustments, purge, or recycle strategies, with a consequent rise in energy demand and process complexity. By selecting a $H_2$ flow rate of 0.4 L/min, not only is the feed brought close to stoichiometric conditions, but the composition of the unconverted syngas after gas-liquid separation, especially in the recycle configuration, remains well balanced, with an $H_2$/CO ratio close to 2. This condition represents a favourable compromise between reaction performance and downstream operability, and was therefore adopted as the reference case for all subsequent process simulations.

### 3.4.5 Effect of reactor staging on methanol synthesis performance

After defining the inlet syngas composition and optimising the $H_2$/CO ratio, the effect of reactor configuration on the overall process performance was investigated by analysing the impact of reactor staging. In particular, simulations were carried out using one, two and three adiabatic multi-tubular fixed-bed reactors operated in series, while keeping all other operating conditions constant (200 °C, 60 bar, fixed bed flow rate and composition). No recycle was considered at this stage, in order to isolate the intrinsic effect of reactor staging on conversion and methanol production.

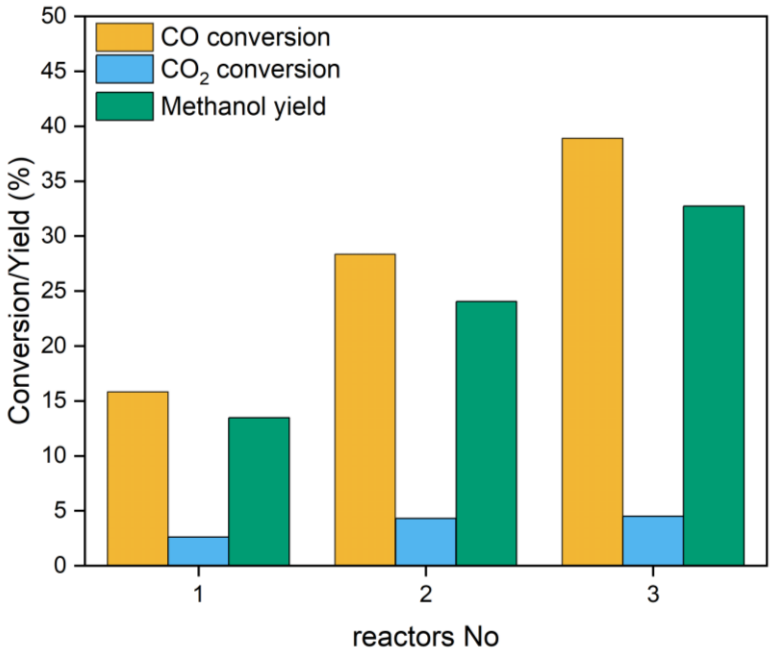


**Figure 3.17. Effect of reactor staging on process performance. CO and $CO_2$ conversion and methanol yield obtained using one, two, and three adiabatic fixed-bed reactors operated in series at 200 °C and 60 bar.**

The results, summarised in Figure 3.17, show a marked improvement in CO conversion as the number of reactors increases. CO conversion rises from approximately 16% in the single-reactor configuration to nearly 39% when three reactors are employed in series. This behaviour reflects the progressive relaxation of equilibrium limitations: after each reactor stage, partial conversion of reactants restores the driving force for methanol synthesis in the subsequent reactor. In contrast, $CO_2$ conversion exhibits only a modest increase with reactor staging, remaining below 5% even in the three-reactor configuration. This confirms that, under the investigated conditions and for the selected CO-rich syngas, methanol formation proceeds predominantly via CO hydrogenation, while $CO_2$ plays a secondary role, mainly associated with the RWGS reaction (as discussed in Section 3.4.1). The enhanced reactant conversion directly translates into a higher methanol yield, which increases from about 13% for a single reactor to more than 32% when three reactors are used in series. These results demonstrate that reactor staging represents an effective strategy to improve methanol productivity without increasing operating pressure or introducing gas recycle.

However, it should be noted that increasing the number of reactors also entails greater process complexity, additional equipment, and more demanding heat-management requirements. As a result, reactor staging alone may not represent the most efficient or economically favourable solution. For this reason, the potential benefits of reactor staging must be evaluated in combination with alternative process configurations, such as gas recycle, which is analysed in the following section.

### 3.4.6 Effect of syngas recycle on process performance

While reactor staging represents an effective strategy to increase the single-pass conversion by extending the overall residence time, it does not fundamentally overcome the thermodynamic limitations of methanol synthesis. A more powerful approach consists in the introduction of a syngas recycle loop, which allows the unreacted species to be reintegrated into the process, significantly enhancing overall conversion and carbon utilisation. For this reason, a fully integrated process configuration including syngas recycle was investigated and implemented in Aspen Plus®.

The complete process flowsheet adopted in this work is reported in Figure 3.18. The plant layout comprises syngas compression, hydrogen adjustment via water electrolysis, feed preheating through heat integration, methanol synthesis in a multi-tubular fixed-bed reactor, gas-liquid separation, downstream purification steps, and a recycle-purge loop for the unreacted syngas. All simulations discussed in this section were carried out at a reactor inlet temperature of 200 °C and a pressure of 60 bar, unless otherwise specified. After methanol synthesis, the reactor effluent is directed to a feed-effluent heat exchanger associated with a separation vessel, where it is cooled by heat integration at low temperature (25-30 °C) with a cool water stream, enabling an effective gas-liquid separation without the need for an additional flashing step. Under these conditions, the condensation of the methanol/water solution occurs primarily as a consequence of sensible heat removal, while the unreacted syngas remains in the gas phase, resulting in a gas stream composed mainly of CO, $H_2$, and $CO_2$, whereas the liquid phase consists predominantly of a methanol-water mixture with dissolved $CO_2$.

The gas stream is then split into a purge and a recycle stream, with a recycle-to-purge ratio fixed at 0.95. This value was selected as a compromise between maximising reactant reutilisation and preventing the accumulation of inert of poorly reactive species in the loop. The recycled syngas is recompressed to compensate for pressure losses and mixed with the fresh syngas feed upstream of the reactor.

A key advantage of the recycle configuration is that the recycled gas stream exhibits a near-stoichiometric $H_2$/CO ratio, confirming the suitability of the hydrogen adjustment previously introduced. As a result, the recycled syngas can be reintegrated without further compositional corrections, reinforcing the robustness of the selected operating conditions. By introducing a recycle loop with a recycle-to-purge ratio of 0.95, the overall CO conversion increases to 76.5%, while $CO_2$ conversion rises to 14.8%, leading to a methanol yield of 65.4%. These results clearly demonstrate the critical role of recycling in overcoming equilibrium constraints and maximising carbon utilisation. From a process perspective, the recycle loop significantly reduces the amount of unreacted syngas leaving the system, thereby minimising the need for downstream handling or storage of off-gas streams and improving the overall carbon efficiency of the plant.

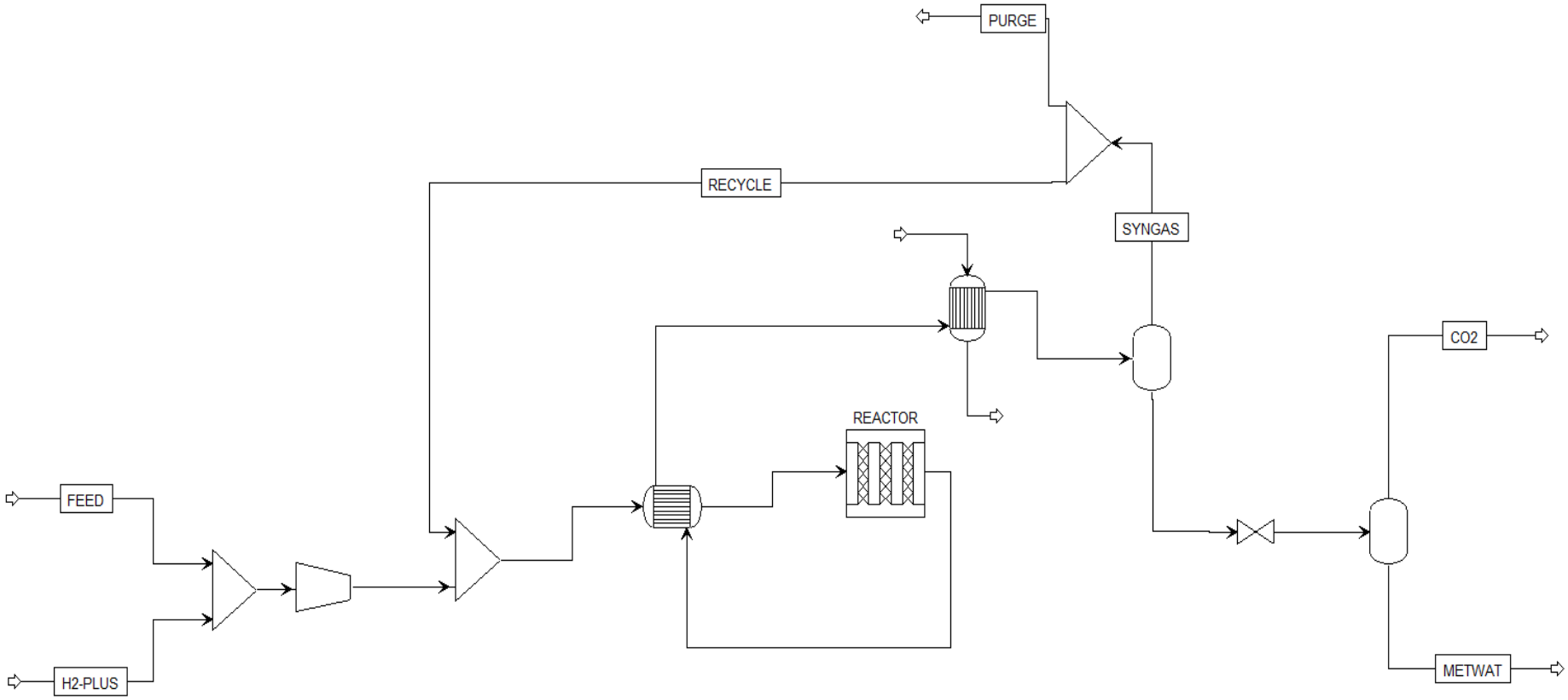


**Figure 3.18. Aspen Plus® flowsheet of the methanol synthesis process.**

By contrast, the introduction of the recycle stream inevitably leads to higher gas flow rates through the reactor, resulting in an increase in reactor volume and catalyst inventory. In the present configuration, the reactor was modelled as a multi-tubular fixed-bed reactor, with a total volume of ~1.8 L, and the higher flow rates associated with recycling translate into a reactor length approximately doubled with respect to the once-through case, together with an increased number of tubes, resulting in a total volume of ~7 L (with a factor of 4). However, this drawback is largely offset by the significant improvement in process efficiency, overall carbon utilisation, and methanol productivity, making the recycle configuration markedly more attractive from an industrial perspective.

Beyond the baseline operating point at 200 °C, the effect of reactor inlet temperature on reactor sizing and process performance was systematically investigated. As reported in Table 3.2, increasing the inlet temperature in the range 200 – 260 °C leads to a pronounced reduction in the required reactor volume and catalyst mass. This behaviour is primarily driven by enhanced reaction kinetics at higher temperatures, which allow the target conversion levels to be reached with shorter reactor lengths. From a process design perspective, this result highlights an important degree of freedom: higher inlet temperatures enable more compact reactor designs, potentially lowering capital costs associated with reactor construction and catalyst loading. An increase in the reactor inlet temperature leads to a slight reduction in methanol yield and a concurrent increase in $CO_2$ conversion. Consistent with the thermodynamic trends discussed earlier (Section 3.4.1), this behaviour may be associated with a gradual shift of the equilibrium towards the RWGS reaction at higher temperatures. However, this effect remains limited within the analysed temperature window and does not negatively affect the overall efficiency of the process. On the contrary, the enhanced kinetics and the marked reduction in reactor volume and catalyst weight make higher inlet temperatures an attractive option form a process design and scale-up perspective.

**Table 3.2. Influence of reactor inlet temperature (200-260 °C) on process performance and reactor sizing. Reported reactor volumes refer exclusively to the catalytic bed volume of the multi-tubular reactor.**

| *Temperature, °C* | *CO Conversion, %* | *$CO_2$ Conversion, %* | *MeOH Yield, %* | *Volume, L* | *Catalyst weight, kg* |
|---|---|---|---|---|---|
| ***200*** | **76.5** | **14.8** | **65.4** | **7.1** | **6.3** |
| ***220*** | **75.4** | **17.8** | **63.2** | **4.7** | **4.2** |
| ***240*** | **72.8** | **12.8** | **63.6** | **3.5** | **3.1** |
| ***260*** | **72.0** | **29.1** | **56.2** | **2.4** | **2.1** |

Due to the highly exothermic nature of methanol synthesis, allowing the reaction to proceed up to thermodynamic equilibrium leads to reactor outlet temperatures approaching 380 °C. Such temperatures are widely reported in the literature to be detrimental to Cu-based catalysts, as they promote sintering, loss

of active surface area, and accelerated structural degradation[317,318]. As a consequence, reactor design cannot rely solely on equilibrium performance but must explicitly account for catalyst lifetime and long-term stability.

To address this issue, additional simulations were performed by limiting the effective reactor length, thus preventing the system from reaching full thermodynamic equilibrium. All simulation discussed in this analysis were carried out at an inlet temperature of 240 °C. The resulting trade-off between methanol productivity, conversion level, and maximum reactor outlet temperature is summarised in Table 3.3.

Although this approach entails a reduction in total conversion and productivity, it enables operation within a significantly milder thermal regime, which is more compatible with prolonged catalyst operation and reduced risks of sintering and thermal deactivation. This design choice represents a realistic industrial compromise, where a moderate loss in performance is accepted in exchange for enhanced catalyst durability, improved process robustness, and potentially longer operating cycles.

Overall, the recycle-based configuration emerges as a robust and industrially relevant solution for methanol synthesis from $CO_2$-containing syngas. The integration of syngas recycle, heat recovery, and controlled reactor operation enables high overall conversion and methanol yield, while maintaining operating conditions compatible with catalyst stability. The analysis presented in this section demonstrates that effective process engineering, rather than equilibrium-limited optimisation alone, is essential to achieve a viable and scalable methanol synthesis process.

**Table 3.3. Effect of reactor outlet temperature limitation on process performance at $T_{in}$ = 240 °C in the recycle configuration.**

| | *CO conversion, %* | *$CO_2$ conversion, %* | *MeOH yield, %* | *MeOH production, kg/h* | *Reactor outlet temperature, °C* |
|---|---|---|---|---|---|
| ***Full equilibrium*** | 72.8 | 12.8 | 63.6 | 0.4 | ~380 |
| ***$T_{out}$ < 300 °C*** | 56.7 | 12.8 | 39.3 | 0.3 | ~297 |

### 3.4.7 Process performance comparison

The Aspen Plus® modelling activity allowed a systematic evaluation of different process configurations for methanol synthesis from a $CO_2$-containing syngas, highlighting the key trade-offs between productivity, conversion efficiency, and process complexity. Starting from a single-pass configuration, the progressive introduction of reactor staging and syngas recycle was used as a process intensification strategy to enhance overall performance.

The use of multiple reactors in series proved to be particularly effective in increasing the single-pass conversion and, most importantly, the net methanol production rate. As summarised in Table 3.4, moving from one to three reactors in

series resulted in a substantial increase in CO conversion (from 15.8% to 38.9%) and methanol yield (from 13.5% to 32.7%).

However, the introduction of a syngas recycle loop (recycle-to-purge ratio of 0.95) led to a further increase in overall conversion and yield, with CO conversion reaching 76.5% and methanol yield increasing to 65.4%, leading also to the highest methanol productivity achieved in this study (0.4 kg/h). This configuration is therefore more effective in maximising carbon utilisation and reducing syngas losses, other than in maximising absolute methanol productivity.

From a broader process and carbon management perspective, the recycle-based configuration emerges as a particularly attractive option. By reintegrating unreacted syngas into the process, the recycle loop minimises downstream syngas handling requirements, avoids the need for syngas storage or disposal, and ensures a more efficient utilisation of the carbon contained in the feed. These aspects are especially relevant in the context of $CO_2$-rich syngas derived from biomass gasification.

Finally, additional simulations demonstrated that reactor inlet and outlet temperature management plays a crucial role in defining a realistic and robust process design. Limiting the maximum reactor outlet temperature below 300 °C leads to a moderate reduction in conversion and methanol yield, but significantly improves the thermal regime of the reactor, which is essential for preserving catalyst stability and lifetime.

**Table 3.4. Comparison of methanol productivity, CO and $CO_2$ conversion, and methanol yield for different process configurations: single reactor, three reactors in series, and syngas recycle configuration, evaluated at $T_{inlet}$ = 200 °C, 60 bar and fixed feed composition.**

| *Configuration* | *MeOH, kg/hr* | *CO Conversion, %* | *$CO_2$ Conversion, %* | *MeOH Yield, %* |
|---|---|---|---|---|
| ***Single reactor*** | 0.1 | 15.8 | 2.6 | 13.5 |
| ***Three reactors*** | 0.2 | 38.9 | 4.5 | 32.7 |
| ***Recycle*** | 0.4 | 76.5 | 14.8 | 65.4 |

## 3.5 Insight on novel Cu-based catalysts for $CO_2$ hydrogenation (screening study)

### 3.5.1 Novel Cu-based catalytic testing at low pressure

A first set of Cu-Fe-Ce-based catalysts supported on HZSM-5 (hereafter denoted as FCC_X, where X represents the (Cu+Fe)/Ce molar ratio) was investigated as a preliminary screening for $CO_2$ hydrogenation reactions. Two series were prepared with total metal loading of 4 wt% and 8 wt%, in order to evaluate the effect of active phase content on catalytic behaviour.

### *FCC_X preparation and characterisation*

The catalysts were synthesised by co-impregnation of metal nitrates (Cu, Fe, and Ce precursors) onto a commercial HZSM-5 zeolite support (Si/Al ratio of 25). The HZSM-5 support was used in powder form and was pre-treated prior to impregnation by calcination in air at 550 °C for 2h, with a heating ramp of 10 °C/min, in order to remove residual organic species or water adsorbed.

The impregnation was carried out by conventional wet impregnation, using a rotary evaporator to ensure uniform contact between the metal-containing solution and the HZSM-5 support and to promote controlled solvent removal. All metal precursors were co-impregnated in a single step.

Two sets of catalysts were prepared. The first step consisted of samples with a total active phase loading of 4 wt%, covering different (Cu+Fe)/Ce ratios (FCC_X_4). Based on the initial screening, selected compositions (FCC_0.5 and FCC_1.3) were further prepared with a higher total metal loading of 8 wt% (FCC_X_8) to investigate the effect of active phase content on catalytic behaviour.

After impregnation, the samples were dried overnight in an oven and subsequently calcined in air under the same conditions adopted for the support pre-treatment (550 °C for h, heating rate 10 °C/min). No in-situ reduction step was applied prior to catalytic testing; all experiments were performed on the calcined materials.

Catalyst characterisation was limited to techniques aimed at providing qualitative information on acidity, reducibility and structural integrity of the support (showed in Figure A.6, Figure A.7, and Figure A.8).

$NH_3$-TPD measurements confirmed the presence of a broad distribution of acid sites typical of HZSM-5[319,320], with no major qualitative differences among the FCC samples, suggesting that metal impregnation did not substantially alter the acidic framework of the zeolite.

$H_2$-TPR profiles indicated the presence of reducible metal oxide species, with reduction features attributed to Cu- and Fe-containing phases, while XRD patterns were dominated by the diffraction peaks of the HZSM-5 structure, indicating high metal dispersion and the absence of detectable bulk oxide phases. Given the exploratory nature of this catalyst set, these characterisations were considered sufficient to support the catalytic analysis.

### *Catalytic tests under RWGS-oriented conditions*

Catalytic tests were performed in $CO_2$ hydrogenation under atmospheric pressure using two different feed composition ($CO_2$:$H_2$ = 1:2 and 1:3). Since the 1:3 ratio systematically led to higher $CO_2$ conversion, the discussion below focuses on this condition.

Figure 3.19 compares the $CO_2$ conversion as a function of temperature for FCC catalysts with 4 wt% and 8 wt% total metal loading. In all cases, $CO_2$ conversion increased monotonically with temperature, reaching values below 7% even at 500 °C. Increasing the active phase loading from 4 wt% to 8 wt% led to a

measurable but limited enhancement in activity, indicating that reaction rates remain intrinsically constrained by the nature of the active phase and/or reaction pathway.

Overall, the observed behaviour is consistent with a reaction regime dominated by the RWGS reaction, with CO as the main carbon-containing product.

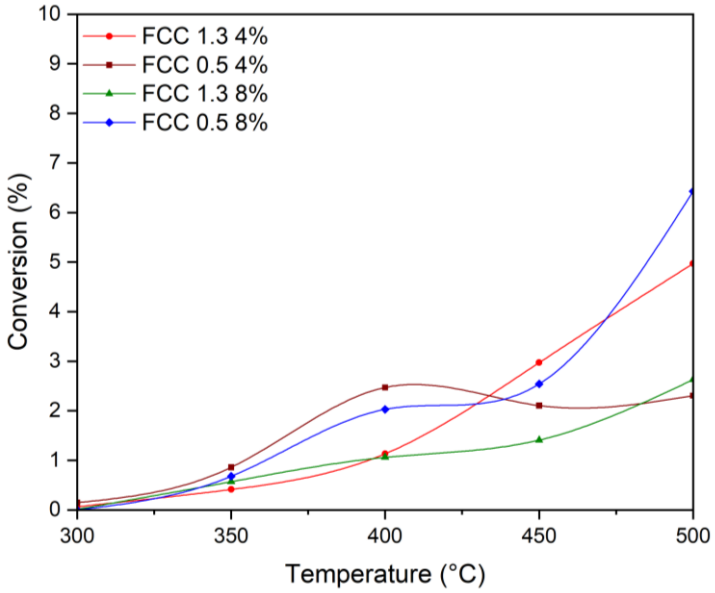


**Figure 3.19. $CO_2$ conversion for FCC catalysts with different (Fe+Cu)/Ce ratios and metal loadings, under $CO_2$ hydrogenation conditions ($CO_2$:$H_2$ = 1:3).**

For selected samples (notably FCC_0,5 at 8 wt% loading), catalytic activity was evaluated in fresh, used, and re-oxidised states (Figure 3.20). Interestingly, the catalyst tested after reaction ("used") showed higher $CO_2$ conversion than the fresh sample across the whole temperature range, whereas an even higher performance is obtained after an oxidative treatment, indicating that the catalyst structure remains stable and responsive to regeneration treatments.

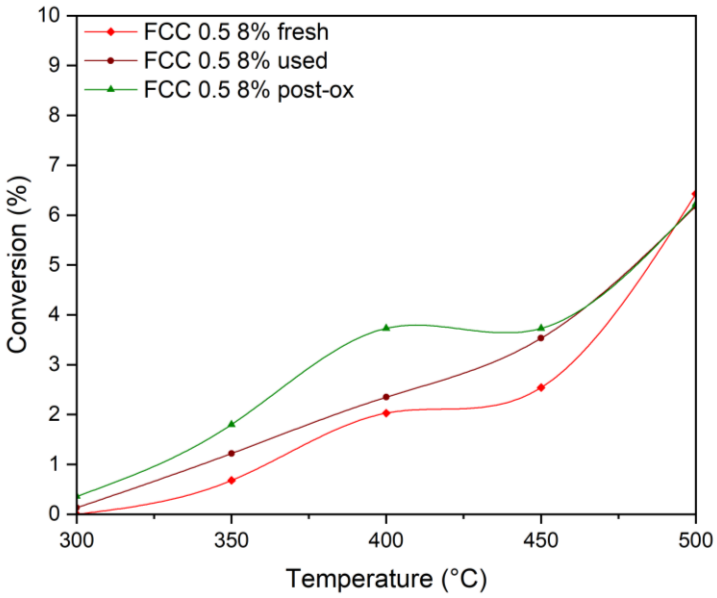


**Figure 3.20. $CO_2$ conversion for FCC 0.5 (8 wt%) catalyst in fresh, used, and post-oxidation samples under $CO_2$ hydrogenation conditions ($CO_2$:$H_2$ = 1:3).**

Although this set of FCC_X catalysts did not exhibit appreciable activity toward methanol or methane synthesis, the results provide important insights. First, they confirm that, under the investigated conditions, these Cu-Fe-Ce systems supported on HXSM-5 zeolite are intrinsically selective toward CO formation rather than oxygenated or other carbon-based products. Second, they highlight the limited impact of increasing metal loading on shifting selectivity away from RWGS. Finally, the observed redox-related activation/deactivation behaviour underscores the complexity of these multimetallic systems.

### 3.5.2 Novel Cu-based catalysts for $CO_2$ hydrogenation at moderate pressure

In addition to Cu-based catalysts discussed in previous sections, a new set of Cu-based materials was investigated to explore alternative reaction pathways in $CO_2$ hydrogenation under moderate-pressure (30 bar) conditions. While these catalysts were initially conceived as potential candidates for oxygenates formation, their behaviour provides valuable insight into the interplay between catalyst composition, reaction environment, and product selectivity, particularly in relation to the competition between RWGS and methanation routes.

#### *Catalyst preparation and characterisation*

Three representative catalysts were selected for this study: a conventional Cu-Zn-Al oxide catalyst (hereafter referred to as CZA), a Cu-Fe-based catalyst (CF), chosen to assess the effect of iron addition on $CO_2$ hydrogenation pathways, and a Cu-Fe (weight ratio 1:1) supported on HZSM-5 zeolite (active phase 8 wt%). CZA and CF were both synthetised following the same co-precipitation protocol

to ensure comparability, while the CF/HZSM-5 was prepared by impregnation (for the synthesis procedure see Section 3.5.1).

The precipitation process was carried out by adding an aqueous solution of $(NH_4)_2CO_3$ dropwise to a solution containing the nitrate salts of copper and the other metals (Zn and Al in CZA and Fe in CF), dissolved in deionised water, under vigorous stirring at 80 °C until a pH of approximately 7 was reached. The resulting suspension was aged at 80 °C to complete precipitation, then filtered and repeatedly washed with deionised water to remove residual ionic species. The obtained precursors were dried overnight at 120 °C and subsequently calcined in air at 400 °C for 2h, yielding the oxide form of the catalysts. Catalyst labels, nominal compositions and physical properties are summarised in Table 3.5.

XRF analysis confirmed a good agreement between nominal and experimental metal compositions for both samples. BET surface area measurements, performed after calcination, revealed a significantly higher surface are for the CF catalyst compared to CZA.

Surface acidity was qualitatively evaluated by $NH_3$-TPD on the calcined catalysts (Figure A.9). Both materials exhibit contributions from weak, moderate and strong acid sites; however, CF shows a higher overall $NH_3$ uptake, particularly in the medium-to-high temperature region, indicating a larger density of stronger acid sites compared to CZA. $H_2$-TPR experiments were used to identify suitable reduction temperatures for catalyst activation prior to catalytic testing. Based on these profiles, both catalysts were reduced in situ under hydrogen to ensure the formation of the active metallic phases. XRD analysis of the calcined samples confirmed the presence of the expected oxide phases, with no additional crystalline species detected, indicating good dispersion of the active components (Figure A.10).

**Table 3.5. Nominal and experimental compositions (XRF) and BET surface area of the Cu-based catalysts investigated in the moderate-pressure $CO_2$ hydrogenation screening tests.**

| *Sample* | *Nominal composition* | *XRF* | *BET ($m^2/g$)* |
|---|---|---|---|
| ***CZA*** | 60% Cu – 30% Zn, 10% Al | 64 – 30 – 5 % | 41.38 |
| ***CF*** | 60% Cu – 40% Fe | 64 – 36 % | 94.27 |

### *Catalytic performance under high-pressure $CO_2$ hydrogenation*

Catalytic tests were carried out in a fixed-bed reactor at 30 bar over a temperature range relevant for $CO_2$ hydrogenation. Two different feed compositions were investigated ($N_2$:$H_2$:$CO_2$ = 80:16:4 and 50:40:10) to evaluate the influence of hydrogen partial pressure and gas dilution on activity and selectivity. Carbon balances were closed within ∓5% in all experiments allowing CO and $CH_4$ to be considered as the only reaction products.

Under these conditions, the CZA catalyst exhibits limited activity towards oxygenated and $CH_4$ formation. CO is the dominant product over the entire

investigated temperature range, indicating that the RWGS reaction is the prevailing pathway as showed in Figure 3.21.

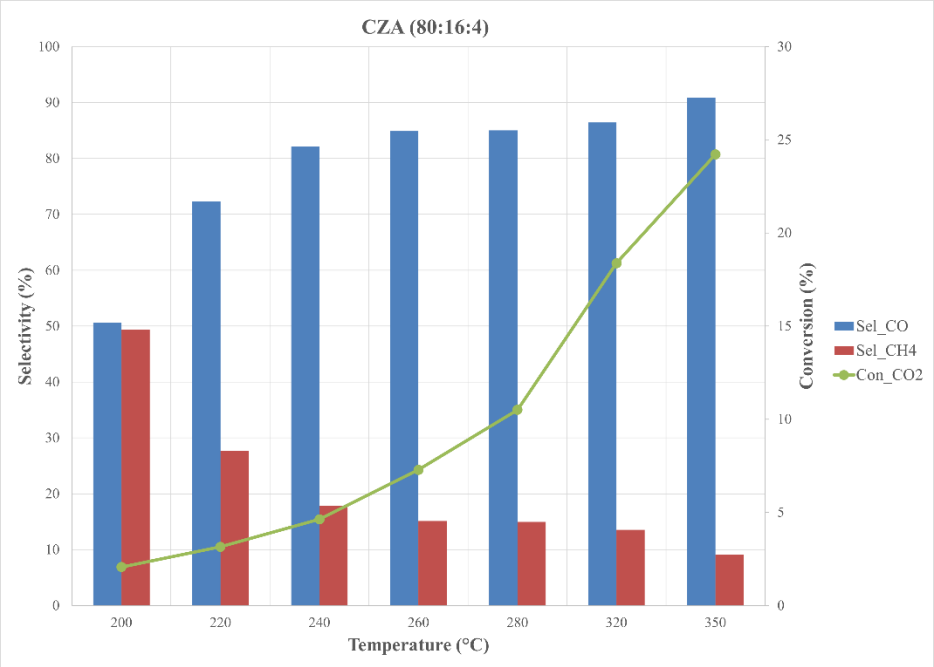


**Figure 3.21. Product selectivity and $CO_2$ conversion as a function of temperature for the CZA catalyst under moderate pressure $CO_2$ hydrogenation (30 bar, $N_2$:$H_2$:$CO_2$ = 80:16:4).**

In contrast, the CF catalyst displays a markedly different catalytic behaviour (Figure 3.22). Methane selectivity is significantly enhanced, particularly at higher temperatures, revealing a clear shift from RWGS-dominated chemistry towards methanation. This effect is further amplified when decreasing the hydrogen content in the feed, as observed when switching from the hydrogen-rich (50:40:10) to the diluted (80:16:4) gas composition. In this case, $CH_4$ formation is strongly favoured, while CO selectivity decreases accordingly.

Overall, this catalyst set provides complementary insight into the structure-performance relationship governing $CO_2$ hydrogenation reactions. While CZA remains predominantly selective towards CO formation under the investigated conditions, iron-containing catalyst enable a transition towards methane production, underscoring the sensitivity of $CO_2$ conversion pathways to both catalyst formulation and reaction environment.

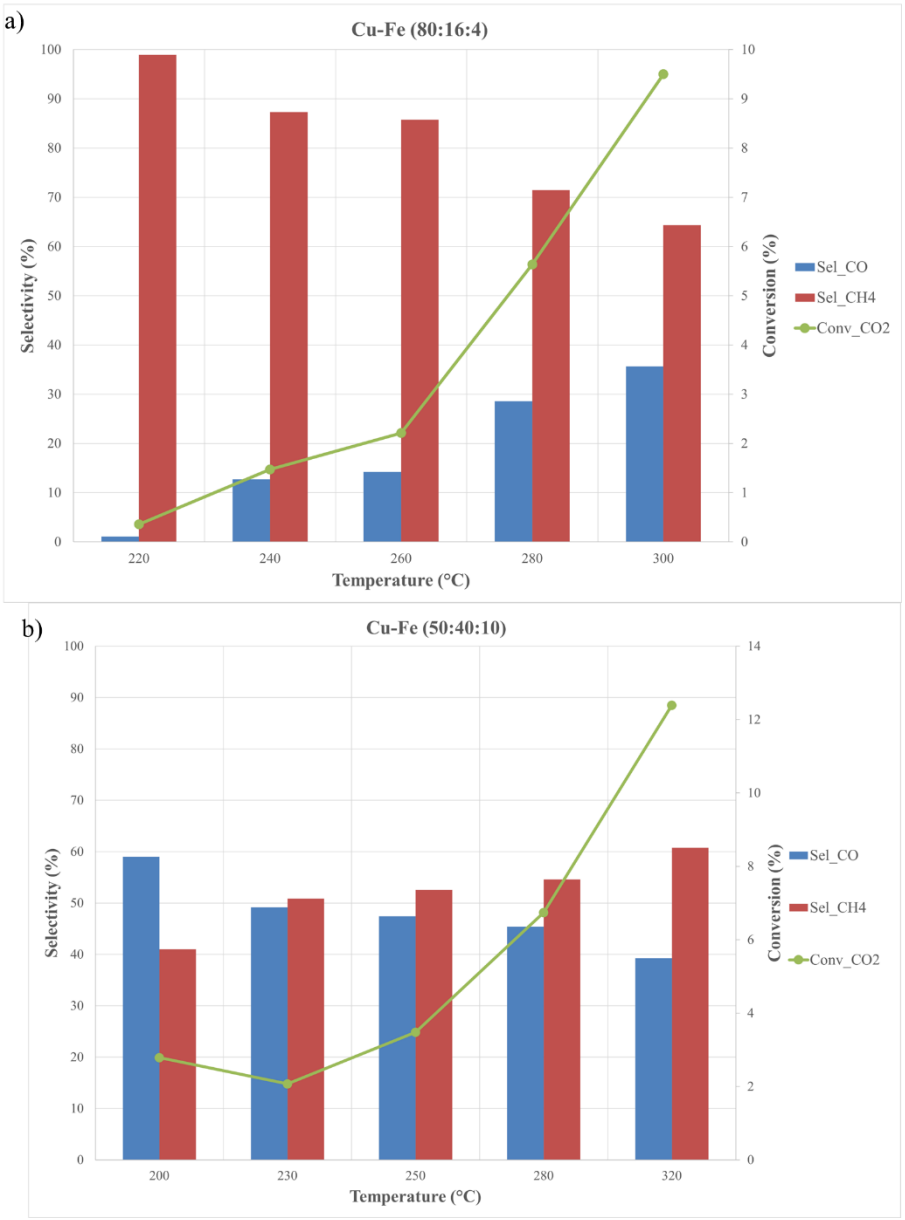


**Figure 3.22. Product selectivity and $CO_2$ conversion as a function of temperature for the Cu-Fe catalyst (CF) under moderate-pressure $CO_2$ hydrogenation (30 bar) using different feed composition: (a) $N_2$:$H_2$:$CO_2$ = 80:16:4 and (b) $N_2$:$H_2$:$CO_2$ = 50:40:10.**

Finally, the CF/HZSM-5 was tested under moderate pressure conditions (Figure 3.23). Although overall $CO_2$ conversion remained limited, the catalytic behaviour observed at low temperature is noteworthy. In the temperature range below 300 °C, the formation of methanol and dimethyl ether was detected, indicating that the catalyst is able to transiently promote methanol synthesis and subsequent acid-catalysed dehydration on the zeolite support[321–324].

Upon increasing temperature, methanol and DME selectivity rapidly decreased, while CO and $CH_4$ became predominant, in line with the activation of RWGS and methanation pathways. This temperature-dependent selectivity inversion is fully consistent with the thermodynamic and kinetic considerations discussed earlier in this chapter.

Although the observed methanol and DME formation occurs only within a narrow temperature window and at low conversion rates, this result is significant as a proof-of-concept. It demonstrates that, even in Cu-Fe based systems typically associated with CO and $CH_4$ production, an appropriate combination of metal composition, support acidity and operating conditions can stabilise a methanol-oriented reaction pathway. These findings suggest that Cu-Fe-zeolite catalysts may represent an interesting starting point for further optimisation, provided that catalysts formulation and process conditions are specifically tailored to stabilise this low-temperature regime.

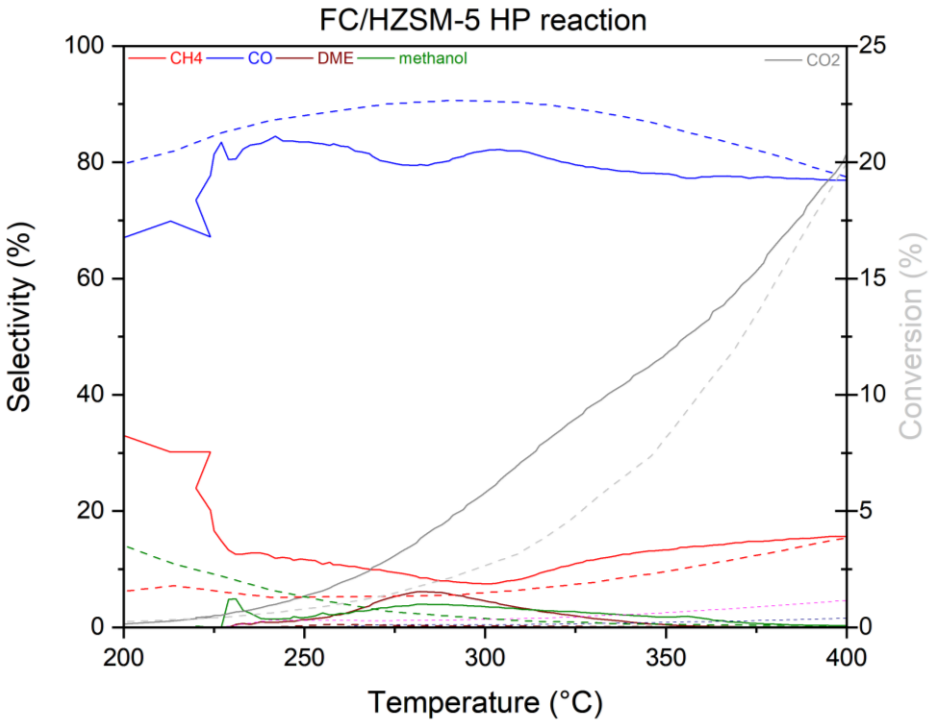


**Figure 3.23. Product selectivity and $CO_2$ conversion for the CF/HZSM-5 catalyst under moderate pressure (30 bar). Methanol and DME (green and wine lines respectively) are detected only under 300 °C.**

# Chapter 4

# 4. Conclusions and outlooks

The transition toward a low-carbon energy system requires technologies that are not only effective in reducing $CO_2$ emissions, but also compatible with existing energy infrastructures. In this perspective, Carbon Capture and Utilisation (CCU), with Power-to-Methane (PtM) and Power-to-Methanol, represents a particularly attractive strategy, as it enables the conversion of captured $CO_2$ into chemical fuels or energy carriers that can be long-time stored, transported, and distributed using well-established infrastructure. PtM and Power-to-Methanol routes are especially relevant as synthetic methane can be readily injected into natural gas grids, while methanol represents a versatile platform molecule for fuels and chemicals already integrated into current industrial value chains.

Within this framework, the central question addressed in this thesis is not whether $CO_2$ hydrogenation is feasible, but how catalyst design, thermodynamics, and process configuration must be coherently integrated to render these technologies effective, scalable, and system-compatible.

For the PtM pathway, the experimental results confirm that $CO_2$ methanation benefits from a fundamentally favourable thermodynamic landscape. As a result, catalyst development for PtM is primarily governed by issues of stability, selectivity, and process integration rather than equilibrium limitations. The investigation of Ni-supported ultra-stable Y (USY) zeolites demonstrated that high methane selectivity and excellent resistance to coke formation can be achieved by controlling metal dispersion and particle size within a hierarchically porous framework. In this system, the zeolite support plays an active role beyond simple metal anchoring, influencing mass transport, metal nucleation, and long-term stability.

From an outlook perspective, these findings suggest that future improvements in Ni-based methanation catalysts should focus on engineering advanced support architectures, increasing meso- and microporosity further enhancing diffusivity and allowing nickel nanoparticles to nucleate and stabilise beyond microporous domains, potentially improving accessibility of active sites without compromising

coking resistance. The development of tailored hierarchical zeolites or hybrid porous support thus represents a promising direction to push Ni-supported systems closer to state-of-art catalysts performance while maintaining robustness under conventional operating conditions.

The work on rhenium-based dual-functional materials operating under integrated carbon capture and utilisation conditions highlights a complementary and conceptually distinct behaviour to PtM. By temporally decoupling $CO_2$ capture and hydrogenation, these systems demonstrate that selectivity limitations associated with continuous methanation can be effectively bypassed, outperforming also Ni-based catalyst, under cyclic operations. Importantly, rhenium emerges from this study not merely as an active metal, but as a platform for designing cyclic capture-conversion strategies, where adsorption and catalysis are intrinsically coupled.

The results indicate that this class of materials is particularly promising for further development, especially considering that rhenium is not classified among the most critical raw materials. Outlooks in this direction may include the exploration of alternative adsorbent phases to further enhance capture efficiency and reaction control, as already suggested by the improved performance observed for $Re/CeO_2$ systems. Extending this concept to other oxide or silicoaluminate adsorbents could open new pathways for improving ICCU efficiency while maintaining high methane selectivity – as DFMs studied in this thesis reached 100% in $CH_4$ selectivity. More broadly, the ICCU approach demonstrated here provides a conceptual starting point for designing catalysts specifically tailored to intermittent renewable energy supply, a feature that will become increasingly important in future energy systems.

In contrast to PtM, the Power-to-Methanol pathway exposes the intrinsic thermodynamic rigidity of $CO_2$ hydrogenation. Experimental studies on Cu-based catalysts confirmed that methanol selectivity is confined to a narrow temperature window, outside of which reverse water-gas shift and methanation reactions dominate. While catalyst synthesis proved essential to achieving measurable methanol formation through precursor selection and metal-support interface, these results also underscore that catalyst optimisation alone cannot overcome equilibrium constraints.

In this context, the Aspen Plus® process simulation represent a key contribution of this thesis, as it frames methanol synthesis as a system-level engineering problem. The simulations demonstrate that reactor staging and syngas recycle can dramatically enhance overall $CO_2$ conversion and methanol yield without modifying catalyst formulation. This highlights that, beyond lab-scale catalyst development, the optimisation of process configuration, in minimising syngas losses, maximising carbon recycling, and ensuring efficient reactant utilisation, is decisive for rendering PtL processes viable and efficient.

Main outlooks in this context rely on the importance of advanced heat management strategies, as methanol synthesis is highly exothermic and temperature control directly impacts catalyst stability and equilibrium conversion. The valorisation of excess reaction heat through integration with downstream units, such as heat recovery systems, power generation, or coupling with endothermic processes, represent a relevant opportunity for improving overall process efficiency. In parallel, alternative synthesis routes toward other oxygenated products, such as dimethyl ether (DME), emerge as an attractive option, which may benefit from integrated or sequential reactor concepts and could offer additional flexibility in product distribution while remaining compatible with existing fuel and chemical infrastructure.

The exploratory screening of Cu-Fe and Cu-Fe-Ce catalysts at moderate pressure further reinforces the importance of aligning catalyst architecture with the target reaction. The observed selectivity toward CO and methane, despite the presence of copper, a benchmark for methanol synthesis, confirms that methanol synthesis requires catalysts specifically engineered to gain a combined effect of metal composition, redox behaviour, and, especially, an improved metal-promoter interface synergy, aiming to stabilise oxygenated intermediates under unfavourable thermodynamic conditions.

In conclusion, this thesis demonstrates that effective $CO_2$ utilisation cannot rely on catalyst development alone. For Power-to-Methane, the inherent thermodynamic favourability enables flexibility in catalyst-process coupling, making this route particularly suitable for integration into existing gas infrastructures and dynamic energy systems. For Power-to-Methanol, stringent thermodynamic constraints demand precise catalyst design supported by sophisticated process configurations that maximise carbon utilisation and minimise losses. Looking forward, the true impact of $CO_2$-based e-fuel technologies will ultimately depend on their performance within real energy systems. In this respect, techno-economic analysis and life cycle assessment represent crucial next steps to quantitatively evaluate the environmental and economic benefits of the process investigated above. The results presented in this thesis underline the importance of coupling catalyst development with process design and system-level evaluation when assessing the potential of $CO_2$ hydrogenation routes in the context of energy transition strategies.

# References


[1] US Environmental Protection Agency. Overview of Greenhouse Gases 2025. https://www.epa.gov/ghgemissions/overview-greenhouse-gases (accessed July 5, 2025).

[2] Yamasaki A. An Overview of $CO_2$ Mitigation Options for Global Warming-Emphasizing $CO_2$ Sequestration Options. J Chem Eng Japan / JCEJ 2003;36:361–75. https://doi.org/10.1252/jcej.36.361.

[3] Scheffer M, Brovkin V, Cox PM. Positive feedback between global warming and atmospheric $CO_2$ concentration inferred from past climate change. Geophysical Research Letters 2006;33:2005GL025044. https://doi.org/10.1029/2005GL025044.

[4] NOAA Global Monitoring Laboratory. Trends in Atmospheric $CO_2$ - Mauna Loa Observatory. NOAA Global Monitoring Laboratory n.d. https://gml.noaa.gov/ccgg/trends/mlo.html (accessed July 5, 2025).

[5] Lindsey R, Dahlman L. Climate Change: Global Temperature. ClimateGov 2025. https://www.climate.gov/news-features/understanding-climate/climate-change-global-temperature (accessed July 5, 2025).

[6] Allen MR, Dube OP, Solecki W, Aragón-Durand F, Cramer W, Humpgreys S, et al. Framing and Context. Global Warming of 1.5°C, Cambridge, UK and New York, NY, USA: Cambridge University Press; 2018, p. 49–92. https://doi.org/10.1017/9781009157940.003.

[7] Hansen J, Sato M, Ruedy R, Lo K, Lea DW, Medina-Elizade M. Global temperature change. Proc Natl Acad Sci 2006;103:14288–93. https://doi.org/10.1073/pnas.0606291103.

[8] Seneviratne SI, Zhang X, Adnan M, Dereczynski C, Di Luca A, Ghosh S, et al. Weather and Climate Extreme Events in a Changing Climate. Climate Change 2021, Cambridge, UK and New York, NY, USA: Cambridge University Press; n.d., p. 1513–766. https://doi.org/10.1017/9781009157896.013.

[9] CRED. Natural Disasters 2018. Brussels, Belgium: Centre for Research on the Epidemiology of Disaster (CRED); 2019.

[10] Fox-Kemper B, Hewitt HT, Xiao C, Aðalgeirsdóttir G, Drijfhout SS, Edwards TL, et al. Ocean, cryosphere, and sea level change. Climate Change 2021: The Physical Science Basis., Cambridge, United Kingdom and New York, NY, USA: Cambridge University Press; 2021, p. 1211–362. https://doi.org/10.1017/9781009157896.001.

[11] European Environment Agency (EEA). How climate change impacts marine life. Copenhagen, Denmark: EEA; 2023. https://doi.org/10.2800/06827.

[12] Intergovernmental Panel on Climate Change (IPCC). Climate Change 2023: Synthesis Report. Geneva, Switzerland.: IPCC; 2023. https://doi.org/10.59327/IPCC/AR6-9789291691647.

[13] International Energy Agency (IEA). Global Energy Review 2025. Paris, France: IEA; 2025.
[14] Eurostat. EU economy greenhouse gas emissions: -4.0% in Q1 2024. Eurostat News 2024. https://ec.europa.eu/eurostat/web/products-eurostat-news/w/ddn-20240816-1 (accessed November 5, 2024).
[15] IEA. GHG emissions of all world countries. Publications Office of the European Union; 2024.
[16] Our World in Data. Total greenhouse gas emissions. Our World in Data 2025. https://ourworldindata.org/grapher/total-ghg-emissions (accessed December 5, 2025).
[17] European Environment Agency (EEA). Greenhouse gas emission intensity of electricity generation in Europe. EEA - European Environment Agency 2025. https://www.eea.europa.eu/en/analysis/indicators/greenhouse-gas-emission-intensity-of-1 (accessed July 10, 2025).
[18] United Nations Framework Convention on Climate Change (UNFCCC). Paris Agreement. Paris, France: UNFCCC; 2015.
[19] Fawzy S, Osman AI, Doran J, Rooney DW. Strategies for mitigation of climate change: a review. Environ Chem Lett 2020;18:2069–94. https://doi.org/10.1007/s10311-020-01059-w.
[20] United Nations Development Programme (UNDP). NDC Global Outlook Report 2019. UNDP; 2019.
[21] Ochedi FO, Yu J, Yu H, Liu Y, Hussain A. Carbon dioxide capture using liquid absorption methods: a review. Environ Chem Lett 2021;19:77–109. https://doi.org/10.1007/s10311-020-01093-8.
[22] Forster PM, Smith C, Walsh T, Lamb WF, Lamboll R, Cassou C, et al. Indicators of Global Climate Change 2024: annual update of key indicators of the state of the climate system and human influence. Earth System Science Data 2025;17:2641–80. https://doi.org/10.5194/essd-17-2641-2025.
[23] Riahi K, Schaeffer R, Arango J, Calvin K, Guivarch C, Hasegawa T, et al. Mitigation pathways compatible with long-term goals. IPCC, 2022: Climate Change 2022: Mitigation of Climate Change, Cambridge, UK and New York, NY, USA: Cambridge University Press; 2022. https://doi.org/10.1017/9781009157926.005.
[24] IEA. Energy Technology Perspectives 2020 2020. https://www.iea.org/reports/energy-technology-perspectives-2020.
[25] Bashmakov IA, Nilsson LJ, Acquaye A, Bataille C, Cullen JM, de la Rue du Can S, et al. Industry. IPCC, 2022: Climate Change 2022: Mitigation of Climate Change, Cambridge, UK and New York, NY, USA: Cambridge University Press; 2022. https://doi.org/10.1017/9781009157926.013.
[26] Global CCS Institute. Global Status of CCS 2025: Staying the Course. Global CCS Institute; 2025.
[27] Cuéllar-Franca RM, Azapagic A. Carbon capture, storage and utilisation technologies: A critical analysis and comparison of their life cycle environmental impacts. Journal of CO2 Utilization 2015;9:82–102. https://doi.org/10.1016/j.jcou.2014.12.001.
[28] Nocito F, Dibenedetto A. Atmospheric CO2 mitigation technologies: carbon capture utilization and storage. Current Opinion in Green and Sustainable Chemistry 2020;21:34–43. https://doi.org/10.1016/j.cogsc.2019.10.002.

[29] Lenzen M. Global Warming Effect of Leakage From CO2 Storage. Critical Reviews in Environmental Science and Technology 2011;41:2169–85. https://doi.org/10.1080/10643389.2010.497442.
[30] Lerche Raadal H, Saur Modahl I. LCA of CCS and CCU compared with no capture: How should multi-functional systems be analysed? E3S Web Conf 2022;349:03001. https://doi.org/10.1051/e3sconf/202234903001.
[31] Wang Z, Li H, Liu S, Xu J, Liu J, Wang X. Risk evaluation of CO2 leakage through fracture zone in geological storage reservoir. Fuel 2023;342:127896. https://doi.org/10.1016/j.fuel.2023.127896.
[32] Müller LJ, Kätelhön A, Bachmann M, Zimmermann A, Sternberg A, Bardow A. A Guideline for Life Cycle Assessment of Carbon Capture and Utilization. Front Energy Res 2020;8. https://doi.org/10.3389/fenrg.2020.00015.
[33] Garcia-Garcia G, Fernandez MC, Armstrong K, Woolass S, Styring P. Analytical Review of Life-Cycle Environmental Impacts of Carbon Capture and Utilization Technologies. ChemSusChem 2021;14:995–1015. https://doi.org/10.1002/cssc.202002126.
[34] CSIRO. Turning carbon from a waste into a resource. CSIRO 2021. https://www.csiro.au/en/news/All/Articles/2021/March/turning-carbon-from-a-waste-into-a-resource (accessed November 18, 2025).
[35] Atsbha TA, Yoon T, Seongho P, Lee C-J. A review on the catalytic conversion of CO2 using H2 for synthesis of CO, methanol, and hydrocarbons. Journal of CO2 Utilization 2021;44:101413. https://doi.org/10.1016/j.jcou.2020.101413.
[36] Abdeen FRH, Mel M, Jami MS, Ihsan SI, Ismail AF. A review of chemical absorption of carbon dioxide for biogas upgrading. Chinese Journal of Chemical Engineering 2016;24:693–702. https://doi.org/10.1016/j.cjche.2016.05.006.
[37] Aydin G. The Modeling of Coal-related $CO_2$ Emissions and Projections into Future Planning. Energy Sources, Part A: Recovery, Utilization, and Environmental Effects 2014;36:2:191–201. https://doi.org/10.1080/15567036.2012.760018.
[38] Baena-Moreno FM, Rodríguez-Galán M, Vega F, Alonso-Fariñas B, Vilches Arenas LF, Navarrete B. Carbon capture and utilization technologies: a literature review and recent advances. Energy Sources, Part A: Recovery, Utilization, and Environmental Effects 2019;41:1403–33. https://doi.org/10.1080/15567036.2018.1548518.
[39] IEA. Net Zero Roadmap: A Global Pathway to Keep the 1.5 °C Goal in Reach. Paris, France: IEA; 2023.
[40] Dubey A, Arora A. Advancements in carbon capture technologies: A review. Journal of Cleaner Production 2022;373:133932. https://doi.org/10.1016/j.jclepro.2022.133932.
[41] Global CCS Institute. Technology Readiness and Costs of CCS. Global CCS Institute; 2021.
[42] IPCC. IPCC Special Report on Carbon Dioxide Capture and Storage. Cambridge, UK and New York, NY, USA: Cambridge University Press; 2005.
[43] Pires JCM, Martins FG, Alvim-Ferraz MCM, Simões M. Recent developments on carbon capture and storage: An overview. Chemical Engineering Research and Design 2011;89:1446–60. https://doi.org/10.1016/j.cherd.2011.01.028.

[44] Jansen D, Gazzani M, Manzolini G, Dijk E van, Carbo M. Pre-combustion $CO_2$ capture. International Journal of Greenhouse Gas Control 2015;40:167–87. https://doi.org/10.1016/j.ijggc.2015.05.028.
[45] IEAGHG. $CO_2$ Capture at Coal-Based Power and Hydrogen Plants. 2014.
[46] Dziejarski B, Krzyżyńska R, Andersson K. Current status of carbon capture, utilization, and storage technologies in the global economy: A survey of technical assessment. Fuel 2023;342:127776. https://doi.org/10.1016/j.fuel.2023.127776.
[47] Olajire AA. $CO_2$ capture and separation technologies for end-of-pipe applications – A review. Energy 2010;35:2610–28. https://doi.org/10.1016/j.energy.2010.02.030.
[48] Jiang L, Gonzalez-Diaz A, Ling-Chin J, Roskilly AP, Smallbone AJ. Post-combustion $CO_2$ capture from a natural gas combined cycle power plant using activated carbon adsorption. Applied Energy 2019;245:1–15. https://doi.org/10.1016/j.apenergy.2019.04.006.
[49] Osman AI, Hefny M, Abdel Maksoud MIA, Elgarahy AM, Rooney DW. Recent advances in carbon capture storage and utilisation technologies: a review. Environ Chem Lett 2021;19:797–849. https://doi.org/10.1007/s10311-020-01133-3.
[50] Wu X, Wang M, Liao P, Shen J, Li Y. Solvent-based post-combustion $CO_2$ capture for power plants: A critical review and perspective on dynamic modelling, system identification, process control and flexible operation. Applied Energy 2020;257:113941. https://doi.org/10.1016/j.apenergy.2019.113941.
[51] Talei S, Fozer D, Varbanov PS, Szanyi A, Mizsey P. Oxyfuel Combustion Makes Carbon Capture More Efficient. ACS Omega 2024;9:3250–61. https://doi.org/10.1021/acsomega.3c05034.
[52] Yuan Y, Wang L, Zhuang Y, Wu Y, Bi X. Energy and Economic Assessment of Oxy-Fuel Combustion CO2 Capture in Coal-Fired Power Plants. Energies 2024;17:4626. https://doi.org/10.3390/en17184626.
[53] Zhu D, Eason JP, Biegler LT. Energy-efficient CO2 liquefaction for oxy-combustion power plant with ASU-CPU integration enhanced by cascaded sub-ambient energy utilization and waste heat recovery. International Journal of Greenhouse Gas Control 2017;61:124–37. https://doi.org/10.1016/j.ijggc.2017.03.023.
[54] Yadav S, Mondal SS. A review on the progress and prospects of oxy-fuel carbon capture and sequestration (CCS) technology. Fuel 2022;308:122057. https://doi.org/10.1016/j.fuel.2021.122057.
[55] Batra VS, Li H-P. Oxygen carrier materials and their role in chemical looping reactions for fuel conversion. Current Opinion in Chemical Engineering 2017;15:44–8. https://doi.org/10.1016/j.coche.2016.11.006.
[56] Zhao H, Tian X, Ma J, Su M, Wang B, Mei D. Development of tailor-made oxygen carriers and reactors for chemical looping processes at Huazhong University of Science & Technology. International Journal of Greenhouse Gas Control 2020;93:102898. https://doi.org/10.1016/j.ijggc.2019.102898.
[57] Zhang Y, Han H, Zhu N, Che Y, Zhang X, Xue Y, et al. Chemical Looping Combustion for Coupling with Efficient CO2 Capture and Utilization: Stable Oxygen Carriers and Carbon Cycle. Ind Eng Chem Res 2025;64:1933–67. https://doi.org/10.1021/acs.iecr.4c03713.

[58] Adanez J, Abad A, Garcia-Labiano F, Gayan P, de Diego LF. Progress in Chemical-Looping Combustion and Reforming technologies. Progress in Energy and Combustion Science 2012;38:215–82. https://doi.org/10.1016/j.pecs.2011.09.001.
[59] Alalwan HA, Alminshid AH. CO2 capturing methods: Chemical looping combustion (CLC) as a promising technique. Science of The Total Environment 2021;788:147850. https://doi.org/10.1016/j.scitotenv.2021.147850.
[60] Sodiq A, Abdullatif Y, Aissa B, Ostovar A, Nassar N, El-Naas M, et al. A review on progress made in direct air capture of $CO_2$. Environmental Technology & Innovation 2023;29:102991. https://doi.org/10.1016/j.eti.2022.102991.
[61] Jiang L, Liu W, Wang RQ, Gonzalez-Diaz A, Rojas-Michaga MF, Michailos S, et al. Sorption direct air capture with CO2 utilization. Progress in Energy and Combustion Science 2023;95:101069. https://doi.org/10.1016/j.pecs.2022.101069.
[62] Breyer C, Fasihi M, Bajamundi C, Creutzig F. Direct Air Capture of CO2: A Key Technology for Ambitious Climate Change Mitigation. Joule 2019;3:2053–7. https://doi.org/10.1016/j.joule.2019.08.010.
[63] IEA. Direct Air Capture 2022. Paris, France: IEA; 2022.
[64] Perpiñán J, Peña B, Bailera M, Eveloy V, Kannan P, Raj A, et al. Integration of carbon capture technologies in blast furnace based steel making: A comprehensive and systematic review. Fuel 2023;336:127074. https://doi.org/10.1016/j.fuel.2022.127074.
[65] Global CCS Institute. State of the Art: CCS Technologies 2025. Global CCS Institute; 2025.
[66] Du J, Yang W, Xu L, Bei L, Lei S, Li W, et al. Review on post-combustion CO2 capture by amine blended solvents and aqueous ammonia. Chemical Engineering Journal 2024;488:150954. https://doi.org/10.1016/j.cej.2024.150954.
[67] Samanta A, Zhao A, Shimizu GKH, Sarkar P, Gupta R. Post-Combustion CO2 Capture Using Solid Sorbents: A Review. Ind Eng Chem Res 2012;51:1438–63. https://doi.org/10.1021/ie200686q.
[68] Choi S, Drese JH, Jones CW. Adsorbent Materials for Carbon Dioxide Capture from Large Anthropogenic Point Sources. ChemSusChem 2009;2:796–854. https://doi.org/10.1002/cssc.200900036.
[69] Li J-R, Kuppler RJ, Zhou H-C. Selective gas adsorption and separation in metal–organic frameworks. Chem Soc Rev 2009;38:1477–504. https://doi.org/10.1039/B802426J.
[70] Zhang Y, Sunarso J, Liu S, Wang R. Current status and development of membranes for CO2/CH4 separation: A review. International Journal of Greenhouse Gas Control 2013;12:84–107. https://doi.org/10.1016/j.ijggc.2012.10.009.
[71] Hack J, Maeda N, Meier DM. Review on CO2 Capture Using Amine-Functionalized Materials. ACS Omega 2022;7:39520–30. https://doi.org/10.1021/acsomega.2c03385.
[72] Sumida K, Rogow DL, Mason JA, McDonald TM, Bloch ED, Herm ZR, et al. Carbon Dioxide Capture in Metal–Organic Frameworks. Chem Rev 2012;112:724–81. https://doi.org/10.1021/cr2003272.
[73] Dai Z, Noble RD, Gin DL, Zhang X, Deng L. Combination of ionic liquids with membrane technology: A new approach for CO2 separation. Journal of

Membrane Science 2016;497:1–20. https://doi.org/10.1016/j.memsci.2015.08.060.
[74] Strathmann H. Membrane Separation Processes, 1. Principles. Ullmann's Encyclopedia of Industrial Chemistry, John Wiley & Sons, Ltd; 2011. https://doi.org/10.1002/14356007.a16_187.pub3.
[75] Carbon Dioxide Separation from Flue Gases: A Technological Review Emphasizing Reduction in Greenhouse Gas Emissions - Songolzadeh - 2014 - The Scientific World Journal - Wiley Online Library n.d. https://onlinelibrary.wiley.com/doi/full/10.1155/2014/828131 (accessed December 12, 2025).
[76] Scholes CA. Thermally Rearranged Poly(benzoxazole) Copolymer Membranes for Improved Gas Separation: A Review. Aust J Chem 2016;69:601–11. https://doi.org/10.1071/CH15523.
[77] Mondal MK, Balsora HK, Varshney P. Progress and trends in CO2 capture/separation technologies: A review. Energy 2012;46:431–41. https://doi.org/10.1016/j.energy.2012.08.006.
[78] Norahim N, Yaisanga P, Faungnawakij K, Charinpanitkul T, Klaysom C. Recent Membrane Developments for CO2 Separation and Capture. Chemical Engineering & Technology 2018;41:211–23. https://doi.org/10.1002/ceat.201700406.
[79] Xu J, Wu H, Wang Z, Qiao Z, Zhao S, Wang J. Recent advances on the membrane processes for CO2 separation. Chinese Journal of Chemical Engineering 2018;26:2280–91. https://doi.org/10.1016/j.cjche.2018.08.020.
[80] Gayathri R, Mahboob S, Govindarajan M, Al-Ghanim KA, Ahmed Z, Al-Mulhm N, et al. A review on biological carbon sequestration: A sustainable solution for a cleaner air environment, less pollution and lower health risks. Journal of King Saud University - Science 2021;33:101282. https://doi.org/10.1016/j.jksus.2020.101282.
[81] Liang X, Duan Y, Su Y, Chen J, Zhang M, Ye X, et al. Carbon capture by biological methods. Cambridge Prisms: Carbon Technologies 2025;1:e4. https://doi.org/10.1017/cat.2025.10005.
[82] Wang B, Li Y, Wu N, Lan CQ. CO2 bio-mitigation using microalgae. Appl Microbiol Biotechnol 2008;79:707–18. https://doi.org/10.1007/s00253-008-1518-y.
[83] Zhang S, Liu Z. Advances in the biological fixation of carbon dioxide by microalgae. Journal of Chemical Technology & Biotechnology 2021;96:1475–95. https://doi.org/10.1002/jctb.6714.
[84] Cheah WY, Show PL, Chang J-S, Ling TC, Juan JC. Biosequestration of atmospheric CO2 and flue gas-containing CO2 by microalgae. Bioresource Technology 2015;184:190–201. https://doi.org/10.1016/j.biortech.2014.11.026.
[85] Zhao B, Su Y. Process effect of microalgal-carbon dioxide fixation and biomass production: A review. Renewable and Sustainable Energy Reviews 2014;31:121–32. https://doi.org/10.1016/j.rser.2013.11.054.
[86] Khan MI, Shin JH, Kim JD. The promising future of microalgae: current status, challenges, and optimization of a sustainable and renewable industry for biofuels, feed, and other products. Microb Cell Fact 2018;17:36. https://doi.org/10.1186/s12934-018-0879-x.

[87] Tsai DD-W, Chen PH, Ramaraj R. The potential of carbon dioxide capture and sequestration with algae. Ecological Engineering 2017;98:17–23. https://doi.org/10.1016/j.ecoleng.2016.10.049.
[88] Acién FG, Fernández JM, Magán JJ, Molina E. Production cost of a real microalgae production plant and strategies to reduce it. Biotechnology Advances 2012;30:1344–53. https://doi.org/10.1016/j.biotechadv.2012.02.005.
[89] Natsi PD, Koutsoukos PG. Calcium Carbonate Mineralization of Microalgae. Biomimetics 2022;7:140. https://doi.org/10.3390/biomimetics7040140.
[90] Brunetti A, Scura F, Barbieri G, Drioli E. Membrane technologies for CO2 separation. Journal of Membrane Science 2010;359:115–25. https://doi.org/10.1016/j.memsci.2009.11.040.
[91] Xu G, Liang F, Yang Y, Hu Y, Zhang K, Liu W. An Improved CO2 Separation and Purification System Based on Cryogenic Separation and Distillation Theory. Energies 2014;7:3484–502. https://doi.org/10.3390/en7053484.
[92] Font-Palma C, Cann D, Udemu C. Review of Cryogenic Carbon Capture Innovations and Their Potential Applications. C 2021;7:58. https://doi.org/10.3390/c7030058.
[93] Simonsen KR, Hansen DS, Pedersen S. Challenges in CO2 transportation: Trends and perspectives. Renewable and Sustainable Energy Reviews 2024;191:114149. https://doi.org/10.1016/j.rser.2023.114149.
[94] Lu H, Ma X, Huang K, Fu L, Azimi M. Carbon dioxide transport via pipelines: A systematic review. Journal of Cleaner Production 2020;266:121994. https://doi.org/10.1016/j.jclepro.2020.121994.
[95] Gür TM. Carbon Dioxide Emissions, Capture, Storage and Utilization: Review of Materials, Processes and Technologies. Progress in Energy and Combustion Science 2022;89:100965. https://doi.org/10.1016/j.pecs.2021.100965.
[96] Li Y, Wang W, Chen Z-F, Li Y-X. Integrity assessment of supercritical CO2 transport pipelines. Geoenergy Science and Engineering 2023;221:211355. https://doi.org/10.1016/j.geoen.2022.211355.
[97] Wang G, Cheng Q, Zhao W, Liao Q, Zhang H. Review on the transport capacity management of oil and gas pipeline network: Challenges and opportunities of future pipeline transport. Energy Strategy Reviews 2022;43:100933. https://doi.org/10.1016/j.esr.2022.100933.
[98] Onyebuchi VE, Kolios A, Hanak DP, Biliyok C, Manovic V. A systematic review of key challenges of CO2 transport via pipelines. Renewable and Sustainable Energy Reviews 2018;81:2563–83. https://doi.org/10.1016/j.rser.2017.06.064.
[99] Vitali M, Corvaro F, Marchetti B, Terenzi A. Thermodynamic challenges for CO2 pipelines design: A critical review on the effects of impurities, water content, and low temperature. International Journal of Greenhouse Gas Control 2022;114:103605. https://doi.org/10.1016/j.ijggc.2022.103605.
[100] Al Baroudi H, Awoyomi A, Patchigolla K, Jonnalagadda K, Anthony EJ. A review of large-scale CO2 shipping and marine emissions management for carbon capture, utilisation and storage. Applied Energy 2021;287:116510. https://doi.org/10.1016/j.apenergy.2021.116510.

[101] Weihs GAF, Kumar K, Wiley DE. Understanding the Economic Feasibility of Ship Transport of CO2 within the CCS Chain. Energy Procedia 2014;63:2630–7. https://doi.org/10.1016/j.egypro.2014.11.285.
[102] Patchigolla K, Oakey JE. Design Overview of High Pressure Dense Phase CO2 Pipeline Transport in Flow Mode. Energy Procedia 2013;37:3123–30. https://doi.org/10.1016/j.egypro.2013.06.198.
[103] IEAGHG. Impact of Impurities on $CO_2$ Capture, Transport and Storage. IEAGHG; 2024.
[104] Wetenhall B, Aghajani H, Chalmers H, Benson SD, Ferrari M-C, Li J, et al. Impact of CO2 impurity on CO2 compression, liquefaction and transportation. Energy Procedia 2014;63:2764–78. https://doi.org/10.1016/j.egypro.2014.11.299.
[105] European Technology Platform for Zero Emission Fossil Fuel Power Plants. The Costs of $CO_2$ Transport. Zero Emissions Platform (ZEP); 2011.
[106] Offshore CO2 storage: Sleipner natural gas field beneath the North Sea. Geological Storage of Carbon Dioxide (CO2), Woodhead Publishing; 2013, p. 227–253e. https://doi.org/10.1533/9780857097279.3.227.
[107] Marchetti C. On geoengineering and the CO2 problem. Climatic Change 1977;1:59–68. https://doi.org/10.1007/BF00162777.
[108] IEA. CO2 storage resources and their development. Paris, France: IEA; 2022.
[109] Lau HC, Ramakrishna S, Zhang K, Radhamani AV. The Role of Carbon Capture and Storage in the Energy Transition. Energy Fuels 2021;35:7364–86. https://doi.org/10.1021/acs.energyfuels.1c00032.
[110] De Silva GPD, Ranjith PG, Perera MSA. Geochemical aspects of CO2 sequestration in deep saline aquifers: A review. Fuel 2015;155:128–43. https://doi.org/10.1016/j.fuel.2015.03.045.
[111] Celia MA, Bachu S, Nordbotten JM, Bandilla KW. Status of CO2 storage in deep saline aquifers with emphasis on modeling approaches and practical simulations. Water Resources Research 2015;51:6846–92. https://doi.org/10.1002/2015WR017609.
[112] Ringrose PS, Furre A-K, Gilfillan SMV, Krevor S, Landrø M, Leslie R, et al. Storage of Carbon Dioxide in Saline Aquifers: Physicochemical Processes, Key Constraints, and Scale-Up Potential. Annual Review of Chemical and Biomolecular Engineering 2021;12:471–94. https://doi.org/10.1146/annurev-chembioeng-093020-091447.
[113] Li Z, Dong M, Li S, Huang S. CO2 sequestration in depleted oil and gas reservoirs—caprock characterization and storage capacity. Energy Conversion and Management 2006;47:1372–82. https://doi.org/10.1016/j.enconman.2005.08.023.
[114] Agartan E, Gaddipati M, Yip Y, Savage B, Ozgen C. CO2 storage in depleted oil and gas fields in the Gulf of Mexico. International Journal of Greenhouse Gas Control 2018;72:38–48. https://doi.org/10.1016/j.ijggc.2018.02.022.
[115] IEA. Can CO2-EOR really provide carbon-negative oil? Paris, France: IEA; 2019.
[116] Bashir A, Ali M, Patil S, Aljawad MS, Mahmoud M, Al-Shehri D, et al. Comprehensive review of CO2 geological storage: Exploring principles, mechanisms, and prospects. Earth-Science Reviews 2024;249:104672. https://doi.org/10.1016/j.earscirev.2023.104672.

[117] Chadwick A, Williams G, Delepine N, Clochard V, Labat K, Sturton S, et al. Quantitative analysis of time-lapse seismic monitoring data at the Sleipner CO2 storage operation. The Leading Edge 2010;29:170–7. https://doi.org/10.1190/1.3304820.
[118] Furre AK, Warchoł MJ, Alnes H, Pontén ASM. Sleipner 26 years: how well-established subsurface monitoring work processes have contributed to successful offshore $CO_2$ injection. Geoenergy 2024;2:geoenergy2024-015. https://doi.org/10.1144/geoenergy2024-015.
[119] Maldal T, Tappel IM. CO2 underground storage for Snøhvit gas field development. Energy 2004;29:1403–11. https://doi.org/10.1016/j.energy.2004.03.074.
[120] Global CCS Institute. Global Status of CCS 2024 - Collaborating for a net-zero future. Global CCS Institute; 2024.
[121] Bois von Kursk O, Roth J, Junqueira Fujii R, Schiavo C, Hurtado Verazaín L, Erhan E. Brazil at a Crossroads: Rethinking Petrobras oil and gas expansion. International Institute for Sustainable Development (IISD); 2025.
[122] Robertson B, Mousavian M. Carbon Capture to Serve Enhanced Oil Recovery: Overpromise and Underperformance. Institute for Energy Economics and Financial Analysis (IEEFA); 2022.
[123] Alam MMM, Hassan A, Mahmoud M, Sibaweihi N, Patil S. Dual Benefits of Enhanced Oil Recovery and CO2 Sequestration: The Impact of CO2 Injection Approach on Oil Recovery. Front Energy Res 2022;10. https://doi.org/10.3389/fenrg.2022.877212.
[124] IEA. Storing CO2 through Enhanced Oil Recovery. Paris, France: IEA; 2015.
[125] Burnison SA, Bosshart NW, Salako O, Reed S, Hamling JA, Gorecki CD. 4-D Seismic Monitoring of Injected CO2 Enhances Geological Interpretation, Reservoir Simulation, and Production Operations. Energy Procedia 2017;114:2748–59. https://doi.org/10.1016/j.egypro.2017.03.1539.
[126] Institute for Energy Economics and Financial Analysis (IEEFA). Boundary Dam 3 Coal Plant Achieves $CO_2$ Capture Goal Two Years Late. IEEFA; 2021.
[127] Institute for Energy Economics and Financial Analysis (IEEFA). Norway's Sleipner and Snøhvit CCS — Industry models or cautionary tales. Institute for Energy Economics and Financial Analysis (IEEFA); 2023.
[128] Martinez CG, Tumara D, Mountraki A, Letout S, Jaxa-Rozen M, Schmitz A, et al. Clean Energy Technology Observatory: Carbon Capture, Utilisation and Storage in the European Union - 2025 Status Report on Technology Development, Trends, Value Chains and Markets. JRC Publications Repository 2025. https://doi.org/10.2760/0214409.
[129] Duan H-B, Fan Y, Zhu L. What's the most cost-effective policy of CO2 targeted reduction: An application of aggregated economic technological model with CCS? Applied Energy 2013;112:866–75. https://doi.org/10.1016/j.apenergy.2013.01.047.
[130] Bruhn T, Naims H, Olfe-Kräutlein B. Separating the debate on CO2 utilisation from carbon capture and storage. Environmental Science & Policy 2016;60:38–43. https://doi.org/10.1016/j.envsci.2016.03.001.

[131] Koytsoumpa EI, Bergins C, Kakaras E. The CO2 economy: Review of CO2 capture and reuse technologies. The Journal of Supercritical Fluids 2018;132:3–16. https://doi.org/10.1016/j.supflu.2017.07.029.
[132] Mac Dowell N, Fennell PS, Shah N, Maitland GC. The role of CO2 capture and utilization in mitigating climate change. Nature Clim Change 2017;7:243–9. https://doi.org/10.1038/nclimate3231.
[133] Sanna A, Uibu M, Caramanna G, Kuusik R, Maroto-Valer MM. A review of mineral carbonation technologies to sequester CO2. Chem Soc Rev 2014;43:8049–80. https://doi.org/10.1039/C4CS00035H.
[134] von der Assen N, Müller LJ, Steingrube A, Voll P, Bardow A. Selecting CO2 Sources for CO2 Utilization by Environmental-Merit-Order Curves. Environ Sci Technol 2016;50:1093–101. https://doi.org/10.1021/acs.est.5b03474.
[135] Bui M, Adjiman CS, Bardow A, Anthony EJ, Boston A, Brown S, et al. Carbon capture and storage (CCS): the way forward. Energy Environ Sci 2018;11:1062–176. https://doi.org/10.1039/C7EE02342A.
[136] Langanke J, Wolf A, Hofmann J, Böhm K, Subhani MA, Müller TE, et al. Carbon dioxide (CO2) as sustainable feedstock for polyurethane production. Green Chem 2014;16:1865–70. https://doi.org/10.1039/C3GC41788C.
[137] Aresta M, Dibenedetto A, Angelini A. Catalysis for the Valorization of Exhaust Carbon: from CO2 to Chemicals, Materials, and Fuels. Technological Use of CO2. Chem Rev 2014;114:1709–42. https://doi.org/10.1021/cr4002758.
[138] van der Giesen C, Kleijn R, Kramer GJ. Energy and climate impacts of producing synthetic hydrocarbon fuels from CO(2). Environ Sci Technol 2014;48:7111–21. https://doi.org/10.1021/es500191g.
[139] Aldaco R, Butnar I, Margallo M, Laso J, Rumayor M, Dominguez-Ramos A, et al. Bringing value to the chemical industry from capture, storage and use of CO2: A dynamic LCA of formic acid production. Science of The Total Environment 2019;663:738–53. https://doi.org/10.1016/j.scitotenv.2019.01.395.
[140] IEAGHG. $CO_2$ as a Feedstock: Comparison of CCU Pathways. 2021.
[141] Gabrielli P, Gazzani M, Mazzotti M. The Role of Carbon Capture and Utilization, Carbon Capture and Storage, and Biomass to Enable a Net-Zero-CO2 Emissions Chemical Industry. Industrial and Engineering Chemistry Research 2020;59:7033–45. https://doi.org/10.1021/acs.iecr.9b06579.
[142] Husain Patel G, Havukainen J, Horttanainen M, Soukka R, Tuomaala M. Climate change performance of hydrogen production based on life cycle assessment. Green Chem 2024;26:992. https://doi.org/10.1039/D3GC02410E.
[143] IEAGHG. Low-Carbon Hydrogen from Natural Gas: Global Roadmap. 2022.
[144] IEA. Global Hydrogen Review 2025. Paris, France: IEA; 2025.
[145] European Hydrogen Observatory. Cost of hydrogen production. European Hydrogen Observatory n.d. https://observatory.clean-hydrogen.europa.eu/hydrogen-landscape/production-trade-and-cost/cost-hydrogen-production (accessed January 8, 2026).

[146] Milligan M, Bird L, Lew D. Integrating Variable Renewable Energy: Challenges and Solutions 2013:14. https://doi.org/10.2172/1097911.
[147] IRENA. Green Hydrogen Cost Reduction: Scaling up Electrolysers to Meet the $1.5^0$C Climate Goal. Abu Dhabi: International Renewable Energy Agency; 2020.
[148] Matthes FC, Brauer J. Hydrogen production costs. Öko-Institut e.V.; 2025.
[149] Badger N, Amini S. Comparative life cycle assessment of various hydrogen pathways for cleaner methanol synthesis. Journal of Cleaner Production 2025;533:146993. https://doi.org/10.1016/j.jclepro.2025.146993.
[150] Sollai S, Porcu A, Tola V, Ferrara F, Pettinau A. Renewable methanol production from green hydrogen and captured CO2: A techno-economic assessment. Journal of CO2 Utilization 2023;68:102345. https://doi.org/10.1016/j.jcou.2022.102345.
[151] IRENA, METHANOL INSTITUTE. Innovation Outlook : Renewable Methanol. Abu Dhabi: International Renewable Energy Agency; 2021.
[152] Kamkeng ADN, Wang M, Hu J, Du W, Qian F. Transformation technologies for CO2 utilisation: Current status, challenges and future prospects. Chemical Engineering Journal 2021;409:128138. https://doi.org/10.1016/j.cej.2020.128138.
[153] Valluri S, Claremboux V, Kawatra S. Opportunities and challenges in CO2 utilization. Journal of Environmental Sciences 2022;113:322–44. https://doi.org/10.1016/j.jes.2021.05.043.
[154] Muthuraj R, Mekonnen T. Recent progress in carbon dioxide (CO2) as feedstock for sustainable materials development: Co-polymers and polymer blends. Polymer 2018;145:348–73. https://doi.org/10.1016/j.polymer.2018.04.078.
[155] Peres CB, Resende PMR, Nunes LJR, Morais LC de, Peres CB, Resende PMR, et al. Advances in Carbon Capture and Use (CCU) Technologies: A Comprehensive Review and CO2 Mitigation Potential Analysis. Clean Technologies 2022;4:1193–207. https://doi.org/10.3390/cleantechnol4040073.
[156] IEA. CCUS Projects Database. Paris, France: IEA; n.d.
[157] Koytsoumpa EI, Bergins C, Kakaras E. The CO2 economy: Review of CO2 capture and reuse technologies. The Journal of Supercritical Fluids 2018;132:3–16. https://doi.org/10.1016/j.supflu.2017.07.029.
[158] $CO_2$ Value Europe. $CO_2$ Value Europe n.d. https://database.co2value.eu/ (accessed January 7, 2026).
[159] Chauvy R, De Weireld G. CO2 Utilization Technologies in Europe: A Short Review. Energy Technology 2020;8:2000627. https://doi.org/10.1002/ente.202000627.
[160] Chauvy R, Meunier N, Thomas D, De Weireld G. Selecting emerging CO2 utilization products for short- to mid-term deployment. Applied Energy 2019;236:662–80. https://doi.org/10.1016/j.apenergy.2018.11.096.
[161] Dziejarski B, Krzyżyńska R, Andersson K. Current status of carbon capture, utilization, and storage technologies in the global economy: A survey of technical assessment. Fuel 2023;342:127776. https://doi.org/10.1016/j.fuel.2023.127776.
[162] Jarvis SM, Samsatli S. Technologies and infrastructures underpinning future CO2 value chains: A comprehensive review and comparative analysis. Renewable and Sustainable Energy Reviews 2018;85:46–68. https://doi.org/10.1016/j.rser.2018.01.007.

[163] Otto A, Grube T, Schiebahn S, Stolten D. Closing the loop: captured CO2 as a feedstock in the chemical industry. Energy Environ Sci 2015;8:3283–97. https://doi.org/10.1039/C5EE02591E.
[164] Lehner M, Tichler R, Steinmüller H, Koppe M. Power-to-Gas: Technology and Business Models. Cham: Springer International Publishing; 2014. https://doi.org/10.1007/978-3-319-03995-4.
[165] Hossain Bhuiyan MM, Siddique Z. Hydrogen as an alternative fuel: A comprehensive review of challenges and opportunities in production, storage, and transportation. International Journal of Hydrogen Energy 2025;102:1026–44. https://doi.org/10.1016/j.ijhydene.2025.01.033.
[166] Mazloomi K, Gomes C. Hydrogen as an energy carrier: Prospects and challenges. Renewable and Sustainable Energy Reviews 2012;16:3024–33. https://doi.org/10.1016/j.rser.2012.02.028.
[167] Akpasi SO, Smarte Anekwe IM, Tetteh EK, Amune UO, Mustapha SI, Kiambi SL. Hydrogen as a clean energy carrier: advancements, challenges, and its role in a sustainable energy future. Clean En 2025;9:52–88. https://doi.org/10.1093/ce/zkae112.
[168] Li W, Wang H, Jiang X, Zhu J, Liu Z, Guo X, et al. A short review of recent advances in CO 2 hydrogenation to hydrocarbons over heterogeneous catalysts. RSC Advances 2018;8:7651–69. https://doi.org/10.1039/C7RA13546G.
[169] Ye R-P, Ding J, Gong W, Argyle MD, Zhong Q, Wang Y, et al. CO2 hydrogenation to high-value products via heterogeneous catalysis. Nat Commun 2019;10:5698. https://doi.org/10.1038/s41467-019-13638-9.
[170] Ronda-Lloret M, Rothenberg G, Shiju NR. A Critical Look at Direct Catalytic Hydrogenation of Carbon Dioxide to Olefins. ChemSusChem 2019;12:3896–914. https://doi.org/10.1002/cssc.201900915.
[171] Blanco H, Nijs W, Ruf J, Faaij A. Potential of Power-to-Methane in the EU energy transition to a low carbon system using cost optimization. Applied Energy 2018;232:323–40. https://doi.org/10.1016/j.apenergy.2018.08.027.
[172] Tommasi M, Degerli SN, Ramis G, Rossetti I. Advancements in CO2 methanation: A comprehensive review of catalysis, reactor design and process optimization. Chemical Engineering Research and Design 2024;201:457–82. https://doi.org/10.1016/j.cherd.2023.11.060.
[173] Duyar MS, Treviño MAA, Farrauto RJ. Dual function materials for CO2 capture and conversion using renewable H2. Applied Catalysis B: Environmental 2015;168–169:370–6. https://doi.org/10.1016/j.apcatb.2014.12.025.
[174] Liu G, Sun S, Sun H, Zhang Y, Lv J, Wang Y, et al. Integrated CO2 capture and utilisation: A promising step contributing to carbon neutrality. Carbon Capture Science & Technology 2023;7:100116. https://doi.org/10.1016/j.ccst.2023.100116.
[175] Sun H, Wang J, Zhao J, Shen B, Shi J, Huang J, et al. Dual functional catalytic materials of Ni over Ce-modified CaO sorbents for integrated CO2 capture and conversion. Applied Catalysis B: Environmental 2019;244:63–75. https://doi.org/10.1016/j.apcatb.2018.11.040.
[176] Marocco Stuardi F, MacPherson F, Leclaire J. Integrated CO2 capture and utilization: A priority research direction. Current Opinion in Green and Sustainable Chemistry 2019;16:71–6. https://doi.org/10.1016/j.cogsc.2019.02.003.

[177] Chen J, Xu Y, Liao P, Wang H, Zhou H. Recent Progress in Integrated CO2 Capture and Conversion Process Using Dual Function Materials: A State-of-the-Art Review. Carbon Capture Science & Technology 2022;4:100052. https://doi.org/10.1016/j.ccst.2022.100052.
[178] Iyer SS, Bajaj I, Balasubramanian P, Hasan MMF. Integrated Carbon Capture and Conversion To Produce Syngas: Novel Process Design, Intensification, and Optimization. Ind Eng Chem Res 2017;56:8622–48. https://doi.org/10.1021/acs.iecr.7b01688.
[179] Qiao Y, Liu W, Guo R, Sun S, Zhang S, Bailey JJ, et al. Techno-economic analysis of integrated carbon capture and utilisation compared with carbon capture and utilisation with syngas production. Fuel 2023;332:125972. https://doi.org/10.1016/j.fuel.2022.125972.
[180] Lu B, Fan Y, Zhi X, Han Z, Wu F, Li X, et al. Material design and prospect of dual-functional materials for integrated carbon dioxide capture and conversion. Carbon Capture Science & Technology 2024;12:100207. https://doi.org/10.1016/j.ccst.2024.100207.
[181] Sabri MA, Al Jitan S, Bahamon D, Vega LF, Palmisano G. Current and future perspectives on catalytic-based integrated carbon capture and utilization. Science of The Total Environment 2021;790:148081. https://doi.org/10.1016/j.scitotenv.2021.148081.
[182] Lv Z, Chen S, Huang X, Qin C. Recent progress and perspective on integrated CO2 capture and utilization. Current Opinion in Green and Sustainable Chemistry 2023;40:100771. https://doi.org/10.1016/j.cogsc.2023.100771.
[183] Panzone C, Philippe R, Chappaz A, Fongarland P, Bengaouer A. Power-to-Liquid catalytic CO2 valorization into fuels and chemicals: focus on the Fischer-Tropsch route. Journal of CO2 Utilization 2020;38:314–47. https://doi.org/10.1016/j.jcou.2020.02.009.
[184] Zang G, Sun P, Elgowainy AA, Bafana A, Wang M. Performance and cost analysis of liquid fuel production from H2 and CO2 based on the Fischer-Tropsch process. Journal of CO2 Utilization 2021;46:101459. https://doi.org/10.1016/j.jcou.2021.101459.
[185] Blanco H, Nijs W, Ruf J, Faaij A. Potential for hydrogen and Power-to-Liquid in a low-carbon EU energy system using cost optimization. Applied Energy 2018;232:617–39. https://doi.org/10.1016/j.apenergy.2018.09.216.
[186] Aurud P, Srifa A, Koo-Amornpattana W, Assabumrungrat S, Wongsakulphasatch S, Fukuhara C, et al. The improvement of heat transfer using Co/SiO2 spiral structured catalyst for green diesel production by Fischer–Tropsch synthesis. Sci Rep 2024;14:19782. https://doi.org/10.1038/s41598-024-70503-6.
[187] Zhang C, Jun K-W, Kwak G, Lee Y-J, Park H-G. Efficient utilization of carbon dioxide in a gas-to-methanol process composed of CO2/steam–mixed reforming and methanol synthesis. Journal of CO2 Utilization 2016;16:1–7. https://doi.org/10.1016/j.jcou.2016.05.005.
[188] König DH, Freiberg M, Dietrich R-U, Wörner A. Techno-economic study of the storage of fluctuating renewable energy in liquid hydrocarbons. Fuel 2015;159:289–97. https://doi.org/10.1016/j.fuel.2015.06.085.
[189] Varone A, Ferrari M. Power to liquid and power to gas: An option for the German *Energiewende*. Renewable and Sustainable Energy Reviews 2015;45:207–18. https://doi.org/10.1016/j.rser.2015.01.049.

[190] Fasihi M, Bogdanov D, Breyer C. Techno-Economic Assessment of Power-to-Liquids (PtL) Fuels Production and Global Trading Based on Hybrid PV-Wind Power Plants. Energy Procedia 2016;99:243–68. https://doi.org/10.1016/j.egypro.2016.10.115.
[191] Dieterich V, Buttler A, Hanel A, Spliethoff H, Fendt S. Power-to-liquid via synthesis of methanol, DME or Fischer–Tropsch-fuels: a review. Energy & Environmental Science 2020;13:3207–52. https://doi.org/10.1039/D0EE01187H.
[192] Martìnez I. Fuel properties n.d.
[193] Villora-Picó JJ, González-Arias J, Pastor-Pérez L, Odriozola JA, Reina TR. A review on high-pressure heterogeneous catalytic processes for gas-phase CO2 valorization. Environmental Research 2024;240:117520. https://doi.org/10.1016/j.envres.2023.117520.
[194] Torres-Sempere G, Pastor-Perez L, Odriozola JA, Yu J, Duran-Olivencia FJ, Bobadilla LF, et al. Recent advances on gas-phase CO2 conversion: Catalysis design and chemical processes to close the carbon cycle. Current Opinion in Green and Sustainable Chemistry 2022;36:100647. https://doi.org/10.1016/j.cogsc.2022.100647.
[195] Murena F, Esposito S, Deorsola FA, Galletti C, Prati MV. CO2 abatement and CH4 recovery at vehicle exhausts: Comparison and characterization of Ru powder and pellet catalysts. International Journal of Hydrogen Energy 2020;45:8640–8. https://doi.org/10.1016/j.ijhydene.2020.01.120.
[196] Estevez R, Aguado-Deblas L, Bautista FM, López-Tenllado FJ, Romero AA, Luna D, et al. A Review on Green Hydrogen Valorization by Heterogeneous Catalytic Hydrogenation of Captured CO2 into Value-Added Products. Catalysts 2022;12. https://doi.org/10.3390/catal12121555.
[197] Rönsch S, Schneider J, Matthischke S, Schlüter M, Götz M, Lefebvre J, et al. Review on methanation – From fundamentals to current projects. Fuel 2016;166:276–96. https://doi.org/10.1016/j.fuel.2015.10.111.
[198] Younas M, Loong Kong L, Bashir MJK, Nadeem H, Shehzad A, Sethupathi S. Recent Advancements, Fundamental Challenges, and Opportunities in Catalytic Methanation of CO2. Energy Fuels 2016;30:8815–31. https://doi.org/10.1021/acs.energyfuels.6b01723.
[199] Rostrup-Nielsen JR, Pedersen K, Sehested J. High temperature methanation: Sintering and structure sensitivity. Applied Catalysis A: General 2007;330:134–8. https://doi.org/10.1016/j.apcata.2007.07.015.
[200] Du J, Gao J, Gu F, Zhuang J, Lu B, Jia L, et al. A strategy to regenerate coked and sintered Ni/Al2O3 catalyst for methanation reaction. International Journal of Hydrogen Energy 2018;43:20661–70. https://doi.org/10.1016/j.ijhydene.2018.09.128.
[201] Dias YR, Perez-Lopez OW. Carbon dioxide methanation over Ni-Cu/SiO2 catalysts. Energy Conversion and Management 2020;203:112214. https://doi.org/10.1016/j.enconman.2019.112214.
[202] Gao J, Liu Q, Gu F, Liu B, Zhong Z, Su F. Recent advances in methanation catalysts for the production of synthetic natural gas. RSC Advances 2015;5:22759–76. https://doi.org/10.1039/C4RA16114A.
[203] Zhang J, Xin Z, Meng X, Tao M. Synthesis, characterization and properties of anti-sintering nickel incorporated MCM-41 methanation catalysts. Fuel 2013;109:693–701. https://doi.org/10.1016/j.fuel.2013.03.037.

[204] Gac W, Zawadzki W, Rotko M, Greluk M, Słowik G, Kolb G. Effects of support composition on the performance of nickel catalysts in CO2 methanation reaction. Catalysis Today 2020;357:468–82. https://doi.org/10.1016/j.cattod.2019.07.026.
[205] Enhanced CO2 methanation at mild temperature on Ni/zeolite from kaolin: effect of metal–support interface. RSC Advances 2021;11:16376–87. https://doi.org/10.1039/d1ra01014j.
[206] Ma Y, Liu J, Chu M, Yue J, Cui Y, Xu G. Cooperation Between Active Metal and Basic Support in Ni-Based Catalyst for Low-Temperature CO2 Methanation. Catal Lett 2020;150:1418–26. https://doi.org/10.1007/s10562-019-03033-w.
[207] Guo X, Traitangwong A, Hu M, Zuo C, Meeyoo V, Peng Z, et al. Carbon Dioxide Methanation over Nickel-Based Catalysts Supported on Various Mesoporous Material. Energy Fuels 2018;32:3681–9. https://doi.org/10.1021/acs.energyfuels.7b03826.
[208] Quatorze IF, Gonçalves LPL, Kolen'ko YV, Soares OSGP, Pereira MFR. CO2 methanation over Ni supported on Carbon–ZrO2: An optimization of the composite composition. Catalysis Today 2023;422:114215. https://doi.org/10.1016/j.cattod.2023.114215.
[209] Gopalakrishnan S, Faga MG, Miletto I, Coluccia S, Caputo G, Sau S, et al. Unravelling the structure and reactivity of supported Ni particles in Ni-CeZrO2 catalysts. Applied Catalysis B: Environmental 2013;138–139:353–61. https://doi.org/10.1016/j.apcatb.2013.02.036.
[210] Costa-Serra JF da, Cerdá-Moreno C, Chica A, Costa-Serra JF da, Cerdá-Moreno C, Chica A. Zeolite-Supported Ni Catalysts for CO2 Methanation: Effect of Zeolite Structure and Si/Al Ratio. Applied Sciences 2020;10. https://doi.org/10.3390/app10155131.
[211] Wei L, Haije W, Kumar N, Peltonen J, Peurla M, Grenman H, et al. Influence of nickel precursors on the properties and performance of Ni impregnated zeolite 5A and 13X catalysts in CO2 methanation. Catalysis Today 2021;362:35–46. https://doi.org/10.1016/j.cattod.2020.05.025.
[212] Bacariza MC, Bértolo R, Graça I, Lopes JM, Henriques C. The effect of the compensating cation on the catalytic performances of Ni/USY zeolites towards CO2 methanation. Journal of CO2 Utilization 2017;21:280–91. https://doi.org/10.1016/j.jcou.2017.07.020.
[213] Hu F, Ye R, Jin C, Liu D, Chen X, Li C, et al. Ni nanoparticles enclosed in highly mesoporous nanofibers with oxygen vacancies for efficient CO2 methanation. Applied Catalysis B: Environmental 2022;317:121715. https://doi.org/10.1016/j.apcatb.2022.121715.
[214] Qin Z, Ren J, Miao M, Li Z, Lin J, Xie K. The catalytic methanation of coke oven gas over Ni-Ce/Al2O3 catalysts prepared by microwave heating: Effect of amorphous NiO formation. Applied Catalysis B: Environmental 2015;164:18–30. https://doi.org/10.1016/j.apcatb.2014.08.047.
[215] Nganga JK, Wolf LM, Mullick K, Reinheimer E, Saucedo C, Wilson ME, et al. Methane Generation from CO2 with a Molecular Rhenium Catalyst. Inorg Chem 2021;60:3572–84. https://doi.org/10.1021/acs.inorgchem.0c02579.
[216] Gothe ML, Silva KLC, Figueredo AL, Fiorio JL, Rozendo J, Manduca B, et al. Rhenium – A Tuneable Player in Tailored Hydrogenation Catalysis. European Journal of Inorganic Chemistry 2021;2021:4043–65. https://doi.org/10.1002/ejic.202100459.

[217] Luo J, Liang C. Rhenium in Heterogeneous Catalysis: A Rising Star for Hydrogenation Reactions. ACS Catal 2024;14:7032–49. https://doi.org/10.1021/acscatal.4c00298.
[218] Ting KW, Toyao T, Siddiki SMAH, Shimizu K. Low-Temperature Hydrogenation of CO2 to Methanol over Heterogeneous TiO2-Supported Re Catalysts. ACS Catal 2019;9:3685–93. https://doi.org/10.1021/acscatal.8b04821.
[219] Duyar MS, Treviño MAA, Farrauto RJ. Dual function materials for CO2 capture and conversion using renewable H2. Applied Catalysis B: Environmental 2015;168–169:370–6. https://doi.org/10.1016/j.apcatb.2014.12.025.
[220] Omodolor IS, Otor HO, Andonegui JA, Allen BJ, Alba-Rubio AC. Dual-Function Materials for CO2 Capture and Conversion: A Review. Ind Eng Chem Res 2020;59:17612–31. https://doi.org/10.1021/acs.iecr.0c02218.
[221] Sun S, Sun H, T. Williams P, Wu C. Recent advances in integrated CO 2 capture and utilization: a review. Sustainable Energy & Fuels 2021;5:4546–59. https://doi.org/10.1039/D1SE00797A.
[222] Sabri MA, Al Jitan S, Bahamon D, Vega LF, Palmisano G. Current and future perspectives on catalytic-based integrated carbon capture and utilization. Science of The Total Environment 2021;790:148081. https://doi.org/10.1016/j.scitotenv.2021.148081.
[223] Bermejo-López A, Pereda-Ayo B, Onrubia-Calvo JA, González-Marcos JA, González-Velasco JR. Enhancement of the CO2 adsorption and hydrogenation to CH4 capacity of Ru–Na–Ca/γ–Al2O3 dual function material by controlling the Ru calcination atmosphere. Journal of Environmental Sciences 2024;140:292–305. https://doi.org/10.1016/j.jes.2023.08.041.
[224] Teixeira P, Bacariza C, Correia P, Pinheiro CIC, Cabrita I. Hydrogen Production with In Situ CO2 Capture at High and Medium Temperatures Using Solid Sorbents. Energies 2022;15:4039. https://doi.org/10.3390/en15114039.
[225] Arellano-Treviño MA, He Z, Libby MC, Farrauto RJ. Catalysts and adsorbents for CO2 capture and conversion with dual function materials: Limitations of Ni-containing DFMs for flue gas applications. Journal of CO2 Utilization 2019;31:143–51. https://doi.org/10.1016/j.jcou.2019.03.009.
[226] Choi S, Drese JH, Jones CW. Adsorbent materials for carbon dioxide capture from large anthropogenic point sources. ChemSusChem 2009;2:796–854. https://doi.org/10.1002/cssc.200900036.
[227] Ahmadpour A, Do DD. Characterization of modified activated carbons: Equilibria and dynamics studies. Carbon 1995;33:1393–8. https://doi.org/10.1016/0008-6223(95)00085-R.
[228] Atci E, Erucar I, Keskin S. Adsorption and Transport of CH4, CO2, H2 Mixtures in a Bio-MOF Material from Molecular Simulations. J Phys Chem C 2011;115:6833–40. https://doi.org/10.1021/jp200429x.
[229] Megías-Sayago C, Bingre R, Huang L, Lutzweiler G, Wang Q, Louis B. CO2 Adsorption Capacities in Zeolites and Layered Double Hydroxide Materials. Front Chem 2019;7. https://doi.org/10.3389/fchem.2019.00551.
[230] Ramírez-Moreno MJ, Romero-Ibarra IC, Hernández-Pérez MA, Pfeiffer H. CO2 Adsorption at Elevated Pressure and Temperature on Mg–Al Layered

Double Hydroxide. Ind Eng Chem Res 2014;53:8087–94. https://doi.org/10.1021/ie5010515.
[231] Lee CH, Mun S, Lee KB. Characteristics of Na–Mg double salt for high-temperature CO2 sorption. Chemical Engineering Journal 2014;258:367–73. https://doi.org/10.1016/j.cej.2014.07.082.
[232] Wang Q, Luo J, Zhong Z, Borgna A. CO2 capture by solid adsorbents and their applications: current status and new trends. Energy & Environmental Science 2011;4:42–55. https://doi.org/10.1039/C0EE00064G.
[233] Tageldin A, Ismail R, Sardar A, Saad MAH, Benamor Abdelbaki. Synthesis and evaluation of novel and efficient Ni-based dual functional materials (DFMs) for integrated CO2 capture and hydrogenation. Chemical Engineering Research and Design 2023;197:628–42. https://doi.org/10.1016/j.cherd.2023.07.025.
[234] Le TA, Kim TW, Lee SH, Park ED. Effects of Na content in Na/Ni/SiO2 and Na/Ni/CeO2 catalysts for CO and CO2 methanation. Catalysis Today 2018;303:159–67. https://doi.org/10.1016/j.cattod.2017.09.031.
[235] Bian Z, Chan YM, Yu Y, Kawi S. Morphology dependence of catalytic properties of Ni/CeO2 for CO2 methanation: A kinetic and mechanism study. Catalysis Today 2020;347:31–8. https://doi.org/10.1016/j.cattod.2018.04.067.
[236] Merkouri L-P, Reina TR, Duyar MS. Closing the Carbon Cycle with Dual Function Materials. Energy Fuels 2021;35:19859–80. https://doi.org/10.1021/acs.energyfuels.1c02729.
[237] Rizzetto A, Piumetti M, Pirone R, Sartoretti E, Bensaid S. Study of ceria-composite materials for high-temperature CO2 capture and their ruthenium functionalization for methane production. Catalysis Today 2024;429:114478. https://doi.org/10.1016/j.cattod.2023.114478.
[238] Thu Ha NT, Minh Hue VT, Trinh BC, Ha NN, Cam LM. Study on the Adsorption and Activation Behaviours of Carbon Dioxide over Copper Cluster (Cu4) and Alumina-Supported Copper Catalyst (Cu4/Al2O3) by means of Density Functional Theory. Journal of Chemistry 2019;2019:4341056. https://doi.org/10.1155/2019/4341056.
[239] Fang X, Chen C, Jia H, Li Y, Liu J, Wang Y, et al. Progress in Adsorption-Enhanced Hydrogenation of CO2 on Layered Double Hydroxide (LDH) Derived Catalysts. Journal of Industrial and Engineering Chemistry 2021;95:16–27. https://doi.org/10.1016/j.jiec.2020.12.027.
[240] Wang J, Huang L, Yang R, Zhang Z, Wu J, Gao Y, et al. Recent advances in solid sorbents for CO2 capture and new development trends. Energy Environ Sci 2014;7:3478–518. https://doi.org/10.1039/C4EE01647E.
[241] Zhu X, Chen C, Wang Q, Shi Y, O'Hare D, Cai N. Roles for K2CO3 doping on elevated temperature CO2 adsorption of potassium promoted layered double oxides. Chemical Engineering Journal 2019;366:181–91. https://doi.org/10.1016/j.cej.2019.01.192.
[242] Li S, Zheng A, Su Y, Zhang H, Chen L, Yang J, et al. Brønsted/Lewis Acid Synergy in Dealuminated HY Zeolite: A Combined Solid-State NMR and Theoretical Calculation Study. J Am Chem Soc 2007;129:11161–71. https://doi.org/10.1021/ja072767y.
[243] Schroeder C, Hansen MR, Koller H. Ultrastabilization of Zeolite Y Transforms Brønsted–Brønsted Acid Pairs into Brønsted–Lewis Acid Pairs. Angewandte Chemie International Edition 2018;57:14281–5. https://doi.org/10.1002/anie.201808395.

[244] Huang C, Li A, Chao Z-S. Heterogeneous catalytic synthesis of quinoline compounds from aniline and C1–C4 alcohols over zeolite-based catalysts. RSC Adv 2017;7:48275–85. https://doi.org/10.1039/C7RA08442K.
[245] Da Costa-Serra JF, Navarro MT, Rey F, Chica A. Bioethanol steam reforming on Ni-based modified mordenite. Effect of mesoporosity, acid sites and alkaline metals. International Journal of Hydrogen Energy 2012;37:7101–8. https://doi.org/10.1016/j.ijhydene.2011.10.086.
[246] Verboekend D, Vilé G, Pérez-Ramírez J. Hierarchical Y and USY Zeolites Designed by Post-Synthetic Strategies. Advanced Functional Materials 2012;22:916–28. https://doi.org/10.1002/adfm.201102411.
[247] Hartmann M, Machoke AG, Schwieger W. Catalytic test reactions for the evaluation of hierarchical zeolites. Chem Soc Rev 2016;45:3313–30. https://doi.org/10.1039/C5CS00935A.
[248] Spataru D, Canastreiro D, Świrk Da Costa K, Quindimil A, Lopes JM, Da Costa P, et al. Doping Ni/USY zeolite catalysts with transition metals for CO2 methanation. International Journal of Hydrogen Energy 2024;53:468–81. https://doi.org/10.1016/j.ijhydene.2023.12.045.
[249] Hu F, Ye R, Lu Z-H, Zhang R, Feng G. Structure–Activity Relationship of Ni-Based Catalysts toward CO2 Methanation: Recent Advances and Future Perspectives. Energy Fuels 2022;36:156–69. https://doi.org/10.1021/acs.energyfuels.1c03645.
[250] Tian X, Wei Y, Zhao H. Evaluation of a hierarchically-structured CuO@TiO2-Al2O3 oxygen carrier for chemical looping with oxygen uncoupling. Fuel 2017;209:402–10. https://doi.org/10.1016/j.fuel.2017.08.022.
[251] Moon D-S, Lee J-K. Tunable Synthesis of Hierarchical Mesoporous Silica Nanoparticles with Radial Wrinkle Structure. Langmuir 2012;28:12341–7. https://doi.org/10.1021/la302145j.
[252] Lee S-U, Lee Y-J, Kwon S-J, Kim J-R, Jeong S-Y, Lee S-U, et al. Pt-Sn Supported on Beta Zeolite with Enhanced Activity and Stability for Propane Dehydrogenation. Catalysts 2020;11. https://doi.org/10.3390/catal11010025.
[253] Gao X, Li J, Zheng M, Cai S, Zhang J, Askari S, et al. Recent progress in anti-coking Ni catalysts for thermo-catalytic conversion of greenhouse gases. Process Safety and Environmental Protection 2021;156:598–616. https://doi.org/10.1016/j.psep.2021.10.051.
[254] Ranjbar A, Irankhah A, Aghamiri SF. Reverse water gas shift reaction and CO2 mitigation: nanocrystalline MgO as a support for nickel based catalysts. Journal of Environmental Chemical Engineering 2018;6:4945–52. https://doi.org/10.1016/j.jece.2018.07.032.
[255] Liu N, Cui S, Jin Z, Cao Z, Liu H, Yang S, et al. Highly Dispersed and Stable Ni/SiO2 Catalysts Prepared by Urea-Assisted Impregnation Method for Reverse Water–Gas Shift Reaction. Processes 2023;11. https://doi.org/10.3390/pr11051353.
[256] Boosting the performance of Ni/Al2O3 for the reverse water gas shift reaction through formation of CuNi nanoalloys. Catalysis Science & Technology 2022;12:474–87. https://doi.org/10.1039/d1cy01585k.
[257] Sun H, Wang J, Zhao J, Shen B, Shi J, Huang J, et al. Dual functional catalytic materials of Ni over Ce-modified CaO sorbents for integrated CO2

capture and conversion. Applied Catalysis B: Environmental 2019;244:63–75. https://doi.org/10.1016/j.apcatb.2018.11.040.
[258] Xuan Law Z, Pan Y-T, Tsai D-H. Calcium looping of CO2 capture coupled to syngas production using Ni-CaO-based dual functional material. Fuel 2022;328:125202. https://doi.org/10.1016/j.fuel.2022.125202.
[259] Buelens L, Voorde L, Singh V, Poelman H, Marin B, Galvita V. Probing the Performance of a Ni–Ca–Ce Dual-Functional Material for Integrated CO 2 Capture and Utilization from a Synthetic Flue Gas Approximating Industrial Composition. Industrial & Engineering Chemistry Research 2023;62. https://doi.org/10.1021/acs.iecr.3c02459.
[260] Gu H, Shen X, Yu M, Niu M, Zhao S, Zhang S, et al. Isothermal CO2 capture and in-situ conversion in dry reforming of methane using a catalytic sorbent of CaO-Ni/CeO2 prepared via sol–gel method. Separation and Purification Technology 2025;372:133460. https://doi.org/10.1016/j.seppur.2025.133460.
[261] Wei L, Han R, Han G, Yan H, Peng M, Li Z, et al. Modulating the Evolution of Metastable CaO* for the Near-Theoretical Performance Breakthrough of Ni/CeO2-CaO in Integrated CO2 Capture and Methanation. Advanced Science 2025;12:2503086. https://doi.org/10.1002/advs.202503086.
[262] Hu J, Hongmanorom P, Chirawatkul P, Kawi S. Efficient integration of CO2 capture and conversion over a Ni supported CeO2-modified CaO microsphere at moderate temperature. Chemical Engineering Journal 2021;426:130864. https://doi.org/10.1016/j.cej.2021.130864.
[263] Sun H, Sun S, Liu T, Zeng J, Wang Y, Yan Z, et al. Integrated CO2 Capture and Utilization: Selection, Matching, and Interactions between Adsorption and Catalytic Sites. ACS Catal 2024;14:15572–89. https://doi.org/10.1021/acscatal.4c03861.
[264] Shen Y, Sun S, Sun H, Xu Y, Zhou H, Wu C, et al. Dual functional materials for integrated CO2 capture and utilization (ICCU): Design, fabrication, performances, and challenges. Chemical Engineering Journal 2025;512:162440. https://doi.org/10.1016/j.cej.2025.162440.
[265] Li C, Sakata Y, Arai T, Domen K, Maruya K, Onishi T. Adsorption of carbon monoxide and carbon dioxide on cerium oxide studied by Fourier-transform infrared spectroscopy. Part 2.—Formation of formate species on partially reduced CeO2 at room temperature. J Chem Soc, Faraday Trans 1 1989;85:1451–61. https://doi.org/10.1039/F19898501451.
[266] Li C, Sakata Y, Arai T, Domen K, Maruya K, Onishi T. Carbon monoxide and carbon dioxide adsorption on cerium oxide studied by Fourier-transform infrared spectroscopy. Part 1.—Formation of carbonate species on dehydroxylated CeO2, at room temperature. J Chem Soc, Faraday Trans 1 1989;85:929–43. https://doi.org/10.1039/F19898500929.
[267] Molinet-Chinaglia C, Vera E, Vernoux P, Piccolo L, Loridant S. Influence of redox treatments on the low-temperature water gas shift reaction over Pt/CeO2 catalysts. Catal Sci Technol 2024;14:6247–58. https://doi.org/10.1039/D4CY00741G.
[268] Phongprueksathat N, Ting KW, Mine S, Jing Y, Toyoshima R, Kondoh H, et al. Bifunctionality of Re Supported on TiO2 in Driving Methanol Formation in Low-Temperature CO2 Hydrogenation. ACS Catal 2023;13:10734–50. https://doi.org/10.1021/acscatal.3c01599.

[269] Yang B, Wang Y, Li L, Gao B, Zhang L, Guo L. Probing the morphological effects of ReOx/CeO2 catalysts on the CO2 hydrogenation reaction. Catal Sci Technol 2022;12:1159–72. https://doi.org/10.1039/D1CY02096J.
[270] Binet C, Daturi M, Lavalley J-C. IR study of polycrystalline ceria properties in oxidised and reduced states. Catalysis Today 1999;50:207–25. https://doi.org/10.1016/S0920-5861(98)00504-5.
[271] Daturi M, Binet C, Lavalley JC, Blanchard G. Surface FTIR investigations on CexZr1−xO2 system. Surface and Interface Analysis 2000;30:273–7. https://doi.org/10.1002/1096-9918(200008)30:1%253C273::AID-SIA715%253E3.0.CO;2-G.
[272] Binet C, Daturi M. Methanol as an IR probe to study the reduction process in ceria–zirconia mixed compounds. Catalysis Today 2001;70:155–67. https://doi.org/10.1016/S0920-5861(01)00415-1.
[273] Siokou A, Nix RM. Interaction of Methanol with Well-Defined Ceria Surfaces: Reflection/Absorption Infrared Spectroscopy, X-ray Photoelectron Spectroscopy, and Temperature-Programmed Desorption Study. J Phys Chem B 1999;103:6984–97. https://doi.org/10.1021/jp991127h.
[274] Sun S, Sun H, Guan S, Xu S, Wu C. Integrated CO2 capture and methanation on Ru/CeO2-MgO combined materials: Morphology effect from CeO2 support. Fuel 2022;317:123420. https://doi.org/10.1016/j.fuel.2022.123420.
[275] Cimino S, Cepollaro EM, Lisi L. Sulfur tolerance and self-regeneration mechanism of Na-Ru/Al2O3 dual function material during the cyclic CO2 capture and catalytic methanation. Applied Catalysis B: Environmental 2022;317:121705. https://doi.org/10.1016/j.apcatb.2022.121705.
[276] Roode-Gutzmer QI, Kaiser D, Bertau M. Renewable Methanol Synthesis. ChemBioEng Reviews 2019;6:209–36. https://doi.org/10.1002/cben.201900012.
[277] Guil-López R, Mota N, Llorente J, Millán E, Pawelec B, Fierro JLG, et al. Methanol Synthesis from CO2: A Review of the Latest Developments in Heterogeneous Catalysis. Materials 2019;12. https://doi.org/10.3390/ma12233902.
[278] Bowker M. Methanol Synthesis from CO2 Hydrogenation. ChemCatChem 2019;11:4238–46. https://doi.org/10.1002/cctc.201900401.
[279] Waugh KC. Methanol Synthesis. Catalysis Today 1992;15:51–75. https://doi.org/10.1016/0920-5861(92)80122-4.
[280] Kung HH. Deactivation of methanol synthesis catalysts - a review. Catalysis Today 1992;11:443–53. https://doi.org/10.1016/0920-5861(92)80037-N.
[281] Terreni J, Trottmann M, Franken T, Heel A, Borgschulte A. Sorption-Enhanced Methanol Synthesis. Energy Technology 2019;7:1801093. https://doi.org/10.1002/ente.201801093.
[282] De S, Dokania A, Ramirez A, Gascon J. Advances in the Design of Heterogeneous Catalysts and Thermocatalytic Processes for $CO_2$ Utilization. ACS Catal 2020;10:14147–85. https://doi.org/10.1021/acscatal.0c04273.

[283] Saeidi S, Amin NAS, Rahimpour MR. Hydrogenation of CO2 to value-added products—A review and potential future developments. Journal of CO2 Utilization 2014;5:66–81. https://doi.org/10.1016/j.jcou.2013.12.005.
[284] Ali KA, Abdullah AZ, Mohamed AR. Recent development in catalytic technologies for methanol synthesis from renewable sources: A critical review. Renewable and Sustainable Energy Reviews 2015;44:508–18. https://doi.org/10.1016/j.rser.2015.01.010.
[285] Dang S, Yang H, Gao P, Wang H, Li X, Wei W, et al. A review of research progress on heterogeneous catalysts for methanol synthesis from carbon dioxide hydrogenation. Catalysis Today 2019;330:61–75. https://doi.org/10.1016/j.cattod.2018.04.021.
[286] Burch R, Golunski SE, Spencer MS. The role of copper and zinc oxide in methanol synthesis catalysts. J Chem Soc, Faraday Trans 1990;86:2683–91. https://doi.org/10.1039/FT9908602683.
[287] Palomino RM, Ramírez PJ, Liu Z, Hamlyn R, Waluyo I, Mahapatra M, et al. Hydrogenation of CO2 on ZnO/Cu(100) and ZnO/Cu(111) Catalysts: Role of Copper Structure and Metal–Oxide Interface in Methanol Synthesis. J Phys Chem B 2018;122:794–800. https://doi.org/10.1021/acs.jpcb.7b06901.
[288] Beck A, Newton MA, van de Water LGA, van Bokhoven JA. The Enigma of Methanol Synthesis by Cu/ZnO/Al2O3-Based Catalysts. Chem Rev 2024;124:4543–678. https://doi.org/10.1021/acs.chemrev.3c00148.
[289] Kattel S, Ramírez PJ, Chen JG, Rodriguez JA, Liu P. Active sites for CO2 hydrogenation to methanol on Cu/ZnO catalysts. Science 2017;355:1296–9. https://doi.org/10.1126/science.aal3573.
[290] Behrens M, Studt F, Kasatkin I, Kühl S, Hävecker M, Abild-Pedersen F, et al. The Active Site of Methanol Synthesis over Cu/ZnO/Al2O3 Industrial Catalysts. Science 2012;336:893–7. https://doi.org/10.1126/science.1219831.
[291] Toyir J, Ramírez de la Piscina P, Homs N. Ga-promoted copper-based catalysts highly selective for methanol steam reforming to hydrogen; relation with the hydrogenation of CO2 to methanol. International Journal of Hydrogen Energy 2015;40:11261–6. https://doi.org/10.1016/j.ijhydene.2015.04.039.
[292] Kourtelesis M, Kousi K, Kondarides DI. CO2 Hydrogenation to Methanol over La2O3-Promoted CuO/ZnO/Al2O3 Catalysts: A Kinetic and Mechanistic Study. Catalysts 2020;10. https://doi.org/10.3390/catal10020183.
[293] Wang L, Etim UJ, Zhang C, Amirav L, Zhong Z. CO2 Activation and Hydrogenation on Cu-ZnO/Al2O3 Nanorod Catalysts: An In Situ FTIR Study. Nanomaterials (Basel) 2022;12:2527. https://doi.org/10.3390/nano12152527.
[294] Lee S, Schneider K, Schumann J, Mogalicherla AK, Pfeifer P, Dittmeyer R. Effect of metal precursor on Cu/ZnO/Al2O3 synthesized by flame spray pyrolysis for direct DME production. Chemical Engineering Science 2015;138:194–202. https://doi.org/10.1016/j.ces.2015.08.021.
[295] Greener and facile synthesis of Cu/ZnO catalysts for CO2 hydrogenation to methanol by urea hydrolysis of acetates. RSC Advances 2021;11:14323–33. https://doi.org/10.1039/d1ra02103f.
[296] Chen J, He Y, Tang C, Wang J, Sun Y, Wen X, et al. Zinc oxide morphology-dependent CuOx-ZnO interactions and catalysis in CO

oxidation and CO2 hydrogenation. Applied Surface Science 2025;680:161295. https://doi.org/10.1016/j.apsusc.2024.161295.
[297] An Insight into Synergistic Metal-Oxide Interaction in CO2 Hydrogenation to Methanol over Cu/ZnO/ZrO2 | MDPI n.d. https://www.mdpi.com/2073-4344/13/10/1337 (accessed January 18, 2026).
[298] Stangeland K, Navarro HH, Huynh HL, Tucho WM, Yu Z. Tuning the interfacial sites between copper and metal oxides (Zn, Zr, In) for CO2 hydrogenation to methanol. Chemical Engineering Science 2021;238:116603. https://doi.org/10.1016/j.ces.2021.116603.
[299] Sun Y, Huang C, Chen L, Zhang Y, Fu M, Wu J, et al. Active site structure study of Cu/Plate ZnO model catalysts for CO2 hydrogenation to methanol under the real reaction conditions. Journal of CO2 Utilization 2020;37:55–64. https://doi.org/10.1016/j.jcou.2019.11.029.
[300] Luo M-F, Fang P, He M, Xie Y-L. In situ XRD, Raman, and TPR studies of CuO/Al2O3 catalysts for CO oxidation. Journal of Molecular Catalysis A: Chemical 2005;239:243–8. https://doi.org/10.1016/j.molcata.2005.06.029.
[301] Stangeland K, Navarro HH, Huynh HL, Tucho WM, Yu Z. Tuning the interfacial sites between copper and metal oxides (Zn, Zr, In) for CO2 hydrogenation to methanol. Chemical Engineering Science 2021;238:116603. https://doi.org/10.1016/j.ces.2021.116603.
[302] Sun Y, Huang C, Chen L, Zhang Y, Fu M, Wu J, et al. Active site structure study of Cu/Plate ZnO model catalysts for CO2 hydrogenation to methanol under the real reaction conditions. Journal of CO2 Utilization 2020;37:55–64. https://doi.org/10.1016/j.jcou.2019.11.029.
[303] Wei X, Su W, Shi Y, Wang J, Lv P, Song X, et al. Cu0 at the Cu/ZnO interface efficiently accelerate CO2 hydrogenation to methanol over Cu/ZnO/C–P catalysts. International Journal of Hydrogen Energy 2024;58:128–36. https://doi.org/10.1016/j.ijhydene.2024.01.162.
[304] Dow W-P, Wang Y-P, Huang T-J. TPR and XRD studies of yttria-doped ceria/γ-alumina-supported copper oxide catalyst. Applied Catalysis A: General 2000;190:25–34. https://doi.org/10.1016/S0926-860X(99)00286-0.
[305] Zhang F, Liu Y, Xu X, Yang P, Miao P, Zhang Y, et al. Effect of Al-containing precursors on Cu/ZnO/Al2O3 catalyst for methanol production. Fuel Processing Technology 2018;178:148–55. https://doi.org/10.1016/j.fuproc.2018.04.021.
[306] Mohamed AT, Ahmad YH, Anwer AH, Soliman A, Saad MAH, Aroua MK, et al. CO2 Conversion to Dimethyl Ether on Cu/ZnO/Al2O3-ZSM-5 Tandem Catalysts in a Double-Bed Reactor: Tuning the ZSM-5 Catalyst Acidity and Porosity. Energy Fuels 2025;39:2059–74. https://doi.org/10.1021/acs.energyfuels.4c04512.
[307] Nagai M, Koizumi K, Omi S. NH3-TPD and XPS studies of Ru/Al2O3 catalyst and HDS activity. Catalysis Today 1997;35:393–405. https://doi.org/10.1016/S0920-5861(96)00214-3.
[308] Liu Z, An X, Song M, Wang Z, Wei Y, Mintova S, et al. Dry gel assisting crystallization of bifunctional CuO–ZnO–Al2O3/SiO2–Al2O3 catalysts for CO2 hydrogenation. Biomass and Bioenergy 2022;163:106525. https://doi.org/10.1016/j.biombioe.2022.106525.

[309] Direct CO2-to-dimethyl Ether Hydrogenation over CuZnZr/zeolite Hybrid Catalyst: New Evidences on the Interaction Between Acid and Metal Sites | IIETA n.d. https://doi.org/10.18280/acsm.430302.
[310] Tursunov O, Kustov L, Tilyabaev Z. Methanol synthesis from the catalytic hydrogenation of CO2 over CuO–ZnO supported on aluminum and silicon oxides. Journal of the Taiwan Institute of Chemical Engineers 2017;78:416–22. https://doi.org/10.1016/j.jtice.2017.06.049.
[311] Hernández WY, Aliç F, Verberckmoes A, et al. Tuning the acidic–basic properties by Zn-substitution in Mg–Al hydrotalcites as optimal catalysts for the aldol condensation reaction. J Mater Sci 2017;52:628–42. https://doi.org/10.1007/s10853-016-0360-3.
[312] Pinheiro AL, Pinheiro AN, Valentini A, Filho JM, Sousa FF de, Sousa JR de, et al. Analysis of coke deposition and study of the structural features of MAl2O4 catalysts for the dry reforming of methane. Catalysis Communications 2009;11:11–4. https://doi.org/10.1016/j.catcom.2009.08.003.
[313] Khani Y, Bahadoran F, Soltanali S, Ahari JS. Hydrogen production by methanol steam reforming on a cordierite monolith reactor coated with Cu–Ni/LaZnAlO4 and Cu–Ni/γ-Al2O3 catalysts. Res Chem Intermed 2018;44:925–42. https://doi.org/10.1007/s11164-017-3144-8.
[314] Freire RM, de Sousa FF, Pinheiro AL, Longhinotti E, Filho JM, Oliveira AC, et al. Studies of catalytic activity and coke deactivation of spinel oxides during ethylbenzene dehydrogenation. Applied Catalysis A: General 2009;359:165–79. https://doi.org/10.1016/j.apcata.2009.02.036.
[315] Graaf GH, Stamhuis EJ, Beenackers AACM. Kinetics of low-pressure methanol synthesis. Chemical Engineering Science 1988;43:3185–95. https://doi.org/10.1016/0009-2509(88)85127-3.
[316] Graaf GH, Sijtsema PJJM, Stamhuis EJ, Joosten GEH. Chemical equilibria in methanol synthesis. Chemical Engineering Science 1986;41:2883–90. https://doi.org/10.1016/0009-2509(86)80019-7.
[317] Sun JT, Metcalfe IS, Sahibzada M. Deactivation of Cu/ZnO/Al2O3 Methanol Synthesis Catalyst by Sintering. Ind Eng Chem Res 1999;38:3868–72. https://doi.org/10.1021/ie990078s.
[318] Fichtl MB, Schlereth D, Jacobsen N, Kasatkin I, Schumann J, Behrens M, et al. Kinetics of deactivation on Cu/ZnO/Al2O3 methanol synthesis catalysts. Applied Catalysis A: General 2015;502:262–70. https://doi.org/10.1016/j.apcata.2015.06.014.
[319] Rodríguez-González L, Hermes F, Bertmer M, Rodríguez-Castellón E, Jiménez-López A, Simon U. The acid properties of H-ZSM-5 as studied by NH3-TPD and 27Al-MAS-NMR spectroscopy. Applied Catalysis A: General 2007;328:174–82. https://doi.org/10.1016/j.apcata.2007.06.003.
[320] Shirazi L, Jamshidi E, Ghasemi MR. The effect of Si/Al ratio of ZSM-5 zeolite on its morphology, acidity and crystal size. Crystal Research and Technology 2008;43:1300–6. https://doi.org/10.1002/crat.200800149.
[321] Bonura G, Todaro S, Frusteri L, Majchrzak-Kucęba I, Wawrzyńczak D, Pászti Z, et al. Inside the reaction mechanism of direct CO2 conversion to DME over zeolite-based hybrid catalysts. Applied Catalysis B: Environmental 2021;294:120255. https://doi.org/10.1016/j.apcatb.2021.120255.
[322] Fan X, Jin B, Ren S, Li S, Yu M, Liang X. Roles of interaction between components in CZZA/HZSM-5 catalyst for dimethyl ether synthesis via

CO2 hydrogenation. AIChE Journal 2021;67:e17353. https://doi.org/10.1002/aic.17353.
[323] Bonura G, Migliori M, Frusteri L, Cannilla C, Catizzone E, Giordano G, et al. Acidity control of zeolite functionality on activity and stability of hybrid catalysts during DME production via CO2 hydrogenation. Journal of CO2 Utilization 2018;24:398–406. https://doi.org/10.1016/j.jcou.2018.01.028.
[324] Frusteri F, Cordaro M, Cannilla C, Bonura G. Multifunctionality of Cu–ZnO–ZrO2/H-ZSM5 catalysts for the one-step CO2-to-DME hydrogenation reaction. Applied Catalysis B: Environmental 2015;162:57–65. https://doi.org/10.1016/j.apcatb.2014.06.035.

# Appendix A

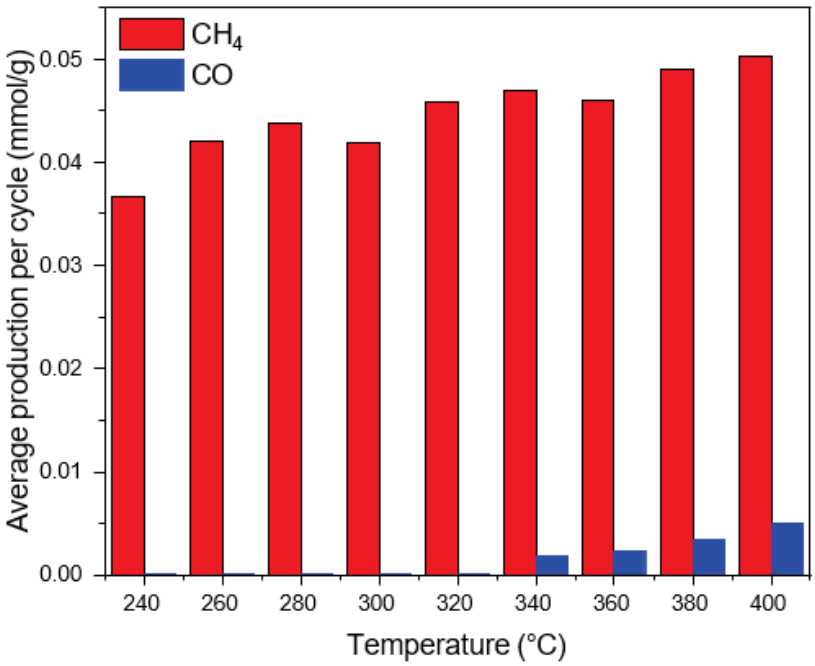


**Figure A.1. Produced $CH_4$ and CO amounts during ICCU tests of $Re/Al_2O_3$ catalyst at increasing temperature (adsorption/reaction times: 3/3 min).**

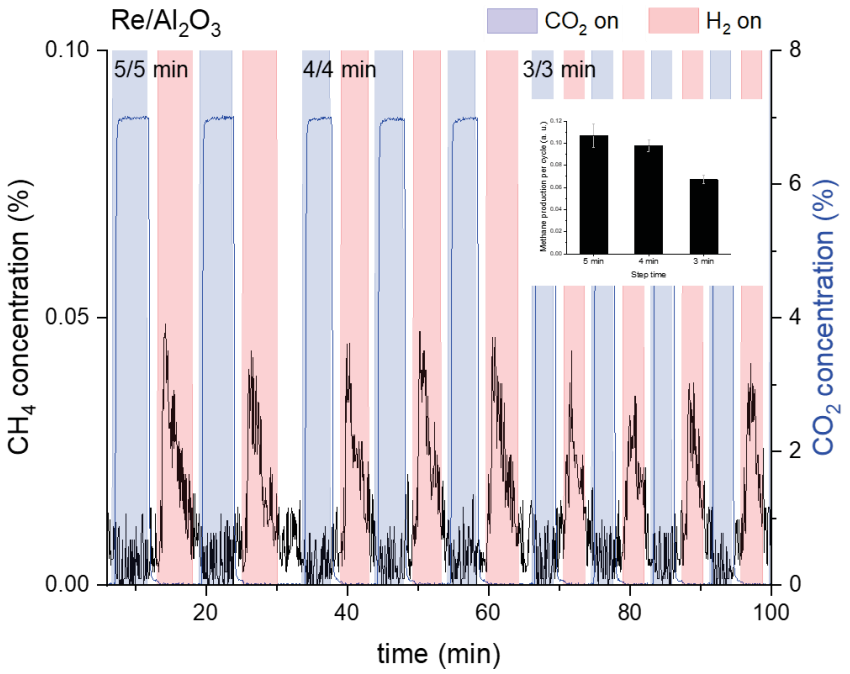


**Figure A.2. $CH_4$ concentration during ICCU test of $Re/Al_2O_3$ to compare three adsorption/reaction times (5/5 min, 4/4 min, and 3/3 min).**

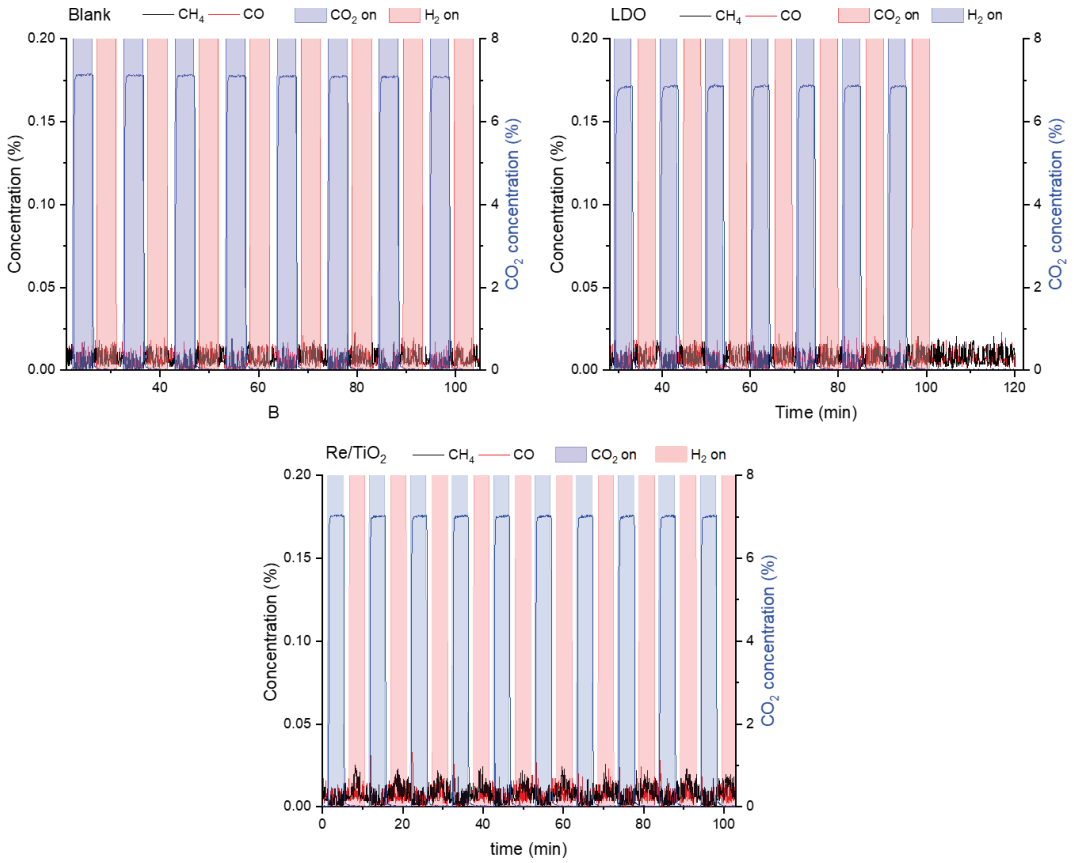


**Figure A.3. ICCU tests on inert SiC powder, pure LDO and $Re/TiO_2$ catalysts under standard conditions (300 °C, 4 min step).**

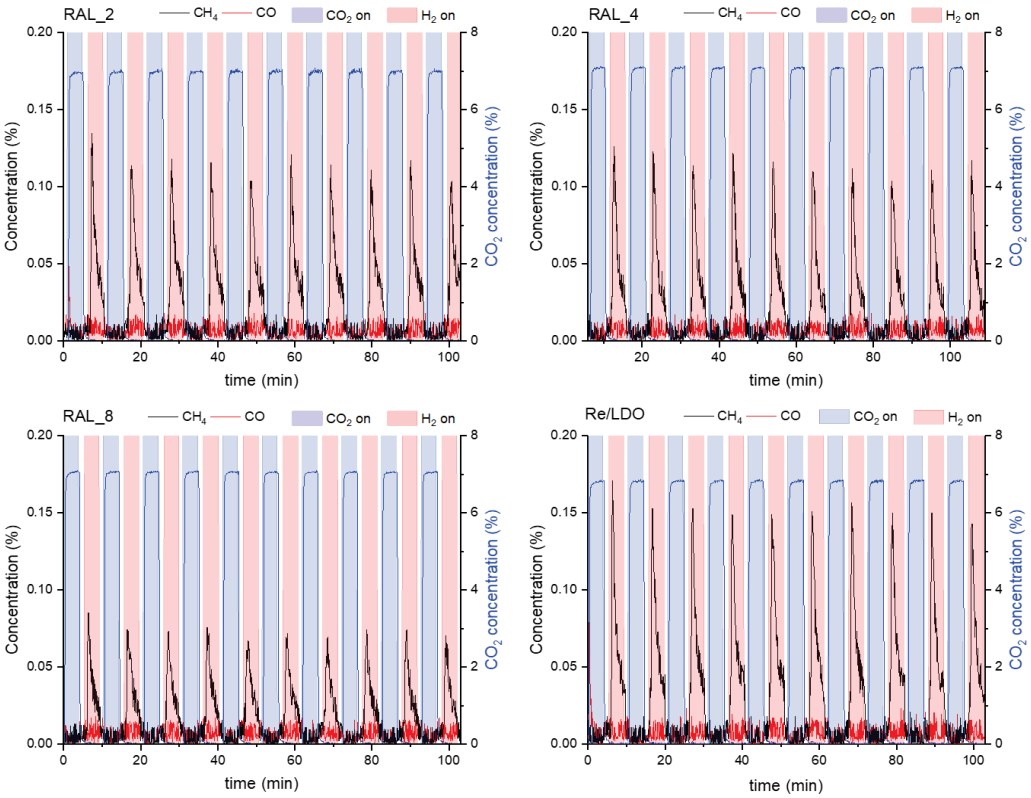


**Figure A.4. First ten cycles of ICCU tests for LDH-diluted Re/$Al_2O_3$ and Re/LDO.**

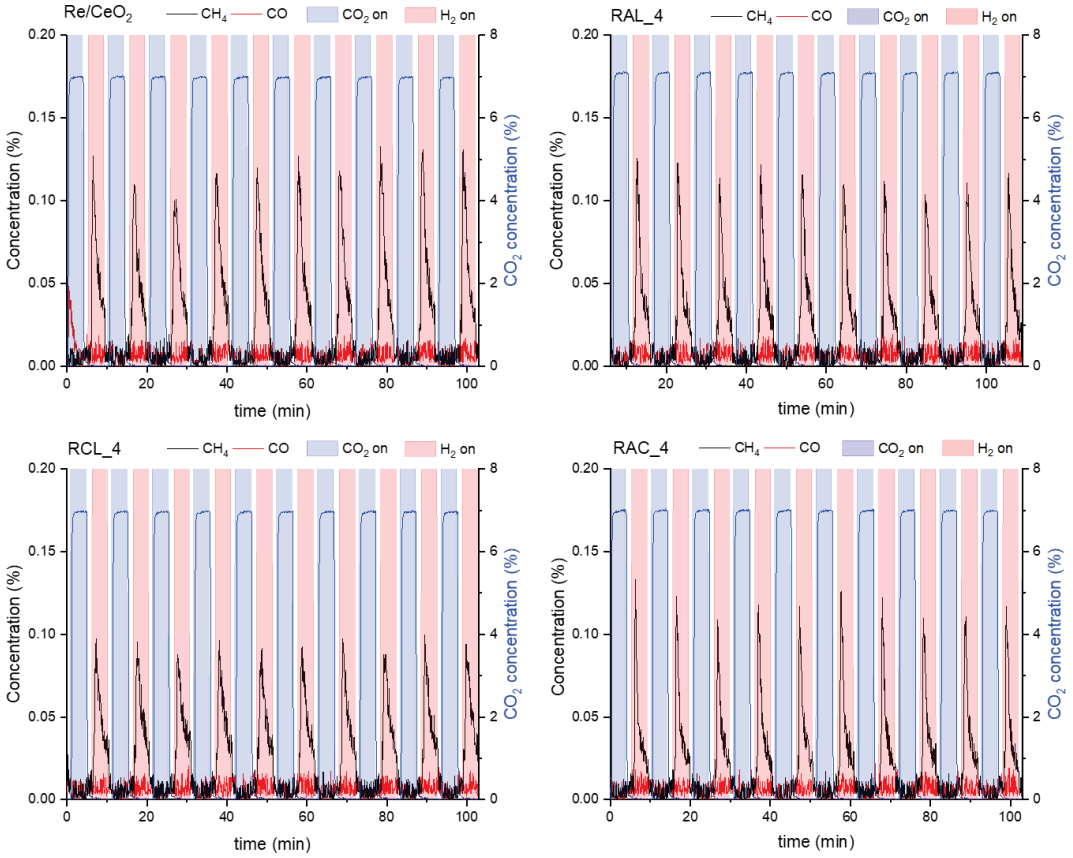


**Figure A.5. First ten cycles of ICCU test of for $Re/CeO_2$, $Re/Al_2O_3$ + LDH (RAL_4), $Re/CeO_2$ + LDH (RCL_4), and $Re/Al_2O_3$ + $CeO_2$ (RAC_4).**

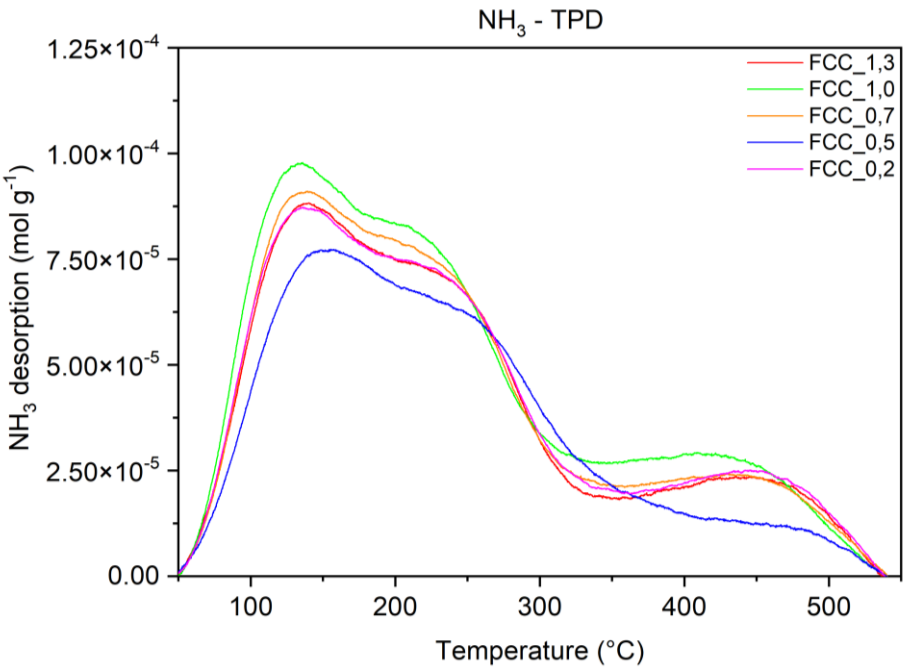


**Figure A.6. $NH_3$-TPD profiles of FCC_X catalysts, supported on HZSM-5. The desorption features indicate the presence of weak, moderate and strong acid sites.**

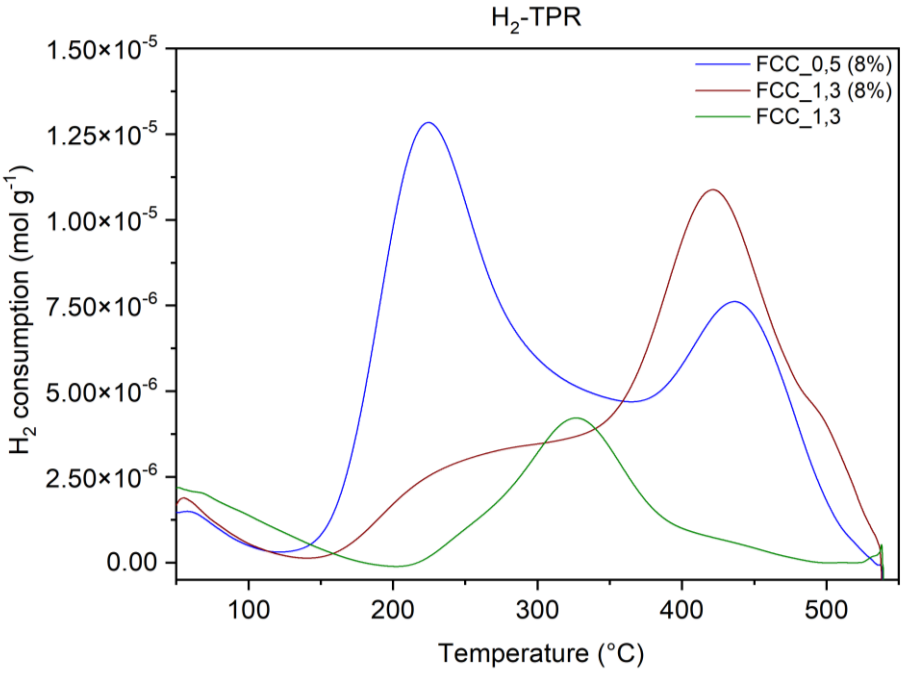


**Figure A.7. $H_2$-TPR profiles of selected FCC catalysts with different metal loadings and compositions. The reduction peaks reflect the progressive reduction of Cu- and Fe-based oxide species, with shifts in peak position and intensity.**

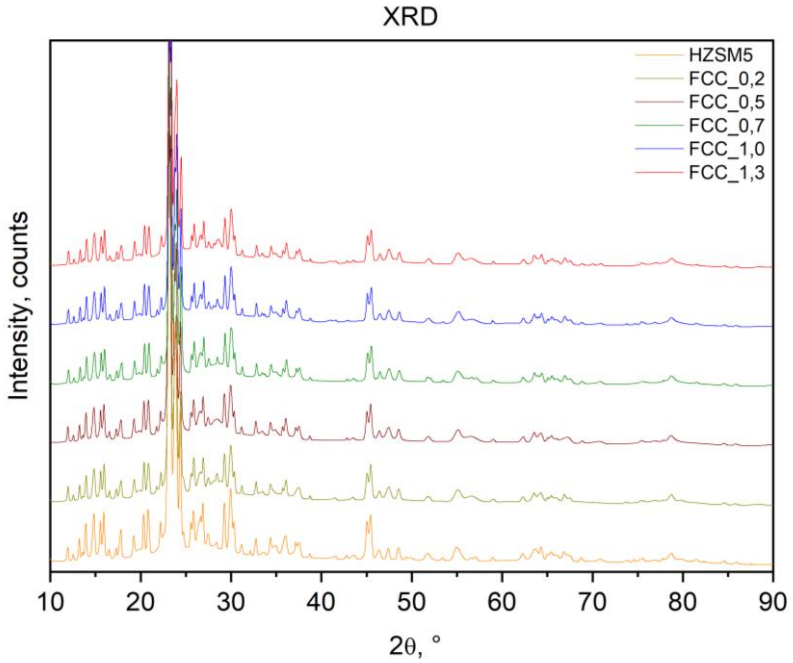


**Figure A.8. XRD patterns of FCC_X catalysts and fresh HZSM-5 zeolite support. All samples exhibit diffraction features characteristic of the zeolite framework, while no distinct reflections attributable to crystalline Cu, Fe, or Ce oxide phases are detected.**

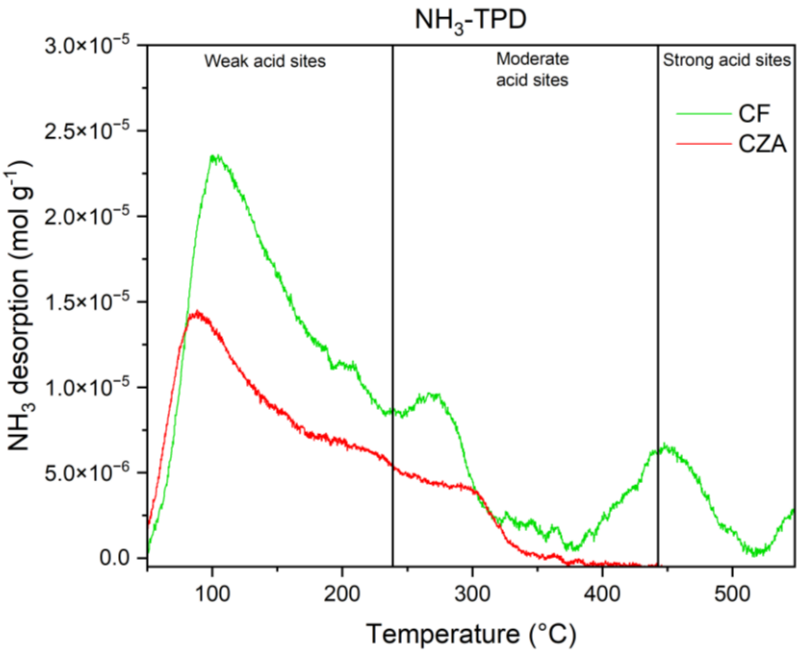


**Figure A.9. $NH_3$-TPD profiles of CF and CZA catalysts. The CF catalyst exhibits as higher contribution of moderate-to-strong acid sites compared to CZA, highlighting differences in surface acidity induced by catalyst composition.**

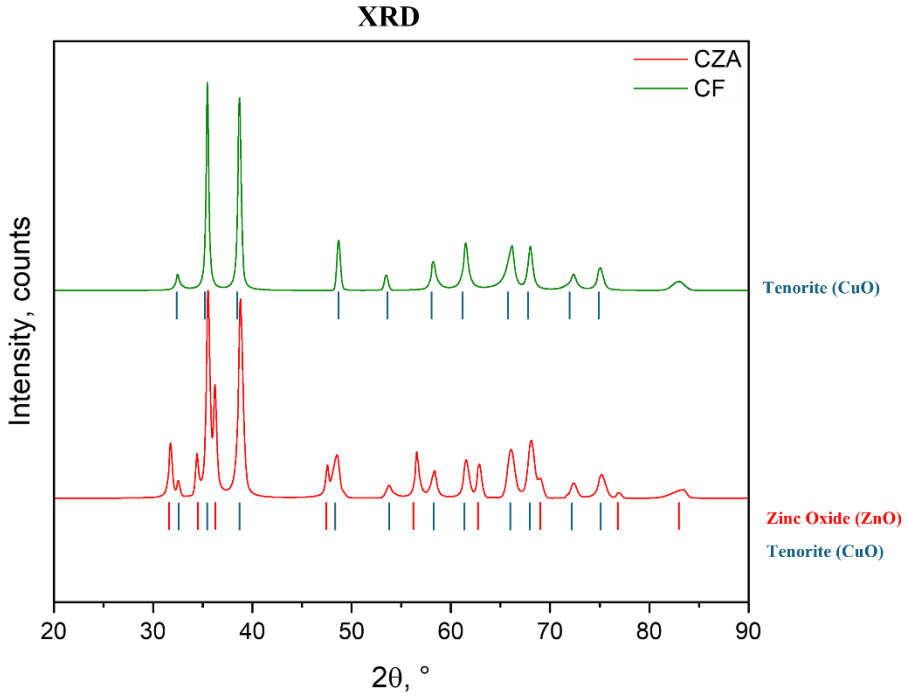


**Figure A.10. XRD patterns of CZA and CF catalysts with reference diffraction line of CuO and ZnO. The experimental patterns confirm the presence of copper oxide phase and, in the case of CZA, zinc oxide.**